UNIVERSIDAD COMPLUTENSE DE MADRID
FACULTAD DE CIENCIAS FÍSICAS

DOCTORAL THESIS

Evolution of interstellar dust grains in molecular cloud envelopes. Observational imprints and theoretical expectations.

Evolución del polvo interestelar en las envolturas de las nubes moleculares. Traza observacional y predicciones teóricas.

A THESIS SUBMITTED FOR THE DEGREE OF
DOCTOR IN ASTROPHYSICS
PRESENTED BY

Leire Beitia Antero

SUPERVISED BY

Ana Inés Gómez de Castro

For my family

Acknowledgements

Esta memoria es el fruto de cuatro años de mucho esfuerzo y dedicación, y si he conseguido llegar hasta aquí, es en gran parte gracias al apoyo de toda esa gente maravillosa que ha estado a mi alrededor.

No tengo espacio suficiente para agradecerle a Jose Ignacio su comprensión, su apoyo, y su cariño, especialmente en la recta final de la tesis. De no ser por ti, habría perdido la cabeza hace tiempo.

Quiero darle las gracias a mi familia: a mi madre, Mireia, a mi padre, Javier, a mi hermana, Amaia, y a mi tía, Begoña. Gracias por vuestro apoyo incondicional a pesar de lo extrañas y descabelladas que os puedan parecer mis ideas.

Y gracias también a mi futura familia: Almudena, Javier, y en especial a José Ramón (he cumplido y tu nombre aparece en la tesis).

Gracias a todos los miembros del grupo de investigación AEGORA con los que he trabajado. Vosotros habéis sido mi familia académica estos años y me alegra haber crecido como científica a vuestro lado. Gracias a Juan Carlos, Sonia, Raúl, Javier, Pablo, Nacho, Boris, Mikhail, Iván, Jennifer, y en especial a mis dos compañeras de despacho: Sabina y Ada. Gracias por todos los buenos momentos que me habéis dado.

Gracias a todas esas personas dispuestas a echar una mano con lo que sea, siempre con una sonrisa. Gracias a David y Elisa por su ayuda con el doctorado y por animarme a ser parte del grupo de innovación docente. Gracias a Emilio por ser mi compañero de fatigas; al final siempre estamos en todos los tinglados, pero tu compañía hace que sea más llevadero.

Gracias también a Xuening Bai por sus comentarios cuando estaba desarrollando el módulo de partículas cargadas, que fueron muy útiles para entender las limitaciones. Y gracias a los dos revisores externos, Luciana Bianchi y Kazunari Iwasaki, por una revisión exhaustiva y crítica que ha ayudado a mejorar la presentación y la claridad de esta memoria.

Por último, pero no menos importante, esta tesis ha podido existir gracias al apoyo económico del proyecto WSO-UV y a la beca de Formación de Personal Investigador de la Universidad Complutense y el Banco Santander...

... y por supuesto, gracias a mi directora, Ana Inés. A ti te debo haber llegado hasta donde estoy hoy. Gracias por darme la oportunidad de colaborar contigo cuando aún era una alumna de grado en matemáticas. Fuiste tu quien me abrió la puerta de la astrofísica y me has animado siempre a continuar mejorando, por muy complicado que me pareciese el reto. Has sido y eres mi madre académica, y espero hacerte sentir orgullosa dando cada día lo mejor de mí misma.

Gracias.

Abstract

Star formation takes place inside cold, dense clouds of molecular material (molecular clouds) that experience a hierarchical fragmentation process. Inside these clouds the material organises itself in filamentary structures, with a density increasing at smaller scales where stars are eventually formed. The evolution of these clouds is affected by the injection of energy into the system. It is now widely accepted that magnetohydrodynamic turbulence contributes to sustain a molecular cloud against collapse and in consequence, directly influences the star formation efficiency. Magnetic fields, therefore, are a fundamental shaping agent of molecular clouds. The most external layers of these clouds, the so-called molecular cloud envelopes, are partially ionised due to their exposure to the ambient radiation field and hence are effectively coupled to the magnetic field. This coupling favours the propagation of hydromagnetic waves inside the clouds, increasing the turbulent state of the gas.

Inside the Milky Way, there is one additional key ingredient that may substantially contribute to the evolution of a molecular cloud: interstellar dust. Interstellar dust grains are aggregates of heavy elements (mainly silicon, oxygen, carbon, magnesium, and iron, with a minor contribution of other elements such as calcium or aluminium) synthesised by the stars that are formed in the stellar atmospheres at the last stages of their evolution, with sizes that span from approximately 1 μm down to the molecular limit (50Å). These grains are found wherever gas (either atomic or molecular) is present, so molecular cloud envelopes are not an exception. The low column densities of the gas together with the metallic nature of the dust results in the charging of the grains, which become effectively coupled to the ambient magnetic field. The presence of these additional charged species in molecular cloud envelopes strongly affects the propagation of hydromagnetic waves inside the cloud, since some waves (particularly those with a frequency equal to the grain's gyrofrequency) will be less damped and will penetrate further into the cloud. Therefore, interstellar dust grains in a molecular cloud envelope may indirectly affect the star formation efficiency of a molecular complex.

This thesis is devoted to the study of the evolution of interstellar dust grains in molecular cloud envelopes and its observational imprint at ultraviolet wavelengths. Due to their small characteristic sizes ($a_d < 1\ \mu$m), these grains effectively interact with ultraviolet photons and produce strong features in the extinction curve; the most remarkable ones are the bump at 2175 Å, produced by large carbonaceous molecules, and the steep slope at far ultraviolet wavelengths, caused by scattering and absorption of ultraviolet photons by the smallest dust grains.

In a first approach, variations in the strength of the 2175Å bump were assessed towards the star-forming complexes of Orion and Rosette. This study made use of two extensive photometric surveys of the Galaxy: the Galaxy Ultraviolet Explorer (GALEX) at ultraviolet wavelengths, and the Two Micron All Sky Survey (2MASS) at near infrared wavelengths. By analysing the relative extinction between GALEX near ultraviolet band, that contains the feature at 2175 Å, and 2MASS K_s band that accounts for the extinction of larger grains, variations in the smallest dust population were identified that arose from either grain growth inside dense regions or photodestruction of dust in strongly irradiated areas. This study provided statistically significant measurements of the variations in the dust population, most likely produced by grain growth in the envelopes of molecular clouds. This is a complex environment and numerical simulations are required to investigate the evolution of small dust grains.

The magnetohydrodynamical evolution of a molecular cloud may be modelled with state-of-the-art numerical codes for astrophysical fluid dynamics. Nevertheless, most of these codes are only focused on the evolution of the gas and often disregard the evolution of interstellar dust grains in the dynamical evolution of the cloud. In this thesis, two modules have been developed for the modelling of the dynamics and evolution of interstellar charged dust grains that can be implemented inside any astrophysical code. These modules are then used to study the dynamics of interstellar charged dust grains in a molecular cloud envelope and their growing and shattering efficiency. It is found that narrow filaments of charged dust grains are formed in molecular cloud envelopes that follow the magnetic field, decoupling from the gas. Inside these filaments, grain growth is enhanced despite the characteristic low densities of the medium, since the propagation of interstellar hydromagnetic waves segregate the dust particles, increasing their growth rate. These variations in the size distribution are then translated into variations in the ultraviolet extinction curve, especially at shorter wavelengths, due to the depletion of small dust grains.

To sum up, this thesis presents the first comprehensive study on the evolution of interstellar dust grains in a molecular cloud envelope from both an observational and a theoretical points of view. While photometric observations of the clouds at ultraviolet wavelengths provide an statistical average of the variations in the dust population, numerical simulations allow to distinguish the physical phenomena that shapes the dust grain-size distribution. It is predicted that narrow filaments of charged dust grains are formed in molecular cloud envelopes under the influence of the magnetic fields, which will undoubtedly affect the propagation of hydromagnetic waves into their interiors. Besides, enhanced grain growth inside those filaments will produce a noticeable variation in the ultraviolet extinction curve, that could be detected through spectroscopic observations.

Resumen

La formación estelar tiene lugar en el interior de densas y frías nubes compuestas fundamentalmente de hidrógeno molecular, denominadas nubes moleculares, y que experimentan un proceso de fragmentación jerarquizado. Debido al estado turbulento del gas, dentro de estas nubes el material se organiza en estructuras filamentosas cuya densidad aumenta a medida que disminuye el tamaño, hasta que el gas es capaz de fragmentarse y formar estrellas. Sin embargo, la evolución de estas nubes puede verse afectada si la inyección de energía dentro del sistema varía. Actualmente, se sabe que la turbulencia magnetohidrodinámica contribuye a sostener una nube molecular frente al colapso, afectando en consecuencia a la eficiencia de formación estelar. Por tanto, los campos magnéticos juegan un papel fundamental en la evolución de las nubes moleculares. Las capas más externas de estas nubes, sus *envolturas*, están expuestas a la radiación ambiente y, por tanto, el gas se ioniza parcialmente, favoreciendo el acoplamiento con el campo magnético. A su vez, este acoplamiento favorece la propagación de ondas hidromagnéticas hacia el interior de las nubes, aumentando el estado turbulento del gas.

En la Vía Láctea, hay un ingrediente fundamental que contribuye a la evolución de una nube molecular: el polvo interestelar. Los granos de polvo interestelar están compuestos por elementos pesados (silicio, oxígeno, carbono, magnesio y hierro, con una contribución menor de otros elementos como el calcio o el aluminio) que son sintetizados por las estrellas a lo largo de su vida, y que en las etapas finales de la evolución estelar son capaces de precipitar y formar conglomerados en las atmósferas estelares. El tamaño de estos granos de polvo es realmente pequeño (menor a una micra) pudiendo alcanzar incluso el límite molecular (50 Å). Además, los granos de polvo interestelar se encuentran allá donde haya gas, tanto atómico como molecular, luego también están presentes en las envolturas de las nubes moleculares. Las bajas densidades de columna que caracterizan estos medios junto con la naturaleza metálica de los granos hace que estos últimos adquieran una carga eléctrica y se acoplen al campo magnético. Este aumento de las especies cargadas en las envolturas de las nubes moleculares afecta a la propagación de ondas hidromagnéticas dentro de la nube, especialmente a aquellas ondas cuya frecuencia es equivalente a la frecuencia de girorresonancia del grano, que sufren un menor amortiguamiento. Por consiguiente, los granos de polvo presentes en la envoltura de una nube molecular afectan indirectamente a la eficiencia de formación estelar del complejo.

Esta tesis está centrada en el estudio de la evolución del polvo interestelar en las envolturas de las nubes moleculares y su traza observacional a longitudes de onda ultravioleta. Debido a los tamaños característicos de los granos de polvo, su interacción con los fotones ultravioleta es altamente efectiva y produce trazas notables en la curva de extinción; los más notables son la joroba o *bump* a 2175 Å, producida por grandes moléculas carbonáceas, y la pendiente en el ultravioleta lejano, que tiene origen en los fenómenos de dispersión y absorción de fotones ultravioleta por los granos de polvo más pequeños.

En una primera aproximación, se han estudiado las variaciones estadísticas del *bump* a 2175 Å en los complejos de formación estelar de Orión y Roseta. Este trabajo hace uso de dos grandes mapeos del cielo: el mapa de fotometría ultravioleta del *Galaxy Evolution Explorer* (GALEX) y el mapa en infrarrojo cercano del *Two Micron All Sky Survey* (2MASS). El estudio de la extinción relativa entre la banda ultravioleta cercana de GALEX, que incluye el bump, y la banda infrarroja K_s de 2MASS, que da cuenta de la extinción de los granos de mayor tamaño, ha permitido identificar variaciones en la población de granos más pequeños debido a procesos de crecimiento en regiones densas, o de destrucción en zonas donde el campo de radiación es más intenso. Este estudio aporta unas medidas estadísticas significativas de las variaciones de la población de polvo, probablemente producidas por el crecimiento de los granos en las envolturas de las nubes moleculares. Este régimen es muy complejo y se requieren simulaciones numéricas para estudiar la evolución de los granos de polvo de menor tamaño.

Los códigos de mecánica de fluidos permiten estudiar la evolución de una nube molecular. Sin embargo, la mayoría de estos códigos no tienen en cuenta la dinámica de los granos de polvo que están embebidos en el gas. En esta tesis se han desarrollado dos módulos que permiten modelizar la dinámica y la evolución de una población de polvo interestelar en las envolturas de las nubes moleculares, teniendo en cuenta los fenómenos de crecimiento y destrucción del polvo. El principal resultado de este trabajo es la identificación de estrechos filamentos de polvo que se forman por la acción de los campos magnéticos, y que se encuentran desacoplados del gas. Estas concentraciones de polvo favorecen el crecimiento de los granos a pesar de la baja densidad del medio, aunque los procesos de destrucción contrarrestan la eficiencia del crecimiento y limitan el tamaño máximo que pueden adquirir los granos. Estas variaciones en la población de polvo se traducen a su vez en variaciones de la curva de extinción, que son especialmente notorias a longitudes de onda cortas debido a la disminución de la población de granos de polvo pequeños.

En resumen, esta tesis presenta el primer estudio completo de la evolución del polvo interestelar en las envolturas de las nubes moleculares, tanto desde el punto de vista teórico como desde el punto de vista observacional. Mientras que la fotometría ultravioleta permite un estudio estadístico de las variaciones en la población de polvo, las simulaciones numéricas permiten distinguir la influencia de los distintos procesos involucrados en dichas variaciones. Este trabajo predice la formación de filamentos de polvo cargado en las envolturas de las nubes moleculares acoplados al campo magnético, lo que sin duda afectará a la propagación de ondas hidromagnéticas. Además, el crecimiento de los granos en estos filamentos

producirá variaciones en la curva de extinción que podrán detectarse a través de observaciones espectroscópicas.

Contents

Acknowledgements ix

Abstract xi

Resumen xiii

List of Acronyms xxv

1 Introduction 1
- 1.1 The interstellar medium 1
- 1.2 Interstellar dust 4
- 1.3 Molecular clouds and star formation 7
- 1.4 The ISM at ultraviolet wavelengths from past and current missions 12
- 1.5 The future of ISM studies at UV wavelengths 17
  - 1.5.1 The World Space Observatory - Ultraviolet 18
- 1.6 Objectives and outline of the thesis 19

2 UV Extinction in Orion and Rosette 21
- 2.1 Orion and Rosette 21
- 2.2 UV extinction curve and star counts 23
- 2.3 Observational data 27
- 2.4 NUV luminosity function 28
- 2.5 Variations in the extinction curve 31
  - 2.5.1 Dust evolution in Orion 31
  - 2.5.2 Rosette and the spectroscopic testing of the method . . . 35
- 2.6 Conclusions 36

3 Numerical simulations of the ISM 39
- 3.1 Astrophysical fluid dynamics 39
  - 3.1.1 Smooth Particle Hydrodynamics: PHANTOM 40
  - 3.1.2 Eulerian Grid-based codes: Athena 42
  - 3.1.3 Moving mesh codes: GIZMO 43
- 3.2 Dust evolution codes 44
- 3.3 Choosing a code 45

4 Interstellar dust in Athena **47**
4.1 Athena: public version 4.2 . . . 47
4.1.1 The aerodynamic particles module . . . 47
4.2 Dynamics of charged dust in Athena . . . 50
4.2.1 Charged particles tests . . . 52
4.3 A simple collision model in Athena . . . 54
4.3.1 Outline of the algorithm . . . 58
4.3.2 Limitations of the collision model . . . 60
4.4 Summary . . . 61

5 Dust filaments in molecular cloud envelopes **63**
5.1 Grain charging in the diffuse ISM . . . 63
5.1.1 Photoelectric emission . . . 64
5.1.2 Ion/electron accretion rate . . . 67
5.1.3 Mean dust charges in a molecular cloud envelope . . . 67
5.2 Formation of dust filaments . . . 69
5.3 Filament properties . . . 72
5.4 Dust filaments and dust-to-gas ratios . . . 75
5.5 Limitations of a 2.5D model . . . 82
5.6 Conclusions . . . 83

6 Dust evolution in a molecular cloud envelope **85**
6.1 Grain growth inside dust filaments . . . 85
6.1.1 Growth of a single-sized population . . . 87
6.1.2 Mass loss and reprocessed small dust grains . . . 91
6.2 Collisions of a realistic dust population . . . 91
6.2.1 Generation of the mock sample . . . 92
6.2.2 Evolution of the dust grain-size distribution . . . 93
6.2.3 Variations of the UV extinction curve . . . 96
6.3 Discussion . . . 98
6.4 Conclusions . . . 100

7 Conclusions and future work **101**
7.1 Improvements of the model . . . 102
7.2 A scientific case for WSO-UV . . . 103

A GALEX photometry for IUE stellar sources **105**
A.1 Introduction . . . 106
A.2 The IUE database of stellar spectra . . . 106
A.3 The GALEX photometric bands in the IUE spectra . . . 107
A.4 Methods . . . 107

- A.4.1 Data Selection . . . 107
- A.4.2 Calculation of the FUV and NUV synthetic magnitudes . 109
- A.4.3 Error determination . . . 109
- A.4.4 Multiple observations. Variable stars . . . 110
- A.5 Photometric accuracy . . . 111
- A.6 The catalogue . . . 116
- A.7 Conclusions . . . 118
- A.A Catalogue excerpt . . . 118
- A.B FUV magnitude - Variable stars . . . 118

B Dust charge distribution routine **121**

List of Tables

1.1 Phases of the ISM 3

2.1 Fitting results of the NUV luminosity function 30
2.2 Galactic Latitude correction fitting 30
2.3 Area of the UV bump for OB stars in Rosette 37

4.1 Particle properties 61

5.1 Comparison of dust charges 68
5.2 Dust charges in a molecular cloud envelope 69
5.3 Properties of the analysed subregions 78

6.1 Region properties for the coagulation simulations 87
6.2 Statistical quantities for the growth of a single-sized population . 90
6.3 Dust grain-size distribution properties of the realistic sample . . . 95
6.4 Characteristic parameters of grain growth and shattering 99

A.1 Synthetic photometry of WDs 112
A.3 Synthetic photometry of WDs without GALEX counterpart . . . 114
A.2 Quadratic fit parameters for the WDs sample 117
A.4 Catalogue contents 119
A.5 Catalogue layout 120
A.6 Variable stars catalogue layout 120

List of Figures

1.1 Interstellar dust particle . . . 5
1.2 UV bump and DIBs for star HD 204827 . . . 6
1.3 Local molecular clouds . . . 8
1.4 Molecular cloud and star formation cycle . . . 11
1.5 Resonance lines in the UV . . . 12
1.6 Past and current UV windows to the Universe . . . 16

2.1 The Orion Molecular Complex . . . 22
2.2 The Rosette Nebula and Molecular Cloud . . . 23
2.3 UV extinction curves . . . 24
2.4 *Gaia*'s view of the Rosette complex . . . 27
2.5 *GALEX* sources in Orion and Rosette . . . 28
2.6 Regions for computing the NUV luminosity function . . . 29
2.7 Galactic Latitude correction fitting . . . 31
2.8 Orion extinction maps - 1 . . . 32
2.9 Orion extinction maps - 2 . . . 32
2.10 Panchromatic view of the region around $l_{gal} \sim 221°$, $b_{gal} \sim -20°$ . . . 33
2.11 Extinction in the Orion A filament . . . 34
2.12 The λ Orionis Ring . . . 34
2.13 Extinction in the Rosette molecular complex . . . 36

3.1 Approaches for solving the MHD equations . . . 40
3.2 Volume and area averages over a cell in Athena . . . 43
3.3 Example of magnetic dust structures . . . 46

4.1 Illustration of the two basic particle structures in Athena. . . . 50
4.2 Charged particles module - Test 1 (stability) . . . 54
4.3 Charged particles module - Test 1 (accuracy) . . . 55
4.4 Charged particles module - Test 3 . . . 56
4.5 Illustration of the modified particle structure in Athena. . . . 57
4.6 Scheme of the interaction between two test particles . . . 58

5.1 Interstellar Radiation Field Spectrum . . . 65
5.2 Snapshots for the gas density, magnetic field, and particles distribution at 0.4 Myr . . . 70
5.3 Post-processed dust maps . . . 71
5.4 Dust filaments identified by FilFinder . . . 73
5.5 Dust-to-gas ratio of filaments . . . 74
5.6 Relative orientation between dust filaments and magnetic field . . . 74

5.7 Dust-to-gas ratio maps 75
5.8 Histogram of the dust-to-gas ratio 76
5.9 Dust-to-gas ratio maps: high-density regions 77
5.10 Dust-to-gas velocity maps: high-density regions 79
5.11 Dust-to-gas ratio maps: low-density regions 79
5.12 Dust-to-gas velocity maps: low-density regions 80
5.13 Dust-to-gas ratio and velocity maps: mid-density region 80
5.14 Evolution of the dust-to-gas ratio 81
5.15 Dust-to-gas ratio maps for the longest and shortest waves 81

6.1 Particles that suffer shattering and coagulation: high-density regions 88
6.2 Particles that suffer shattering and coagulation: low-density regions 89
6.3 Steps for generating a mock sample 94
6.4 Silicate and graphite size distributions fitting 95
6.5 Synthetic extinction curve for region H1 97

A.1 GALEX transmission curves and IUE sensitivity curves 108
A.2 IUE vs. GALEX photometry for WDs 114
A.3 Sources distribution 117

List of Acronyms

AMR	Adaptive Mesh Refinement
CFL	Courant-Friedrichs-Lewy
CNES	Centre National d'Études Spatiales
CNM	Cold Neutral Medium
CRs	Cosmic Rays
CSA	Canadian Space Agency
CTU	Cornered Transport Upwind
DIBs	Diffuse Interstellar Bands
DMG	Dark Molecular Gas
ESA	European Space Agency
EUV	Extreme Ultraviolet
EUVE	Extreme Ultraviolet Explorer
FUSE	Far Ultraviolet Spectroscopic Explorer
FUV	Far ultraviolet
GALEX	Galaxy Evolution Explorer
HD	Hydrodynamics
HIM	Hot Ionised Medium
IUE	International Ultraviolet Explorer
ISM	Interstellar Medium
LISM	Local Interstellar Medium
MC	Monte Carlo
MHD	Magnetohydrodynamics
NASA	National Aeronautics and Space Administration
NUV	Near ultraviolet
PAHs	Polycyclic Aromatic Hydrocarbons
PPD	Protoplanetary Disk
SMR	Static Mesh Refinement
SNR	Supernova Remnant

SPH	Smooth Particle Hydrodynamics
SPMHD	Smooth Particle Magnetodydrodynamics
UV	Ultraviolet
WIM	Warm Ionised Medium
WNM	Warm Neutral Medium
YSOs	Young Stellar Objects
2MASS	Two Micron All Sky Survey

1 Introduction

Among all the elements that can be found in the Universe, molecular clouds are of special interest because they are the main galactic reservoirs of molecular gas and where stars are eventually formed. Besides, inside these clouds, molecules get locked into the solid elements (interstellar grains) that will constitute the planetary systems associated to the stars, and that sets the seed for the possible emergence of life.

Understanding the evolution of molecular clouds coupled with interstellar dust grains is instrumental to comprehend the processes involved in star formation, since dust affects the chemical reactions and the thermodynamical and dynamical evolution of the gas. This is especially true for the outer regions of molecular clouds, where dust grains have a net charge that favours the coupling with the ambient magnetic field. In this thesis, I have studied the influence of this often disregarded constituent, interstellar dust, in the evolution of molecular clouds.

In this chapter, I give a brief overview of the basic constituents of the interstellar medium (ISM, sec. 1.1), with a special emphasis on interstellar dust (sec. 1.2), and review the theories of molecular cloud and star formation (sec. 1.3). There are two sections related to ultraviolet (UV) astronomy: the ISM at UV wavelengths from past and current missions (sec. 1.4) and the future of ISM studies at UV wavelengths (sec. 1.5), where I emphasise the importance of Spektr-UV[1,2], also known as the World Space Observatory - Ultraviolet (WSO-UV) (sec. 1.5.1). As a member of the Research Group on Space Astronomy and Data Mining (AEGORA[3]) at Universidad Complutense de Madrid, I have specialised in UV astronomy. Finally, the motivation and outline of this thesis is presented in sec. 1.6.

1.1 The interstellar medium

The ISM constitutes the base of every galaxy, since it contains its main components: molecular clouds, stars, supernova remnants, etc. As such, it has been the subject of several reviews over the years (Ferrière, 2001; Klessen & Glover, 2016; Hennebelle & Inutsuka, 2019; Girichidis et al., 2020; Ballesteros-Paredes et al., 2020, to cite some recent examples).

The ISM is a complex structure formed by gas, interstellar dust (sec. 1.2), cosmic rays, and magnetic fields (see e.g. the reviews by Ferrière 2001 and Klessen & Glover 2016). The gas is composed by H (70.4%) and He (28.1%), and other

---

[1] https://en.wikipedia.org/wiki/Spektr-UV

[2] http://www.wso-uv.es/index.php?id=33

[3] https://www.mat.ucm.es/~aegora/index_english.html

heavier elements such as C, N, O, or Mg commonly termed as *metals* (1.5%, percentages in mass) (Ferrière, 2001). In the Milky Way, the total mass of the ISM is approximately 10^{10} $M_\odot$ (Kalberla & Kerp, 2009) and most of the volume is dominated by ionised, diffuse gas; the dense, molecular gas where star formation takes place is organised in clouds that occupy only $1-2\%$ of the volume of the ISM.

Classically, the gas is classified according to its thermal properties. Initially, it was thought that only two phases composed by atomic hydrogen (HI) could survive in thermal equilibrium in the ISM (Field et al., 1969): the warm neutral medium (WNM), characterised by temperatures of $T \sim 6000 - 10^4$ K, and densities of $n \sim 0.2 - 0.5$ cm^{-3}, and the cold neutral medium (CNM), with temperatures in the range $T \sim 50 - 100$ K and $n \sim 20 - 50$ cm^{-3} (Ferrière, 2001). These two regions may be detected through the resonant absorption lines of some elements and ions at UV (Jenkins & Tripp, 2001; Jenkins, 2013) and optical (Welsh et al., 2010) wavelengths; it is also possible to detect this diffuse gas through the 21 cm HI absorption line (see, for instance Peek et al., 2018). Later, McKee & Ostriker (1977) pointed out the necessary existence of an extremely hot ionised medium (HIM, $T \sim 10^6$ K) that was formed by the ionised bubbles resulting from supernova explosions; it can be detected by its X-ray emission (Martin & Kennicutt, 1995; Sun et al., 2012), and also at extreme ultraviolet (EUV) wavelengths (Berghöfer et al., 1998). Finally, observations of free-free absorption of the Galactic synchrotron background (Hoyle & Ellis, 1963), dispersion of radio signals from pulsars (Reynolds, 1989; Gaensler et al., 2008), and faint optical emission lines of ionised species (Reynolds et al., 1973; Mierkiewicz et al., 2006) revealed the existence of the warm ionised medium (WIM), that comprises the vast majority of the ionised gas in the ISM (Haffner et al., 2009); this regime shares properties with the WNM but for the ionisation fraction, so resonant absorption lines of ionised species such as MgII (Wood et al., 2005) or CaII (Welsh et al., 2010) are good tracers.

Customarily, the dense, molecular phase is distinguished from the CNM, because of its low temperature $T \sim 10$ K and density $n > 10^2$ cm^{-3}. The first detection of the most abundant molecule in the ISM, H_2, was performed by the *Copernicus* satellite in the far-UV (Carruthers, 1970; Savage et al., 1977) and improved maps of H_2 column densities were obtained with the *Far Ultraviolet Spectroscopic Explorer*, FUSE (Tumlinson et al., 2002; Rachford et al., 2002). However, the densest parts of the clouds suffer from extinction effects and it is impossible to study them at UV wavelengths; for these cases, moving towards radio frequencies solves the problem. The main drawback is that radio emission from the H_2 molecule is not observable because it does not posses a permanent dipole moment. As an alternative, the next most abundant[4] molecule, CO, can

---

[4] The H_2-to-CO ratio, often denoted by X_{CO}, is slightly variable from cloud to cloud, but has a mean value of $X_{CO} = 1.8 \times 10^{20}$ cm^{-2} (K km s^{-1})$^{-1}$ (Dame et al., 2001).

Table 1.1: Phases of the ISM with characteristic temperatures (T), densities (n), ionisation fractions (χ), and the main tracer. Adapted from Ferrière (2001) and Klessen & Glover (2016).

Phase	T [K]	n [cm^{-3}]	χ	Detectability
Molecular	$10 - 20$	$10^2 - 10^6$	$< 10^{-6}$	H_2 – Ly-α CO - 115 GHz
CNM	$50 - 100$	$20 - 50$	$\sim 10^{-4}$	UV/optical resonant lines, HI 21 cm
WNM	$6000 - 10^4$	$0.2 - 0.5$	~ 0.1	UV/optical resonant lines, HI 21 cm
WIM	~ 8000	$0.2 - 0.5$	1.0	UV/optical resonant lines radio pulsars, faint emission lines
HIM	$\sim 10^6$	$\sim 10^{-2}$	1.0	EUV, X-rays

be used to trace the molecular gas since it has a rotational emission line at ~ 115 GHz, first detected by Wilson et al. (1970); since then, great efforts have been made to build extensive CO maps of the main Galactic star forming regions – see, e.g. the CO Composite Survey by Dame et al. (2001).

It is evident that the classification of the gas phases of the ISM is a complex task. Actually, some authors have tried to propose an alternative classification based on visual extinction, relative molecular fractions, temperatures, and densities (Snow & McCall, 2006), but still the extended framework is the one that considers the five classical phases (CNM, WNM, WIM, HIM, and molecular gas); the properties of these phases are summarised in Table 1.1.

The presence of a pervasive magnetic field in our Galaxy was first revealed by the observation of linear polarisation of starlight (Hall, 1949; Hiltner, 1949), which is caused by the interaction of the radiation with interstellar dust grains (sec. 1.2). Briefly, the dust grains tend to align with the magnetic field through several mechanisms (see e.g. Davis & Greenstein 1951), and this alignment causes a preferential absorption of the stellar radiation, which is translated to a polarisation of the observed light. Due to this tight correlation between polarisation and magnetic field orientation, it is possible to construct maps of the morphology of the Galactic magnetic field from polarisation observations. Recently, the European Space Agency mission *Planck* has provided the first polarisation map of the whole Galaxy with a resolution of at most 7.5 arcmin (Planck Collaboration, 2018b,a) and more detailed polarisation maps of dense star forming cores are being built, for example, by the James Clerk Maxwell Telescope (JCMT) BISTRO consortium (Coudé et al., 2019; Pattle et al., 2017).

The strength of the interstellar magnetic field has been constrained to be of a few μG through several methods: Zeeman splitting (Troland & Heiles, 1986; Myers et al., 1995; Crutcher, 1999), Faraday rotation (Rand & Kulkarni, 1989; Rand & Lyne, 1994; Foster et al., 2013), and radio synchrotron emission (Ginzburg & Syrovatskii, 1965); the particular technique depends on the considered regime.

In diffuse regions, such as the CNM, the applied method is the measurement of Zeeman splitting of radio lines: in the presence of a magnetic field, the valence electrons are perturbed and produce a splitting of certain energy levels which amplitude is proportional to the strength of the field (Troland & Heiles, 1986). In ionised regions, such as the WIM, the Faraday rotation of linearly polarised radio signals is the optimal approach. It is based on the decomposition of a linearly polarised wave in two circularly polarised modes, one of which propagates faster resulting in a rotation of the plane of polarisation that, again, is proportional to the strength of the magnetic field (Gardner & Whiteoak, 1966). The last technique is based on the radio synchrotron emission from relativistic electrons, that arises from the spiralling motion of the electrons about the magnetic field lines; the emissivity is proportional to the magnetic field strength (Ginzburg & Syrovatskii, 1965). However, this method is very uncertain because it requires knowing either the magnetic field strength or the spectrum of cosmic ray electrons.

Cosmic rays (CRs) are the final piece of the ISM. They are composed mainly by protons ($\sim$ 10% He nuclei, 1% heavy nuclei), $\sim$ 2% electrons, and small amounts of positrons and antiprotons moving at relativistic speeds (Blandford & Eichler, 1987), and play a fundamental role in grain charging processes, especially in the densest parts of molecular clouds, as will be shown in following sections.

1.2 Interstellar dust

A small fraction of the interstellar material ($\sim$ 1%) is in solid state, and constitutes the so-called interstellar dust. It is formed in the circumstellar envelopes of evolved stars (Gail & Sedlmayr, 1999; Ferrarotti & Gail, 2006), in supernova ejecta (Bianchi & Schneider, 2007; Nozawa et al., 2007), and even from the accretion of metals in the ISM (Jenkins, 2004; Jones & Nuth, 2011). The composition of dust has been inferred through depletion studies of the ISM (Spitzer & Jenkins, 1975; Morton & Hu, 1975) and through the study of cometary (Dorofeeva 2020, Cochran et al. 2015, see also the Presolar Grain Database[5], Hynes & Gyngard 2009) and stratospheric and Antarctica dust samples (dall'Oglio et al., 1994; Hörz et al., 2006): they are mostly nano-diamonds (sizes $\sim$ 2.6 nm), silicon carbides, and graphite with typical sizes ranging from $0.1 - 1 \mu$m (see Zinner 2014 for a review). Laboratory experiments and sample analysis have shown that dust grains are highly porous (Ossenkopf, 1993; Hörz et al., 2006) and very commonly covered by an external layer of molecular ice, mainly H_2O (Dello Russo et al., 2016), see Fig. 1.1.

Interstellar dust was discovered by two observational effects. The first one was the reddening of starlight (Trumpler, 1930). When stellar photons interact with dust grains, they are absorbed (Cardelli et al., 1989; Fitzpatrick & Massa, 2007)

---

[5] `https://presolar.physics.wustl.edu/presolar-grain-database/`

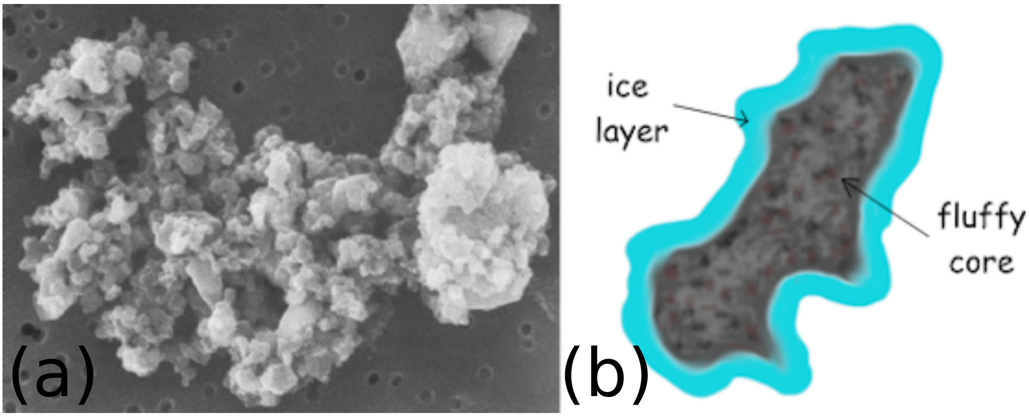

Figure 1.1: (a) Scanning electron microscope image of an interstellar particle, taken from Mautner et al. (2006). Note the porous, fractal appearance of the particle. (b) Artistic impression of the basic structure of an interstellar dust particle, covered by an ice layer.

or scattered (Overbeck, 1965; Hayakawa, 1970) depending on grain composition and size; by studying the properties and features of the so-called extinction curve, it is possible to recover the dust properties. Mathis et al. (1977) were the first ones that successfully reproduced the extinction curve with a mixed dust population of silicate and graphite, and a size distribution that can be approximated by a power law, $N(a)dn \propto a^{-3.5}da$. A more refined model was later developed by Weingartner & Draine (2001a) that took also into account small aromatic hydrocarbon particles, usually called Polycyclic Aromatic Hydrocarbons (PAHs); current dust models have increased in complexity, considering realistic mixtures of amorphous carbon and amorphous silicates (see for instance the THEMIS[6] dust model, Jones et al. 2017). The dependence of dust abundance on particle radius makes clear that the interaction with short wavelength radiation (X-rays, UV, optical) is the most effective. Indeed, the most prominent feature of the extinction curve is the bump at 2175Å, first detected by Stecher (1965) and believed to be caused by PAHs (Draine, 2003a); a more detailed analysis of the UV bump is given in Chapter 2. Other dust imprints on the extinction curve are the infrared bands at 9.7 μm and 18 μm caused by amorphous silicates (Knacke & Thomson, 1973; Draine & Lee, 1984); the diffuse interstellar bands (DIBs) (Heger, 1922), probably caused by PAHs; ice features towards dense molecular clouds at 3.1 μm (H_2O) or 4.7 μm (CO), amongst others (Draine, 2003a); hydrocarbon features of refractory materials at 3.4 μm (Li & Greenberg, 1997); and PAH vibrational features at 3.3 μm, 6.2 μm, 7.7 μm, 8.6 μm, and 11.3 μm (Draine, 2003a). Some of these features are shown in Fig. 1.2.

---

[6] `https://www.ias.u-psud.fr/themis/index.html`.

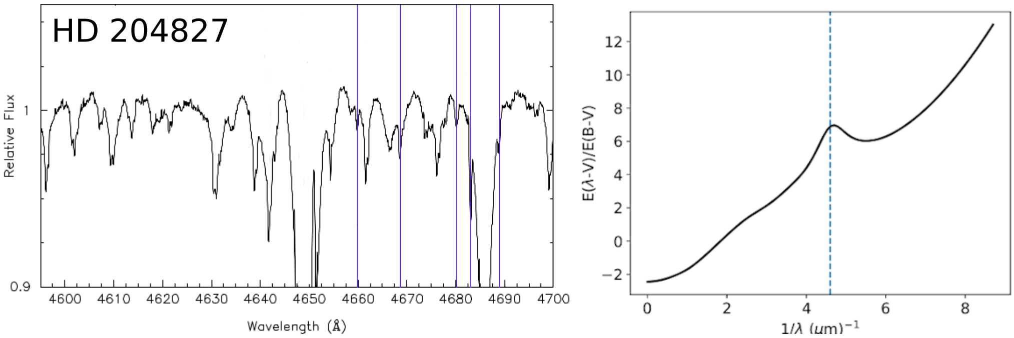

Figure 1.2: Illustration of some of the most prominent dust features in the line of sight of the spectroscopic binary star HD 204827. The left panel shows some DIBs identified over the spectrum (adapted from Hobbs et al. 2008) and the right panel shows the extinction curve built by Fitzpatrick & Massa (2007), where the UV bump is clearly visible and centred at ∼ 2175Å (dashed vertical line).

The second observational effect of dust is the linear polarisation of starlight (Hall, 1949; Davis & Greenstein, 1951). Dust grains align due to radiative torques and the interaction with the magnetic field (Hoang & Lazarian, 2016; Lazarian & Hoang, 2019), and causes a preferential absorption of light that peaks at approximately 5500 Å (Draine, 2003a).

The above mentioned effects, extinction and polarisation, strongly depend on the optical properties of the grains. Although dust grains are known to have mainly a carbonaceous or silicate composition, very small carbonaceous particles are known to suffer a fast processing in the ISM and therefore present a heterogeneous composition (Jones et al., 2013). These changes mainly arise from the interaction with UV radiation (Pilleri et al., 2012) or collisions with electrons in very hot media (Bocchio et al., 2012). This photo-processing results in the alteration of the nature of the chemical bondings of the material, that in turn increases the extinction efficiency, a process known as *photodarkening* (see Jones 2012a,b,c and references therein). Photodarkening of very small hydrocarbon particles, but also of the carbon mantles of larger grains, has succeeded in reproducing some absorption features at infrared wavelengths (see e.g. Jones et al. 2014 and the recent works by Cours et al. 2020 and Do-Duy et al. 2020) and in the intermediate regimes between the diffuse ionised regions and the dense interiors of molecular clouds, is found to be strongly dependent on the extinction at UV wavelengths and on the hydrogenation efficiency of aromatic-rich carbonaceous grain materials (Köhler et al., 2015; Mennella, 2010).

Interstellar dust, however, is not an isolated entity of the ISM. In fact, interstellar dust and gas column densities are tightly correlated (Bohlin et al., 1978; Boulanger et al., 1996; Roman-Duval et al., 2010; Lenz et al., 2017), and dust grains play a fundamental role in the thermal, chemical, and dynamical evolution of the gas in which they are embedded. Due to their small sizes, small dust grains absorb and scatter very efficiently the UV radiation. Moreover, due to this exposure to energetic photons, dust grains contribute to gas heating through the photoelectric effect and acquire a net charge that depends on the dust properties and on the environmental conditions (Bakes & Tielens, 1994; Weingartner & Draine, 2001b). Besides, interstellar grains in cold environments are the main site for the formation of molecules, especially H_2 (Hollenbach & Salpeter, 1971; Cazaux & Tielens, 2004) but also other molecules such as OH^+ (Hollenbach et al., 2012), CH_4 (Qasim et al., 2020), complex organic molecules (Hasegawa et al., 1992; Simons et al., 2020), or sulphur-bearing molecules (Shingledecker et al., 2020). Finally, charged dust grains may affect the electrostatic conductivity of an interstellar plasma (Duan et al., 2012; Zhukhovitskii et al., 2015), the development of several plasma instabilities (Havnes, 1988; Hartquist et al., 1992), and even interfere with the propagation of hydromagnetic waves in the gas (Pilipp et al., 1987; Hopkins et al., 2020). Hence, it is fundamental to take into account interstellar dust when studying the ISM, particularly for molecular cloud evolution and star formation.

1.3 Molecular clouds and star formation

Molecular clouds are the main galactic reservoirs of gas where star formation takes place (Kennicutt & Evans, 2012). They span a wide range of masses ($M \sim 10^2 - 10^6$ $M_\odot$) and sizes ($\sim 10 - 200$ pc) (Miville-Deschênes et al., 2017). The full population of local clouds in our Galaxy is well studied and compiled in several catalogues (Reipurth, 2008a,b; Miville-Deschênes et al., 2017; Chen et al., 2020) and they are mainly located inside a radius of 3 kpc from the Sun (see Fig. 1.3).

An interstellar gas cloud is considered to be molecular when the density is high enough for hydrogen to be mainly in molecular form, which under conditions typical of the Milky Way happens at visual extinction $A_V \sim 0.1 - 0.2$ (Krumholz et al., 2008). However, since the lack of dipole moment of the H_2 molecule makes it difficult to be observed, sometimes the transition to the molecular phase is traced by the formation of the next most abundant molecule, CO, that occurs at $A_V \sim 1$ (Wolfire et al., 2010). This transition is widely accepted to arise as a result of a thermal instability (Field, 1965) that triggers the formation of some cold clumps with the same properties of the CNM embedded in a diffuse WNM (Piontek & Ostriker, 2004; Audit & Hennebelle, 2005; Inoue et al., 2007). Nevertheless, how this instability is triggered is not fully understood yet. The initial model for molecular cloud formation, namely the coagulation model (Oort, 1954), considered that discrete clumps of CNM were embedded in the WNM as a result of the thermal instability. The cold clouds collided and coagulated, forming larger clouds that eventually became molecular due to self-shielding (Field & Saslaw, 1965; Taff & Savedoff, 1973). However, this model failed to explain the observed short lifetimes of molecular clouds (Blitz & Shu, 1980). The current

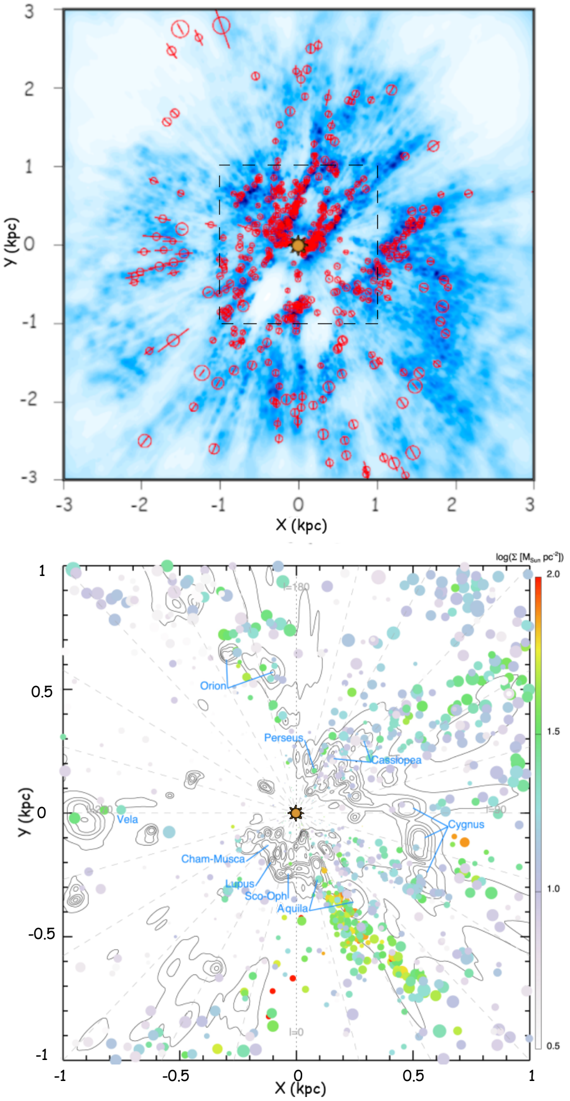

Figure 1.3: *Top*: Dust map distribution of the Solar neighbourhood from *Gaia* DR2 data (Lallement et al., 2019, blue background) with the molecular clouds identified by Chen et al. (2020) within 4 kpc from the Sun and $|b| < 10°$ using *Gaia* DR2, *Wide-field Infrared Survey Explorer* (WISE), and 2MASS data (open circles). The sizes of the circles are proportional to the physical sizes of individual clouds and the error bars represent the distance uncertainties. *Bottom*: H_2 surface density map of the Solar neighbourhood by Miville-Deschênes et al. (2017) built from ^{12}CO observations for $|b| < 5°$. The symbol sizes are proportional to the cloud size, and the colour indicates the mass surface density. The background contour map is a previous version of the dust map shown in the upper panel (Lallement et al., 2014). The dashed box in the upper panel of this figure encloses the region represented in the bottom panel.

framework for molecular cloud formation is the colliding flows model. According to this theory, the collision between converging, turbulent, and magnetised flows of low gas density in post-shock regions triggers the thermal instability, forming cold, dense clumps of gas (Hennebelle & Pérault, 2000; Inoue & Inutsuka, 2008, 2012; Iwasaki et al., 2019). Still, the physical processes responsible for driving the colliding flows have not been unambiguously identified; they could be the result of large scale gravitational instabilities (Elmegreen, 2011), the development of the Parker-Jeans instability (Mouschovias, 1974; Elmegreen, 1982; Blitz & Shu, 1980), or the consequence of stellar feedback (Ntormousi et al., 2011; Dobbs et al., 2012; Hennebelle & Iffrig, 2014).

The transition from atomic to molecular gas is governed by several heating and cooling processes that affect the chemical evolution of the cloud. The main cooling processes are the line emission of HI (for temperatures up to 3×10^4 K, Black 1981; Cen 1992) and other species such as C, O, Ne, and Fe for lower temperatures (Gnat & Ferland, 2012); emission of fine structure lines of C, C^+, and O (Wolfire et al., 1995) is important under conditions characteristic of the CNM and WNM, but only for densities up to $n \sim 10^2 - 10^6$ cm^{-3} (Hollenbach & McKee, 1989); CO cooling dominates for $n \sim 10^3$ cm^{-3} (Goldsmith, 2001); and when the gas temperature exceeds the dust temperature, dust grains contribute to the cooling via collisions with gas particles (Goldreich & Kwan, 1974; Leung, 1975); then, the energy absorbed by the dust grains is re-emitted at infrared wavelengths (Draine & Li, 2001). On the other hand, some heating processes are in competition for the thermal balance of the gas, and they are mainly caused by highly energetic UV radiation: the absorption of UV photons by dust grains causes them to emit photo-electrons, increasing the gas temperature (Bakes & Tielens, 1994); UV radiation may also cause the photodissociation of H_2 (Stephens & Dalgarno, 1973), although this process is not very efficient (Draine & Bertoldi, 1996); most of the time, the excited H_2 molecule decays rapidly back into a lower state of energy, producing moderate heating in dense ($n \gtrsim 10^4$ cm^{-3}) regions, a process known as UV pumping (Burton et al., 1990). In dense molecular regions, the main source of heating are CRs (Dalgarno et al., 1999; Glassgold et al., 2012), while in the diffuse ISM, heating by soft X-rays may be of relative influence (Wolfire et al., 1995). When modelling molecular cloud formation, it is necessary to account for some of the just mentioned thermodynamical processes via chemical reaction networks (Inoue & Inutsuka, 2012; Iwasaki et al., 2019; Hocuk & Cazaux, 2015), that have been compiled in several databases (see e.g. KIDA[7], UMIST[8], or OSU[9]); the complexity of the network depends on the scope of the simulation, because they are computationally expensive.

---

[7] `kida.obs.u-bordeaux1.fr`

[8] `udfa.net`

[9] `physics.ohio-state.edu/~eric/research.html`

Morphologically, molecular clouds are highly hierarchical. Early observations revealed their filamentary structure (Schneider & Elmegreen, 1979; Bally et al., 1987), and later the European Space Agency mission *Herschel* confirmed the ubiquity of these filaments on a wide range of length scales (André et al., 2014). Generally, a main filament with a characteristic width of ~ 0.1 pc (Arzoumanian et al., 2011; Koch & Rosolowsky, 2015) is observed to be surrounded by a diffuse population of fainter filaments apparently connected to it, called striations (Goldsmith et al., 2008; Palmeirim et al., 2013). However, the formation mechanism of these filaments is not fully understood. For dense, self-gravitating clouds, the gravitational force is stronger along the shortest axis and can produce filaments (Nagai et al., 1998; Smith et al., 2014); on the other hand, atomic gas is also observed to be filamentary (Miville-Deschênes et al., 2003; McClure-Griffiths et al., 2006), but it is clearly not self-gravitating. For those cases, the physical phenomenon that has been put forward as a likely explanation for filament formation is magnetohydrodynamic turbulence (Hennebelle, 2013; Inoue & Inutsuka, 2016). Molecular clouds are known to be naturally turbulent (Elmegreen & Scalo, 2004; Hennebelle & Falgarone, 2012) but the origin of that turbulence, again, is not clearly determined; it is very likely to be the result of stellar feedback (Gent et al., 2020; Padoan et al., 2016), but it has to be continuously sustained by some external force (Mac Low et al., 1998; Ostriker et al., 2001).

Star formation is strongly associated with filaments inside molecular clouds (André et al., 2010; Henning et al., 2010). According to the hierarchical structure of the clouds (Elmegreen et al., 2000), denser structures are found at all spatial scales and star formation eventually takes place inside the densest regions of the filaments (Polychroni et al., 2013; Klassen et al., 2017). This process takes less than 10^6 years (Hartmann et al., 2001; Elmegreen, 2007) and is highly inefficient (Zuckerman & Evans, 1974; Kennicutt & Evans, 2012), probably due to bipolar outflows from low-mass stars (Carroll et al., 2009) and radiation fields from high-mass stars (Walch et al., 2012), with a minor contribution of galactic gas escape (Hill et al., 2012; Girichidis et al., 2016), or magnetic field effects (Shu et al., 1987; Basu & Mouschovias, 1995). Most of the stars are observed to form in clusters and associations (Hartmann, 2002; Lada & Lada, 2003), and their properties depend on the so-called initial mass function (Scalo, 1986; Kroupa, 2002; Chabrier, 2003).

The theories of high- and low-mass star formation are conceptually different, and both have evolved considerably over the last decade. For low-mass stars, it was thought (Shu et al., 1987) that pre-stellar cores evolved quasi-statically in magnetically subcritical clouds, where gravitational contraction was mediated by ambipolar diffusion (Mouschovias, 1976) until the cloud became supercritical and fragmented, forming the stars. However, this theory fails to explain why most clouds are observed to be supercritical despite not being forming stars (Mac Low & Klessen, 2004). An alternative explanation for cloud collapse could be magnetohydrodynamical (MHD) turbulence (Mac Low & Klessen, 2004; Klessen, 2011), because although on large scales it can support the cloud against collapse, at the ambipolar diffusion scale, turbulence only affects the charged, tiny fraction of the gas ($\sim 10^{-6}$) and it is unable to brake the gravitational collapse. For high-mass star formation, two theories are considered: in the competitive accretion model, the gas is accreted from the parental cloud towards the centre of the clump, favouring the growth of the central stars (Bonnell et al., 2001). Alternatively, the fragmentation induced starvation model states that the accreting gas fragments before reaching the centre of the core (Peters et al., 2010; Girichidis et al., 2012).

To finish this section, a summary of the cycle of molecular cloud formation, evolution, and star formation is presented in Fig. 1.4.

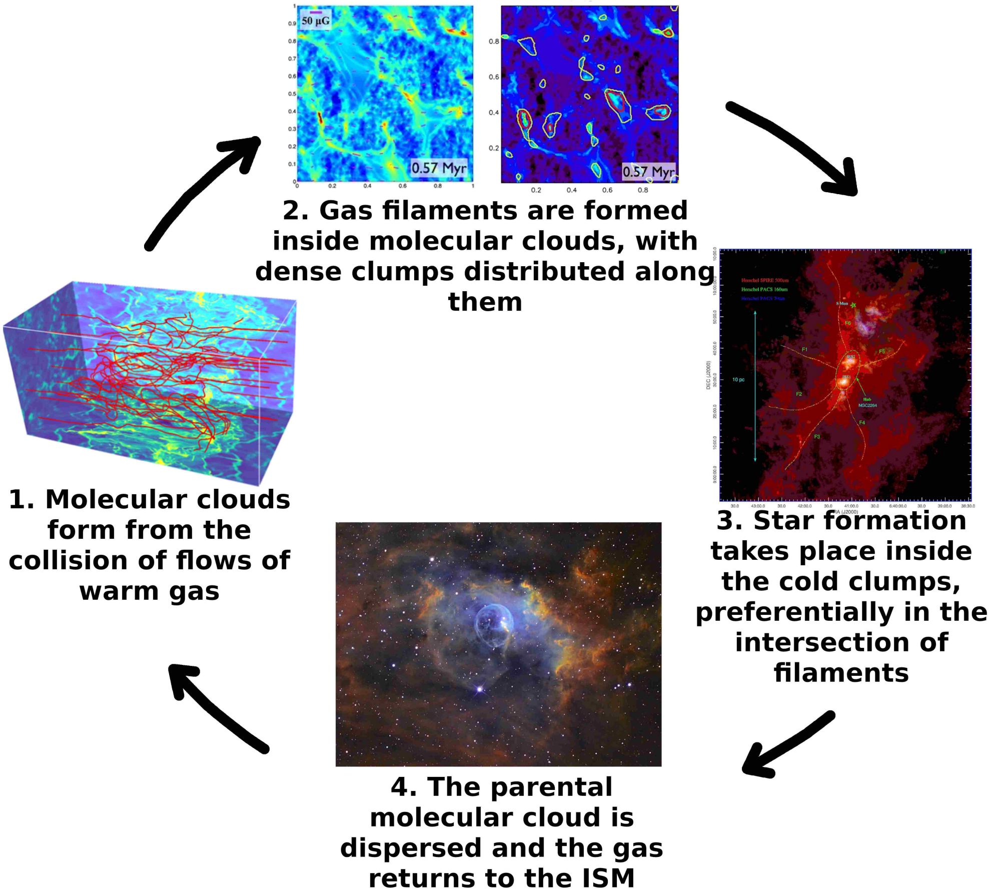

Figure 1.4: Brief scheme of the molecular matter cycle. Figures are taken from Iwasaki et al. (2019) (1), Chen & Ostriker (2014) (2), Kumar et al. (2020) (3), and NASA's service APOD (4, image credit: Russell Croman).

1.4 The ISM at ultraviolet wavelengths from past and current missions

Ultraviolet astronomy is the key to understand the fundamental physical processes that take place in the ISM, since inside the $912 - 3000$ Å spectral range we find the resonance lines of the most abundant molecules and ions (Spitzer & Zabriskie, 1959) and, in general, the highest number of lines from some different species (see Fig. 1.5). However, the effects of atmospheric extinction force UV telescopes to operate in space.

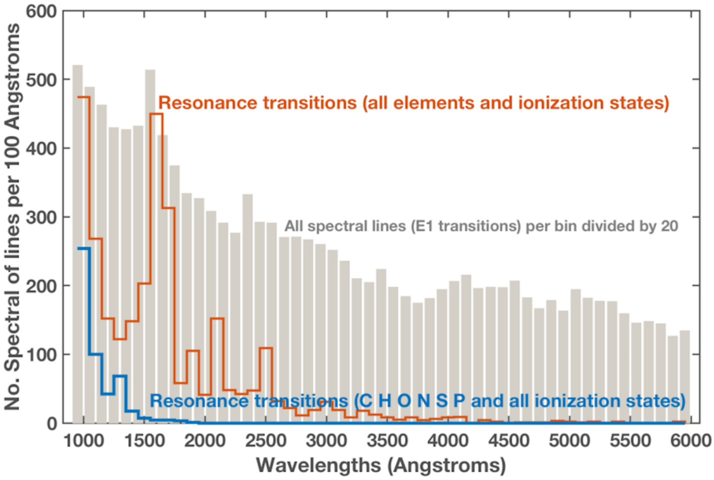

Figure 1.5: Resonance lines per 100 Å in the UV range (Gómez de Castro & Canet, 2021).

Before big space telescopes were put into orbit, observation from rockets flights provided the first measurements of interstellar absorption lines of the most abundant species, such as CII, OI, SiII, HI (Stecher & Milligan, 1962; Morton & Spitzer, 1966; Morton, 1967), and H_2 (Carruthers, 1970). In 1972, two satellites were put into orbit: the European Space Research Organisation launched the *Thor-Delta 1A* (TD-1), that included in its payload a 27-cm UV telescope (Boksenberg et al., 1973); with this telescope, some studies on interstellar UV extinction were carried out (Nandy et al., 1975), but the satellite was very short-lived and ceased operations in 1974. The same year that TD-1 was launched, NASA put into orbit the *third Orbiting Astronomical Observatory* (OAO-3), better known as *Copernicus* (Rogerson et al., 1973). *Copernicus* opened the door to UV studies of the ISM, although sensibility constraints restrained its reach to near O-B stars. However limited, *Copernicus* constituted the base for chemical studies of our Galaxy. Several atoms and molecules were detected in the lines of sight towards massive stars, such as NI (Ferlet, 1981; York et al., 1983), OI (York et al., 1983), CI (Jenkins et al., 1983), and even CO (Jenkins et al., 1973; Federman et al., 1980); it was soon realised that the interstellar abundance of elements heavier than hydrogen was lower than expected (Morton et al., 1973; Morton, 1974; York, 1975), a fact that was early attributed to their being locked into interstellar dust grains (Field, 1974; Snow, 1975). In fact, one of the main scientific achievements of *Copernicus* was the detection and measurement of interstellar absorption lines of H_2 and HI all around the Solar vicinity (Spitzer et al., 1973; Bohlin, 1975; Savage et al., 1977; Bohlin et al., 1978), and it was noticed an apparent hole in HI around the Sun (Frisch & York, 1983), clearly the first hint of what was later identified as the Local Bubble. Finally, the last major interstellar discovery of *Copernicus* was the detection of emission of the OVI line arising from a very hot ($T \sim 10^5 - 10^6$ K) gas (York, 1974; Jenkins & Meloy, 1974), that corresponds to the HIM (see sec. 1.1).

With the launch of the *International Ultraviolet Explorer* (IUE, Boggess et al. 1978) in 1975 by NASA and ESA, ISM related studies culminated. Not only did IUE continue with studies on hydrogen abundances and chemical depletion (Phillips et al., 1982; Shull & van Steenberg, 1985; Murthy et al., 1987), but it also started a whole new area of ultraviolet research in interstellar structures such as planetary nebulae (Aller et al., 1981), supernova remnants (SNRs) (Benvenuti et al., 1979), or Herbig-Haro objects (Bohm & Bohm-Vitense, 1984). But without a doubt, the greatest development of IUE – as long as ISM studies are concerned – was the characterisation of the ultraviolet extinction curve, and the feature at 2175 Å (Fitzpatrick & Massa, 1986). The low resolution spectroscopic capabilities of IUE enabled the study of the interstellar dust population along many lines of sight of our Galaxy (Seab et al., 1981; Witt et al., 1984; Massa & Fitzpatrick, 1986; Clayton & Fitzpatrick, 1987) as well as towards the Magellanic Clouds (Prevot et al., 1984; Clayton & Martin, 1985). These extinction curves served as a proxy for variations in interstellar dust composition, since dust model fitting of the curves revealed that their features were well reproduced by a mixed population of graphite and silicates (Mathis et al., 1977). IUE also revealed that the medium surrounding the Sun is highly diffuse and morphologically resembles the structure of a SNR (Frisch, 1981; Bruhweiler & Kondo, 1982), a structure that was termed as the Local Bubble (Frisch, 1995).

In 1990, NASA and ESA joint efforts to launch the longest-lived space telescope up to date: the *Hubble Space Telescope*[10] (HST). *Hubble* has provided a continuous access to the UV range with high-quality for more than 30 years, and has kept its instrumentation up to date through several maintenance missions. When launched, all the five instruments (the *High Speed Photometer* HSP, the *Goddard High Resolution Spectrograph* GHRS, the *Faint Object Spectrograph*

---

[10] `https://www.spacetelescope.org/`

FOS, the *Faint Object Camera* FOC, and the *Wide Field Planetary Camera 1* WFPC1) were designed to cover (at least partially) the UV range. The first service mission in 1993 allowed to update the WFPC1 by an improved version (WFPC2), and the obsolescence of the original instrumentation motivated the progressive upgrade of the payload through subsequent service missions in 1997, 2002, and 2004. Nowadays, there are four operational instruments onboard *Hubble* that can be used to perform observations at UV wavelengths: the *Space Telescope Imaging Spectrograph* (STIS), the *Cosmis Origins Spectrograph* (COS), the *Advanced Camera for Surveys* (ACS), and the *Wide Field Camera 3* (WFC3). Over the years, *Hubble* has been used for UV studies on polarisation (Somerville et al., 1994), chemical evolution (Cardelli, 1994; Meyer et al., 1998), highly ionised high-velocity clouds (Collins et al., 2005; Lehner et al., 2012), characterisation of the LISM (Redfield & Linsky, 2002; Redfield et al., 2004), and even the distribution of dust in other galaxies (Dong et al., 2016). Currently, it is mainly dedicated to studies of the circumgalactic medium (Keeney et al., 2017; Pointon et al., 2019), protoplanetary disks (Arulanantham et al., 2018, 2020), quasars (Punsly, 2015; Prochaska et al., 2019), and exoplanetary research (Peacock et al., 2020; Hu et al., 2020).

After all these missions mainly focused on the far and near UV parts of the spectra (from $\sim$ 1200 Å to $\sim$ 3000 Å), it was the turn of the EUV range ($\sim 70 - 900$ Å). The first mission to come was the *Extreme Ultraviolet Explorer* (EUVE, Bowyer & Malina 1991, see also Sirk et al. 1997) in 1992. One of its main objectives was to perform the first survey of the sky at EUV wavelengths, that revealed the presence of a diffuse sky background (Lieu et al., 1993; Jelinsky et al., 1995) as well as of some clouds optically thick in the EUV (Berghöfer et al., 1998). The other interstellar scientific goal was to study the H and He abundance and fractional ionisation in the Local Interstellar Medium (LISM), since their cross sections are maximum at EUV wavelengths (Vennes et al., 1993; Dupuis et al., 1995; Cassinelli et al., 1995). These measurements revealed the presence of a gap in the Local Bubble towards high galactic latitudes, named the "Local Chimney" (Welsh et al., 1999). This survey at EUV wavelengths was later improved by the EURD (*Espectrógrafo Ultravioleta para la detección de Radiación Difusa*) spectrograph onboard the Spanish MINISAT-01 mission (launched in 1997), with a sensitivity approximately two orders of magnitude better than previous spacecrafts (Edelstein et al., 2001).

A few years later, in 1999, FUSE (Moos et al., 2000) was launched by NASA, CSA, and CNES. FUSE continued with the study of the LISM (Jenkins et al., 2000; Lehner et al., 2003) and the abundance of H_2, but most of the work was focused on the study of hot gas, both Galactic (Savage et al., 2000; Oegerle et al., 2000; Sembach et al., 2000) and extragalactic (Murphy et al., 2000; Oegerle et al., 2000). FUSE measurements of the `OVI` spectral line dismissed the idea that the local cavity was filled by hot gas responsible of this emission (Oegerle et al., 2005;

Savage & Lehner, 2006; Welsh & Lallement, 2008); actually, the observational evidence pointed towards the interface between the Local Bubble and the dense surrounding medium (Oegerle et al., 2005; Barstow et al., 2010), although the emission at few lines of sight could be associated with gas in the Galactic halo (Dixon et al., 2006). FUSE data were also used to study the steep rise of the extinction curve in the far ultraviolet (Sofia et al., 2005), and again, maps of the diffuse background were built (Murthy & Sahnow, 2004).

Up to the 2000s, virtually all UV telescopes had been devoted to spectroscopy, but a systematic and complete photometric coverage of the sky at UV wavelengths was lacking. In 2003 NASA launched the *Galaxy Evolution Explorer* (GALEX) to perform the first UV survey of the sky in two photometric bands that have become a standard: far-UV (FUV) and near-UV (NUV). Actually, due to sensitivity constraints, the Galactic Plane was generally avoided, but GALEX opened the door to star formation studies in other galaxies. GALEX's potential for interstellar studies, however, has remained scarcely exploited, mainly due to the complex task of flux calibrating its slitless spectral database (Bohlin & Bianchi, 2019). Most of the work related to the ISM has been based on GALEX photometry and focused on the characterisation of the UV background in FUV and NUV bands (Sujatha et al., 2009; Henry et al., 2015; Akshaya et al., 2018; Armengot & Gómez de Castro, 2019), although some efforts have been made to study both Galactic and extragalactic extinction (Peek & Schiminovich, 2013; Gómez de Castro et al., 2015; Sun et al., 2018) and dust attenuation effects at other galaxies (Battisti et al., 2016, 2017).

Apart from HST, there are three other space telescopes that provide access (although not exclusively) to the UV range nowadays. XMM-Newton is an ESA's space telescope put in orbit in 1999 and designed to observe the sky at X-Rays (Jansen et al., 2001), while the Neihl Gehrels Swift Observatory is a telescope launched by NASA in 2004 dedicated to the study of gamma-ray bursts (Gehrels et al., 2004). Both of them are equipped by a small UV/optical telescope for guiding, providing partial access to the UV range, and respective catalogues of serendipitously detected UV sources have been published (Page et al., 2012, 2014). However, their usage in the UV is restricted and only few works have focused on interstellar studies at UV wavelengths using these instruments (see e.g. Blustin et al. 2006; Brown et al. 2015).
The most recently launched space observatory with UV capabilities is Astrosat. Astrosat is a mini-satellite launched by India's space agency ISRO that has been operating since 2015 (Singh et al., 2014). Of the five instruments included in its payload, UVIT provides imaging capabilities in the far UV and near UV ranges at an angular resolution that is approximately three times better than GALEX's (Tandon et al., 2017), and slitless spectroscopy through grisms. Most of UVIT results are focused on studies of extragalactic star formation (Mondal et al., 2019), the morphology of Planetary Nebulae (Kameswara Rao et al., 2018), or on globular

clusters (Subramaniam et al., 2017; Kumar et al., 2021), but the exploitation of UVIT's capabilities for interstellar medium studies is bound to come in the following years.

To complete this section, a picture illustrating the UV coverage of each telescope is shown in Fig. 1.6.

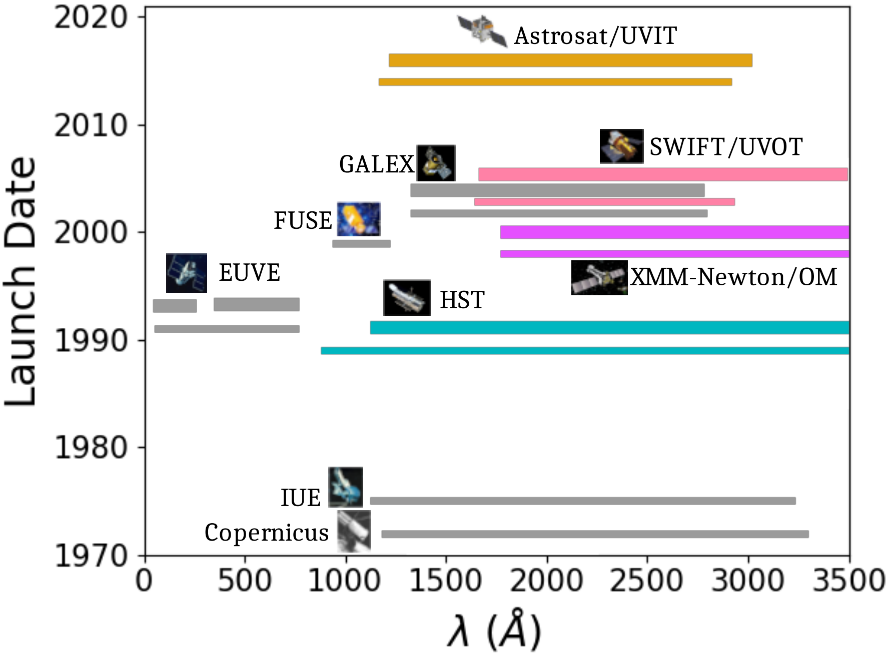

Figure 1.6: Past and current UV windows to the Universe. Telescopes currently operational are displayed in bright colours, while past missions are displayed in grey. Thick lines represent imaging filters, while thin lines represent spectroscopy. When both photometric and spectroscopic capabilities are available, they have a positive/negative offset (respectively) with respect to the launch date for better visualisation. Note that the wavelength coverage for each mission is displayed as a whole.

1.5 The future of ISM studies at UV wavelengths

It is evident from the review presented in the previous section that most of the facilities that provide access to the UV range are coming to the end of their lifetime (as is the case of *Hubble*) or the observation at UV wavelengths is not a priority of the mission (as happens with XMM-Newton or Swift). The only exception is Astrosat/UVIT that has already reached its five nominal years of operation, although it is expected to continue providing FUV imaging capabilities for many years. However, the access to the UV range in the 2020s and 2030s is deemed to be very limited unless new facilities are planned and launched in the near future.

The global UV community is very active and several missions have been proposed over the last years. Some of them are medium-sized (1-2 m) telescopes with both imaging and spectroscopic capabilities; examples of these missions are CETUS (Hull et al., 2018), presented to NASA's Decadal Survey Astro 2020, SIRIUS (Barstow et al., 2014) that was preselected for a FAST Mission Possibility in ESA's Science Programme, and CASTOR (Cote et al., 2019) that was recommended as the Canada's highest priority for space astronomy in December, 2020 and has entered now into Phase 0 of study. Larger space telescopes (over 6 m) are also being considered by space agencies all over the world; such are the cases of LUVOIR (The LUVOIR Team, 2019) and HabEx (Gaudi et al., 2020), two competitors in NASA's 2020 Astrophysics Decadal Survey. In Europe, the UV community has presented the mission concept EUVO (Gómez de Castro & EUVO Collaboration, 2019), a 6-10 m telescope, to several ESA calls, the last one being ESA's Voyage 2050 call for white papers raised in 2019; and the mission concept Arago[11], a 1.3 m telescope for spectropolarimetry in the UV presented as a candidate for an ESA M5 mission. Another proposal for a UV Fresnel Interferometer Array (Koechlin et al., 2009) is also supported by the European UV community.

In contrast to these medium/large missions, that require a considerable financial investment, small-sized telescopes (such as cubesats or minisats) are arising as a cheap and fast alternative for carrying out UV research in the near future. Examples of these missions are ULTRASAT (Sagiv et al., 2014), MESSIER (Valls-Gabaud & MESSIER Collaboration, 2017), Earth-ASAP (Gómez de Castro et al., 2019), CUTE (France et al., 2020), and SPARCE (Scowen et al., 2020); all of them have a diameter < 50 cm.

Currently, the future of medium-sized UV telescopes is ensured by the World Space Observatory- Ultraviolet (WSO-UV). This mission is presented in greater detail in the next section.

---

[11] `http://arago-mission.obspm.fr/#fermer`

1.5.1 The World Space Observatory - Ultraviolet

WSO-UV is an international mission led by Russia (INASAN) with Spanish participation (AEGORA research group, Universidad Complutense de Madrid). Currently scheduled for launching in October, 2025, it is by now the only 2-m class facility under construction with ultraviolet instrumentation for the next decade. Besides, its privileged position in a High Earth Orbit will considerably reduce the pollution arising from the Earth's atmosphere, making WSO-UV an strategic base for UV studies unfeasible until now.

WSO-UV will provide access to spectroscopy and photometry in the $1150-3150$ Å range, with the possibility of simultaneous operation of the instruments. The WSO-UV spectrograph unit (WUVS) provide both high dispersion ($R \sim 50,000$) échelle spectroscopy at FUV (VUVES, $1150-1760$ Å) and NUV (UVES, $1740-3100$ Å) channels, and low-dispersion ($R \sim 1,000$) spectroscopy in the full range $1150-3050$ Å. There is an additional instrument, UVSPEX, that is optimised for the observation in the range $1150-1350$ Å, especially developed for exoplanetary studies. The WSO-UV Field Camera Unit (FCU) will provide imaging capabilities in two channels: the FUV channel ($1150-1900$ Å) is optimised for high resolution imaging and slitless spectroscopy, while the NUV channel ($1850-810$ Å) is designed for wide field imaging.

The scientific objectives of WSO-UV may be summarised in four categories: study of the baryonic content of the Universe and its chemical evolution, formation and evolution of the Milky Way, the physics of accretion and outflows, and the study of exoplanetary atmospheres and astrochemistry in the presence of strong UV fields. The observing time of WSO-UV will be divided amongst the Core Program, that will guarantee the observing time to the participant countries for science related with any of the four mentioned research areas; the National Programs from the participating countries (currently Russia and Spain); and the international community will have approximately 40% of the time available in the Open Time calls. During the expected 10 years of the mission (five nominal, with a planned extension of five more), groundbreaking discoveries will be undoubtedly made with WSO-UV.

The Spanish participation in WSO-UV is mainly focused in the imaging instrument (FCU): it is actively involved in the technical development of the instrument and will provide optical elements and the FUV detector. Spain will also host one of the two Science Operation Centres (SOCs), with headquarters at Universidad Complutense de Madrid and coordinated from the Joint Center for Ultraviolet Astronomy, JCUVA[12].

A recent review of the status of WSO-UV can be found in Shustov et al. (2018), and updated information is available at JCUVA's web page.

---

[12] `https://jcuva.ucm.es/`

1.6 Objectives and outline of the thesis

The interface between the densest parts of molecular clouds and the diffuse ISM is of outmost importance for any studies on star formation. These regions, that will be referred to as *molecular cloud envelopes*, are diffuse (share properties with the CNM/WNM, section 1.1) so can be probed at UV wavelengths (section 1.4) and present a significant population of interstellar charged dust grains that interferes with the propagation of MHD waves (section 1.2), directly affecting the energy input of the cloud. This regime, however, has been systematically ignored in previous studies of molecular cloud formation and evolution.

The results presented in this thesis reflect my efforts to give a comprehensive view on the behaviour of interstellar dust in molecular cloud envelopes and its signal at ultraviolet wavelengths, from both an observational and a theoretical points of view. My main objectives are: (1) to study the variations in the dust grain-size distribution inside molecular cloud envelopes using UV photometric observations, and (2) to analyse the dynamics and evolution of interstellar dust grains inside a molecular cloud envelope, and their coupling to the gas and the ambient magnetic field.

In the first part of this thesis (Chapter 2), I show evidence of variations in the grain size distribution due to grow and/or depletion phenomena towards two prototypical star forming regions: Orion and Rosette. This chapter is based on the article *Interstellar extinction in Orion: variation of the strength of the ultraviolet bump across the complex* published in MNRAS (Beitia-Antero & Gómez de Castro, 2017). The second part of the thesis is oriented to the theoretical study of the ISM, and is based on the articles *Formation of dust filaments in the diffuse envelopes of molecular clouds* published in ApJ (Beitia-Antero et al., 2021), and *Dust growth in molecular cloud envelopes: a numerical approach*, also accepted for publication in ApJ. In Chapter 3, I present a brief summary of the state-of-the-art of astrophysical numerical codes especially developed for ISM studies and motivate the code selection. Then, in Chapter 4 the numerical code is introduced with the implementation of two modules for interstellar dust. Finally, in Chapters 5 and 6 a study on the dynamical evolution and growth of dust in the envelopes of molecular clouds is presented in detail.

In the final part of the thesis (Chapter 7), the conclusions of the work are drawn, and an outline of my future research on the topic of ultraviolet extinction, interstellar dust, and molecular clouds is summarised.

There is also one additional work indirectly related with this thesis that is presented in Appendix A for completeness, since some of the products from that work are used in the observational study of Chapter 2. The article has been reproduced with the permission of the journal and of the co-authors.

2 Ultraviolet extinction in star forming complexes

Star forming complexes are the ideal places to study the influence of interstellar dust on molecular cloud fragmentation. They are usually governed by feedback from young stellar objects (YSOs) and the UV radiation field is very strong. This is, however, a handicap for the only photometric UV sky survey up to date, GALEX (see the discussion in sec. 1.4). GALEX avoided the brightest regions of the sky so as not to saturate its detectors (Bianchi, 2014), but it observed the external parts of the clouds, that will be referred to as *molecular cloud envelopes*, and by the end of its lifetime, the sensitivity constraints were relaxed and some bright regions were included for the final (GR6/GR7) release (Bianchi et al., 2014).

This chapter presents an observational study on the ultraviolet extinction law towards the star forming complexes of Orion and Rosette. The extinction curve is very sensitive to the presence of dust grains and comparing the variations at UV and infrared wavelengths it is possible to retrieve information about the relative abundance between the small and large dust grains due to coagulation and shattering processes. First, a brief introduction to both complexes is presented in sec. 2.1. Then, the properties of the ultraviolet extinction curve and the applied method are explained in sec. 2.2, and the observational data are summarised in sec. 2.3. In sec. 2.4 the slope of the NUV luminosity function is computed for the analysis of the strength of the bump in Orion and Rosette (sec. 2.5). The conclusions of this chapter are enumerated in sec. 2.6.

2.1 The molecular complexes of Orion and Rosette

The Orion molecular complex is the nearest ($d(\text{Ori A}) = 371 \pm 10$ pc, $d(\text{Ori B}) = 398 \pm 12$ pc, $d(\lambda\ \text{Ori}) = 445 \pm 50$ pc, Lombardi et al. 2011) massive star forming complex and the prototype for multiple studies on star formation. It contains several interesting structures such as the Barnard's Loop (Barnard, 1894), a wide HII region interacting with a molecular cloud; the λ-Orionis bubble, another HII region with a diameter of 60 pc (Lombardi et al., 2011); the Orion Nebula, the nearest region of massive star formation (Zuckerman & Palmer, 1975; Peimbert, 1982); and the photodissociation region of the Horsehead nebula (Schirmer et al., 2020; Murga et al., 2020), to cite some. The two densest parts of the complex are the Orion A and B clouds, where star formation is more active (see Fig. 2.1). Both clouds show the characteristic filamentary structure (see sec. 1.3), and are perpendicular to the ambient magnetic field (Planck Collaboration et al.,

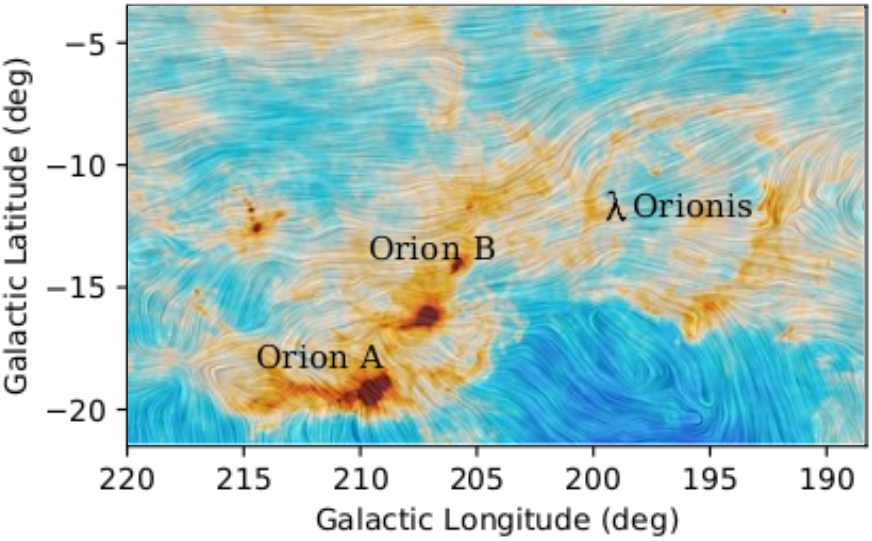

Figure 2.1: Column density map of the Orion Molecular Complex measured by *Planck* (Planck Collaboration et al., 2016c). The drapery pattern indicates the orientation of the magnetic field lines, assumed to be perpendicular to the sub-millimetre polarisation. The main structures of Orion A, Orion B, and λ-Orionis are identified.

2016c). This seems to imply that the filaments were formed under the influence of a magnetic field that forced the contraction along the field lines (Nakamura & Li, 2008; Li et al., 2013).

The Rosette nebula is one of the nearest Galactic OB regions (de Zeeuw et al., 1999), at a distance of 1330 ± 48 pc (Lombardi et al., 2011). Also known by the name of the open cluster responsible for the ionisation of the nebula, NGC 2244 (Martins et al., 2012), Rosette is one of the best places to study gas and dust evolution at early stages of star formation, since most of the parental molecular cloud is still present (Blitz & Thaddeus, 1980). It has been widely studied over the years: *Herschel* measured dust temperature and column density of the molecular cloud (Schneider et al., 2010, 2012); the kinematics of the cloud has been recently studied using *Gaia* DR2 data of the young stellar population (Kuhn et al., 2019); magnetic field strength (Savage et al., 2013; Costa et al., 2016) and orientation (Planck Collaboration et al., 2016b) have been measured at radio frequencies; and it was also mapped by GALEX in the NUV band at the end of the mission (see Fig. 2.2). Besides, the Rosette nebula is regarded as a prototype for triggered star formation, and exhaustive lists of the YSO population have been compiled (see e.g. Román-Zúñiga et al. 2008; Ybarra et al. 2013).

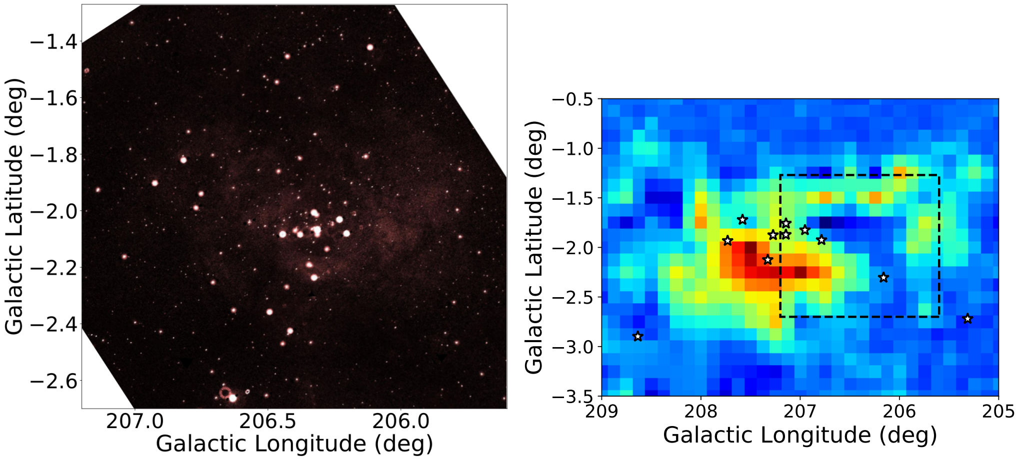

Figure 2.2: Left: *GALEX* NUV image of the Rosette nebula (angular resolution of 5.6 arcsec), built with the MOSAIX tool (Armengot et al., 2014). Right: velocity-integrated CO map of the Rosette molecular complex by Dame et al. (2001) (angular resolution of 8.5 arcmin) with the YSO clusters catalogued by Phelps & Lada (1997), Ybarra et al. (2013), and Cambrésy et al. (2013) plotted as white stars. The colour code corresponds to velocity-integrated values ranging from ~ -10 K km s^{-1} (blue) to $\sim +30$ K km s^{-1} (red), and is proportional to the gas column density. The dashed region corresponds to the GALEX image on the left panel.

2.2 The ultraviolet extinction curve and the star counts method

Extinction and reddening effects were early noticed in optical observations (Trumpler, 1930), and an inverse dependence with wavelength – the shorter the wavelength, the stronger the extinction – was also reported (see e.g. Greenstein 1946). However, with the advent of UV astronomy a whole new extinction curve characterised by strong features and variations was revealed (see sec. 1.4). The most striking feature of the UV extinction curve is a peak centred approximately at 2175 Å, the so-called UV bump. The first report of the bump is due to Stecher (1965), and was early attributed to be caused by graphite grains (Stecher & Donn, 1965). Even before the launch of *Copernicus* (see Sec. 1.4), its predecessor OAO-2 allowed the study of the UV extinction curve of some stars, and reported variations in the strength of the bump and especially in the steep rise of the FUV slope (Bless & Savage, 1972). It was also noticed that a general extinction law is not applicable, since strong variations are observed towards some lines of sight (Nandy et al. 1976, see Fig. 2.3).

Taking advantage of its low resolution spectroscopic capabilities, IUE provided the most extensive ultraviolet stellar database for the analysis of the extinction curve (see Seab et al. 1981 and Witt et al. 1984, and references therein); these data were used to provide a detailed parametrisation of the UV extinction curve

(Fitzpatrick & Massa, 1986) that has been improved over the years (Fitzpatrick & Massa, 2007; Fitzpatrick et al., 2019). Although several averaged extinction laws have been presented (see e.g. Cardelli et al. 1989) for the Milky Way and the Magellanic Clouds, one must be wary, since as has been already said, the UV extinction depends on the dust properties along the line of sight (see Fig. 2.3).

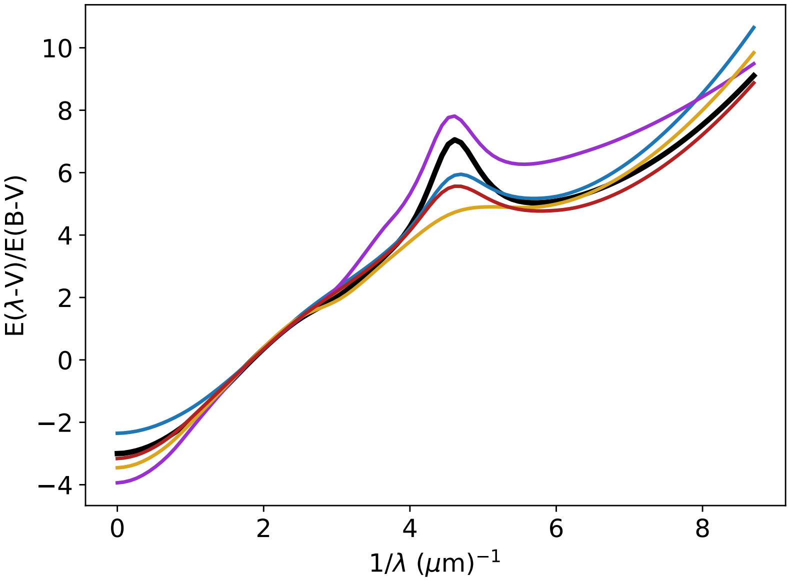

Figure 2.3: Averaged UV extinction curve for the Milky Way (black solid line) and for four stars, from top to bottom (at bump's location): HD 29647, HD 38023, BD+44 1080, HD 698 (from Fitzpatrick & Massa 2007).

Taking as a baseline the parametrisation of the UV extinction curve by Fitzpatrick & Massa (2007) (hereafter FM07), Gómez de Castro et al. (2015) (hereafter GdC2015) developed a method to estimate the strength of the bump from photometric UV data based on the star counts method. The extinction curve, usually represented as $k(\lambda - V) = E(\lambda - V)/E(B - V)$, is commonly fitted taking as free parameter $R_V = A_V/E(B - V)$. At infrared wavelengths, a cubic interpolation provides satisfactory results, but at near UV wavelengths, where the UV bump is located, a more complex parametrisation is needed; five parameters $(c_1, c_2, c_3, x_0, \gamma)$ are required to define the Lorentzian profile of the bump:

$$k(\lambda - V) = c_1 + c_2 x + c_3 D(x, x_0, \gamma) \tag{2.1}$$

where $x = 1/\lambda$ $\mu\mathrm{m}^{-1}$ and

$$D(x, x_0, \gamma) = \frac{x^2}{(x^2 - x_0^2)^2 + x^2\gamma^2} \tag{2.2}$$

Since eq. 2.1 is valid for any λ in the UV range, it can be averaged over the NUV GALEX band giving (GdC2015):

$$k(\mathrm{NUV}-V) = c_1 + 4.49c_2 + c_3(-0.82\gamma + 1.38) \tag{2.3}$$

In fact, the area of the bump measured over the extinction curve can be expressed as a function of c_3 and γ, $A_{\mathrm{bump}} = \pi c_3/2\gamma$ (FM07), so the averaged NUV extinction curve may be written as:

$$k(\mathrm{NUV}-V) = c_1 + 4.49c_2 + c_3(-1.29A_{\mathrm{bump}}^{-1} + 1.38) \tag{2.4}$$

It can be useful to study the relative extinction towards a line of sight at UV and infrared wavelengths, since dust grains scatter and absorb UV radiation and re-emit it at near-infrared wavelengths; besides, infrared photons are also efficiently extinguished by larger grains (~ 1 μm). In particular, one can study the relationship between the extinction in the GALEX NUV band and the infrared K_s band, and find it to be:

$$\frac{A_{\mathrm{NUV}}}{A_K} = \frac{R_V + c_1 + 4.49c_2 + c_3(-1.29A_{\mathrm{bump}}^{-1} + 1.38)}{0.15R_V - 0.19} \tag{2.5}$$

Evaluating eq. 2.5 for several lines of sight, GdC2015 found that the area of the bump can be expressed as a linear function of the ratio A_{NUV}/A_K:

$$A_{\mathrm{bump}} = (0.106 \pm 0.008)\frac{A_{\mathrm{NUV}}}{A_K} + (2.0 \pm 0.3) \tag{2.6}$$

This method provides an estimation of the strength of the bump based on the relative extinction in NUV and K_s bands, so its application to large photometric surveys is an advantage compared to the spectroscopic approach, which is very time consuming.

Several infrared extinction maps have been built up to date (see sec. 2.3) that can be used for our extinction study in Orion and Rosette. However, UV extinction maps are not commonly distributed. For the estimation of the extinction in NUV band, A_{NUV}, the same approach as GdC2015 has been adopted and the extinction is computed by applying the star counts method (Bok & Cordwell, 1973); this method has been applied to the study of galactic extinction since the seminal work by van Rhijn (1929) (see e.g. Lombardi et al. 2011). In the following, the discussion of the star counts method will be restricted to the computation of extinction in NUV band, although it is straightforward to extrapolate it to other wavelengths.

Given a star, its apparent magnitude m_{NUV} may be computed as:

$$m_{\mathrm{NUV}} - M_{\mathrm{NUV}} = -5 + 5 \log d + A_{\mathrm{NUV}} \tag{2.7}$$

where M_{NUV} is the absolute magnitude, d is the distance to the star (in pc), and A_{NUV} is the extinction we aim to estimate.
In its most usual form, the star counts on a given field, N_{NUV}, are compared to the expected counts on a nearby, non-extinguished field, N^*_{NUV}, so that the extinction can be computed as:

$$A_{\mathrm{NUV}} = \frac{1}{b_{\mathrm{NUV}}} \log \left(\frac{N^*_{\mathrm{NUV}}}{N_{\mathrm{NUV}}} \right) \tag{2.8}$$

In the above equation, the term $b_{\mathrm{NUV}} = d \log(N(m_{\mathrm{NUV}}))/dm_{\mathrm{NUV}}$ is a measure of the slope of the NUV luminosity function in the area of study. The error on the extinction is given by (Dickman, 1978):

$$\delta A_{\mathrm{NUV}} = \frac{1}{b_{\mathrm{NUV}}} \left(\frac{N^*_{\mathrm{NUV}} + N_{\mathrm{NUV}}}{N^*_{\mathrm{NUV}} N_{\mathrm{NUV}}} \right)^2 \tag{2.9}$$

It must be noted that this method may only be applied when the number of foreground stars is negligible. Since Orion is relatively nearby, most of the observed stars will be background and the method is valid. However, for the Rosette complex the resulting extinction maps should be treated with caution because of the non-negligible effects of foreground sources (see Fig. 2.4). Additional care has to be taken in the selection of the reference non-extinguished field. If its angular distance with respect to the area of study was too short, it might suffer from extinction from the cloud as well, while if it was too large the stellar density would not be comparable to that of the cloud. Therefore, the approach followed in this work has consisted in selecting a reference field in the surroundings of the molecular complexes, where the highly-extinguished areas have been discarded by comparison with dust extinction maps at infrared and radio wavelengths.

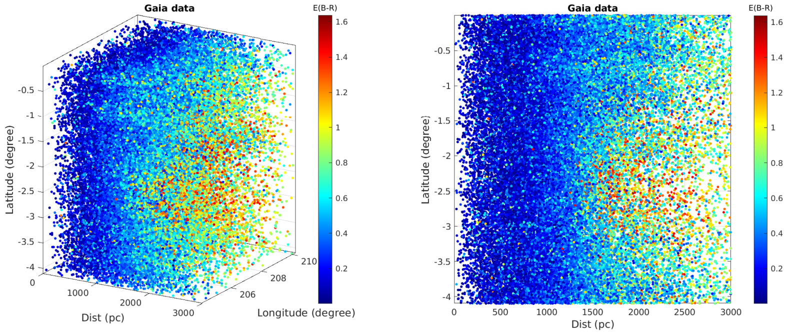

Figure 2.4: *Gaia* DR2 (Gaia Collaboration et al., 2018) sources towards the Rosette molecular complex. The colour code corresponds to the reddening of the sources (Andrae et al., 2018). Note the extended structure of the cloud (yellow-to-red points) and the elongated stripes of moderate reddening (E(B-R) $\sim$ 0.6, cyan points) at several longitudes. The paucity of data at cloud's distance and beyond is very likely due to extinction effects.

2.3 Observational data

As explained in the previous section, one can quantify the variations in the UV bump by studying the relative extinction in GALEX NUV band and in the infrared K band.

The GALEX all sky survey mapped $\sim$ 406 deg^2 of Orion and $\sim$ 78 deg^2 of Rosette. In Orion, the sources were selected from GALEX GR5 catalogue by Sanchez et al. (2014), while for Rosette, the sources were taken from GALEX GR6/7; both GR5 and GR6/7 catalogues provide a list of unique sources, so there are no duplicate entries in the data. For both samples, the bona fide sources were those with a 2MASS counterpart in a search radius of 3" (Bianchi et al., 2011b; Gómez de Castro et al., 2011); this amounts for 289 968 NUV sources in Orion, and 52 833 sources in Rosette that are displayed in Fig. 2.5.

2MASS has provided the most complete mapping of the near-infrared sky in the J, H, and K_s photometric bands (Skrutskie et al., 2006). Among all the available extinction maps based on 2MASS data, the one derived by Froebrich et al. (2007) (hereafter F07) following the NICE method (Lada et al., 1994) was chosen because of its availability for download. The only troublesome issue is that for dense regions (such as the Orion A and B filaments) extinction values are underestimated, while for distant regions the extinction effects are diluted. However, provided that the extinction measurements A_{NUV} and A_K are performed over the same region and with the same angular resolution, there should not be any appreciable geometrical effects. The map was re-sampled to three different resolutions based on the number of NUV sources; the optimal choices were identified to be 30', 15', and 10'.

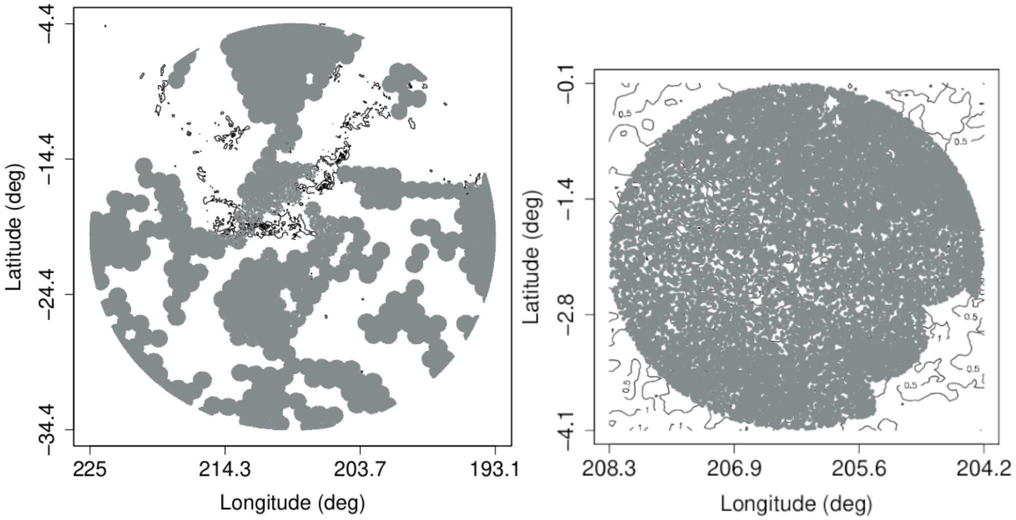

Figure 2.5: *GALEX* NUV sources in Orion (left) and Rosette (right) plotted over the 2MASS extinction map by Froebrich et al. (2007) (background contours) in Galactic coordinates. In both cases, the GALEX bona fide point-like sources are represented by grey dots. Note the difference in resolution and scale between the two regions.

2.4 NUV luminosity function

The luminosity function gives information about the population under study, but extinction effects can produce a decrease of the apparent magnitude of the objects. Hence, it is necessary to find apparently unreddened regions to determine the slope of the luminosity function.

In the first place, the NUV luminosity function for Orion was analysed. The map was divided in squared 2° × 2° regions to guarantee a representative number of sources inside each region. Then, the infrared F07 and ultraviolet (Fig. 2.5) maps were compared to select regions with low extinction values in K_s band but enough number of UV sources; in this way, regions with warm dust emission were discarded. For removing also the regions with a significant cold dust population, the resulting maps were compared with the *Infrared Astronomical Satellite* (IRAS) IRIS and *Planck* maps using the Virtual Observatory tool Aladin (Bonnarel et al., 2000). In the end, ten apparently non-extinguished regions distributed all over the Orion complex were selected, with the aim to determine possible variations in the slope of the luminosity function; these control regions are shown in Fig. 2.6.

For the determination of the slope of the luminosity function, histograms were built by binning the sources in intervals of 0.5 mag; this width was chosen based on the criterion that the number of sources with a photometric error greater than 0.5 inside the field were negligible. The fitting of the slope was performed in the

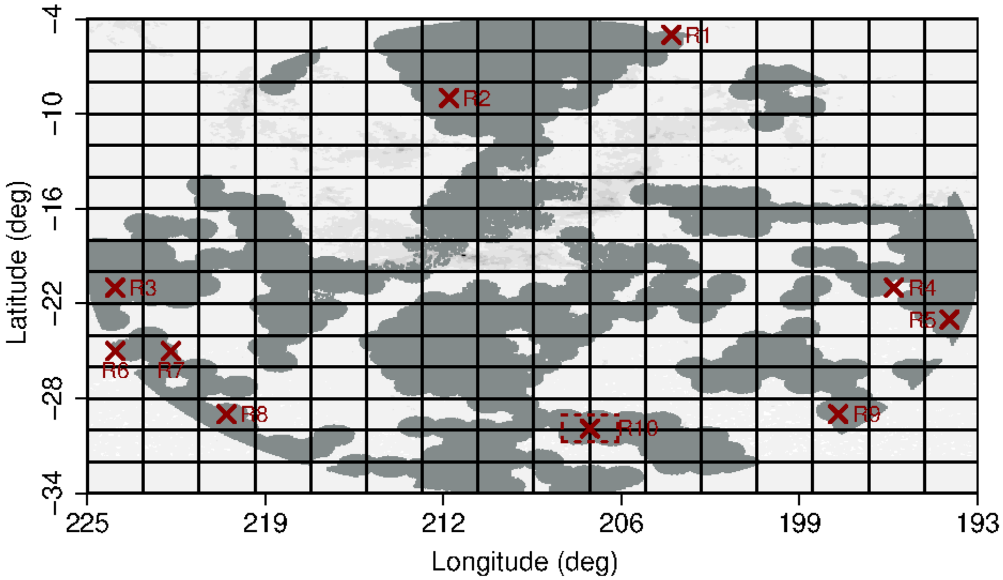

Figure 2.6: Selected regions for the computation of the NUV luminosity function across the Orion complex. GALEX point-like sources are displayed over the background A_K extinction map outlying the coverage (note the recognisable GALEX footprint).

completeness range of $16 - 20$ mag; the bright limit is slightly larger than the nominal value of NUV $= 13.85$ ABmag but the faint end corresponds to the typical exposure of the GALEX AIS observations (150 s, NUV $= 20.8$ ABmag), see for instance Bianchi et al. (2014). Three different fitting techniques were applied[1] to compare the results: classical least squares, bootstrap simulations, and via the Theil-Sen method[2]. The least squares method is widely applied in astrophysics and is based on the minimisation of the squared of the residuals; however, this method is based on several hypothesis, such as the dispersion is only due to errors in the dependant variable and that these errors are normally distributed, and is very sensitive to the presence of outliers. On the other hand, the bootstrap method is based on the generation of random samples from the original one taking into account the error (if available); then a least squares fitting of the simulated sample is performed. Finally, the Theil-Sen method consists on computing the slope and intercept for each pair of points, and then taking the median value for each possible pair; this method is computationally expensive for large datasets, but the small size of the considered sample allows its application to this particular case and provides a robust estimate of the parameters. In the end, it was found that the three methods produced similar results, so the least squares method was selected for its simplicity; the results are shown in Table 2.1.

---

[1] These fittings were performed with R (R Core Team, 2020).

[2] For this fitting, the R package *zyp* was used (Bronaugh & Werner, 2013).

Table 2.1: Fitting results of the NUV luminosity function slope in Orion by least squares, in the magnitude interval 16 − 20 mag. Two measures of the error, $e_{b_{\mathrm{NUV}}}$, and the residual standard error, S_t^*, are computed.

Region	R1	R2	R3	R4	R5	R6	R7	R8	R9	R10
Stars	678	1982	1062	971	1003	443	795	702	671	772
b_{NUV}	0.264	0.280	0.279	0.303	0.276	0.292	0.263	0.253	0.253	0.261
$e_{b_{\mathrm{NUV}}}$	0.019	0.011	0.007	0.016	0.023	0.024	0.017	0.020	0.019	0.018
S_t^*	0.061	0.036	0.024	0.051	0.073	0.078	0.056	0.066	0.062	0.058

Table 2.2: Theil-Sen linear fitting results for the galactic latitude correction term. m denotes the slope, while n is the intercept.

Map	m	e_m	n	e_n	S_r^*
30’	-0.075	0.045	-0.307	0.192	0.218
15’	-0.082	0.056	-0.421	0.223	0.250
10’	-0.073	0.042	-0.401	0.192	0.220

A global mean value for the slope was computed using weighted least squares, obtaining a value of $b_{\mathrm{NUV}} = 0.276 \pm 0.004$; this value is similar to that obtained by GdC2015 for the Taurus complex, although slightly lower.

Finally, before applying the star counts method to compute the A_{NUV} maps it is necessary to derive a correction for Galactic latitude, since the stellar density decreases when moving away from the Galactic Plane. Then, a correction term must be introduced, dA_{NUV}, such that the real extinction A^0_{NUV} can be derived by $A^0_{\mathrm{NUV}} = A_{\mathrm{NUV}} - dA_{\mathrm{NUV}}$, where A_{NUV} is computed from eq. 2.8 taking as a reference the most crowded field (the least extinct) at $b_{gal} \sim 8°$, and the correction factor is:

$$dA_{\mathrm{NUV}} = \frac{1}{b_{\mathrm{NUV}}} \log\left(\frac{N^{*,b_0}_{\mathrm{NUV}}}{N^{*,b}_{\mathrm{NUV}}}\right) \tag{2.10}$$

This correction has been evaluated in a set of non-extinguished fields taking as a reference the maximum possible value for N^{*,b_0}_{NUV}, reached at $b_{gal} \sim 8°$. An additional field at the Galactic Plane ($l_{gal} \sim 208.7°$, $b_{gal} \sim +0.83°$) has also been included for completeness. The value dA_{NUV} was fitted as a linear function of b_{gal} using the same methods as before (least squares, bootstrap, and Theil-Sen) for the three considered resolutions (see the next section), and this time notable differences in the results were found. Due to its robustness, the Theil-Sen results were finally adopted (see Fig. 2.7 and Table 2.2). Although these fits are derived for the Orion region, it was found that they are also applicable to the Rosette nebula.

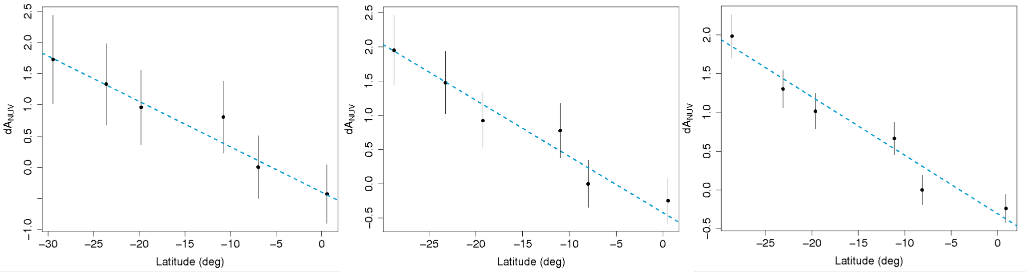

Figure 2.7: Theil-Sen linear fitting for the Galactic latitude correction term dA_{NUV} for the three considered extinction maps with resolution 10' (left), 15' (middle), and 30' (right). In all cases, the reference value was taken at $l_{gal} \sim 208.7°$, $b_{gal} \sim +0.83°$.

2.5 Variations in the extinction curve

Following the procedure described in the previous section, three NUV extinction maps were built at a resolution of 30', 15', and 10'; note that since GALEX's field of view covered an area of 1.25°, each GALEX tile is divided into, at least, three bins for the low-resolution map. Regions that were not observed by GALEX, especially those in Orion, were excluded from the study. The NUV extinction maps were then divided by the A_K maps by F07 (Sec. 2.3) and a saturation level[3] of $A_{\mathrm{NUV}}/A_K = 33$ was set, based on the results by GdC2015. Low values of the A_{NUV}/A_K maps (low UV or very large infrared extinction) will highlight regions were the small-sized dust population is depleted with respect to the larger one.

First, the the Orion extinction maps will be presented (sec. 2.5.1) since they are the most representative ones due to the proximity of the complex. In the last part of this chapter (sec. 2.5.2), results for the Rosette nebula are compared with spectroscopic measurements to test the accuracy of the applied method.

2.5.1 Dust evolution in Orion

The three relative extinction maps are displayed in Figs. 2.8 and 2.9.

In the low resolution 30' map (Fig. 2.8, left), the main areas of interest for a detailed study can be identified, that will be those where the ratio A_{NUV}/A_K reaches the lowest values. Further insights of the regions are revealed by the more precise 15' (Fig. 2.9) and 10' maps (Fig. 2.8, right).

Near to the Galactic Plane ($l_{gal} \sim 212°$, $b_{gal} \sim -8°$), there is an area where the A_{NUV}/A_K ratio reaches very low values. The 15' map shows that this region has a filamentary structure, where a main filament is oriented approximately

---

[3] This value corresponds to the mean value of the interstellar medium, where the infrared extinction is very low and produces large values of the ratio A_{NUV}/A_K.

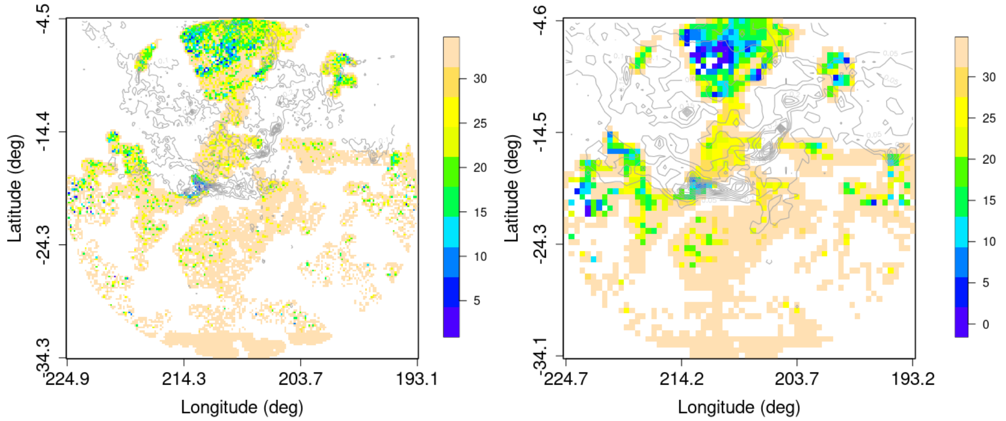

Figure 2.8: Orion relative extinction maps with a resolution of 30' (left) and 10' (right). The colour code represents the ratio A_{NUV}/A_K, and the A_K map is plotted in the background as a tracer for gas distribution. Low values of A_{NUV}/A_K (darker colours) indicate a decrease of the strength of the UV bump.

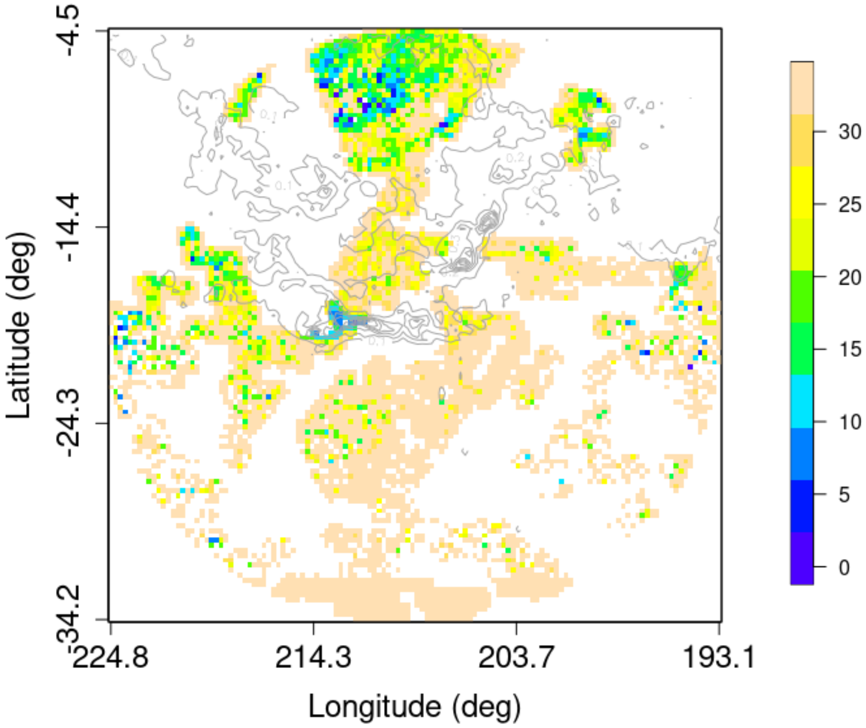

Figure 2.9: Same as Fig. 2.8 but for a mid resolution of 15'.

parallel to the Orion B cloud, and another one intersects it perpendicularly. Inside these filaments, the 10' map reveals certain pixels with very low values of the $A_{\rm NUV}/A_K$ ratio; these variations in the extinction curve may be an indicative for dust coagulation, as will be shown later.

At one extreme of the cloud ($l_{gal} \sim 221°$, $b_{gal} \sim -20°$), a decrease of the small-sized dust population is detected. As can be seen from Fig. 2.10, this region is not characterised by high gas column densities, so large dust grains are unlikely to produce this variation in the $A_{\rm NUV}/A_K$ ratio. However, the Hα map by Finkbeiner (2003) reveals tenuous structures that might correspond to clumps or filaments where small dust grains might experience a moderate growth.

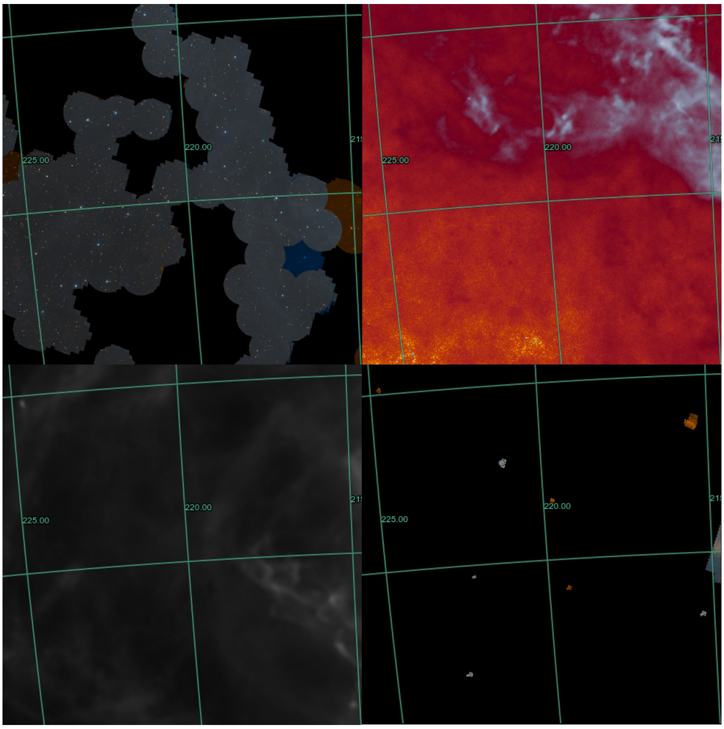

Figure 2.10: Panchromatic view of the region around $l_{gal} \sim 221°$, $b_{gal} \sim -20°$ obtained with ESASky[4]. The four panels show the same region of the sky but at different wavelengths: the top-left panel shows the *GALEX* FUV+NUV composite image, the top-right one is the Planck 353 GHz map, the bottom-left image is an Hα map and the bottom-right one shows the *Herschel* PACS composite ($70 + 160$ μm) image.

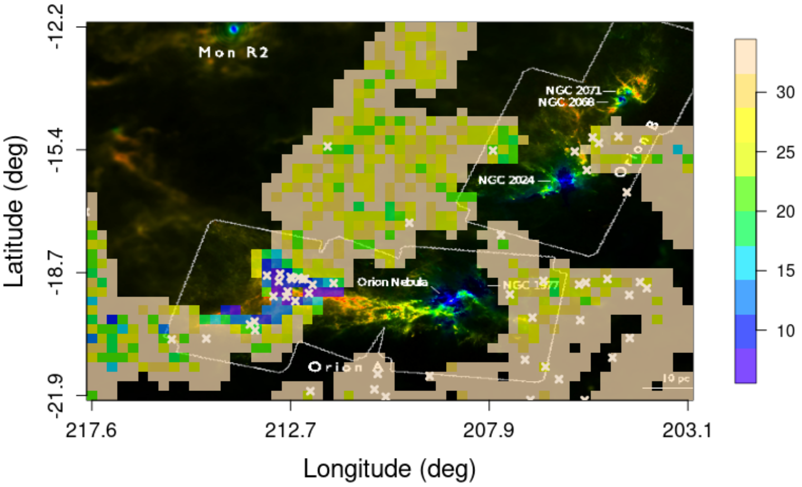

Figure 2.11: Extinction map for the Orion A filament (15') overlaid to the dust temperature map by Lombardi et al. (2014) (red, $T \leq 12$ K; blue, $T \geq 30$ K), where the intensity is proportional to the optical depth. YSO candidates identified by Sanchez et al. (2014) are represented as white crosses, where low values of the A_{NUV}/A_K are observed.

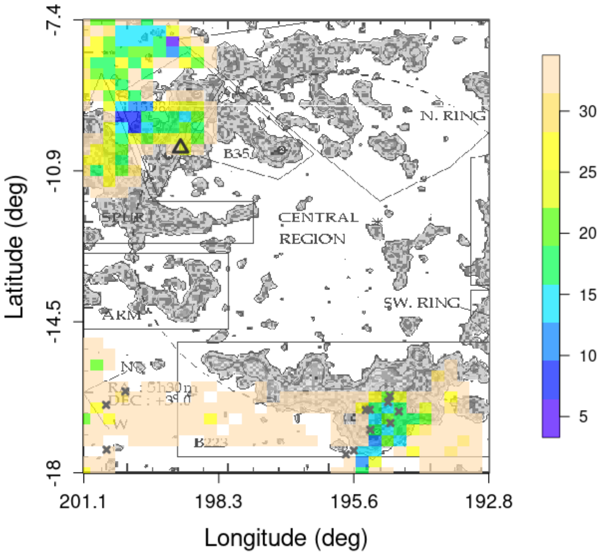

Figure 2.12: Mid resolution (15') A_{NUV}/A_K map and CO map by Lang et al. (2000). Low values of the relative extinction ratio in this region may be due to the photodestruction of PAHs by the strong ionising radiation from the central stellar binary system. Especially remarkable are the B223 region, where some YSOs are located, and the L1599 cloud identified by a triangle.

Another region of interest is the surrounding area of the Orion A filament, partially observed by GALEX. Consistently with the scenario of dust coagulation in dense regions, low values of the $A_{\rm NUV}/A_K$ ratio are found. Additional conclusions can be drawn from the comparison of this map with the optical-depth-temperature map derived by Lombardi et al. (2014), see Fig. 2.11: towards the densest region of the clouds, low values of the $A_{\rm NUV}/A_K$ ratio are observed together with an overdensity of YSO candidates (Sanchez et al., 2014). Also in this region, a mid intensity filament ($A_{\rm NUV}/A_K \sim 20$) appears to be perpendicular to the Orion B cloud, and more YSOs are identified over another diffuse filament of low relative extinction values at $l_{gal} \sim 206°$, $b_{gal} \sim -19°$.

Up to now, variations in the relative extinction ratio have been attributed to dust coagulation effects in some dense regions. However, in the strongly irradiated region of the λ Orionis bubble, that hosts a massive binary stellar system (O8III + B0.5V, Conti & Alschuler 1971), low $A_{\rm NUV}/A_K$ values are also observed that can be a result of photodestruction of PAHs. It is more evident in Fig. 2.12, where there are two localised regions at $l_{gal} \sim 200°$, $b_{gal} \sim -8°$ and $l_{gal} \sim 194°$, $b_{gal} \sim -16°$ (approximately coincident with the L1599 and B223 clouds) where more extinguished regions (comparatively speaking) are observed. In B223, the low values match approximately the emission of dark globules identified by Lang et al. (2000), so again in this case the variations in the relative extinction ratio may be due to dust coagulation effects. Besides, the presence of YSOs in this region may be an indicative of triggered star formation. On the other hand, in the direction of L1599 where the molecular gas is being pushed away, moderate values of the $A_{\rm NUV}/A_K$ ratio lower than the interstellar mean may indicate the destruction of small grains by the ambient radiation field.

2.5.2 Rosette and the spectroscopic testing of the method

Since the Rosette nebula is significantly further away than Orion, the extinction maps built from the star counts method are less accurate. In fact, they only reveal the Rosette molecular cloud and (roughly) its filamentary structure, see Fig. 2.13.

The main advantage of the Rosette nebula is that it was completely mapped by GALEX and some bright B stars were observed by IUE, providing an ideal framework for testing the accuracy of the applied method. For this purpose, high-quality spectra of non-variable OB sources in Orion and Rosette were selected from the catalogue presented in Appendix A. The query returned only one source in Orion (HD 32023), foreground to the cloud and very diluted; but three OB stars were found at Rosette's distance for which FM07 provided extinction curves. Hence, for these sources a spectroscopic measurement of the strength of the bump ($A_{bump} = \pi c_3/2\gamma$) as well as a statistical one from the $A_{\rm NUV}/A_K$ extinction maps (making use of the relationship derived in eq. 2.6) was possible; the results are summarised in Table 2.3. Two sources (HD 46106 and 46149) are

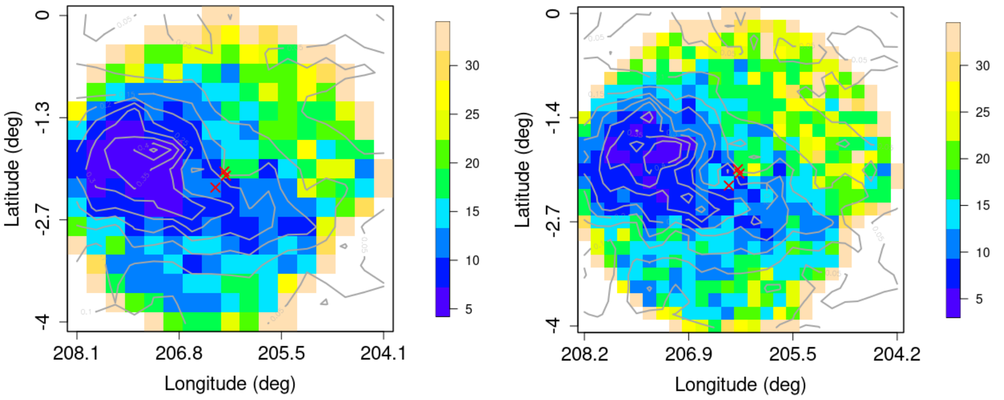

Figure 2.13: Relative extinction A_{NUV}/A_K maps for Rosette of 15' (left) and 10' (right) plotted over the A_K map. Locations of the three OB stars observed by IUE discussed in the text are highlighted by red crosses.

located foreground to the cloud and show a bump which strength increases with distance, in agreement with theoretical expectations (FM07). The lowest value of A_{bump} is reached for the star at Rosette's distance, HD 46056, and indicates a decrease of the small dust population due to either dust coagulation or photodestruction. In average, spectroscopic determinations of the area of the bump are significantly larger from the statistical ones and hence more realistic, since the latter are diluted due to random fluctuations of the stellar population. Another important contribution for these systematic differences may come from the fact that the extinctions are computed taking into account the stellar fluxes over the whole NUV band, that covers the whole range between $1750 - 2750$ Å, so they might be sensitive to the spectral energy distribution of individual sources. This effect, however, should be of little significance since a considerable number of stars are averaged inside a bin.

2.6 Conclusions

In this chapter, an observational study on the dust evolution in the molecular clouds of Orion and Rosette has been presented. Following the method derived by GdC2015, relative extinction maps in GALEX NUV band and infrared 2MASS K_s band have been built for the two complexes and the main conclusions of this study can be summarised as follows:

Table 2.3: Area of the 2175 Å bump computed for the three OB stars found in Rosette and the parameters used for the calculation. The errors in $A_{\rm bump}^{\rm spec}$ were propagated from the errors in the coefficients c_3 and γ obtained by FM07, while the errors in $A_{\rm bump}^{stat}$ were obtained with equation 2.6.

Star	HD 46106	HD 46149	HD 46056
d (pc)	809.6	1123.1	1343.9
l_{gal}	206.199°	206.220°	206.336°
b_{gal}	−2.094°	−2.039°	−2.247°
c_3	2.93 ± 0.10	3.25 ± 0.14	2.87 ± 0.12
γ	0.86 ± 0.01	0.90 ± 0.02	0.88 ± 0.01
$A_{\rm bump}^{\rm spec}$	5.35 ± 0.24	5.67 ± 0.37	5.12 ± 0.27
$\left(\frac{A_{\rm NUV}}{A_{\rm K}}\right)_{\rm map}$	20	20	12
$A_{\rm bump}^{\rm stat}$	4.1 ± 0.3	4.1 ± 0.3	3.3 ± 0.3

- The calculation of the NUV luminosity function for the Orion and Rosette complexes (sec. 2.4) reveals that there are not any significant variations in the direction of the Galactic anticentre. The slope of the luminosity function derived in this work is compatible with the one obtained for the Taurus molecular complex by GdC2015.

- Evidence of dust evolution in Orion and Rosette has been found (sec. 2.5). Dust coagulation in dense regions as well as photodestruction of the smallest dust grains in heavily irradiated regions are detected from variations of the $A_{\rm NUV}/A_K$ ratio.

- Spectroscopic measurements of the area of the bump reveal that the star counts method provides acceptable estimates of the variations in the ultraviolet extinction curve. However, the statistical results may only be regarded as an average and are systematically lower than the spectroscopic values. This effect may be negligible for nearby complexes as Orion, but it introduces dilution effects for regions further away such as Rosette due to the presence of a considerable amount of foreground stars.

To sum up, this work has provided an ultraviolet observational evidence for dust evolution. The remaining of this thesis is devoted to the numerical study of interstellar dust evolution in the low density regions that can be probed by ultraviolet wavelengths: the diffuse envelopes of molecular clouds.

3 Numerical simulations of the ISM

Over the last decade, an outburst of numerical codes has occurred due to the availability of very powerful computers at a low cost. The Astrophysics Source Code Library (1999), the main repository of astrophysical codes, contains more than 2000 codes, dating the oldest ones from the 80s.

The mathematical treatment of the problem and the numerical implementation will strongly depend on the scientific case. Codes developed for N-body dynamics, fluid dynamics (Athena, Stone et al. 2008, GIZMO, Hopkins 2015, RAMSES, Teyssier 2002), dust evolution (SAND, Dominik & Nübold 2002), or radiative transfer (RADMC-3D, Dullemond 2017) are fundamentally different. In this chapter, we present a brief review of the state-of-the-art of astrophysical fluid dynamics codes (sec. 3.1) and dust evolution codes (sec. 3.2). An evaluation of the pros and cons of these codes is presented in sec. 3.3 as a justification for the selection made for this thesis.

3.1 Astrophysical fluid dynamics

Codes oriented for fluid dynamics focus on solving the standard equations of (magneto)hydrodynamics (MHD):

$$\frac{\partial \rho}{\partial t} + \nabla \cdot (\rho \vec{\boldsymbol{v}}) = 0 \tag{3.1}$$

$$\frac{\partial \rho \vec{\boldsymbol{v}}}{\partial t} + \nabla \cdot (\rho \vec{\boldsymbol{v}} \vec{\boldsymbol{v}} - \vec{\boldsymbol{B}} \vec{\boldsymbol{B}} + \vec{\boldsymbol{P}}) = 0 \tag{3.2}$$

$$\frac{\partial E}{\partial t} + \nabla \cdot ((E + P)\vec{\boldsymbol{v}} - \vec{\boldsymbol{B}}(\vec{\boldsymbol{B}} \cdot \vec{\boldsymbol{v}})) = 0 \tag{3.3}$$

$$\frac{\partial \vec{\boldsymbol{B}}}{\partial t} - \nabla \times (\vec{\boldsymbol{v}} \times \vec{\boldsymbol{B}}) = 0 \tag{3.4}$$

$$\tag{3.5}$$

In the above equations, ρ is the gas density, $\vec{\boldsymbol{v}}$ is the gas velocity, $\vec{\boldsymbol{B}}$ is the magnetic field, $\vec{\boldsymbol{P}}$ is a diagonal tensor with components $P = P_{hydro} + (\vec{\boldsymbol{B}} \cdot \vec{\boldsymbol{B}})/2$, $P_{hydro} = (\gamma - 1)e$ is the gas pressure (assuming the equation of state of an ideal gas) where γ is the ratio of specific heat and e is the internal energy density, and E is the total energy density defined as:

$$E = \frac{P_{hydro}}{\gamma - 1} + \frac{\rho(\vec{\boldsymbol{v}} \cdot \vec{\boldsymbol{v}})}{2} + \frac{\vec{\boldsymbol{B}} \cdot \vec{\boldsymbol{B}}}{2}$$

All the equations are written in units such that the magnetic permeability $\mu = 1$.

There are basically two approaches to solve these equations (see Fig. 3.1): the Eulerian one that consists of solving (3.1) - (3.4) in a discrete grid (Fig. 3.1, middle panel); and the Lagrangian one, that treats the particles that compose the fluid individually and solves their dynamics and the interactions among them (Fig. 3.1, left panel). These two approaches together with a third technique that combines both of them, the so-called moving mesh codes (Fig. 3.1, right panel), are reviewed in the following sections showing a particular numerical code as an illustration.

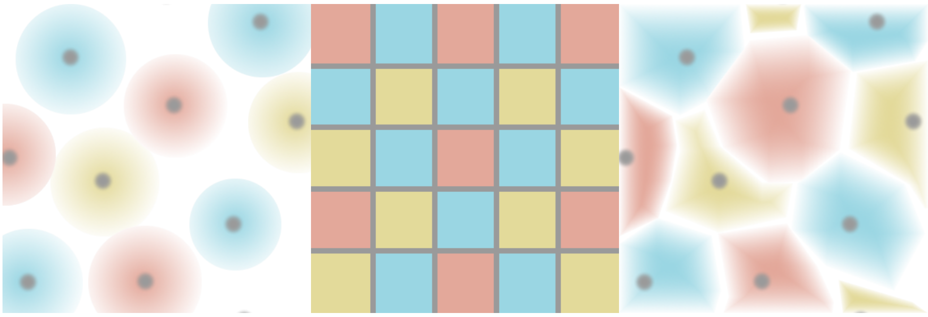

Figure 3.1: Illustration of the three different approaches for solving the fluid equations presented in this chapter: Smooth Particle Hydrodynamics (left), Grid-based codes (centre), and Moving Meshes (right).

3.1.1 Smooth Particle Hydrodynamics: PHANTOM

Smooth Particle Hydrodynamics (SPH) is a numerical approach for studying complex astrophysical problems in three dimensions developed originally by Lucy (1977) and Gingold & Monaghan (1977), suitable for problems where the magnetic fields do not play an important role (hydrodynamics). The method in essence considers a finite number of fluid particles N that evolve according to the equations of hydrodynamics on its Lagrangian form and whose interaction is mediated by an interpolation kernel $W(\vec{\boldsymbol{r}} - \vec{\boldsymbol{r}'}, h)$, which is taken to be in a first approach a Gaussian function:

$$W(\vec{\boldsymbol{r}}, h) = \frac{1}{h\sqrt{\pi}} \mathrm{e}^{-(x^2/h^2)} \tag{3.6}$$

that depends on a scaling factor h.

SPH codes are very useful for studying in detail complex processes at large scales such as the gravitational collapse of dark matter (GADGET-2, Springel 2005); however, those codes are not in general suitable for simulations of phenomena that dominate at smaller scales. The PHANTOM[1] code (Price et al., 2018) represents the state-of-the-art of SPH codes and Smooth Particle Magnetohydrodynamics (SPMHD) devoted to the study of the turbulent ISM (Kitsionas et al., 2009; Price & Federrath, 2010; Price et al., 2011), and stellar (Wurster et al., 2016, 2017) and planetary formation (Laibe & Price, 2014). A brief review of the numerical methods implemented in PHANTOM is included here as an illustration of how a SPMHD code works, something to take into account when choosing a numerical code for a particular scientific case.

As an illustration, below are shown the equations for SPMHD solved by PHANTOM:

$$\frac{\mathrm{d}\rho}{\mathrm{d}t} = -\rho(\nabla \cdot \vec{\boldsymbol{v}}) \tag{3.7}$$

$$\frac{\mathrm{d}v^i}{\mathrm{d}t} = -\frac{1}{\rho}\frac{\partial}{\partial x^j}\left(\left(P_{hydro} + \frac{1}{2}\frac{B^2}{\mu}\right)\delta^{ij} - \frac{B^iB^j}{\mu}\right) + \Pi_{shock} + f^i_{divB} \tag{3.8}$$

$$\frac{\mathrm{d}E}{\mathrm{d}t} = -\frac{P}{\rho}(\nabla \cdot \vec{\boldsymbol{v}}) + \Lambda_{shock} \tag{3.9}$$

$$\frac{\mathrm{d}}{\mathrm{d}t}\left(\frac{\vec{\boldsymbol{B}}}{\rho}\right) = \frac{1}{\rho}\left((\vec{\boldsymbol{B}} \cdot \nabla)\vec{\boldsymbol{v}} - \nabla\psi + D_{diss}\right) \tag{3.10}$$

$$\frac{\mathrm{d}}{\mathrm{d}t}\left(\frac{\psi}{c_h}\right) = -c_h(\nabla \cdot \vec{\boldsymbol{B}}) - \frac{1}{2}\frac{\psi}{c_h}(\nabla \cdot \vec{\boldsymbol{v}}) - \frac{\psi}{c_h\tau_c} \tag{3.11}$$

Equations (3.7) - (3.10) are essentially the same as equations (3.1) - (3.4) but for a few terms: δ^{ij} is the Kronecker delta function, Π_{shock} and Λ_{shock} are dissipation terms required for an appropriate treatment of entropy increase at a shock, and the terms f^i_{divB}, ψ, D_{diss}, c_h and τ_c are related with the divergence cleaning error and magnetic dissipation. In fact, there is a whole new equation (3.11) that controls the evolution of the divergence error. This is necessary because when evolving the magnetic field, the divergence free condition $\nabla \cdot \vec{\boldsymbol{B}} = 0$ must hold, but it is not possible to ensure this condition when discretising the MHD equations at particles' positions. Besides, in equations (3.7) - (3.10) the magnetic permeability $\mu \neq 1$.

To preserve the divergence-free condition, the approach implemented in PHANTOM consists of propagating divergence errors according to a damped wave equation controlled by a scalar field ψ coupled to the magnetic field (Tricco & Price, 2012; Tricco et al., 2016). This should be enough to conserve or dissipate mag-

---

[1] `https://phantomsph.bitbucket.io`

netic energy, but requires the user to check if the simulation results are correct or might be affected by errors arising from the divergence cleaning.

3.1.2 Eulerian Grid-based codes: Athena

The Eulerian approach for solving the full set of MHD equations (3.1) - (3.4) considers the fluid as a whole entity and follows variations of the conserved (momentum and energy) or primitive (velocity and pressure) variables together with the gas density and magnetic field in discrete uniform cells. Although in high-density regimes the resolution is poorer than that of SPH methods (sec. 3.1.1), in low-density regimes their performance tends to be better, especially when magnetic fields are taken into account.

Godunov[2] methods based on the integral form of the MHD equations written in conservative form as (3.1) - (3.4) are very popular nowadays, although some codes still apply finite differences methods (e.g. the Pencil Code, Brandenburg & Dobler 2002). A good example of a Godunov-based code is Athena (Stone et al., 2008), an evolution of the ZEUS code (Stone & Norman, 1992a,b; Stone et al., 1992) that emerged with the advent of Static and Adaptive Mesh Refinement (SMR and AMR, respectively) techniques. The mathematical description of the methods implemented in Athena is given in Gardiner & Stone (2005) and Gardiner & Stone (2008), but in the following a simple explanation of the basics of the method is given for the comparison with SPH (sec. 3.1.1) and moving mesh (sec. 3.1.3) codes.

If we denote by $\vec{\boldsymbol{U}}$ the vector of conserved variables and by $\vec{\boldsymbol{F}}$, $\vec{\boldsymbol{G}}$, and $\vec{\boldsymbol{H}}$ the vector of fluxes in x-, y-, and z- directions respectively, the fluid equations may be written as:

$$\frac{\partial \vec{\boldsymbol{U}}}{\partial t} + \frac{\partial \vec{\boldsymbol{F}}}{\partial x} + \frac{\partial \vec{\boldsymbol{G}}}{\partial y} + \frac{\partial \vec{\boldsymbol{H}}}{\partial z} = 0 \tag{3.12}$$

The conserved variables $\vec{\boldsymbol{U}}$ are computed in the centre of each cell by evolving the fluxes in finite volumes, while the magnetic fields are evolved in finite areas and evaluated at cell edges as illustrated in Figure 3.2. The main advantage of the evolution of the induction equation in finite areas is that conserves the divergence-free constraint by construction of the method.

---

[2] Godunov schemes solve a system of partial differential equations through the finite-volume approximation instead of using finite differences. They take their name after S. K. Godunov, who was the one that first suggested this kind of schemes in 1959 (Godunov, 1959).

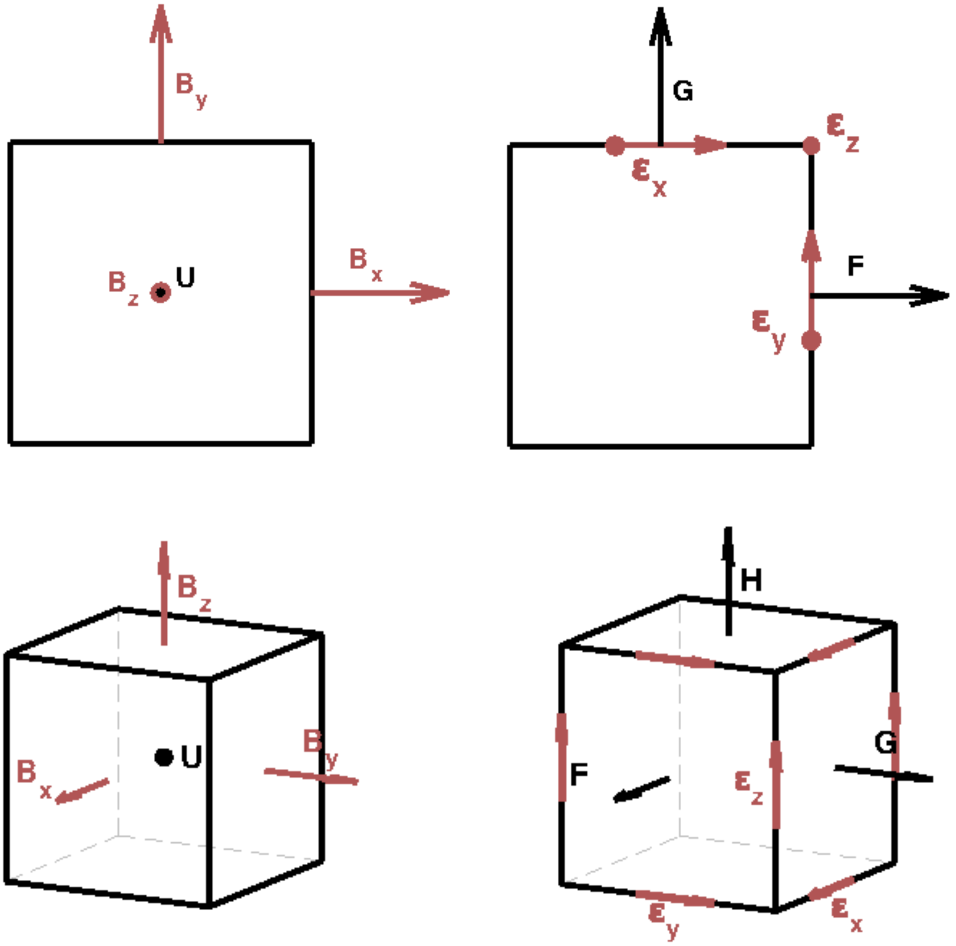

Figure 3.2: Illustration of area and volume averages over a cell in Athena in 2D (upper panel) and 3D (lower panel). Conserved variables $\vec{U}$ are evaluated at cell centres and computed from volume-averaged fluxes ($\vec{F}, \vec{G}, \vec{H}$); magnetic fields are updated from area averages of the electromotive force $\varepsilon = -\vec{v} \times \vec{B}$.

3.1.3 Moving mesh codes: GIZMO

Finally, moving mesh codes have emerged recently as an intermediate solution between SPH and AMR codes that takes the best of the two worlds while being computationally efficient. This approach has been barely explored in astrophysics, but in the last decade serious attempts have been made to develop numerical codes based on moving meshes for a general use (Springel, 2010; Duffell & MacFadyen, 2011). The best example is GIZMO (Hopkins, 2015) currently under development but with a publicly available version[3].

The numerical approach of GIZMO is very similar to that of Athena, because they consider the fluid equations in the conservative form

$$\frac{\partial \vec{\boldsymbol{U}}}{\partial t} + \nabla \cdot (\vec{\boldsymbol{F}} - \vec{\boldsymbol{v}}_{frame} \otimes \vec{\boldsymbol{U}}) = 0 \tag{3.13}$$

but with a reference frame moving at a speed $v_{frame} \neq 0$. Notice that if $v_{frame} = 0$, eq.3.13 is equivalent to eq. 3.12. Then, these equations are converted to integral form and discretised, as in every Godunov finite-volume scheme:

$$\frac{d}{dt}(V_i \vec{\boldsymbol{U}}_i) + \sum_j \tilde{\mathbf{F}}_{ij} \cdot \vec{\boldsymbol{A}}_{ij} = 0 \tag{3.14}$$

where V_i is the effective volume of particle i, $\tilde{\mathbf{F}}_{ij}$ is the flux and the vector $\vec{\boldsymbol{A}}_{ij}$ is a factor that accounts for local volume. Then, the volume is partitioned among the nearest particles/cells through the use of a weighting function $W(\vec{\boldsymbol{x}} - \vec{\boldsymbol{x}}_i), h(\vec{\boldsymbol{x}})$, similarly to SPH methods.

Again, the main drawback of this code resides in the implementation of the induction equation. GIZMO applies the same algorithms as PHANTOM for evolving the magnetic field (Hopkins & Raives, 2016), and although this code seems to be ground-breaking one must still be concerned with the $\nabla \cdot \vec{\boldsymbol{B}} = 0$ issue.

3.2 Dust evolution codes

There is a great interest nowadays on understanding the processes that dominate dust evolution as a first step towards understanding protoplanetary formation. The current studies are centred in either neutral dust particles that suffer from aerodynamical drag, or very small charged grains that are influenced by a background magnetic field, and there are two widely used approaches for following grain growth.

The first approach (Simons & Williams, 1975; Hirashita & Yan, 2009; Paruta et al., 2016) is to evolve in time the grain size distribution. Then, given a range of particle sizes $[a_{min}, a_{max}]$, the mass density is evolved in a series of N discrete bins taking into account shattering and coagulation:

$$\frac{d\rho_i}{dt} = \left[\frac{d\rho_i}{dt}\right]_{shat} + \left[\frac{d\rho_i}{dt}\right]_{coag}, \quad i = 1, 2, ..., N \tag{3.15}$$

In this formulation, the particles have a characteristic mean velocity that is considered for the computation of the collision outcome.

---

[3] `http://www.tapir.caltech.edu/~phopkins/Site/GIZMO.html`

A second approach developed by Zsom & Dullemond (2008) relies on Monte Carlo (MC) sampling. Their method takes a full set of n particles representative of a whole population of N that follows a prescribed dust distribution, where n is a reasonable number that can be handled by a computer. In a nutshell, they compute at the beginning of the simulation the collision rates for each dust grain family that are later used to choose randomly (MC) the particle that will suffer an interaction. The key point of their approach is that representative dust grains (n) are only considered to interact with real dust particles (N), and in this way the number of computational particles does not vary, while the properties of each of the interacting (n) particles do change after every interaction.

Although basically different, the methods explained above share a common point: dust particles are only considered to be neutral. Only Hirashita & Yan (2009) consider charged dust grains but indirectly, taking mean dust velocities for charged grains from Yan et al. (2004). However, laboratory experiments have shown that coagulation of very small grains is indeed enhanced when they are charged and in presence of a background magnetic field (Nuth et al., 1994; Nübold et al., 2003). Actually, the collision cross section for a charged dust grain is slightly greater than that of a neutral one (Dominik & Nübold, 2002) and the resulting aggregates form coherent filamentary structures (see Fig. 3.3). This area is basically unexplored in astrophysics, and its study is fundamental to understand the evolution of dust grains in diffuse environments where the grains are charged and the magnetic fields play an important role, as in the molecular cloud envelopes of Orion and Rosette. Another important factor that could affect the evolution of dust grains in molecular clouds is the processing of their carbon-rich mantles in the ISM (see section 1.2). However, rather than photodarkening playing a significant role in coagulation and shattering processes, collisions between particles as well as the effects of the radiation field and the gas properties will definitely alter the composition of the aggregates, and will therefore affect the shape of the UV extinction curve.

3.3 Choosing a code

As outlined in the Introduction (sec. 1.6), the problem I aim to explore is the evolution of interstellar dust in molecular cloud envelopes, and how it may affect the later evolution of the cloud. For this purpose, an MHD code was clearly needed. An optimal choice of the code would consider several aspects: the first one, the code should be reliable and stable, with a strong support team behind; the second one, it should be optimised for ISM simulations; the third one, it should include a particles module, ideally with the physics of charged particles included.

The three codes presented in this chapter, Athena, PHANTOM, and GIZMO, suit one of the most stringent requirements: the inclusion of a particles module. However, save GIZMO, which considers the basic physics of charged grains

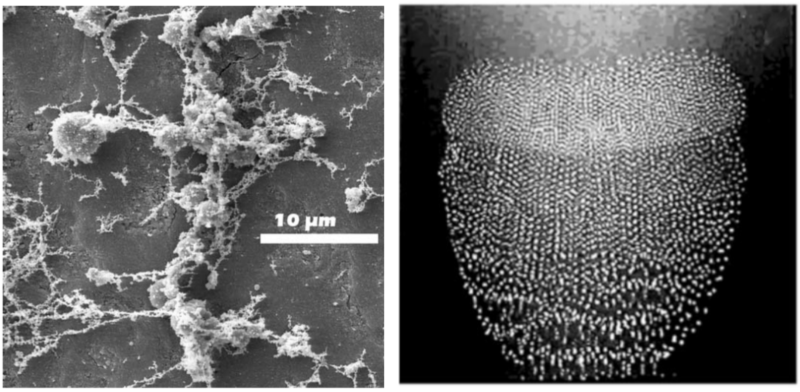

Figure 3.3: Illustration of some magnetic dust structures. The left panel is adapted from Nübold et al. (2003) and shows a scanning electron microscope image of a particle aggregate of charged dust that grows in the presence of a magnetic field. The right panel is adapted from Fortov et al. (2004) and shows the behaviour of charged dust particles when submitted to an electric discharge.

(Lee et al., 2017), both Athena (Bai & Stone, 2010) and PHANTOM (Laibe & Price, 2012a,b; Price & Laibe, 2015) implemented solid neutral particles in the context of protoplanetary formation. However, GIZMO presented other potential problems, mainly the novelty of its methods that makes it difficult to assess if the algorithms always produce the correct results. Actually, the greatest concern was the divergence-free constraint, as highlighted in sec. 3.1, and it was what finally inclined the balance towards Athena. There is an additional issue that also supported the selection of Athena, which is the computational resources available. SPH and moving-mesh codes are computationally expensive because a large number of particles is required for high-resolution simulations. As a member of the AEGORA Research group, I got access to a Fell PowerEdge R630 high performance computing server (HPC) server with two Intel Xeon E5-2600 v4 processors (32 cores, cache of 2.5 MB per core) and 32 GB of high-performance DDR4 RAM. The simulations presented in Chapter 5 (which are 2D with a resolution of 1024×1024 pixels^2) were performed with this facility and took a month of calculations using 16 cores. Therefore, for simplicity and due to time constraints derived from the maximum duration of the PhD period only 2D models have been considered for this thesis. The development and data analysis of the contents of this thesis have been carried out on a workstation with an Intel i7-6700 CPU 3.40GHz with 8 cores and 16 GB of RAM. The simulations presented in Chapter 6 have been also carried out with this workstation, and took only a few hours on a single processor.

In the next chapter, the implementation of two additional modules in Athena (one for charged particles and one for dust growth) is explained in detail.

4 Dynamics and growth of interstellar dust in Athena

This chapter is fully devoted to the modifications of the Athena code (briefly introduced in sec. 4.1) to include the dynamics of charged dust grains (sec. 4.2) and a simple collision model (sec. 4.3). The application of these modules to study a realistic astrophysical problem is left for Chapter 5.

4.1 Athena: public version 4.2

Athena[1] is an open-source code developed at Princeton University. The first public version was released in 2008 (Stone et al., 2008) but its development started back in 2004 and took four years (see Gardiner & Stone 2005 and Gardiner & Stone 2008). Over the next five years, it experienced a progressive evolution and new physics was implemented, such as heat conduction (Parrish et al., 2008; Choi & Stone, 2012), viscosity (Dong & Stone, 2009; Kunz et al., 2012), non-ideal MHD effects (Fromang & Stone, 2009; Bai & Stone, 2011), relativistic MHD (Beckwith & Stone, 2011), self-gravity (Gong & Ostriker, 2011), and radiative cooling (Gendelev & Krumholz, 2012; Choi & Stone, 2012). It also supports cylindrical coordinates (Gendelev & Krumholz, 2012) and shearing-box and orbital advection for the simulation of rotating disks (Stone & Gardiner, 2010; Sorathia et al., 2012). Currently, a new version of Athena is being developed in C++, called Athena++[2], but the stable C version was preferred to include the additional physics.

The starting point of the implementation presented in this thesis is the aerodynamic particles module developed by Bai & Stone (2010), hereafter BS10. In the next section, the essentials of this module are summarised.

4.1.1 The aerodynamic particles module

BS10 implemented a module of aerodynamic particles in Athena. Their main purpose was to study the streaming instability in protoplanetary disks (PPDs) caused by the interaction of dust grains with the gas in those dense environments (Youdin & Goodman, 2005). For the numerical treatment of the problem, the computational particles were considered to be superparticles, where each of them represents a swarm of real particles.

---

[1] https://princetonuniversity.github.io/Athena-Cversion/

[2] https://princetonuniversity.github.io/athena

The implemented scheme integrates the evolution of both gas and dust in the corner transport upwind[3] (CTU) fluid integrator. It considers not only the aerodynamic drag of dust grains, but also the possible feedback of those grains to the gas. The resulting algorithm is a predictor-corrector scheme on which the gas is evolved half a time step taking into account the predicted effect of dust over the gas. Then the particle's positions and velocities are updated. Finally, the gas is evolved a full time step, correcting for the effects of the updated properties of dust grains.

Since this thesis is focused on the study of the dynamics of dust grains in a diffuse regime where the dust-to-gas density ratio is very low ($\rho_d/\rho_g \sim 0.01$, Spitzer 1954) the back reaction of dust grains into the gas will be negligible, at least in a first approach. Henceforth, the particles feedback feature is turned off in Athena and the rest of the discussion will be restricted to the evolution of passive dust particles.

The equation of motion of a particle dragged by the gas is given by:

$$\frac{d\vec{\boldsymbol{v}}}{dt} = -\frac{\vec{\boldsymbol{v}} - \vec{\boldsymbol{u}}}{t_s} \tag{4.1}$$

where $\vec{\boldsymbol{v}}$ denotes the particle velocity and $\vec{\boldsymbol{u}}$ is the gas velocity at particle's position. The variable t_s is the stopping time: it is a measure of the coupling of the neutral particle with the fluid and depends on the particle's size, a_d, and the mean free path of the gas particles. In the diffuse ISM , the dust particles are much smaller than the mean free path of the gas (Epstein regime) and the stopping time is given by (Weidenschilling, 1977):

$$t_s = \frac{\rho_d^{int} a_d}{\rho c_s} \tag{4.2}$$

where ρ_d^{int} is the particle's internal density, ρ is the gas density at particle's position, and c_s is the gas thermal velocity.

The particle's position, $\vec{\boldsymbol{x}}$, and velocity, $\vec{\boldsymbol{v}}$ evolve according to the equations:

$$\frac{d\vec{\boldsymbol{x}}}{dt} = \vec{\boldsymbol{v}}, \quad \frac{d\vec{\boldsymbol{v}}}{dt} = \vec{\boldsymbol{a}}(\vec{\boldsymbol{v}}, \vec{\boldsymbol{x}}, \vec{\boldsymbol{u}}^{(n+1/2)}(\vec{\boldsymbol{x}})) \tag{4.3}$$

where $\vec{\boldsymbol{a}}$ collects all the acceleration terms involved in the equation of motion (eq. 4.1). Although it seems trivial, this notation will be very useful when additional acceleration forces besides aerodynamic drag are included.

---

[3] The corner transport upwind is a numerical scheme first presented by Colella (1990) that takes into account the effect of information propagating across corners of computational zones in calculating the flux in Godunov schemes. In Athena, this scheme is slightly modified and combined with the constrained transport (CT) method for the conservation of the divergence-free constraint (for more information, see Gardiner & Stone, 2005).

The particle's integrator is a semi-implicit integrator based on the Crank-Nicholson method:

$$\begin{cases} \vec{\boldsymbol{x}}' = \vec{\boldsymbol{x}}^{(n)} + h\vec{\boldsymbol{v}}^{(n)}/2, \\ \vec{\boldsymbol{v}}^{(n+1)} = \vec{\boldsymbol{v}}^{(n)} + h\vec{\boldsymbol{a}}((\vec{\boldsymbol{v}}^{(n)} + \vec{\boldsymbol{v}}^{(n+1)})/2, \vec{\boldsymbol{x}}', \vec{\boldsymbol{u}}(\vec{\boldsymbol{x}}')) \\ \vec{\boldsymbol{x}}^{(n+1)} = \vec{\boldsymbol{x}}' + h\vec{\boldsymbol{v}}^{(n+1)}/2 \end{cases} \tag{4.4}$$

The velocity update can be computed by solving the following system of equations (BS10):

$$\vec{\boldsymbol{v}}^{(n+1)} = \vec{\boldsymbol{v}}^{(n)} + h\Lambda^{-1}\vec{\boldsymbol{a}}(\vec{\boldsymbol{v}}^{(n)}, \vec{\boldsymbol{x}}', \vec{\boldsymbol{u}}(\vec{\boldsymbol{x}}')), \quad \Lambda = 1 - \frac{h}{2}\frac{\partial \vec{\boldsymbol{a}}}{\partial \vec{\boldsymbol{v}}} \tag{4.5}$$

where $\frac{\partial \vec{\boldsymbol{a}}}{\partial \vec{\boldsymbol{v}}}$ is the Jacobian matrix evaluated at the predicted position $\vec{\boldsymbol{x}}'$:

$$\frac{\partial \vec{\boldsymbol{a}}}{\partial \vec{\boldsymbol{v}}} = \begin{pmatrix} -1/t_s & 0 & 0 \\ 0 & -1/t_s & 0 \\ 0 & 0 & -1/t_s \end{pmatrix} \tag{4.6}$$

Then, the algorithm can be summarised as:

- At time $t = n + 1/2$, compute gas-related quantities (momentum, density) at particle's position.
- Compute particle velocity (eq. 4.5).
- Compute particle position (eq. 4.3).
- Evolve gas a full time step.

At code level, the particles are managed via two structures (see Fig. 4.1): `GrainS` stores the basic dynamical quantities, such as position, velocity and type for each individual computational particle; `Grain_Property` is a less extensive structure that contains one entry per particle type with basic information about its composition, such as radius, mass, or solid density. These structures are mentioned here explicitly because they have been drastically modified with the implementation of the collision model (see sec. 4.3).

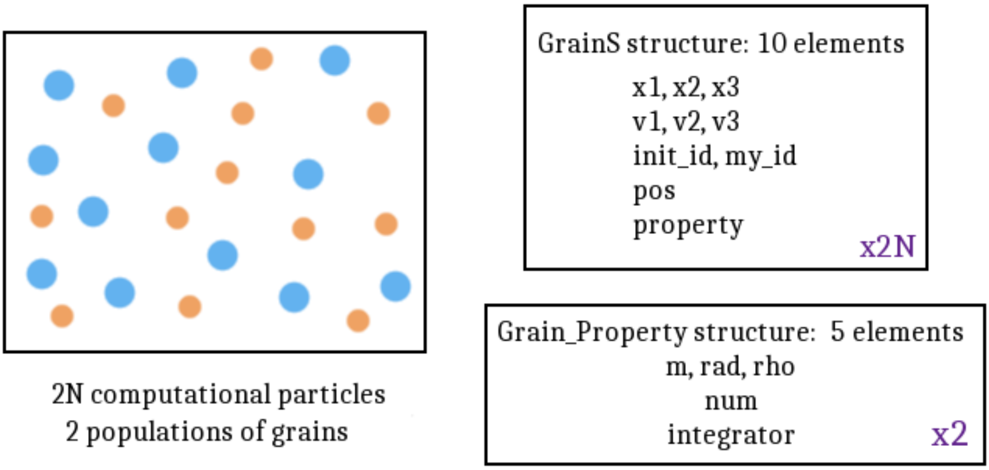

Figure 4.1: Illustration of the two basic particle structures in Athena. In a given simulation, there are N particles from two different families (blue and orange points). The position and velocity of the 2N particles are stored individually in the structure GrainS, while their global properties such as radius, mass, or internal density are stored in a common structure called Grain_Property.

4.2 Dynamics of charged dust in Athena

Taking the particles module presented in sec. 4.1 as a base, the dynamics of charged dust grains was first implemented.

Solid particles in the diffuse ISM are submitted to the ambient UV radiation field that ionises them. In particular, dust grains acquire a net charge that can be computed from the statistical equilibrium amongst several phenomena (Draine 2011, see also sec. 5.1 for more details). The charge depends on the dust composition and size as well as on the environment, but in general will be non-zero, $Z_d e \neq 0$.

Charged grains will interact with the permeating Galactic magnetic fields, but also with the ions and electrons of the partially ionised gas. Hence, the equation of motion for a charged particle has two additional terms with respect to eq. 4.1:

$$\frac{\partial \vec{\boldsymbol{v}}}{\partial t} = -\frac{\vec{\boldsymbol{v}} - \vec{\boldsymbol{u}}}{t_s} - \nu_C(\vec{\boldsymbol{v}} - \vec{\boldsymbol{u}}) + \frac{Z_d e}{m_d c}((\vec{\boldsymbol{v}} - \vec{\boldsymbol{u}}) \times \vec{\boldsymbol{B}}) \tag{4.7}$$

The first term in eq. (4.7) accounts for the interaction of charged dust grains with the ions/electrons in the plasma. Under the MHD approximation, the dynamics of ions and electrons in the gas cannot be explicitly resolved, so they are supposed to move together with the neutral gas at the same speed $\vec{\boldsymbol{u}}$. Therefore, the interaction between dust grains and charged gas species is modelled as an additional drag term characterised by the Coulomb interactions rate (Pilipp et al., 1987):

$$\nu_C = \frac{4}{3}\frac{\sqrt{2\pi}Z_d^2 e^4 \ln\Lambda}{(kT)^{3/2} m_d}\left(\frac{\rho_{ion}\delta}{\sqrt{m_{ion}}} + \frac{\rho_e(1-\delta)}{\sqrt{m_e}}\right) \tag{4.8}$$

In this equation, $Z_d e$ is the grain charge, m_d is the dust mass, $\ln\Lambda = \ln\frac{3kT}{2e^3}\sqrt{\frac{kTm_e}{\rho_e\pi}}$ is the Coulomb logarithm, k is the Boltzmann constant, T the gas temperature, m_{ion} and m_e are the ion and electron masses respectively with densities ρ_{ion} and ρ_e, and $\delta = 1$ if $Z_d e < 0$, and $\delta = 0$ in other case. This means that negatively charged grains only interact with ions and positively ones with electrons.

The second term in eq. 4.7 accounts for the interaction with the magnetic fields, the so-called Lorentz force[4]. This term was first implemented in Athena by Lehe et al. (2009) in order to study the heating of test charged particles in Alfvénic turbulence, but their particles were massless and the modified code was not made public. However, their work has served as a guide for the numerical integration of the Lorentz term in the equation of motion.

To simplify the notation, the multiplicative constant in the Lorentz force will be denoted by:

$$Q_m \doteq \frac{Z_d e}{m_d c} \tag{4.9}$$

To integrate the dynamics of charged particles, Lehe et al. (2009) chose the semi-implicit integrator by Boris (1970), which gives second-order accuracy and performs well even for relativistic particles. Since it is very similar to the semi-implicit integrator already implemented in Athena (see sec. 4.1) they have been combined, resulting in the following modified Jacobian matrix:

$$\frac{\partial\vec{\boldsymbol{a}}}{\partial\vec{\boldsymbol{v}}} = \begin{pmatrix} -\frac{1}{t_s} - \nu_C & Q_m B_z & -Q_m B_y \\ -Q_m B_z & -\frac{1}{t_s} - \nu_C & Q_m B_x \\ Q_m B_y & -Q_m B_x & -\frac{1}{t_s} - \nu_C \end{pmatrix} \tag{4.10}$$

and the numerical scheme (4.4) still applies. The magnetic fields that appear in matrix (4.10) are evaluated also at particle's position at $t = n + 1/2$ from the cell-centred magnetic fields. Careful attention has been put to ensure that the constraint $\nabla \cdot \vec{\boldsymbol{B}} = 0$ holds even if non-ideal MHD terms are included.

---

[4] Actually, the complete Lorentz force term in the laboratory reference frame reads $(Z_d e/m_d c)(c\vec{\boldsymbol{E}} + (\vec{\boldsymbol{v}}) \times \vec{\boldsymbol{B}})$.

There is one more issue that must be taken into account for an accurate integration of the Lorentz force: the time step must be smaller than the Larmor time. As a compromise between accuracy and computational cost, the time step has been chosen to be at least ten times smaller than the Larmor time, as in Lee et al. (2017):

$$\Delta t = \frac{\mathrm{CFL}}{10} \min\left(\frac{m_d c}{Z_d e|\vec{\boldsymbol{B}}|}, \Delta t_{\mathrm{MHD}}\right) \tag{4.11}$$

where CFL is the Courant-Friedrichs-Lewy[5] number.

4.2.1 Charged particles tests

The behaviour of the charged particles integrator in 2D is tested from several simple problems with analytical solution. These tests consider a positively charged dust grain at rest embedded in a uniform medium that moves at a constant speed $u_x = v_{th}$ (the isothermal sound speed). There is also an ambient magnetic field perpendicular to the domain, and hence parallel to the z-axis.

Test 1: Lorentz force

The first test is designed to check the accuracy of the integration of the Lorentz force. The equations to be solved are:

$$\frac{d\vec{\boldsymbol{x}}}{dt} = \vec{\boldsymbol{v}}, \quad \frac{d\vec{\boldsymbol{v}}}{dt} = -\frac{\vec{\boldsymbol{v}} - \vec{\boldsymbol{u}}}{t_s} + Q_m(\vec{\boldsymbol{v}} - \vec{\boldsymbol{u}}) \times \vec{\boldsymbol{B}} \tag{4.12}$$

$$\vec{\boldsymbol{x}}(0) = (x_0, y_0), \ \vec{\boldsymbol{v}}(0) = (0, 0)$$

Denoting $A \doteq 1/t_s$, $B \doteq Q_m B_z$ and $C = A^2 + B^2$, the analytical solution reads:

$$\begin{cases} x(t) = x_0 + u_x\left[t - \left(1 + \frac{|B|^2}{A^2}\right)^{-1}\left(\frac{1}{A}(1 - \mathrm{e}^{-At}\cos(|B|t)) + \frac{|B|}{A^2}\mathrm{e}^{-At}\sin(|B|t)\right)\right] \\ y(t) = y_0 - \frac{u_x|B|}{B}\left(1 + \frac{|B|^2}{A^2}\right)^{-1}\left(\frac{1}{A}\mathrm{e}^{-At}\sin(|B|t) - \frac{|B|}{A}(1 - \mathrm{e}^{-At}\cos(|B|t))\right) \\ v_x(t) = -u_x\mathrm{e}^{-At}\cos(|B|t) + u_x \\ v_y(t) = \frac{u_x|B|}{B}\mathrm{e}^{-At}\sin(|B|t) \end{cases}$$

---

[5] The CFL number determines the convergence of a numerical scheme when solving partial differential equations. Then, the method is convergent if the chosen timestep is smaller than the CFL number.

Depending on the ratio between the Lorentz and the aerodynamic forces, the particle motion will be dominated by gas drag ($t_s^{-1} \gg Q_m|\vec{\boldsymbol{B}}|$) or tied to the magnetic fields ($t_s^{-1} \ll Q_m|\vec{\boldsymbol{B}}|$). To cover both regimes, four tests have been run for a fiducial stopping time $t_s = 1$ and up to $t = 10t_s$ with the following values for the pair $(Q_m, |\vec{\boldsymbol{B}}|)$: Test A $(0.1, 0.1)$, Test B $(0.1, 1)$, Test C $(0.1, 10)$, and Test D $(1, 10)$.

In Fig. 4.2 the L_2 norm[6] of the errors in position and velocity is shown. From these results, it is evident that the integrator is numerically stable and produces accurate results, since the errors are of the order of at most 10^{-2} and do not increase with time. Moreover, from Fig. 4.3 it is evident that for media where the magnetic and aerodynamic forces are balanced, the integrator is second-order accurate, while for magnetically dominated media the results are only first-order accurate. It is then worth noting that for magnetically dominated media the constraint imposed to the time step in eq. (4.11) must be further restrained, and the accuracy of the integrator has to be checked before performing the calculations. These are not, however, typical conditions for the ISM, so it is safe to follow this implementation for the studies of interest.

Test 2: Lorentz force and Coulomb drag

Additionally, the effect of the Coulomb interactions with the plasma has been checked. This test resolves the full equation of motion (4.7) for Test D parameters ($Q_m = 1, |\vec{\boldsymbol{B}}| = 10$) and three values of $\nu_C = 0.1, 1, 10$ to study the transition from the gas-dominated to the magnetic field-dominated phase, and the results are shown in Figure 4.4; these tests are equivalent to Test 1, since the Coulomb drag only increases the coupling with the gas. However, they are shown here as independent tests so that the reader can easily assess the influence of each of the terms included in eq. 4.7. As can bee seen, the Coulomb drag suppresses the magnetic oscillation of the grain for large values of ν_C, since it increases the relevance of the aerodynamic drag term, and the second-order accuracy of the method shown in Test 1 still holds.

---

[6] The L_2 norm, or Euclidean norm, is the ordinary vectorial norm defined as $\|x\| = \sqrt{x_1^2 + x_2^2 + \cdots + x_n^2}$ for a n-dimensional space.

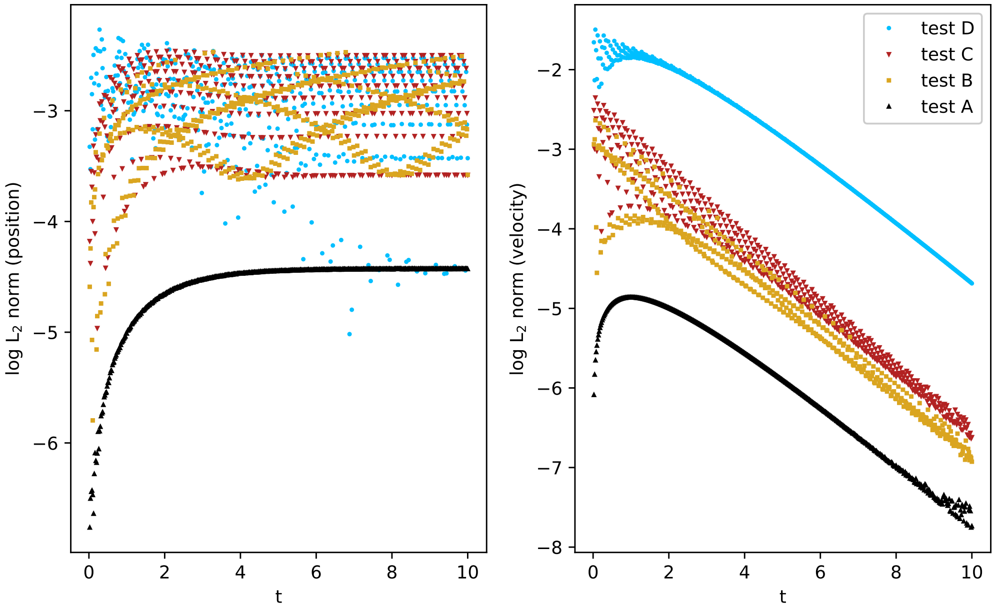

Figure 4.2: Results of the test of the Lorentz force. The figure shows the L_2 norm of the errors in position (left) and velocity (right) for CFL = 0.8. In Test A (black triangles) the gas drag dominates, while in Tests B (orange squares) and C (red up-down triangles), the magnetic field becomes to affect the particle's motion, producing variations in the errors. For Test D, the Lorentz force is the dominant term and the errors in velocity are the largest ones, but are always bounded and below 10^{-2}.

4.3 A simple collision model in Athena

Dust growth is a very complex phenomenon key to understand the formation of planetary systems. For that reason, several collision models for dust in PPDs have been developed based on laboratory experiments (Nakagawa et al., 1981; Nomura & Nakagawa, 2006; Ormel et al., 2007; Zsom et al., 2010; Windmark et al., 2012; Paruta et al., 2016; Ishihara et al., 2018; Lorek et al., 2018; Tamfal et al., 2018). It has been shown that when particles begin to grow, other collision outcomes apart from coagulation or shattering are possible (Zsom et al., 2010), such as bouncing, but they are only significant for sizes greater than 100 μm.

Since the scope of this thesis is to study the evolution of interstellar dust in the envelopes of molecular clouds under the action of the Galactic magnetic field, the density regime and particle abundance under study will be completely different from those for PPDs. At the scales considered (dust grain sizes ranging from 50 Å to 1 μm, as in Weingartner & Draine 2001a) the dust grain structure will be mainly porous (fractal) and depending on the collision energy, the collision outcome will be simple coagulation, compaction of the aggregates, or shattering

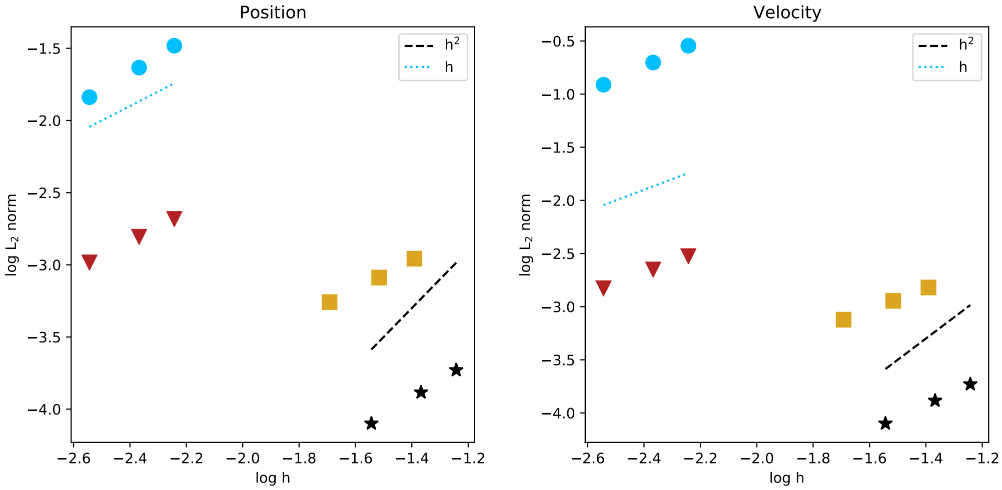

Figure 4.3: Analysis of the convergence of the charged particle integrator considering only the Lorentz force. The errors have been evaluated at $t = 1$ with different timestep sizes (h). The colour code is the same as in Fig. 4.2 and corresponds to tests A (black stars), B (gold squares), C (red up-down triangles), and D (blue points).

(Ormel et al., 2007). The other phenomena that could play an important role in grain fragmentation are thermal sputtering (Draine & Salpeter, 1979), only relevant at very high gas temperatures ($T \sim 10^6$K); and sublimation of the dust icy mantles in shocked regions (Draine, 2004). None of them are relevant in the regimes here considered.

For the sake of simplicity, a very simple collision model that includes dust coagulation and shattering has been implemented in Athena. This module is called at the end of each time step and evaluates the interaction of, at most, two particles at a time. Besides, due to the computational limitations (see section 3.3) it is developed with a 2D cartesian geometry in mind, although the extension to 3D is straightforward.

Each test particle represents a swarm of real particles with fixed properties. This means that a test particle i will have some individual attributes, such as mass m_i, radius, a_i, internal density ρ_i^{int}, charge[7] $Q_{m,i}$, or Coulomb parameter $\nu_{C,i}$; and other ones related to the collective of real particles, which are the represented mass M_i and the impact parameter b_i. It will be assumed that all the particles represented by a test particle have the same velocity, so they will not interact with each other. To avoid confusion, for the rest of this section the test particles will be referred to as 'clouds' with a size dependent on the impact parameter b, while the word 'particle' will be reserved for the real particles contained inside

---

[7] In the following we will refer by charge to $Q_m = Z_d e/m_d c$, the numerical parameter involved in the Lorentz force as explained in sec. 4.2.

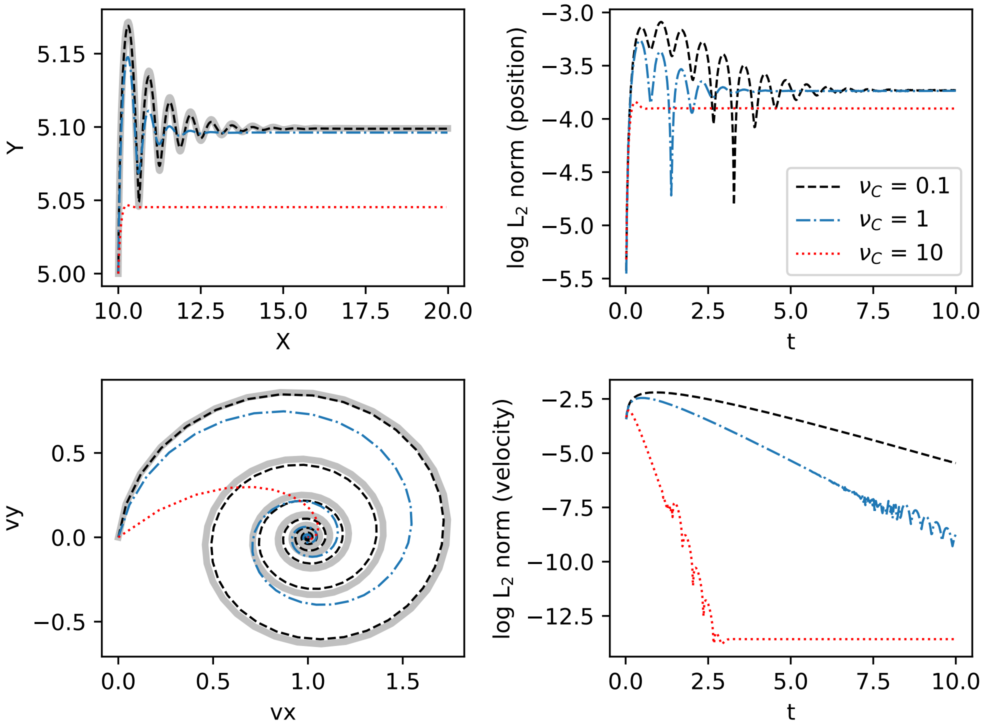

Figure 4.4: Results of the test for the Coulomb drag term in the equation of motion of a charged particle. In the left column, position (top) and velocity (bottom) diagrams are shown for several values of ν_C ($\nu_C = 0.1$ black dashed line, $\nu_C = 1$ blue dashed-dotted line, $\nu_C = 10$ red dotted line). The background thick grey curve shows the results without considering the Coulomb drag. The right column plots show the respective L$_2$ norm of the errors.

the cloud. It should be noted that, since each cloud will grow at a different rate, it is more efficient and comprehensible to gather all particle properties under the same code structure. Hence, the two main particle structures shown in Fig. 4.1 have been merged into the `GrainS` structure, see Fig. 4.5.

Before presenting the algorithm, it is convenient to explain in detail the basic parameters involved in the collision model.

- The **real mass**, m, is the mass of a real particle contained inside a cloud. If a_d is its radius and ρ^{int} its internal density, then $m = \frac{4}{3}\pi\rho a_d^3$.
- If a cloud represents n real particles, then the **represented mass** is $M = n \cdot m$.
- Finally, the **impact parameter**, b, is the maximum distance at which a cloud can interact. If a cloud represents a collective of n real particles

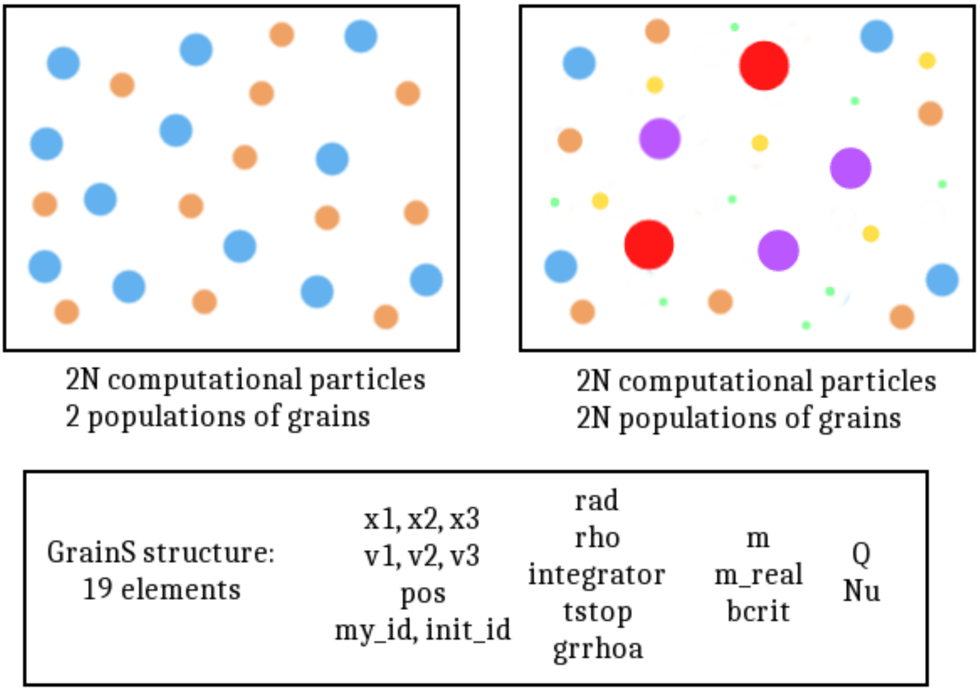

Figure 4.5: Illustration of the modified particle structure in Athena. Although at an initial time it is possible to have a given number of dust populations of N test particles, for instance 2 (blue and orange circles), each dust grain evolves individually, resulting in 2N individual particles at $t > 0$ (different colours and sizes). Hence, the optimal solution is to include all the grain properties inside the `GrainS` structure, resulting in the disappearance of the `Grain_Property` structure.

uniformly distributed, it can be assumed that they are enclosed by a square of side $2b$, $b = \sqrt{n a_d}$, centred at test particle's position (see Fig. 4.6).

The algorithm presented in the next section is inspired in the work by Zsom & Dullemond (2008): N computational particles are followed that do not interact as solid projectiles, but instead exchange represented mass with adjacent particles (see Fig. 4.6).

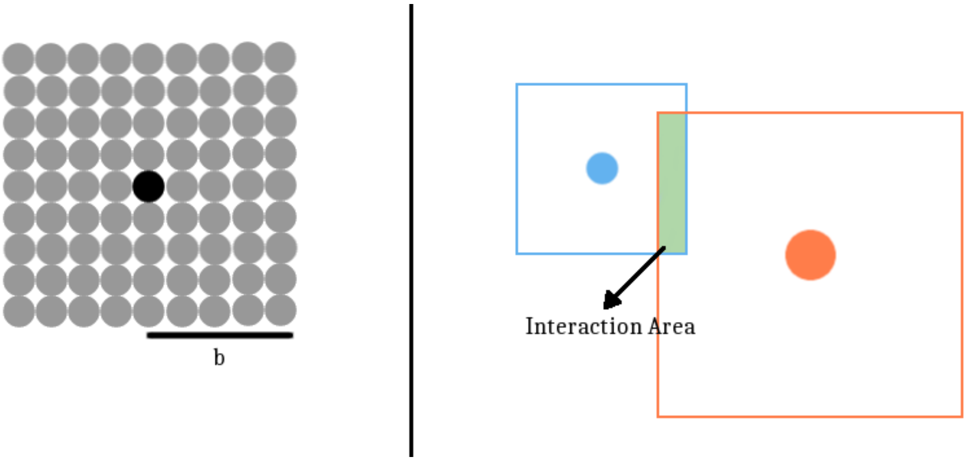

Figure 4.6: Scheme of the interaction between two test particles. *Left*: definition of the impact parameter b as a function of the number of particles n. *Right*: illustration of the interaction between two particles. Instead of considering a physical interaction, they will exchange a mass proportional to the intersection area.

4.3.1 Outline of the algorithm

This coagulation algorithm is introduced in the CTU integrator after the particles have evolved, but *before* the particle feedback is computed (if proceeds). For each test particle, the following steps are applied:

1. If the chosen particle has not interacted with any other one at this computational time, compute its interaction area and check if there is any particle inside it; if so, a collision takes place.

2. Determine the outcome of the collision: coagulation or shattering. It will depend on the relative velocity between the particles:

$$\begin{cases} |v_1 - v_2| < v_{\rm crit}, & \text{coagulation} \\ |v_1 - v_2| > v_{\rm crit}, & \text{shattering} \end{cases}$$

   where $v_{\rm crit} = 2.7$ km s^{-1} for silicates and $v_{\rm crit} = 1.2$ km s^{-1} for graphites (Hirashita & Yan, 2009).

3. Determine the dust mass involved in the interaction. It depends on the interaction area $A_{\rm inter}$ and the total area and mass of the smallest particle, $A_{\rm total}$ and M_i:

$$M_i^{\rm transf} = \frac{A_{\rm inter}}{A_{\rm total}} M_i \tag{4.13}$$

4. Compute the new represented masses for each particle involved in the collision. If coagulation takes place, the smallest particle transfers mass to the biggest one. If shattering occurs, the cloud of smaller particles loses mass, so $M' = M - M_{\text{inter}}$. In this manner, the dust mass contained inside the interaction area is assumed to return to the gas phase, so mass transfer does not occur. In the former case, the represented mass is conserved in the simulation, while in the latter it is not.

5. Compute the radius for each particle and its dependent quantities (real mass and stopping time). After a shattering event, the particle sizes are conserved, but after a coagulation event the largest particle grows and its radius a_j is computed from a weighted mean:

   $$a'_j = a_j^{\text{inter}} \frac{A_{\text{inter}}}{A_j} + \left(1 - \frac{A_{\text{inter}}}{A_j}\right) a_j \tag{4.14}$$

   where A_j is the area enclosed by the largest test particle.

6. If coagulation has taken place, momentum is transferred together with mass from the smallest to the largest test particle. If the relative velocity between two colliding particles, Δv, is greater than the critical velocity v_{crit}, shattering takes place and the dust mass contained inside the interaction area is assumed to return to the gas phase, so momentum transfer does not happen. For $\Delta v = 0$ perfect coagulation takes place and all the momentum is transferred from one particle to another. And for $0 < \Delta v < v_{\text{crit}}$, some amount of energy is lost during the collision (e.g. in forming the chemical bonds of the new particles). Hence, an efficiency factor χ has been included that represents the percentage of momentum transferred in the collision; $(1 - \chi)$ is the amount of energy lost. For simplicity, it has been chosen $\chi = -\Delta v / v_{\text{crit}} + 1$. Then, when computing the updated speed of a particle, the most massive one (for instance, P1) gains momentum, particularly $\chi M_2^{\text{transf}} v_2$, while the velocity of the less massive one (P2) is computed from the following relationship:

   $$m_1 \vec{\boldsymbol{v}}_1 + m_2 \vec{\boldsymbol{v}}_2 = m'_1 \vec{\boldsymbol{v}}'_1 + m'_2 \vec{\boldsymbol{v}}'_2 + (1 - \chi) M^{\text{transf}} \vec{\boldsymbol{v}}_2 \tag{4.15}$$

7. If charged particles are considered, update the parameter Q_m. Since the charge of a dust grain depends on its properties as well as on the environmental conditions, an analytical relationship between the parameter Q_m and the real mass of the particle m has been derived, see sec. 5.1.3 in Chapter 5.

8. If Coulomb drag of charged particles is considered, update the parameter ν_C. This also depends on Q_m, so it is dependent on the relationship 5.14.

4.3.2 Limitations of the collision model

The collision model implemented in this thesis presents several limitations inherent to the physical regime under consideration (the diffuse ISM) and the high computational cost of including discrete dust particles, that has restrained the studies presented in Chapters 5 and 6 to be 2D.

- The treatment of dust particles as *superparticles* can be computationally expensive, so only a limited number of superparticles can be included in any simulation. Hence, the dust mass of the global system is distributed amongst these computational particles that are assumed to trace the behaviour of the whole population.

- Real particles represented by a test superparticle share the same properties (sizes, charges, masses) and they move with the same velocity and in the same direction. Hence, they do not interact with each other.

- Only pure coagulation and shattering are considered for this model. In a diffuse regime characteristic of a molecular cloud envelope, these are the most probable outcomes for a grain-grain interaction.

- After a shattering event, the cloud of smallest dust particles loses mass. It is assumed that this dust mass corresponds to very small dust grains (with sizes of a few Å) that return to the gas phase. This assumption will lead to an underestimation of the mass contained in the smallest dust population and should be taken into account when interpreting the results; however, there is no direct way to properly account for the mass transfer to the smallest dust population without increasing the computational cost (creating new test particles) or including some prescribed (and in principle arbitrary) size distribution for this population.

- A test particle is allowed to interact with another one once per timestep. Then, even if more than two particles are near enough to interact, only two of them will be chosen. For the simulations presented in Chapter 6, section 6.1, typically 35% of the interactions are subject to this multiplicity at the initial stage, but neighbouring particles quickly interact with each other after a few time steps and the ambiguity is resolved.

- Only two dust compositions are available in the current implementation of the algorithm, graphite and silicates, and each of them has to be evolved separately.

4.4 Summary

In this chapter, the implementation of two independent modules in Athena has been presented. The main modifications to the code structure are summarised in Table 4.1.

The first module (sec. 4.2) implements the dynamics of charged dust grains submitted to the Lorentz force and the Coulomb drag of charged gas species. This module is coupled to the semi-implicit integrator already available for aerodynamic particles.

The second module (sec. 4.3) implements a very simple collision model for interstellar dust grains; only coagulation and fragmentation are considered. The collision algorithm, detailed in sec. 4.3.1, is coupled to the CTU gas integrator and does not interfere with any additional physics implemented in Athena v4.2.

The source code is available for its revision and has been presented in the article *Formation of dust filaments in the diffuse envelopes of molecular clouds*, (Beitia-Antero et al., 2021).

Table 4.1: List of particle properties available in the modified version of Athena (GrainS structure).

Property	Description	Module
x1, x2, x3	Position	particles
v1, v2, v3	Velocity	particles
pos	1 = grid/0 = ghost particle	particles
my_id	particle identifier	particles
init_id	processor identifier	particles+ MPI
rad	radius (cm)	particles
rho	internal density (g cm^{-3})	particles
integrator	1 (explicit), 2 (semi-implicit), 3 (fully-implicit)	particles, coagulation
	2 (semi-implicit)	charged particles
tstop	stopping time (code units)	particles
grrhoa	$\rho^{int} a_d$ (code units)	particles
m	represented mass (code units)	feedback, coagulation
m_real	real mass (code units)	coagulation
b_crit	impact parameter (code units)	coagulation
Q	$Z_d e/m_d c$ (code units)	charged particles
Nu	ν_C (code units)	microphysics of charged particles

5 Dust filaments in molecular cloud envelopes

The most external layers of molecular clouds are characterised by low column densities ($n_{\mathrm{H}} \sim 10$ cm^{-3}), and their exposure to the interstellar radiation field results in a medium partially ionised where interstellar dust grains acquire a net charge (Weingartner & Draine 2001b, hereafter WD01). These grains contribute to the coupling of the cloud with the Galactic magnetic field, may interfere with the propagation of MHD waves (Pilipp et al., 1987; Cramer & Vladimirov, 1997), and could even affect the star formation efficiency of the cloud (Nakano, 1998).

This chapter presents a numerical study on the formation of dust filaments in a diffuse regime typical of a molecular cloud envelope and, together with Chapter 6, may be regarded as a complementary view of the observational work presented in Chapter 2. After a first introductory section where the main mechanisms of grain charging are reviewed (sec. 5.1), the module presented in Chapter 4, sec. 4.2, is used to study the evolution of a given population of dust in a molecular cloud envelope; it will be shown that dust grains tend to form filaments due to the propagation of Alfvén waves (sec. 5.2). The properties of these filaments are analysed in sec. 5.3 and discuss the results in sec. 5.4. The main conclusions of this chapter are drawn in sec. 5.6.

5.1 Grain charging in the diffuse ISM

Following WD01, the mean charge of a dust grain in the diffuse ISM can be computed from the statistical equilibrium amongst photoelectric[1] emission (J_{pe}), and ion (J_{ion}) and electron (J_e) accretion rates:

$$f_{Z_d}(Z_d)(J_{pe}(Z_d) + J_{ion}(Z_d)) = f_{Z_d}(Z_d+1)J_e(Z_d+1) \tag{5.1}$$

where Z_d is the grain charge and $f_{Z_d}(Z_d)$ is the grain's probability of having charge Z_d. For harsher regions where EUV and X-Ray radiation are important, more terms have to been taken into account (e.g. secondary electron emission, Weingartner et al. 2006), but for the standard, diffuse ISM, these three phenomena are representative enough. In the following sections, each term of eq. 5.1 is explained in detail.

---

[1] When an energetic photon impacts on a solid surface (for instance, a dust grain) it may produce the emission of one electron, that is called a photoelectron.

5.1.1 Photoelectric emission

In the presence of an ambient radiation field u_ν, the photoelectric effect may produce the detachment of some electrons from the surface of a dust grain, either from the valence ($J_{\rm pe}^{\rm val}$) or from the conduction ($J_{\rm pe}^{\rm cond}$) bands. The photoemission rate is then given by:

$$J_{\rm pe} = J_{\rm pe}^{\rm val} + J_{\rm pe}^{\rm cond} = \pi a^2 \int_{\nu_{pet}}^{\nu_{max}} d\nu Y Q_{abs}(\nu) \frac{c u_\nu}{h\nu} + \int_{\nu_{pdt}}^{\nu_{max}} d\nu \sigma_{pdt}(\nu) \frac{c u_\nu}{h\nu} \tag{5.2}$$

where Y is the photoelectric yield, Q_{abs} is the absorption coefficient, σ_{pdt} is the photodetachment[2] cross section, h is Planck's constant, and ν_{pet} and ν_{pdt} are the minimum frequencies at which photoelectric emission and photodetachment occur, respectively. In the rest of this section, a detailed explanation of all the terms involved in eq. (5.2) is presented.

For studies of grain charging in the ISM, it is customary to consider the interstellar radiation field by Mathis et al. (1983) with the modifications by Draine (2011) (see Fig. 5.1):

$$\nu u_\nu^{ISRF} = \begin{cases} 0 & , h\nu > 13.6 \text{ eV} \\ 3.328 \times 10^{-9} \text{ erg cm}^{-3} \left(\frac{h\nu}{\text{eV}}\right)^{-4.4172} & 11.2 \text{ eV} < h\nu < 13.6 \text{ eV} \\ 8.463 \times 10^{-13} \text{ erg cm}^{-3} \left(\frac{h\nu}{\text{eV}}\right)^{-1} & 9.26 \text{ eV} < h\nu < 11.2 \text{ eV} \\ 2.005 \times 10^{-14} \text{ erg cm}^{-3} \left(\frac{h\nu}{\text{eV}}\right)^{0.6678} & 5.04\text{eV} < h\nu < 9.26 \text{ eV} \\ \frac{4\pi\nu}{c} \sum_{i=1}^{3} w_i B_\nu(T_i) & , h\nu < 5.04\text{eV} \end{cases} \tag{5.3}$$

where

$$w = 10^{-14}, T = 7500K$$
$$w = 11.65 \times 10^{-13}, T = 4000K$$
$$w = 7 \times 10^{-13}, T = 3000K$$

and $B_\nu = 2h\nu^3/c^2(\exp^{h\nu/kT} - 1)^{-1}$ is the blackbody radiation spectrum.

---

[2] If a dust grain has additional electrons in the conduction band, these may be also released after the impact of one energetic photon. However, the energy required to release electrons in the conduction band is lower than that for electrons in the valence band, so in this case the photoelectric effect is termed *photodetachment*.

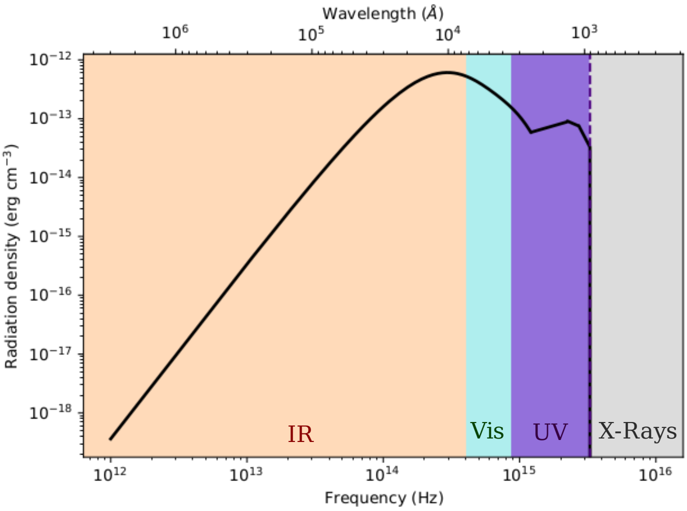

Figure 5.1: Spectrum of the interstellar radiation field by Mathis et al. (1983). Background coloured stripes are shown to distinguish the contribution of the infrared (IR), visible (VIS), ultraviolet (UV), and high-energy (X-Rays) radiation.

The photoelectric yield Y is a measure of the emission probability of a photoelectron, and is given by (WD01):

$$Y(h\nu, Z_d, a) = y_2(h\nu, Z_d, a)\min\left(y_0(\Theta)y_1(a, h\nu), 1\right) \tag{5.4}$$

where the product y_0y_1 accounts for the amount of electrons that acquire enough energy to escape and y_2 is the percentage of electrons that are eventually released. The minimum energy required for the photoelectric emission to take place is given by:

$$h\nu_{pet}(Z_d, a) = \begin{cases} IP_V(Z_d, a) & , Z_d \geq -1 \\ IP_V(Z_d, a) + E_{min}(Z_d, a) & , Z_d < -1 \end{cases} \tag{5.5}$$

where $IP_V = W + (Z_d + \frac{1}{2})\frac{e^2}{a} + (Z_d + 2)\frac{e^2}{a}\frac{0.3\text{Å}}{a}$ is the ionisation potential; for carbonaceous grains, $W = 4.4$ eV while for silicates, $W = 8$ eV. The term E_{min} accounts for an additional energy intake required for negatively charged grains and that is given by:

$$E_{min} = \begin{cases} 0 & , Z_d \geq -1 \\ -(Z_d + 1)\frac{e^2}{a}\left[1 + \left(\frac{27\text{Å}}{a}\right)^{0.75}\right]^{-1} & , Z_d < -1 \end{cases} \tag{5.6}$$

The photoelectric yield (eq. 5.4) depends on the charge of the grain through the term y_0, and on the dust grain size and the ambient radiation field through y_1. The exact formulae for these terms are (WD01):

$$y_0 = \frac{0.5(\Theta/8)}{1+5(\Theta/8)}, \quad \Theta = \begin{cases} h\nu - h\nu_{pet} + \frac{(Z_d+1)e^2}{a} & , Z_d \geq 0 \\ h\nu - h\nu_{pet} & , Z_d < 0 \end{cases} \tag{5.7}$$

and

$$y_1(a, h\nu) = \left(\frac{\beta}{\alpha}\right)^2 \frac{\alpha^2 - 2\alpha + 2 - 2\exp(-\alpha)}{\beta^2 - 2\beta + 2 - 2\exp(-\beta)} \tag{5.8}$$

The term y_1 has been written as a function of two parameters, $\alpha = a/l_a + a/l_e$ and $\beta = a/l_a$, that in turn depend on the electron escape length l_e (~ 10 Å), and on the photon attenuation length $l_a = \lambda/4\pi\Im(m)$; the latter quantity depends on the complex part of the material refraction index, denoted by $\Im(m)$.

Finally, the amount of released electrons may be parameterised as:

$$y_2 = \begin{cases} E_{high}^2(E_{high} - 3E_{low})/(E_{high} - E_{low})^3 & , Z_d \geq 0 \\ 1 & , Z_d < 0 \end{cases} \tag{5.9}$$

$$E_{high} = h\nu - h\nu_{pet}, \; E_{low} = -(Z_d + 1)\frac{e^2}{a}$$

The absorption coefficient Q_{abs} depends on the material and on the wavelength, and can be measured through laboratory experiments. For this work, the tabulated values by Draine[3] for astronomical silicate and graphite have been used.

The last term in eq. 5.2 accounts for the photodetachment of electrons for negatively charged grains. The additional electrons are stored in the conduction band and they require a lower energy input to be detached that is given by:

$$h\nu_{pdt}(Z_d < 0) = EA(Z_d + 1, a) + E_{min}(Z_d, a) \tag{5.10}$$

where EA is the electron affinity that can be computed as:

$$EA(Z_d) = W + \left(Z_d - \frac{1}{2}\right)\frac{e^2}{a} - \delta_{carb}\frac{e^2}{a}\frac{4\text{Å}}{a + 7\text{Å}} - \delta_{sil}5\text{eV} \tag{5.11}$$

---

[3] These tabulated values are available at `https://www.astro.princeton.edu/~draine/dust/dust.diel.html`.

with $\delta_{carb} = 1$ (δ_{sil}) for carbonaceous (silicate) grains, 0 otherwise. The photodetachment cross section σ_{pdt} gives the probability of occurrence for such an event:

$$\sigma_{pdt}(h\nu, Z_d, a) = 1.2 \times 10^{-17}\mathrm{cm}^{-2}|Z_d|\frac{x}{(1+x^2/3)^2},\ Z_d < 0 \tag{5.12}$$

where $x = (h\nu - h\nu_{pdt})/3$ eV.

5.1.2 Ion/electron accretion rate

The accretion rate of charged species (ions and electrons) has been computed as:

$$J_i(Z_d) = n_i s_i(Z_d)\left(\frac{8kT}{\pi m_i}\right)^{1/2}\pi a^2 \tilde{J}(\tau_i, \xi_i) \tag{5.13}$$

where n_i is the density of the charged species and s_i is the sticking coefficient ($s_{ion} = 1$, $s_e = 0.5$, WD01). The term $\tilde{J}(\tau_i, \xi_i)$ is defined in Draine & Sutin (1987) and may be approximated by:

$$\tilde{J}(\tau,\nu)\begin{cases} 1+(\frac{\pi}{2\tau})^{1/2} & ,\ \nu = 0 \text{ (neutral grain)} \\ \left(1-\frac{\nu}{\tau}\right)\left(1+(\frac{2}{\tau-2\nu})^{1/2}\right) & ,\ \nu < 0 \text{ (opposite charges)} \\ \left(1+(4\tau+3\nu)^{-1/2}\right)^2 \exp(-\theta_\nu/\tau) & ,\ \nu > 0 \text{ (same charge)} \end{cases}$$

where

$$\xi \simeq 1 + (3\nu)^{-1/2},\ \theta_\nu = \frac{\nu}{\xi_\nu} - \frac{1}{2\xi^2(\xi^2-1)}$$

and $\tau_i = akT/q_i^2$, $\nu = Z_d e/q_i$ ($q_{ion} = e$, $q_e = -e$).

5.1.3 Mean dust charges in a molecular cloud envelope

The methodology described in the two precedent sections has been implemented in python to compute the charge distribution of dust grains. The source code is included in Appendix B.

All the quantities have been computed as in WD01 but for the absorption coefficients Q_{abs} (see eq. 5.2). Instead of using an average over the interstellar radiation field, the tabulated values for Q_{abs} are used for the computation of $J_{\mathrm{pe}}^{\mathrm{val}}$ (in case of need, a linear interpolation between the two nearest values is performed). Besides, for computing y_1 (eq. 5.8) the imaginary part of the refractive index is needed. Since tabulated values correspond to discrete wavelengths, two interpolation functions are considered for retrieving the exact value at any frequency: a cubic interpolation produces good results for wavelengths lower than 0.2 μm, while for greater values the curve is better fitted by a linear function.

It is worth noting that working with the exact values of Q_{abs} and $\Im(m)$ results in slightly different grain charges than those computed with WD01's method, and are typically a factor of two greater, see Table 5.1. However, charges of carbonaceous grains are consistently lower than those of silicates, in concordance with WD01. This discrepancy is mainly due to the fact that the averaged values underestimate the results at UV wavelengths, where the photoelectric emission is effective. Besides, the grain mean charges presented in this work are all derived considering the interstellar radiation field by Mathis et al. (1983), that is an estimate of the mean radiation field in the Solar neighbourhood (10 kpc). However, in harsher environments, such as in the vicinity of a massive stellar cluster or in the upper layers of the Earth's atmosphere, the radiation spectrum will strongly differ from the interstellar model. In consequence, the mean grain charges will be different and the dynamical evolution of dust grains may not be similar to the one shown in this work.

Table 5.1: Comparison of dust charges with those by Draine (2004) (Fig. 30) under conditions typical of the CNM: $n_{\rm H} = 30$ cm^{-3}, $\chi = 0.001$, $T = 100$ K, interstellar radiation field intensity $G = 1$.

a_d	0.05 μm	0.1 μm	0.5 μm
carbonaceous - this work	15	22	68
Draine (2004)	7.9	11.1	34
silicate - this work	16	24	86
Draine (2004)	9.3	13.8	47

To finish this section, the mean charge for silicate and graphite grains under the typical conditions of a molecular cloud envelope is computed for several representative dust grain sizes, see Table 5.2. These values will be later used for the simulations presented in Chapters 5 and 6, and in general can be fitted to a function of the form:

$$Q_m \times 10^4 \ [\mathrm{cm}^{1/2}\mathrm{g}^{1/2}] = \frac{a}{m \times 10^{12} \ [\mathrm{g}] + b} \tag{5.14}$$

where $a = -9.272 \times 10^{-3}$, $b = 4.429 \times 10^{-3}$ with $\chi^2_R = 0.9948$ for silicates and $a = -8.427 \times 10^{-4}$, $b = 5.94 \times 10^{-7}$ with $\chi^2_R = 0.9991$ for graphite (values computed with the curve fitting tool `cftool` in Matlab).

Table 5.2: Dust charges for some representative dust grain sizes under conditions typical of a molecular cloud envelope: $T = 6000$ K, $\chi = 0.1$, $n_{\mathrm{H}} = 10$ cm^{-3}, $|\vec{\boldsymbol{B}}| = 10^{-6}$ G, interstellar radiation field intensity $G = 1$.

a_d	50Å	12 nm	50 nm	0.105 μm	0.25 μm
graphite	-3.5	-6	-20	-47	-123
silicate	-3	-5	-17	-43	-115

5.2 Formation of dust filaments in a molecular cloud envelope

As a first approach, a molecular cloud envelope is modelled as a 2D isothermal medium with $T = 6000$ K and a uniform density of $n = 10$ cm^{-3}, that evolves in the presence of a magnetic field with strength $B = 10^{-6}$ G, initially uniform in the horizontal direction. The medium is assumed to be a squared box of length $L = 1$ pc with periodic boundary conditions, an ionisation fraction of $\chi = 0.1$, and that evolves according to the ideal MHD equations (eqs. 3.1 – 3.4). If one compares the adopted values to those of the WNM (see Table 1.1), it is evident that they share many properties but for the density of the medium. This is intentionally done, since as explained in sec. 1.3, molecular clouds are formed from accretion of gas from the WNM and the most external layers of these clouds, not shielded from the interstellar radiation field, keep sharing properties with the WNM. The higher density of the medium ($n = 10$ cm^{-3}) is chosen to be representative of a molecular cloud envelope according to observational evidence (Blitz et al., 2007; Fukui et al., 2009, 2017).

Immersed inside the gas, a population of dust grains is considered with radius $a_d = 0.05$ μm and solid internal density $\rho_d^{\mathrm{int}} = 1$ g cm^{-3} represented by 80,000 test particles, uniformly distributed. Initially, they have a velocity taken from a Gaussian distribution with deviation v_{th}, the isothermal sound speed, and their electric charge is $Z_d = -17$, computed as explained in sec. 5.1 and assuming a silicate composition.

At the initial stage, some perturbations in the velocity field are introduced as the superposition of four waves with wavelengths ranging from $L = 1/24$ pc to $L = 1$ pc, and amplitudes characteristic of a turbulent spectrum as in Ostriker et al. (1999), $u_0 = v_{th}(k_n/k_0)^{3/2}$:

$$\begin{cases} u_x = u_0 \sum_{n=0}^{3} \cos(k_n y) \\ u_y = u_0 \sum_{n=0}^{3} \sin(k_n x) \\ u_z = 0 \end{cases}$$

The complexity of the wave spectrum is set as a compromise between the traceability of the individual contribution of each wave and an energy injection that reproduces the input energy values for the ISM. The longest wavelength is set by the size of the domain ($\lambda_{\text{max}} = 1$ pc) while the shortest one is conditioned by the resolution of the domain; it is found that a value of $\lambda_{\text{min}} = 1/24$ pc is suitable for the purposes of this work, since the simulation is run with a resolution of 1024×1024 pixels^2. The intermediate wavelengths of the spectrum are taken from the relationship $\lambda_n = \lambda_{\text{min}} + n(\lambda_{\text{max}} - \lambda_{\text{min}})/(N_{\text{waves}} - 1)$.

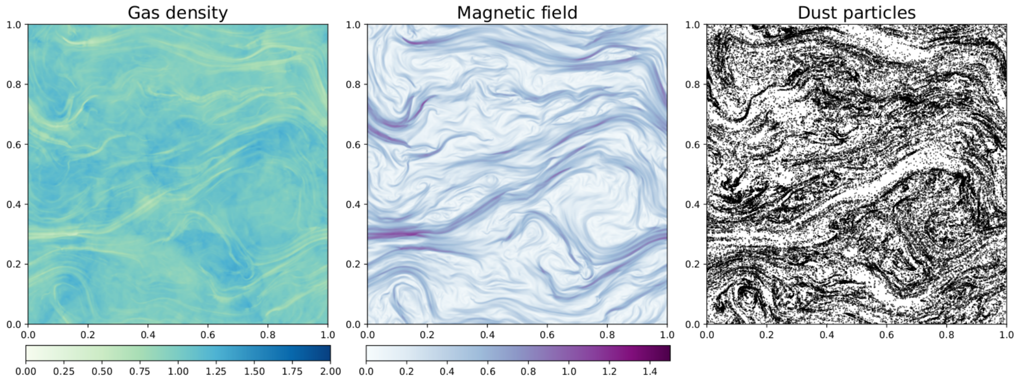

Figure 5.2: Snapshots for the gas density (left), magnetic field (middle), and dust particle distribution (right) for the simulation of a turbulent molecular cloud envelope after 0.4 Myr of evolution, when the gas and dust structures have stabilised. The linear size of the box is 1 pc and the spatial resolution is 1024 × 1024 pixels. Dark colours for gas density and magnetic field highlight regions with a higher density and a stronger magnetic field, respectively.

This model for a molecular cloud is evolved with the Athena MHD code presented in sec. 4.1, and the dust particles evolve according to the module described in sec. 4.2. The final time for the simulation is set at $t = 5$ (code units, ~ 0.4 Myr), since by that time the initial perturbations have been damped to a half of their starting values and for $t > 5$ they are bounded, so one can consider that the system has been stabilised. In Fig. 5.2, the final snapshots of the gas density, magnetic field, and dust particles distribution are presented. From these plots, one can extract a direct conclusion that will be the key of the discussion for the rest of this chapter:

In a molecular cloud envelope, charged dust grains are decoupled from the gas and organise themselves in filaments under the action of the magnetic field.

In order to analyse the properties of such dust filaments, it is necessary to transform the discrete image of dust particles in the right panel of Fig. 5.2 into a pixeled dust map. With that purpose, and starting with an assumed dust-to-gas ratio $\rho_d/\rho_g = 0.01$ for the diffuse ISM (Spitzer, 1954), the total dust mass contained initially in the domain (a square of area 1 pc^2 with an assumed height of 1 pc) is equally distributed over the 80,000 test particles. These test particles are considered to be representative of all the real dust grains contained in the domain, too large to be followed, so they are assumed to be uniformly distributed around the test particles. In this way, a post-processed dust map is generated for the final snapshot of the simulation ($t = 5$) that will be useful to analyse the properties of the dust filaments as well as the local variations in the dust-to-gas ratio; this map is shown in Fig. 5.3. In the remaining of this Chapter, as well as in Chapter 6, the term *dust-to-gas ratio* will be abbreviated as DGR and corresponds to the ratio between the normalised dust density map (Fig. 5.3, left) and the gas density map.

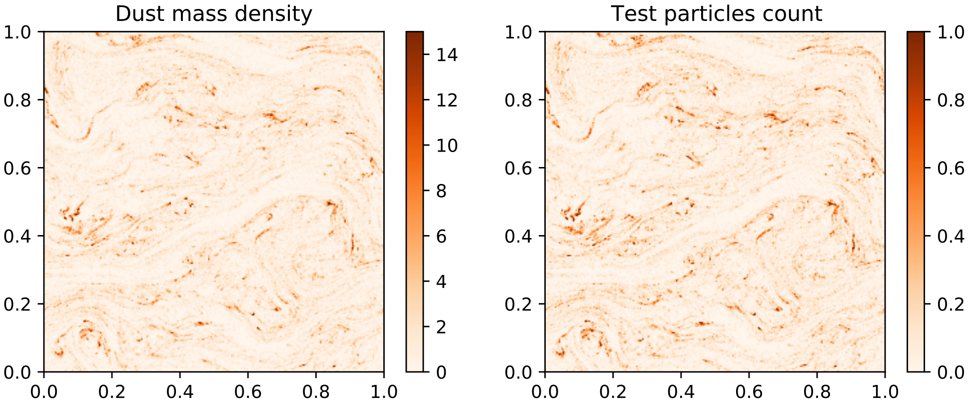

Figure 5.3: Post-processed dust maps at the final stage of the simulation; the linear size of these boxes is again 1 pc. The left map has been built taking into account the total amount of dust contained in the domain as explained in the text, and it has been further normalised such that a value of 1 corresponds to the mean initial dust mass. The right map has been built simply from particle counts inside each cell. From the comparison between both maps, it is straightforward that the procedure described to build the final dust map (left panel) does not introduce any geometrical bias.

5.3 Dust filament properties

A fundamental parameter of the filaments is their width. Several authors have reported to have found a characteristic width of $\sim$ 0.1 pc for molecular gas filaments inside dense clouds based on *Herschel* images (Arzoumanian et al., 2011; Koch & Rosolowsky, 2015). However, Clark et al. (2014) found diffuse HI filaments at all scales up to 0.04 pc, a limit imposed by the instrumental resolution, and other authors have also questioned the existence of such a characteristic width for the molecular gas filaments (Panopoulou et al., 2017). It is thus of great interest to measure the typical widths of the dust filaments in the simulations and compare them with those of the gas filaments.

The software FilFinder (Koch & Rosolowsky, 2015) has been used for the analysis of the filament widths. FilFinder is an open-source code written in python especially developed for the analysis of filamentary structures in astronomical images (see e.g. Henshaw et al. 2020; Sharma et al. 2020). The philosophy behind the algorithm is very straightforward: at an initial stage, a mask that retains only the filaments over a given threshold is created, and it is used to further decompose the image into a skeleton (a graph) that is pruned based on several statistical criteria. As a final product, it provides a file with the pruned skeleton as well as with the longest paths for each identified filament. However, the masking process of the dust map shown in Fig. 5.3 has proven to be challenging since the structures are very narrow and clumpy. Hence, this initial step has been performed independently with the additional python packages scikit-image (van der Walt et al., 2014) and scikit-learn (Pedregosa et al., 2011). Taking the median value of the map as a threshold, the dust map is binarised, and only connected regions of at least ten pixels are retained. This mask is then passed as an argument to FilFinder together with the original dust map in order to obtain the final pruned skeletons.

The lumpiness of the dust maps in Fig. 5.3 that prevented the creation of the mask with FilFinder also affects the algorithm of filament identification, resulting in numerous fragmented filaments. Although the real structure of the dust filaments is well reproduced, it has been found useful to study the morphology of the filaments over a degraded version of the dust map; the skeletons for both maps are shown in Fig. 5.4. As expected, the typical length of a filament in the original image is 0.04 pc, while in the degraded version longer filaments of 0.21 pc are found.

The filament width has been measured for both maps in Fig. 5.4 as the mean width perpendicular to the longest path, obtaining a value of 3.5×10^{-3} pc for the high-resolution map and 8.7×10^{-3} pc for the low-resolution one. Both values are well above the limiting resolution of the simulation, which is 9.8×10^{-4} pc for the 1024×1024 map, and 3.9×10^{-3} pc for the 256×256 one. Besides, since the dynamics of the dust particles is solved with particle-in-cell methods

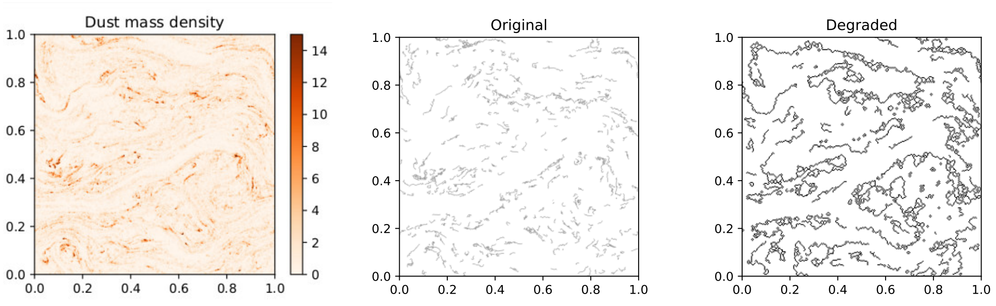

Figure 5.4: Dust filaments identified by FilFinder. The left panel show the original dust map as in Fig. 5.3 (1024×1024 pixels^2); the middle and right panels show the filaments identified by FilFinder for the original image and for a degraded version of the map (256×256 pixels^2), respectively.

(see Chapter 4), increasing the resolution of the simulation would only contribute to smooth the magnetic field and gas density structures, but the dynamics of the dust particles should remain unchanged. However, a quantity that does affect the filament widths is the wave spectrum, as will be discussed in sec. 5.4. Since the dust filaments are shaped by the longest waves, the box size indirectly affects their widths, because the wave spectrum is dependent on the domain length as explained in sec. 5.2.

To further ascertain if the dust filament widths previously found are characteristic for the medium, and how do they depend on the ambient conditions, histograms of the dust-to-gas ratio along the longest paths of filaments have been built and are shown in Fig. 5.5. In general, dust-to-gas ratios much greater than the mean expected value are found, which constitutes the first hint of the decoupling of dust filaments from the gas. Besides, along a given filament the dust-to-gas ratio is nearly constant and is proportional to its length by a factor that oscillates between 0.1 and 0.3 (see Fig. 5.5, right panel). No clear relationship between the dust-to-gas ratio of a filament and its width has been found, which may suggest a characteristic value, but additional simulations that consider a more realistic dust distribution will be decisive to determine if such a characteristic width exists for dust filaments.

Finally, since it is evident that the magnetic field is the main agent that shapes the dust filaments, it is of interest to study their relative orientation. This is done on a local basis for each dust filament, taking groups of three pixels and computing the dot product between the magnetic field at the intermediate pixel and the direction of the dust filament; the final angle is then restricted to be in the range $[-\pi/2, \pi/2]$. As a general rule, the dust filaments are aligned with the magnetic field (see Fig. 5.6): ~ 15 % are essentially parallel to the magnetic field (angles between ± 0.05 rad), while almost all of them (~ 98 %) have inclinations of at most $\pm\pi/4$.

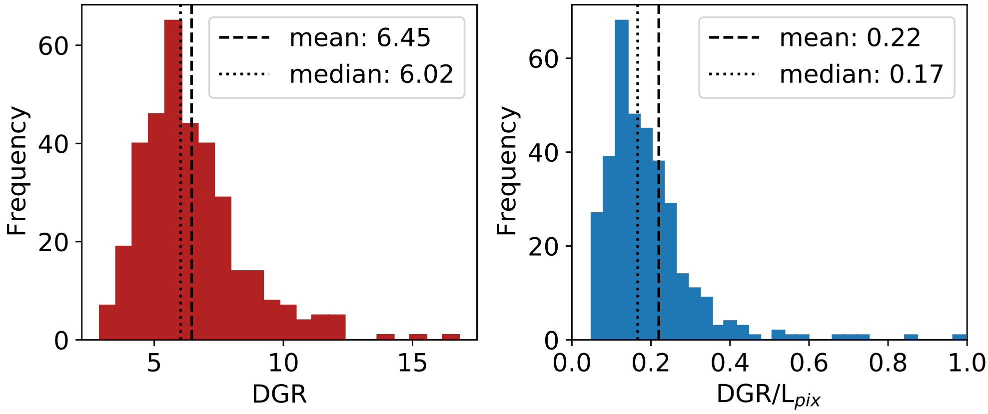

Figure 5.5: Histogram of the dust-to-gas ratio of the filaments for the high-resolution map (1024 × 1024). The right panel shows the same histogram, but the dust-to-gas values are normalised by the filament length in pixels.

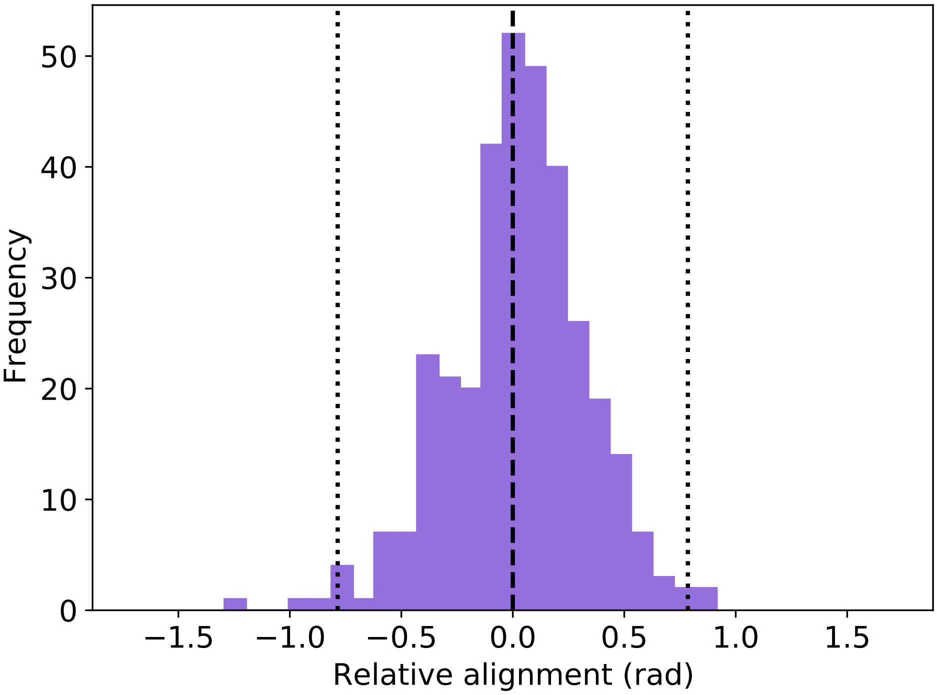

Figure 5.6: Relative orientation between the dust filaments identified over the high-resolution map and the magnetic field. The vertical dotted lines correspond to angle values of $\pm\pi/4$.

5.4 Dust filaments and the mean interstellar dust-to-gas ratio

In the previous sections, it has been stated that dust filaments are decoupled from the gas due to the action of the turbulent magnetic field. However, many authors have reported that there exists a linear relationship between gas and dust column densities in the ISM (Savage et al., 1977; Bohlin et al., 1978; Predehl & Schmitt, 1995; Lenz et al., 2017). This last section is devoted to the discussion of the validity of such an statement in the view of the results presented in this chapter.

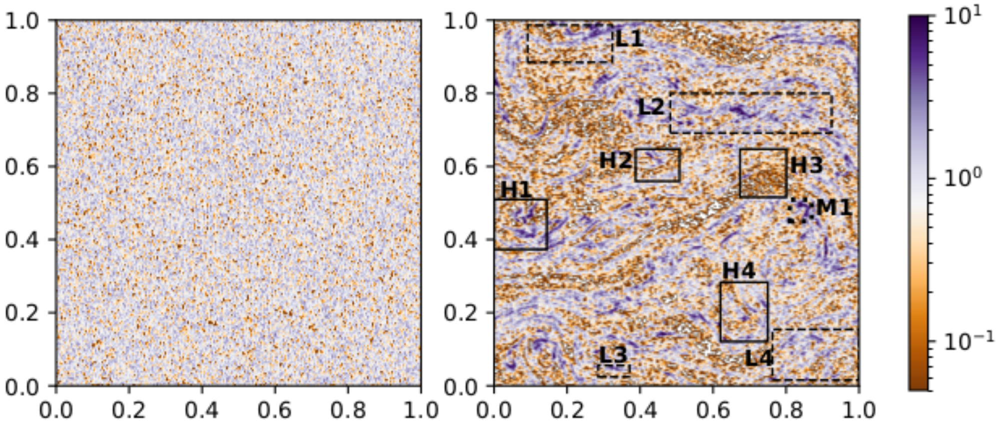

Figure 5.7: Dust-to-gas ratio maps for the initial (left, $t = 0$) and final (right, $t \sim 0.4$ Myr) stages of the simulation. As in previous plots, the linear size of the boxes is 1 pc and the resolution is 1024 × 1024 pixels. The colour scale is chosen to be logarithmic to highlight the differences between regions with high dust-to-gas ratio values (dark purple colours) and those devoid of dust (brown colours). A value of 1 (0 in log-scale) corresponds to the assumed dust-to-gas ratio $\rho_d/\rho_g = 0.01$.

Fig. 5.7 shows clearly the dust overdensities that arise after the propagation of a turbulent spectrum of Alfvén waves. Starting from a nearly homogeneous medium with an initial dust-to-gas ratio of $\rho_d/\rho_g = 0.01$, dust filaments with ten times and almost a hundredfold that initial value are formed; this effect is more apparent in the histogram of the dust-to-gas ratio values shown in Fig. 5.8. The lumpiness on the image for $t = 0$ (left panel of Fig. 5.7) is a natural result of the discrete treatment of the dust particles, but the mean 0.01 value is conspicuous.

One of the reasons behind the decoupling between gas and dust may be the large difference between the particle stopping time t_s (see Chapter 4, section 4.1.1 for a definition) and its Larmor time $t_L = m_d c / Z_d e |\vec{B}|$, which is the inverse of the particle's gyrofrequency. At the final stage of the simulation, all the test particles have Larmor times much smaller than the stopping time, what implies that the magnetic effects dominate over the aerodynamic ones.

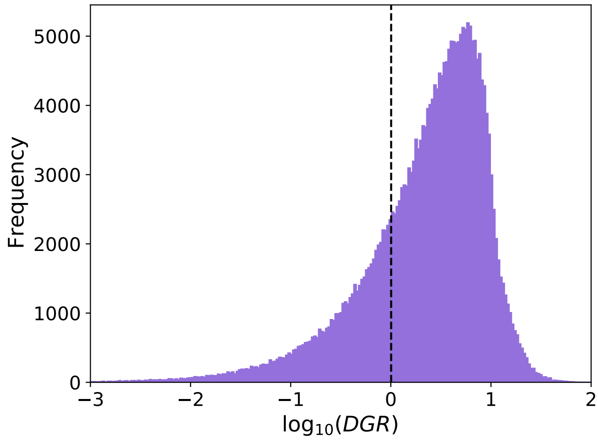

Figure 5.8: Histogram of the dust-to-gas ratio for the final stage of the simulation. The dashed vertical line corresponds to the initial assumed value $\rho_d/\rho_g = 0.01$; note that the quantity is normalised for the analysis ($\overline{\rho_d/\rho_g} = 1$) and that the plot is in log-scale.

To further explore the mechanisms that decouple the dust grains from the gas, several subregions have been selected from the final dust-to-gas ratio map (Fig. 5.7, right panel). The selection has been based on the local value of the gas density, which has a Gaussian distribution, and the final sample includes four high-density regions named H1 - H4 (values greater than 1σ), four low-density regions named L1 - L4 (values lower than 1σ), and one mid-density region named M1. Individual plots for these regions are shown in Figs. 5.9, 5.11, and 5.13 (left) for the dust-to-gas ratios, and in Figs. 5.10, 5.12, and 5.13 (right) for the relative velocity maps; additional information, such as region coordinates and mean filament widths are collected in Table 5.3. The following conclusions may be drawn from these plots:

- In high-density regions, the dust filaments are mainly parallel to the magnetic field and their velocity is similar to the Alfvén velocity, which further supports the argument of the magnetic field coupling. The only exception is the region H3, but it is virtually devoid of dust.

- In low-density regions, the dust filaments are again parallel to the magnetic field with near-Alfvénic velocities. However, the global shape of the filaments appears to be narrower and present more granulation. In these regions, the magnetic field strength is 2.5 times greater than in high-density regions.

- The mid-density region presents a mixed behaviour, with dust velocities comparable to the gas one (see Fig. 5.13, right panel). In this case, there seems to be an extended dust filament oriented perpendicularly to the magnetic field, which is ramified into several subfilaments, all parallel to the magnetic field. It is very likely that this phenomenon is caused by the decrease of the magnetic field strength along the dust filament.

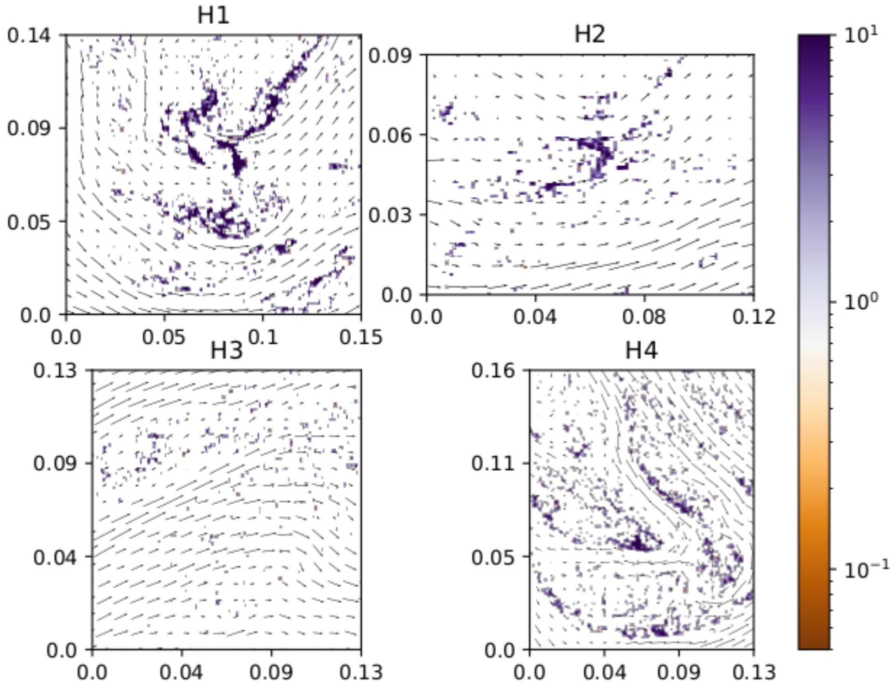

Figure 5.9: Dust-to-gas ratio maps for the high-density regions. The box limits have been modified so that their size reflect their physical sizes in pc (see Table 5.3 for more details). The colour code is the same as in Fig. 5.7, and the vectorial magnetic field is represented by black arrows.

The fluctuations in the dust-to-gas ratio reported above are expected to arise in a turbulent medium (Padoan et al., 2006; Hopkins, 2014), especially if the dust particles are charged (Lazarian & Yan, 2002). There have been several attempts to measure these variations from observations, but were always focused on the dense interiors of molecular clouds (Flagey et al., 2009; Chen et al., 2015) or are based on average statistics, as the work presented in Chapter 2. For more diffuse media, there are few recent theoretical works that analyse the deviations of the dust-to-gas ratio in the CNM (Lee et al., 2017) and the relative motion of charged dust and magnetised gas in the WNM (Hopkins & Squire, 2018). As already stated, the expectation is that in a diffuse medium, dust filaments are formed aligned with the magnetic field (Planck Collaboration et al., 2016a; Fissel et al., 2019), and that the relative velocity between dust particles gas is subsonic (Hopkins &

Table 5.3: Properties of the analysed subregions. Mean quantities for the dust-to-gas ratio (denoted by DGR), magnetic field, Alfvén velocity, gas velocity, and dust velocity. Also included are the mean dust filament widths on each region for the original map (w_{1024}) and for a degraded version (w_{256}).

Region	Dimensions pc × pc	$< DGR >$	$< B >$ 10^{-6} G	$< v_A >$ 10^5 cm s^{-1}	$< v_{gas} >$ 10^5 cm s^{-1}	$< v_{dust} >$ 10^5 cm s^{-1}	w_{1024} 10^{-3} pc	w_{256} 10^{-3} pc
H1	0.145 × 0.138	1.403	0.737	0.476	2.997	0.205	4.385	10.449
H2	0.121 × 0.089	0.798	0.829	0.534	2.402	0.135	2.981	9.975
H3	0.128 × 0.133	0.280	1.262	0.806	3.069	0.361	3.818	6.331
H4	0.131 × 0.163	1.090	1.015	0.649	2.629	0.558	4.109	9.827
L1	0.233 × 0.103	1.597	2.703	2.124	6.293	0.479	3.046	8.523
L2	0.443 × 0.109	1.767	2.437	1.841	5.935	0.597	3.300	11.728
L3	0.087 × 0.032	1.921	1.862	1.368	1.982	0.162	4.112	8.464
L4	0.238 × 0.140	1.459	2.514	1.910	5.010	0.280	3.362	10.919
M1	0.062 × 0.060	2.514	0.777	0.532	6.104	1.534	4.939	17.578

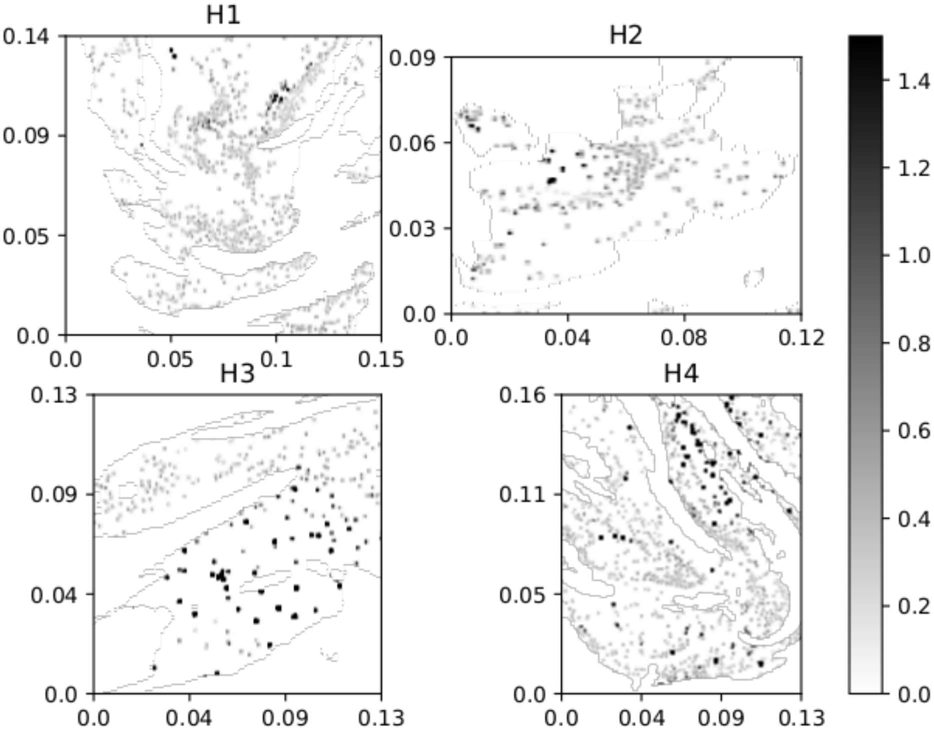

Figure 5.10: Dust-to-gas velocity maps for the high-density regions. The physical sizes are the same as in Fig. 5.9.

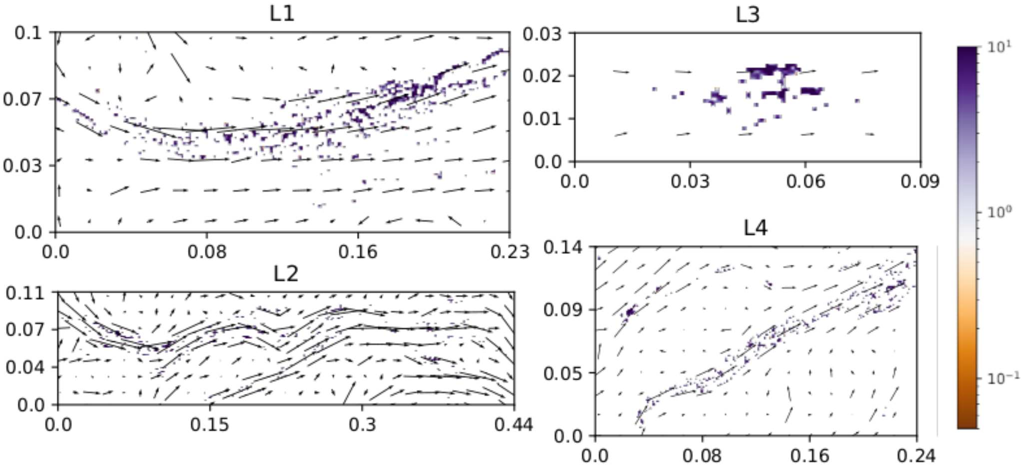

Figure 5.11: Same as Fig. 5.9, but for low-density regions.

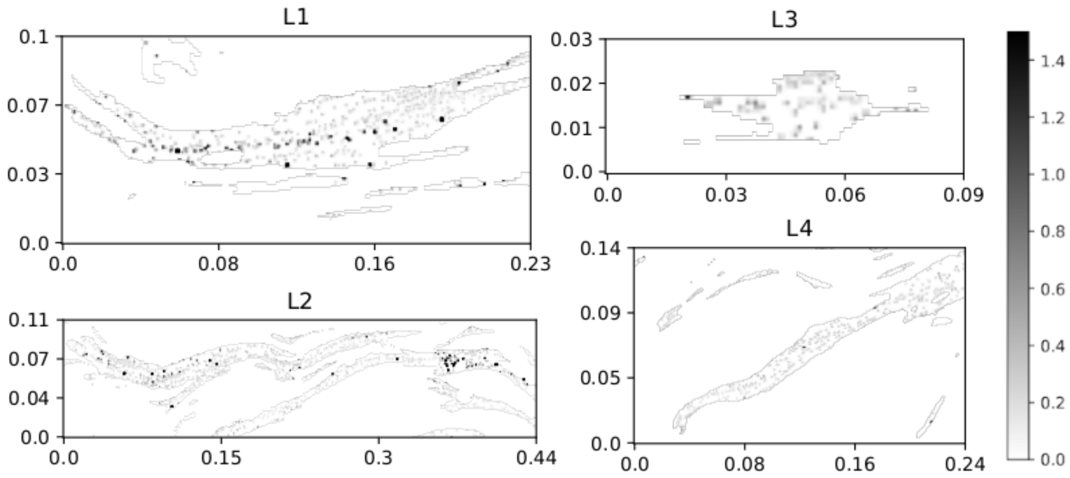

Figure 5.12: Same as Fig. 5.10 but for low-density regions.

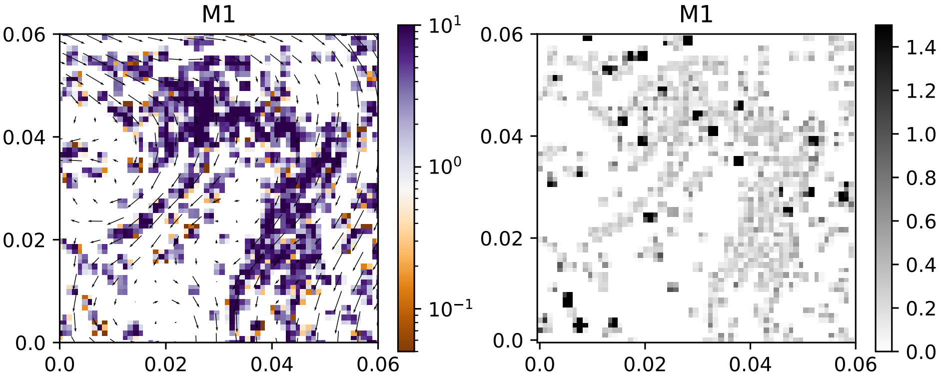

Figure 5.13: Same as Figs. 5.9 and 5.10 but for the mid-density region M1.

Squire, 2018). The results presented in this chapter are in agreement with these hypothesis, as can be inferred from the above discussion and from Table 5.3.

It is worth noting that, although large deviations of the dust-to-gas ratio are observed, the mean initial value is always conserved at large scales, as can be seen in Fig. 5.14. In consequence, although localised variations in the dust-to-gas ratio are observed in the simulations here presented, the results at large scales are compatible with the claims of the empirical works cited previously in this section, which measure the average dust column density along a line of sight.

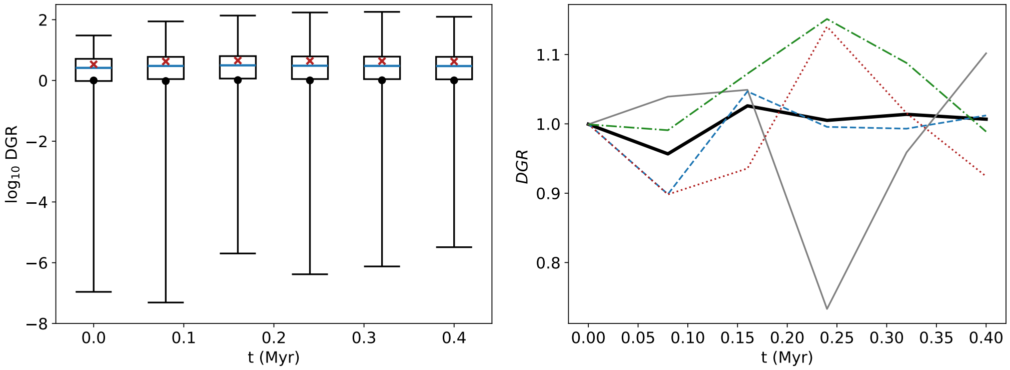

Figure 5.14: Time evolution of the dust-to-gas ratio, denoted by *DGR*. *Left*: boxplot for strictly positive (> 0) dust-to-gas ratio values. The horizontal blue line limits the median, the mean is represented by a red cross, and the whiskers limits have been set to the minimum and maximum values. If all the pixels are taken into account, the mean dust-to-gas ratio matches the initial adopted value (black point) and barely varies with time. *Right*: Variations of the mean global dust-to-gas ratio (black line) and inside four quadrants to see the local differences (grey solid line, blue dashed line, red dotted line, and green dotted dashed line).

Finally, it is instructive to analyse separately the influence of each wave of the turbulent spectrum that governs the velocity amplitudes (see the model setup at the beginning of section 5.2) in the shape of the dust filaments. For the sake of illustration, independent simulations have been carried out for the shortest and the longest waves, and the respective dust-to-gas ratio maps are shown in Fig. 5.15.

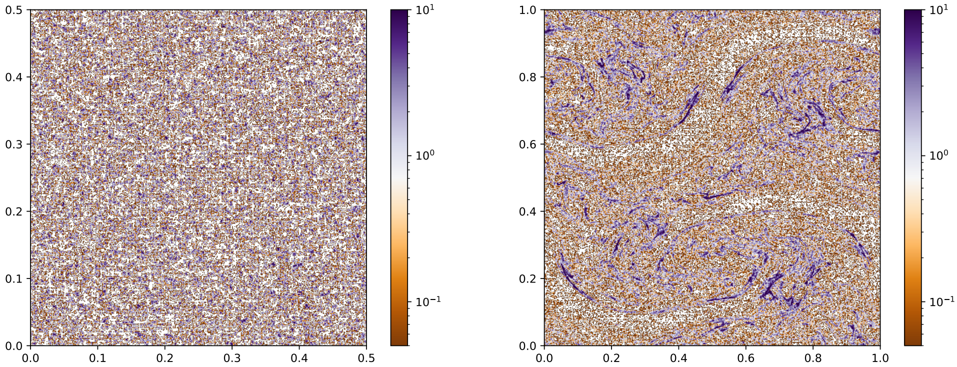

Figure 5.15: Dust-to-gas ratio maps for the shortest (left) and longest (right) waves after ∼ 0.4 Myr of evolution as in Fig. 5.2.

As may be expected, the shortest waves do not inject enough energy so as to greatly perturb the system, although small clumps of a few (≤ 10) pixels are formed at the nodes of the wave. On the other hand, the longest waves dominate the energy input and produce strong fluctuations in the gas density, momentum, and magnetic fields that result in the formation of dust filaments as those shown in Fig. 5.7. However, for both cases the histogram of the dust-to-gas ratio strongly resembles the one shown in Fig. 5.8. Consequently, the following conclusions may be drawn: that the propagation of a wave in a molecular cloud envelope is expected to produce variations in the dust-to-gas ratio, no matter the energy of the wave; and that the morphology of the resulting filaments will depend on the wave spectrum.

5.5 Limitations of a 2.5D model

The model for a molecular cloud envelope presented in this Chapter is a fair approximation to the study of the dynamical evolution of charged dust grains, but presents some limitations:

1. The assumption of a 2.5D geometry constrains the motion of the charged particles into a plane, so it is indirectly assumed that the Alfvén waves that propagate into the media are polarised. However, in 3D one would expect the stirring of the plasma to develop in all directions and the waves would produce shorter, helical dust filaments.

2. In this simulation, a single-sized dust population with silicate composition is evolved. In a more realistic environment, however, both silicate and carbonaceous particles are present, and their properties may be altered under the action of the ambient conditions (e.g. radiation fields, grain-grain collisions). Therefore, dust evolution has to be included coupled with its dynamics (see Chapter 6 for a first approximation to this problem).

3. Last but not least, a molecular cloud envelope is expected to be an astrophysical plasma where resistive process, as well as ambipolar and Hall diffusion, will play a fundamental role. A more realistic model will include this effects.

5.6 Conclusions

In this chapter, a theoretical study on dust filament formation in a molecular cloud envelope has been presented. The numerical model is based on the implementation of the equation of motion of a charged particle in the MHD code Athena (Chapter 4, sec. 4.2) and it considers a magnetised medium with uniform density $n = 10$ cm^{-3}, $T = 6000$ K, $B = 10^{-6}$ G, an ionisation fraction $\chi = 0.1$, and a single population of charged dust grains with sizes $a_d = 0.05$ μm.

It has been shown that charged dust grains in a molecular cloud envelope follow preferentially the magnetic field and organise themselves along filaments of widths $3.5 \times 10^{-3} - 8.7 \times 10^{-3}$ pc. This implies that local variations of the dust-to-gas ratio are expected in molecular cloud envelopes, although the mean value is always preserved.

6 Dust evolution in a molecular cloud envelope

Interstellar dust grains embedded in a molecular cloud envelope are subject to several external forces that produce variations in their size distribution. These variations may be studied through ultraviolet observations, as explained in Chapter 2, but the mechanisms responsible for these departures from the initial distribution cannot be properly assessed only from observational data. For these situations, numerical simulations provide an ideal tool to study the effects of all the processes involved in shaping the dust grain-size distribution.

In Chapter 5, the formation of dust filaments in a molecular cloud envelope was discussed, but dust grains were not allowed to interact each other. This chapter demonstrates the performance of the dust collision model presented in Chapter 4, sec. 4.3, and its potential to analyse the variations on the dust grain-size distribution produced solely by grain growth and shattering mechanisms. Two frameworks are considered: in the first one (sec. 6.1), grain growth of a single-sized population inside dust filaments is analysed; these simulations are based on the results from the previous chapter. Then, the ambient conditions (gas density, velocity, and magnetic field strength) are maintained but a full dust grain-size distribution is introduced to study the variations on the dust grain-size distribution and the derived effects on the ultraviolet extinction curve (sec. 6.2). The results of this preliminary work are discussed in sec. 6.3 and the main conclusions are summarised in sec. 6.4.

6.1 Grain growth inside dust filaments

It has been shown that the propagation of a spectrum of Alfvén waves inside a molecular cloud envelope induces the formation of filaments of small-sized dust grains due to the large charge-to-mass ratio of the particles. Therefore, it is to expect that grain-grain collisions will be frequent enough so as to produce substantial grain growth inside these dense filaments.

Taking the simulations from Chapter 5 as a baseline, grain growth and shattering have been studied for seven regions that span different gas properties, particularly different densities and magnetic field strengths. The selected regions are taken amongst those analysed in Chapter 5 although with their limits slightly modified to fit within the 2D cartesian mesh of the simulation; however, and for consistency, the names of the regions are maintained for this chapter: H1, H2, H4, L1, L2, L4, and M1. Regions H3 and L3 have been discarded because they contained so little dust mass that grain-grain collisions were almost nonexistent.

The simulation setup is taken from the final snapshot of the turbulent simulation (see Fig. 5.7). The initial conditions (gas cell-centred values and dust positions and velocities) are taken from the turbulent simulation, but the collision module (sec. 4.3) requires three additional parameters: the impact parameter, b, that sets the size of the cloud of real particles distributed around the test ones; the mass of a real particle, m; and the total mass represented by a test particle, M. In order to set those parameters, it is assumed that in the global simulation, the total dust mass M^{tot} may be obtained from the relationship $\rho_d/\rho_g = 0.01$. Then, since the dust population is homogeneous, it is assumed that each of the 80,000 test particles represent the same fraction of the total mass, $M^{tot}/80,000$. It is then straightforward to compute the parameters M and b, that will be the same for every test particle at the initial stage.

After setting the initial conditions, the simulations are left to evolve with open boundary conditions to ensure that the divergence-free constraint ($\nabla \cdot \vec{\boldsymbol{B}} = 0$) holds. The total integration time is chosen based on the state of the system, and therefore is a subjective quantity: it is considered that the simulation has finished when the dust filaments have evolved enough to produce substantial coagulation and/or shattering, but most of the dust grains are still inside the computational domain. A typical integration time is $t_{lim} = 10^{11}$ s, that is approximately a 7% of the total integration time of the simulation presented in Chapter 5. Therefore, the results presented in this chapter may be considered to be representative of the behaviour of dust filaments in a turbulent molecular cloud envelope (Chapter 5) but at short timescales, so it is correct to study the evolution of dust grains from a snapshot of the global turbulent simulation. Besides, this scale is really small when compared to the typical mean molecular cloud lifetime ($\sim 10^6$ Myr, Hartmann et al. 2001) and therefore, the results from this work may be considered to reflect the stationary state of a molecular cloud envelope provided that the ambient conditions are maintained. This fact further justifies the choice of individual regions with open boundary conditions instead of evolving the whole computational domain, that would be computationally more expensive and would affect the collisions due to the different time and length scales.

In the following sections, grain growth (sec. 6.1.1) and shattering (sec. 6.1.2) mechanisms are analysed separately. The main parameters of the simulations are summarised in Table 6.1.

Table 6.1: Properties of the seven regions analysed in this chapter. Note that the dimensions are slightly different from those in Table 5.3 due to the imposed square symmetry.

Region	Length	Resolution	M_{dust}	$< \rho_g >$	$< B >$	t_{lim}
	pc	px	10^{29} g	10^{-23} g cm^{-3}	10^{-6} G	10^{10} s
H1	0.145	148	1.571	1.861	1.011	7.282
H2	0.121	124	6.854	1.828	1.057	9.987
H4	0.166	170	1.654	1.878	1.425	12.122
L1	0.117	120	0.832	1.526	1.609	9.665
L2	0.109	112	1.056	1.576	1.471	9.021
L4	0.180	184	1.822	1.609	1.333	14.820
M1	0.063	64	0.478	1.711	0.080	5.155

6.1.1 Growth of a single-sized population

The enhanced dust densities inside dust filaments increase the collision rate between particles, otherwise expected to be rather small in a diffuse medium such as a molecular cloud envelope. According to the collision model presented in section 4.3, dust particles will experience growth or will lose mass (shattering), so the lower limit of the dust grain-size distribution is imposed by the smallest dust particle introduced in the initial conditions. In this case, all the particles have the same size, $a_d = 0.05$ μm, so only grains with $a_d > 0.05$ μm will be formed. The lost mass in an shattering event is considered to return to gas phase and it will not be followed by the algorithm.

In Table 6.2, several quantities that characterise grain growth are summarised. It is evident that a significant fraction of the dust population ($\sim 30 - 40\%$) has grown, but only few grains grow up to twice their initial size ($a_d = 0.1$ μm). In general, the growth is enhanced by the large dust-to-gas ratios of the filaments, but the largest grains are only formed inside regions where the ratio is greater than ten times the mean value of the domain, and the magnetic field strength decreases. This is consistent with the underlying physics of the systems, since the considered dust particles are so small that very strong magnetic fields would accelerate them, reducing the probability of a coagulation event. Actually, a close inspection of the values in Table 6.2 reveals that some dust grains acquire sizes up to $0.5 - 1$ μm, and they are initially placed inside regions with a magnetic field strength lower than the mean.

The influence of the magnetic field morphology on the growth of the dust grains is better assessed from the diagrams shown in Figs. 6.1 and 6.2. For every region, three plots are shown: in the first one, grains that grow up to twice their initial size are plotted over the vectorial magnetic field. In the second one, all the test particles are plotted over the gas density map, and those that suffer growth are highlighted. Finally, those particles that suffer from shattering are also displayed over the density map as mentioned above. The main conclusion that may be extracted from these plots is that grain growth takes place inside the dust filaments and that the largest grains are formed inside magnetic loops. The analysis of the eroded grains is presented in the following section.

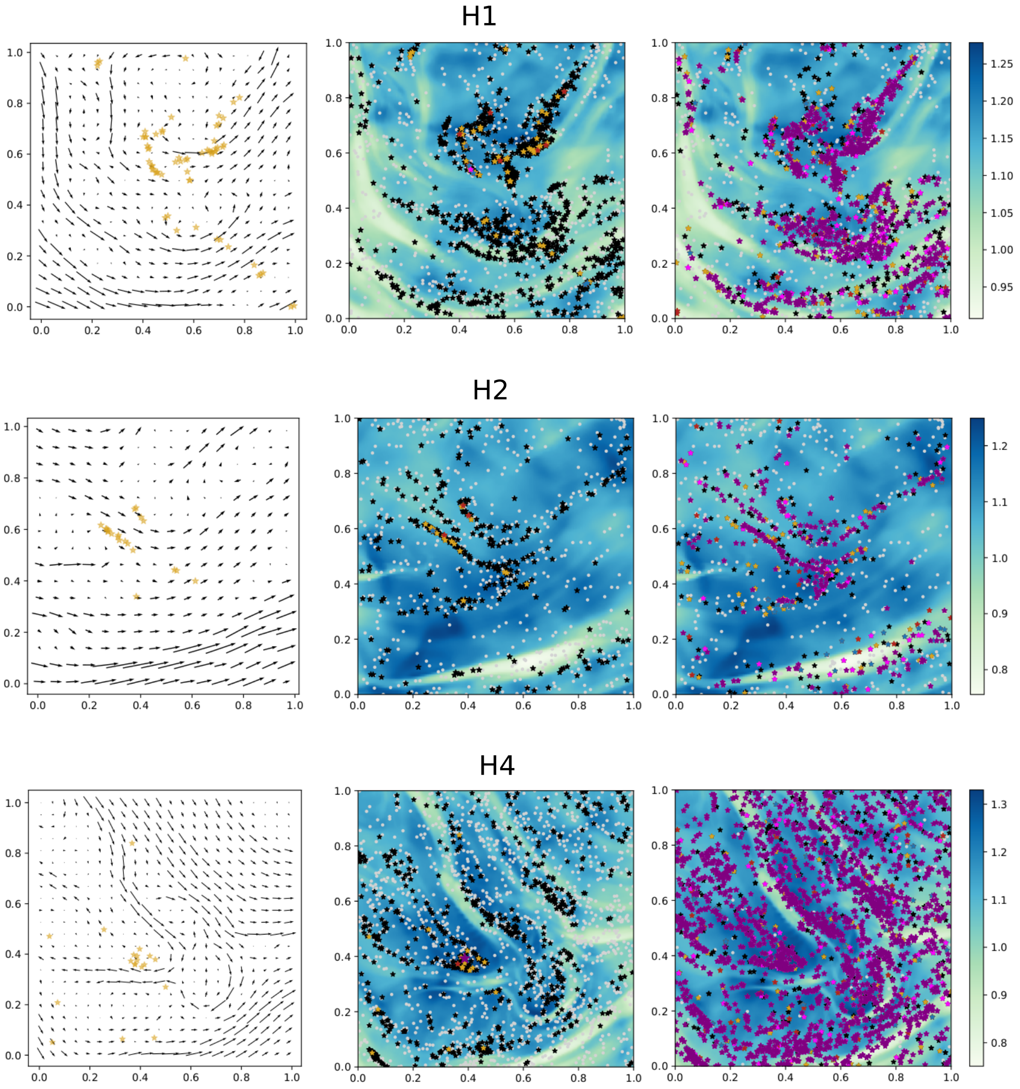

Figure 6.1: *Left*: particles that acquire twice their initial size plotted over the magnetic field. *Middle*: test particles considered in the simulation over the gas density map. Grey circles are those that do no experience growth, and the coloured stars are those that acquire the following sizes: $a_{fin} > a_0$ (black), $> 2a_0$ (gold), $> 4a_0$ (red), $> 6a_0$ (blue), $> 8a_0$ (magenta). *Right*: same as the previous one, but the colour code correspond to particles of $a_{fin} = 0.05$ μm that lose mass: $M_{fin} < M_0$ (black), $< 10^{-1}M_0$ (gold), $< 10^{-2}M_0$ (red), $< 10^{-3}M_0$ (blue), $< 10^{-4}M_0$ (magenta), and $< 10^{-5}M_0$ (purple).

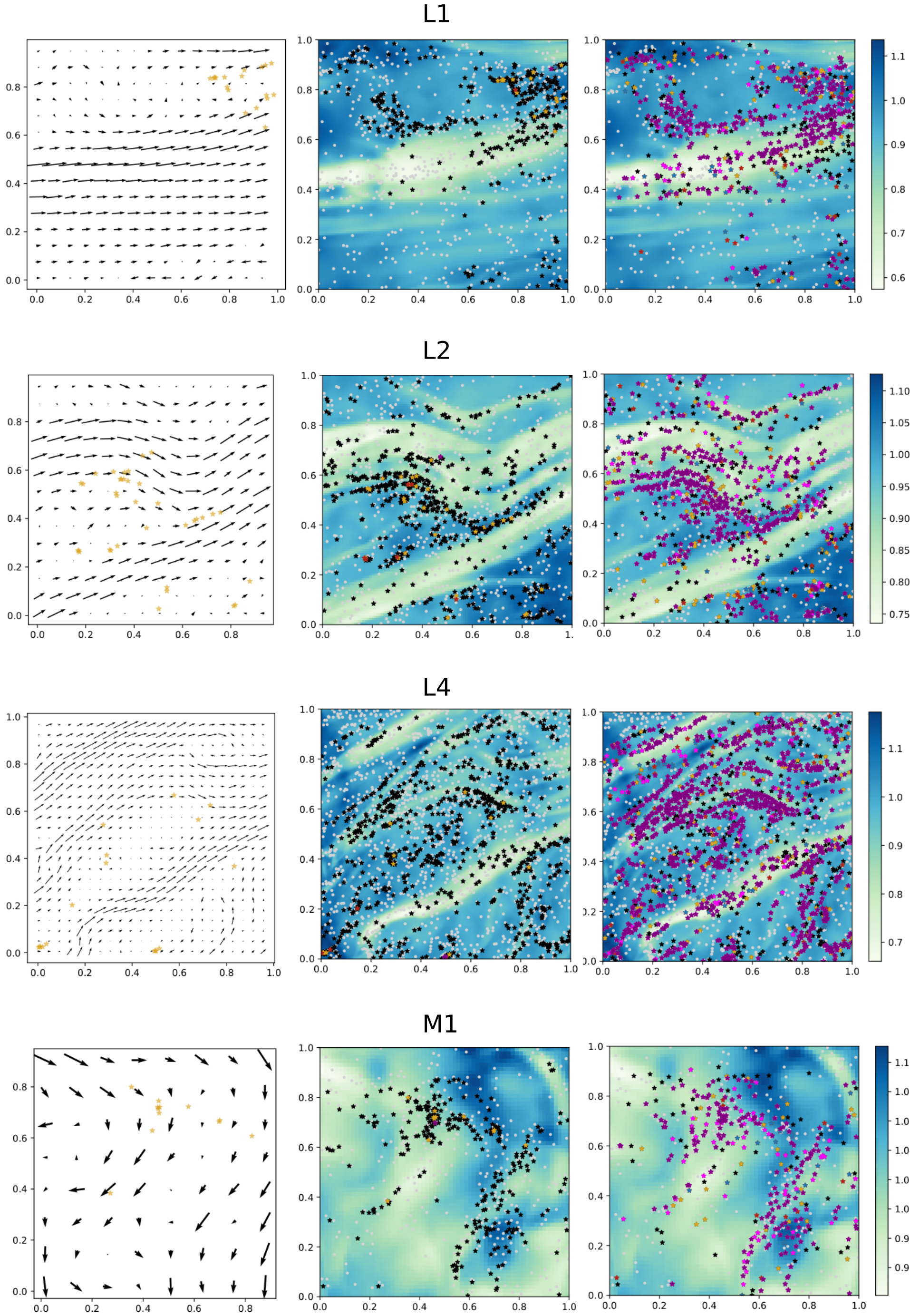

Figure 6.2: Same as Fig. 6.1, but for regions L1, L2, L4, and M1.

Table 6.2: Statistical quantities that characterise the growth of a single-sized population of $a_0 = 0.05$ μm in a molecular cloud envelope. The displayed dust-to-gas ratios (DGR) are normalised by the mean value inside each region. The lost dust mass in outgoing particles M_{lost}^{out} is only an approximation based on the assumption that these grains have not experienced any shattering or coagulation events.

Region	N_{par}	N_{par}	a_{max}	$a_d > a_0$		$a_d > 2a_0$		$M < M_0$	$M < 10^{-5} M_0$	M_{lost}^{shat}	M_{lost}^{out}
	$t = 0$	t_{lim}	μm	N_{par}	$< DGR >$	N_{par}	$< DGR >$	N_{par}	N_{par}	%	%
H1	2555	2489	0.48	1057	3.32	64	8.29	1100	678	35.50	2.50
H2	1115	1041	0.36	345	4.11	21	12.23	475	236	24.30	6.70
H4	2691	2548	0.75	703	2.18	19	3.80	1438	801	34.00	5.00
L1	1353	1230	5.61	364	4.26	18	9.48	631	385	17.34	24.66
L2	1718	1621	0.55	619	3.02	36	7.31	777	452	25.22	5.78
L4	2964	2735	1.21	817	3.52	17	10.82	1449	964	34.79	8.21
M1	778	723	0.6	306	2.58	12	6.96	346	185	49.92	7.08

6.1.2 Mass loss and reprocessed small dust grains

Since mass is not being introduced in the domain, the system loses dust mass through two mechanisms: either the test particles escape from the domain due to the opened boundary conditions (M_{lost}^{out}), or a fraction of the represented mass is destroyed after a shattering event (M_{lost}^{shat}); this is a realistic approximation because the timescale of dust evolution is much shorter than the dynamical one, as mentioned before. The total dust mass lost in each situation has been estimated as follows: knowing the initial and final dust masses of the system, and the number of particles that have gone out of the computational domain, it is assumed that the outgoing particles do not suffer any coagulation or shattering events before escaping. In this way, it is possible to obtain an upper limit for the total dust mass that has not been reprocessed into smaller dust grains. It is indeed an upper limit since shattering is much more frequent than coagulation, as may be inferred from the data displayed in Table 6.2 and in Figs. 6.1 and 6.2.

It is expected that dust grains in a diffuse medium (such as a molecular cloud envelope) do not acquire very large sizes, due to the low dust densities that reduce the collision rates, the relatively large velocities of the particles, and the efficiency of shattering events. In the simulations presented in this section, very few particles grow above the limit of $2a_0$, but a considerable fraction lose virtually all their represented mass (see Table 6.2). This is a result of the effective acceleration of charged dust grains under the action of the magnetic fields. Therefore, when evaluating the collision outcome between two particles, most of the times the relative velocity between them will be greater than the critical threshold for shattering and the population of very small dust grains (not followed by the algorithm) will be enlarged.

6.2 Collisions of a realistic dust population

Up to now, a single-sized population of dust grains with $a_d = 0.05$ μm has been considered. However, it has been known for many years that interstellar dust grains exist in the diffuse ISM with sizes that span from $a_d \sim 1$ μm down to the molecular threshold ($a_d \sim 50$Å). Mathis et al. (1977) were the first ones to show that the UV extinction curve could be reproduced by a population of silicate and carbonaceous grains with abundances distributed according to a power law, $dn/da \propto a^{-3.5}$. This distribution, usually termed as the MRN distribution, is expected to be representative also for molecular cloud envelopes, and this section is devoted to study its variations in regions with the same properties as those presented in section 6.1. With that purpose, a synthetic MRN dust population is generated as explained in section 6.2.1.

The advantage of considering a full dust grain-size distribution is that variations of its power-index will be translated into variations on the UV extinction curve. Hence, it is possible to predict the expected variations of the UV extinction curve and to identify which mechanism (grain growth or shattering) produces the most conspicuous effects. These analysis are presented in sections 6.2.2 and 6.2.3.

6.2.1 Generation of the mock sample

For the generation of the mock dust sample, some assumptions have been made. First, two dust populations are considered to coexist, one of silicate grains with solid density $\rho_d^{int} = 3.5$ g cm^{-3}, and another one of graphite grains with solid density $\rho_d^{int} = 2.24$ g cm^{-3}. The total dust mass of the system, M_{tot}, is equally distributed between these two populations, $M_{tot} = M_{sil} + M_{gra}$. Then, since following a continuous dust distribution is computationally unfeasible, ten dust families are taken to be representative of the full population. The particle sizes are chosen to be in the range 50 Å $-$ 0.25 μm as for the MRN distribution, and logarithmically spaced to have a better sampling of the small size population: 5 nm, 7.7 nm, 11.9 nm, 18.4 nm, 28.4 nm, 43.9 nm, 67.9 nm, 104.8 nm, 161.9 nm, 250 nm. For the sake of simplicity, each dust family is represented by the same number of test particles (100), so in practice there will be 1000 test particles in the domain, and those that represent the smallest particles will have the largest dust masses (MRN distribution).

The position of the test particles is set according to their sizes and based on the following hypothesis: the smallest dust grains follow the magnetic field due to their large charge-to-mass ratio; on the contrary, the largest grains will follow the gas density. And for grains with $a_d = 0.05$ μm, the position is chosen based on the dust distribution matrix obtained in the previous chapter (Fig. 5.3). Finally, for $a_{min} < a_d < 0.05$ μm and 0.05 μm $< a_d < a_{max}$, an intermediate behaviour is expected. This approximation is further justified if one compares the ratio between the Larmor and stopping times for the smallest and largest particles considered: for silicate particles with sizes of 50 Å, the ratio $t_L/t_s \sim 10^{-4}$, while for particles of 0.25 μm, $t_L/t_s \sim 10^{-2}$. Although the biggest dust particles will not be perfectly coupled to the gas, this approach is fair enough for assessing the evolution of a realistic dust population. Therefore, the position of a given test particle will be determined based on three probability matrices: one built from the magnetic field strength, M_B, another one for the gas density, M_g, and the dust matrix built in Chapter 5, section 5.2, M_d. First, these matrices are normalised in order to restrict the values to be in the range $[0, 1]$. Then, based on the particle radius, the final probability matrix is computed as:

$$M_{prob} = |A| M_B + (1 - |A|) M_d, \quad A = \frac{a_0 - a_i}{a_0 - a_{min}}, \quad \text{if } a_d \leq a_0 \tag{6.1}$$

$$M_{prob} = |C| M_g + (1 - |C|) M_d, \quad C = \frac{a_i - a_0}{a_{max} - a_0}, \quad \text{if } a_d > a_0 \tag{6.2}$$

where $a_0 = 0.05$ μm is the radius of the particles in the global simulations in Chapter 5.

The probability matrix M_{prob} may be regarded as the 2D probability distribution of a particle's position, that can be randomly generated as follows: the first particle coordinate (x-coordinate) is generated based on the marginalised[1] probability distribution of M_{prob} over x, $M_{prob,x}$, which can be computed by taking the sum of the elements of M_{prob} by columns. Then, a random number is generated from a uniform distribution and the x-position is chosen from the cumulative distribution of $M_{prob,x}$. Finally, once the x-coordinate has been set, the y-coordinate is generated analogously, but this time the conditional probability[2] matrix $M_{prob,y}|x$ is used to build the cumulative distribution. In Fig. 6.3, each of these steps are schematically presented for illustration.

The velocity of the test particles is chosen based on their position in the grid. Since the mock particles are placed in the centres of the computational cells, the initial velocity is set based on the Alfvén, gas, and dust velocities ($\vec{\boldsymbol{v}}_A$, $\vec{\boldsymbol{v}}_g$, and $\vec{\boldsymbol{v}}_d$ respectively). This is done according to equations analogous to 6.1 and 6.2 on a component-by-component basis.

The remaining particle parameters are independent on its position. For each particle family, the corresponding electric charge is computed as explained in Chapter 5, sec. 5.1, and the Coulomb parameter is obtained from eq. 4.8. Finally, the represented mass of each test particle, M, is obtained from the product between the number of real particles represented by the test one, k, and the mass of such particles, m. The number of real particles is in turn computed from the abundance of each population, which must satisfy the condition $n = n_{min}(a/a_{min})^{-3.5}$ to satisfy the MRN distribution. Since for each dust family, 100 test particles are introduced, it follows that $k = n/100$.

6.2.2 Evolution of the dust grain-size distribution

Initially, the dust grain-size distribution for the graphite and silicate populations is identical. However, the differences in the critical velocity for a shattering event to occur (section 4.3.1) and in the dust grain charges (Table 5.2) result in a slightly different evolution of both families. To further simplify the simulations, it is assumed that only particles of the same material may interact with each other.

First, the maximum achievable size is compared for silicate and graphite populations. As expected, the lower value of the critical velocity for graphite particles

---

[1] When a probability function depends on more than one variable, it is possible to remove the dependency with respect to all but one variables. This function is called the *marginal probability distribution* of the variable. For instance, if a probability function depends on two variables, $p(x, y)$, the associated marginal distributions are $p_X(x)$ and $p_Y(y)$.

[2] The conditional probability measures the probability of an event occurring, given that another event has occurred before. The standard notation is $P(Y|X)$, and it is read as *the probability of Y to happen given X.*

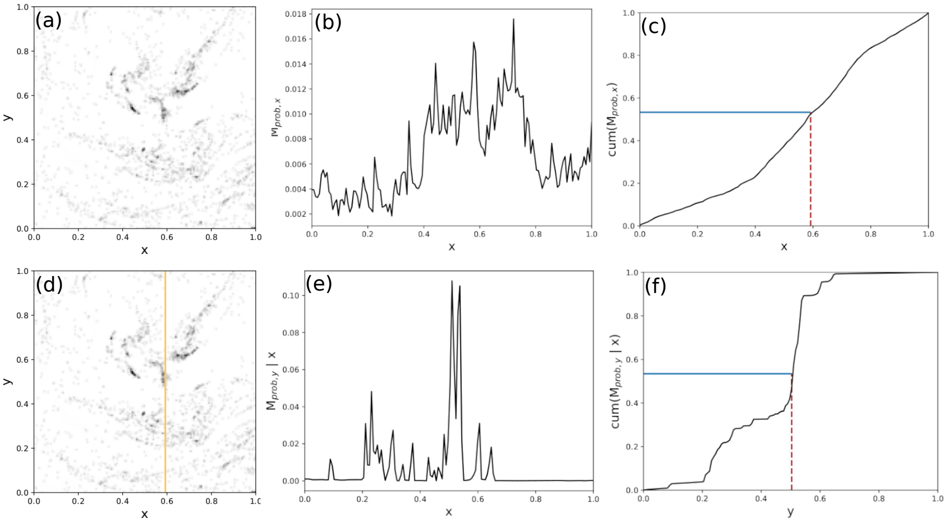

Figure 6.3: Generation of the random position for a particle with radius $a_d = 0.03$ μm. Starting from the 2D probability matrix built from eqs. 6.1 and 6.2 (a), the marginal probability distribution for x is built taking the sum by columns (b). Then, a random number is generated from a uniform distribution $r_x \in [0, 1]$, and the x-position is obtained by taking the inverse of the associated cumulative distribution function (c), $x = \mathrm{cum}^{-1}_{\mathrm{Mx}}(r_x)$. The y-position is conditioned by x (gold stripe, panel d), so this time the marginal probability is simply the corresponding column of the probability matrix (e). A new random number is generated $r_y \in [0, 1]$ and the y-position is computed from the inverse of the cumulative distribution function (f), $y = \mathrm{cum}^{-1}_{\mathrm{My|x}}(r_y)$.

prevents them to grow above the upper size limit of $a_d = 0.25$ μm, while silicate particles acquire sizes up to $a_d \sim 0.34$ μm. However, in some of the analysed regions deviations from the mean trend are observed.

One of the silicate clouds that represents dust particles of size $a_d = 28.4$ nm in region L4 grows up to 1.58 μm inside one of the densest dust filaments where the biggest particles were formed in the single-sized dust simulation (section 6.1.1). This is a clear example of enhanced dust growth inside dust filaments in a molecular cloud envelope.

There are also two graphite grains, one in region H2 and another one in region L1, that grow over $a_d = 0.3\mu$m. These grains, however, have an initial size of $a_d = 0.25$ μm, so they do not feel the action of the magnetic field. Besides, due to the structure of the collision algorithm, they are not either candidates to be eroded unless the colliding particle has the same size than them, so generally, the largest dust grains will only experience growth.

For each region, the final dust grain-size distributions for graphite and silicate grains have been fitted to a MRN-like power law, $dn/da \propto a^q$, by least squares; an example is shown in Fig. 6.4. The smallest dust grain sizes have been excluded for the fitting because, by the construction of the algorithm, they are more likely to lose mass after a collision event; besides, part of the dust mass that is assumed to return to the gas phase should in principle increase the represented mass of these clouds, so the extrapolation of the fitting for larger grains (a common q value) is considered to be representative for the smallest population. The results of these fitting, as well as of additional parameters that characterise the evolution of the dust grain-size distribution, are displayed in Table 6.3. In concordance with the previous discussion, the power index of silicate particles is shallower than that of graphite grains because the former grow more efficiently. Nevertheless, both power indexes are always around $q \sim -3.3$.

Table 6.3: Dust grain-size distribution properties of the realistic sample.

Region	a^{sil}_{max} μm	a^{gra}_{max} μm	$q^{\rm sil}$	$q^{\rm gra}$	$M^{\rm sil}_{\rm lost}$ %	$M^{\rm gra}_{\rm lost}$ %	$b_{\rm FUV}/b^{\rm MRN}_{\rm FUV}$
H1	0.338	0.250	-3.31	-3.33	45.56	50.28	0.76
H2	0.338	0.325	-3.33	-3.39	48.83	50.03	0.79
H4	0.332	0.250	-3.28	-3.35	45.51	54.30	0.75
L1	0.358	0.356	-3.28	-3.40	47.69	52.57	0.78
L2	0.338	0.250	-3.26	-3.36	44.97	49.13	0.75
L4	1.580	0.250	-3.39	-3.33	48.89	54.33	0.86
M1	0.352	0.250	-3.07	-3.11	61.33	65.79	0.55

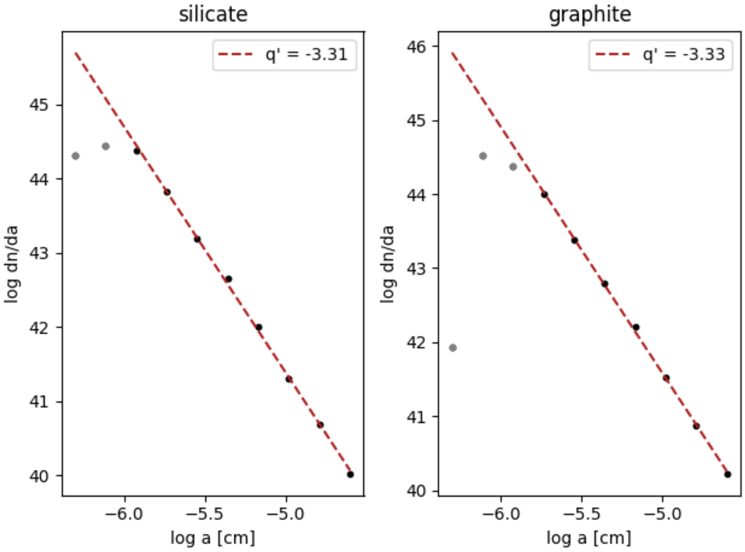

Figure 6.4: Fitting of the dust grain-size distribution for silicate and graphite grains in region H1. Only black points are considered, since the grey points (smaller particles) have lost mass and do not represent the abundance of the real population.

It is worth studying the amount of mass lost in these simulations as was done for the single-sized case, since now the fraction of dust lost is approximately 50% (see Table 6.3), much greater than the typical value of 35% for the turbulent case (Table 6.2). The reason behind this phenomenon is that most of the lost mass (~ 80 %) is carried out by the smallest dust particles with sizes 5 nm and 7 nm. These tiny grains are effectively accelerated by the magnetic fields and escape rapidly from the domain, taking with them a significant fraction of the dust mass due to the MRN initial mass distribution. This is most noticeably for the graphite dust population because their (absolute) charge parameters are slightly larger (see Table 5.2).

6.2.3 Variations of the UV extinction curve

It has already been mentioned that the UV extinction curve may be reproduced by a MRN size distribution. Reciprocally, starting from a given dust grain-size distribution, it is possible to retrieve the associated extinction curve.

The UV extinction curve may be computed from a very simple equation as in Nozawa & Fukugita (2013) (hereafter NF13) that takes into account an arbitrary number of dust species. In particular, the extinction curve of a dust population of graphite and silicate grains can be computed as:

$$A_\lambda = 1.086\left(\int_{a_{min}}^{a_{max}} \pi a^2 Q^{ext}_{\lambda,sil}(a) n_{sil}(a)da + \int_{a_{min}}^{a_{max}} \pi a^2 Q^{ext}_{\lambda,gra}(a) n_{gra}(a)da\right) \tag{6.3}$$

where $a_{min} = 50$ Å, $a_{max} = 0.25$ μm. The dust grain-size distribution is given by $n(a) = K n_H a^q$, where q is taken from Table 6.3 and differs from simulation to simulation and between dust species, and $K = 10^{-25.11}$ cm$^{2.5}$ for silicates, $K = 10^{-25.13}$ cm$^{2.5}$ for graphites (Weingartner & Draine 2001a, hereafter WD01). The coefficient Q_λ is the extinction efficiency of each dust species, and has been computed from the optical constants by Draine (2003b) available at his web page[3]. For graphite particles, the extinction coefficient is computed for sizes of 0.01 μm and according to the $1/3 - 2/3$ approximation, $Q_{\lambda,gra} = (Q^{\parallel}_{\lambda,gra} + 2Q^{\perp}_{\lambda,gra})/3$ (WD01; NF13).

The extinction curves are then normalised by the value at $\lambda = 540$ nm, which is the effective wavelength of the photometric V band, to compare the results amongst each region. In section 2.2, a detailed explanation of the UV extinction curve was presented with a special emphasis in the 2175 Å UV bump. This feature is thought to be caused by PAHs (WD01) with a possible contribution of other large molecules such as multishell furellenes (Iglesias-Groth, 2004). However, a grain-size distribution with a significant fraction of small graphite grains (Stecher & Donn, 1965) is also able to produce it as shown in Fig. 6.5. Actually, the UV bump is caused by the C-H chemical bond in PAHs and the C-C, sp^2

---

[3] `https://www.astro.princeton.edu/~draine/dust/dust.diel.html`.

bond in graphite particles. In this work, only graphite particles are considered so variations in the UV bump will not be analysed.

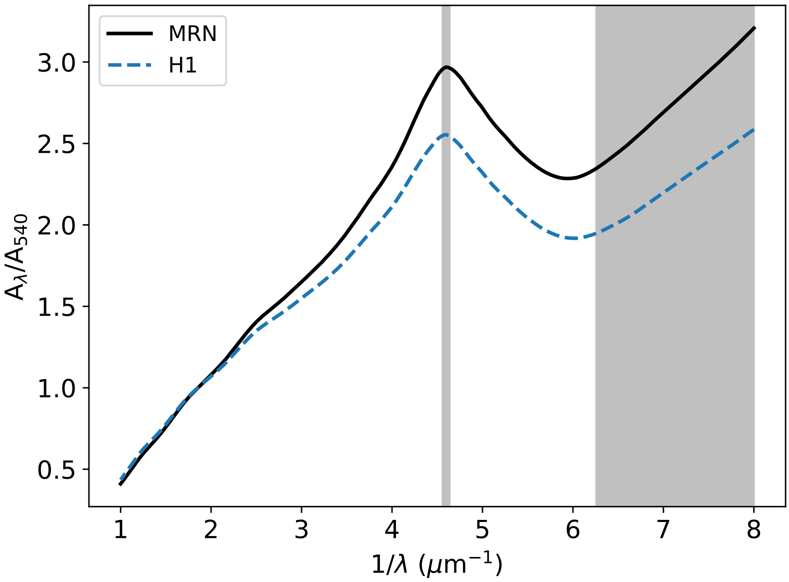

Figure 6.5: Normalised extinction curve for a MRN dust grain-size distribution composed by graphite and silicates (black solid line) compared to the extinction curve for region H1 (blue dashed line). The vertical line shows the central position of the UV bump, and the shadowed region corresponds to the FUV part of the curve where the linear fitting is performed.

The other characteristic feature of the UV extinction curve that has been analysed here is the steep slope at FUV wavelengths, due to the effective absorption and scattering of very small dust grains (Rai & Rastogi, 2012); actually, a contribution of PAHs to this feature might be important depending on the metallicity of the medium. For this study, however, the discussion is only restricted to the contribution of graphites. The FUV part of the extinction curves has been fitted by least squares to a linear function with slope b_{FUV} (see Table 6.3). The growing mechanisms reported in section 6.2.2 and the consequent depletion of small dust particles are translated into variations of the FUV slope by a factor of approximately 20%, but there are two regions that stand out. For region M1, the slope is dramatically reduced to half the standard MRN value due mainly to the destruction of small dust grains during shattering events, since only a small fraction of the mass (26% for silicates and 30.5% for graphites) is carried away by outgoing particles. On the other hand, region L4 is the one that shows the weakest variations and, at the same time, the one where the graphite population has been less depleted. This seems to imply that variations in the FUV part of the extinction curve are mainly caused by carbonaceous (graphite) grains.

In order to assess the validity of that statement, synthetic extinction curves have been built for size distributions with power indices ranging from $q = -3.0$ to $q = -3.5$ for both graphite and silicate grains. Size distributions with $q_{sil} \geq q_{gra}$ do not produce noticeable variations of the FUV slope, but for a given q_{sil}, b_{FUV} strongly varies for $q_{gra} \geq q_{sil}$. This supports the argument that variations on the FUV slope are mainly caused by the depletion and destruction of the small carbonaceous grains (graphites in this case). However, the contribution of PAHs and the photochemical processing of the carbonaceous grains and mantles (photodarkening, see sec. 1.2) is bound to be significant for the UV bump (a feature not analysed in this work) but also for the FUV slope. Therefore, the conclusions drawn from this analysis have to be taken as valid only for the particular case where only graphite and silicate grains are present.

6.3 Discussion

Dust evolution codes have been mainly developed for the study of planetesimal formation (Tamfal et al., 2018) or in a hydrodynamical framework (McKinnon et al., 2018), so the results are not comparable to the ones here presented because the regimes considered are very different. There are, however, two works that followed the evolution of a realistic distribution of charged dust grains in the diffuse ISM: Yan et al. (2004) (hereafter YLD04) estimated the grain velocities for two populations of silicate and carbonaceous grains through an statistical description of MHD turbulence and damping processes, and the critical sizes they may acquire at different regimes of the diffuse ISM, particularly in the WNM. In a subsequent work, Hirashita & Yan (2009) (hereafter HY09) used the grain velocities derived by YLD04 to study the evolution of dust grains via an equation similar to equation 3.15, section 3.2. Both evolution models consider only coagulation and shattering mechanisms, as the model implemented in Athena (section 4.3). Since the basis is common for both works, it is natural that the extracted conclusions are compatible between them. According to these works, only the smallest particles ($a_d \leq 0.02$ μm for silicates and $a_d \leq 0.04$ μm for graphites) experience a substantial growth. On the other hand, the upper size limits $a_{max} = 0.25$ μm cannot be superseded because grain shattering is very efficient for larger grains.

The results presented in this chapter are in clear contradiction with the latter statement, since all dust populations grow more or less efficiently depending on the ambient conditions. In order to better quantify the efficiency of the coagulation and shattering events, Table 6.4 shows the number of interactions of each type for each simulation along with their mean duration. Even for the single-sized distribution (section 6.1) both coagulation and shattering events are equally important for three of the regions (H1, H2, L2); for regions H4, L1, L4, and M1 shattering is far more frequent. In the view of these results, especially for those of the realistic simulations, it is evident that grain growth in a molecular cloud envelope is very limited due to the high efficiency of grain shattering events. As inferred from the previous discussion, only silicate grains are likely to grow because their critical velocities for shattering are larger (HY09) and their net charges are systematically smaller than for graphite grains (Table 5.2) so they are less accelerated by the magnetic fields. In consequence, the mean duration of shattering events for silicates is shorter than that for graphites (see Table 6.4) and grain growth is indirectly favoured.

Table 6.4: Coagulation and shattering parameters

	H1	H2	H4	L1	L2	L4	M1
		Turbulent	simulation				
$N_{\rm coag}$	2664	895	1725	959	1635	1841	577
$< t_{\rm coag} >$ (10^9 s)	0.71	1.45	1.42	1.39	1.70	2.24	0.23
median $t_{\rm coag}$ (10^7 s)	11.3	29.9	2.05	6.44	4.51	3.21	1.17
$N_{\rm shat}$	2680	803	2682	1341	1592	2695	1190
$< t_{\rm shat} >$ (10^9 s)	1.11	1.78	1.25	1.18	1.26	1.70	0.82
median $t_{\rm shat}$ (10^8 s)	1.21	3.53	1.16	1.40	1.70	1.16	0.59
		Realistic:	silicate				
$N_{\rm coag}$	174	144	149	160	179	154	221
$< t_{\rm coag} >$ (10^9 s)	0.54	0.65	1.00	1.20	1.75	1.43	0.13
median $t_{\rm coag}$ (10^7 s)	2.59	2.10	3.83	1.19	5.11	1.38	1.15
$N_{\rm shat}$	772	878	805	883	979	873	1113
$< t_{\rm shat} >$ (10^8 s)	7.57	4.09	5.07	4.74	4.03	6.22	6.00
median $t_{\rm shat}$ (10^7 s)	5.24	1.60	1.76	1.42	1.19	2.31	9.71
		Realistic:	graphite				
$N_{\rm coag}$	165	144	136	155	189	150	167
$< t_{\rm coag} >$ (10^8 s)	4.4	5.36	5.8	4.06	14.30	8.94	0.43
median $t_{\rm coag}$ (10^7 s)	1.13	0.81	2.16	0.33	1.76	0.64	0.38
$N_{\rm shat}$	908	943	1068	1039	1041	1024	1259
$< t_{\rm shat} >$ (10^8 s)	8.23	5.13	6.94	5.99	6.56	9.48	7.25
median $t_{\rm shat}$ (10^7 s)	3.42	1.91	2.07	1.28	1.32	1.80	7.44

The origin of the discrepancies between this work and that by YLD04 and HY09 is very likely the fundamentally different treatment of the particle interactions. When it is only interesting to follow the global behaviour of the system, the statistical approach by YLD04 is likely to provide fair results. However, when complex dust structures are present, a more realistic approach that fully solves the particles equation of motion is required. This is particularly true for a magnetised medium and small charged dust particles, such as a molecular cloud envelope. Nevertheless, it is also possible that the simplifications made in the coagulation model here presented, mainly the assumption that real particles inside a cloud do not interact with each other, may be affecting the results. The exploration of this issue will be carried out in future works.

6.4 Conclusions

In this chapter, the performance of the dust evolution module implemented in Athena has been demonstrated. It has been shown that both a single-sized population and a realistic full size distribution experience a substantial growth enough to produce variations on the FUV end of the UV extinction curve, although this growth is countered by shattering events. The most noticeable extinction effects are caused by the depletion of small carbonaceous particles, either by moderate growth or efficient shattering.

7 Conclusions and future work

In this thesis, I have presented the first comprehensive study on the evolution of small dust grains in molecular cloud envelopes from both an observational (Chapter 2) and a theoretical (Chapters 5 and 6) point of view. The main conclusions of this work may be summarised as follows:

- **Variations in the UV extinction curve are caused by the depletion of small carbonaceous dust grains.**
  According to the observational study presented in Chapter 2, the strength of the UV bump decreases whenever the small sized population is depleted from the medium, either by grain growth in dense regions or by photodestruction in highly irradiated areas. The slope of the FUV part of the curve also decreases when the smaller grains experience growth, especially those of a carbonaceous nature, as shown in Chapter 6.

- **In the diffuse envelopes of molecular clouds, narrow dust filaments are likely to exist decoupled from the gas**. This is especially true for very small dust grains (Chapter 5) that follow preferentially the magnetic field.

- **Grain growth may be enhanced inside dust filaments, even in a molecular cloud envelope**. The joint results from Chapters 5 and 6 indicate that interstellar grains may grow even in a diffuse regime characteristic of a molecular cloud envelope, producing variations in the dust grain-size distribution. Although these results are based on simplified models that need to be further improved, it is reasonable to hypothesise that grain growth may take place in molecular cloud envelopes due to the formation of filaments of charged dust.

There is an added value from this thesis, that is the development of two modules for the astrophysical MHD code Athena especially designed for the diffuse ISM. These modules are are available for a private use upon request.

Amongst the numerous possibilities, I identify two main lines of research derived from this thesis: one is focused on the improvement of the numerical model, and the other is related to the scientific exploitation of WSO-UV. However, the numerical modules here presented may be useful for studies on molecular cloud formation, dust evolution in supernova remnants, and on the formation of molecules in protoplanetary disks, to cite some examples.

7.1 Towards a characterisation of dust filaments in molecular cloud envelopes

The model for a molecular cloud envelope presented in Chapter 5 has some limitations inherent to the assumed hypothesis of ideal MHD, the restriction to a 2D domain, and the fact that the dust population is passive. Immediate improvements of the model are:

- The inclusion of a full dust grain size population.
- The consideration of non-ideal MHD effects, mainly ambipolar and Hall diffusion.
- An extension to 3D.

I am in the process of defining a set of simulations that consider several turbulent spectra and dust grain size distributions to assess, in the first place, the ability of each dust population to form filaments in a molecular cloud envelope. These simulations will be carried out with and without coagulation to study the possible differences that may arise. From this work, I will be able to discern if there is any characteristic dust filament width and to determine the potential detectability of such structures with current and future observational instrumentation. Once this study has been finished, I will increment the complexity of the model by adding non-ideal MHD effects. At that point, I will consider moving to the more recent version of Athena, Athena++, and to make the module publicly available.

Besides, the coagulation algorithm presented in Chapter 6 may also be improved. Some of the priority lines of action include:

- An appropriate treatment to ensure dust mass conservation.
- Extend the model to make it applicable to other astrophysical environments, including for instance grain growth by the accretion of metals.

Finally, I will consider to apply for time to super-computational facilities in order to build full 3D models that grow on the experience from these previous studies.

7.2 A scientific case for WSO-UV

There are two scientific cases of potential interest for WSO-UV derived from this thesis.

The first one is the detectability of diffuse dust structures that depends on the improved models presented in the previous section. Once more realistic models have been analysed (3D, full dust grain-size distributions), I will choose some particular star forming regions (yet to be determined) and will assess the detectability of the predicted dust filaments using the UV photometric capabilities of WSO-UV, as well as other UV facilities such as Astrosat/UVIT. These observations will be then compared to the theoretical predictions.

The second one is focused on the study of the dust small-sized population in the Rosette molecular complex. It is evident from Chapter 2 that variations of the UV extinction curve cannot be properly assessed from statistical measurements for distant molecular clouds such as Rosette. However, Rosette provides an ideal environment for the study of the UV extinction curve at different column densities due to the large number of B stars in the line-of-sight towards the complex. With an exhaustive spectroscopic survey of a selected sample of B stars both foreground and inside the cloud, it will be possible to build a 3D map of dust coagulation and UV bump strength for densities that span from 1 cm^{-3} to 10^4 cm^{-3}.

A A database of synthetic photometry in the GALEX ultraviolet bands for the stellar sources observed with the International Ultraviolet Explorer

L. Beitia Antero & A. I. Gómez de Castro

Article originally published in Astronomy & Astrophysics (2016), volume 596, id. A49

Abstract

Context: The Galaxy Evolution Explorer (GALEX) has produced the largest photometric catalogue of ultraviolet (UV) sources. As such, it has defined the new standard bands for UV photometry: the near UV band (NUV) and the far UV band (FUV). However, due to brightness limits, the GALEX mission has avoided the Galactic plane which is crucial for astrophysical research and future space missions.

Aims: The International Ultraviolet Explorer (IUE) satellite obtained 63 755 spectra in the low dispersion mode ($\lambda/\delta\lambda \sim 300$) during its 18-year lifetime. We have derived the photometry in the GALEX bands for the stellar sources in the IUE Archive to extend the GALEX database with observations including the Galactic plane.

Methods: Good quality spectra have been selected for the IUE classes of stellar sources. The GALEX FUV and NUV magnitudes have been computed using the GALEX transmission curves, as well as the conversion equations between flux and magnitudes provided by the mission.

Results: Consistency between GALEX and IUE synthetic photometries has been tested using White Dwarfs (WD) contained in both samples. The non-linear response performance of GALEX inferred from this data agrees with the results from GALEX calibration. The photometric database is made available to the community through the services of the Centre de Données Stellaires at Strasbourg (CDS). The catalogue contains FUV magnitudes for 1628 sources, ranging from FUV = 1.81 to FUV = 18.65 mag. In the NUV band, the catalogue includes observations for 999 stars ranging from NUV = 3.34 to NUV = 17.74 mag.

Conclusions: UV photometry for 1490 sources not included in the GALEX AIS GR5 catalogue is provided; most of them are hot (O-A spectral type) stars. The sources in the catalogue are distributed over the full sky, including the Galactic plane.

Keywords. astronomical databases:miscellaneous – catalogs – surveys – ultraviolet:stars

A.1 Introduction

The catalogue of ultraviolet (UV) sources generated by the Galaxy Evolution Explorer[1] (GALEX) mission constitutes the most extensive database of UV photometry (Martin et al. 2005, hereafter Ma2005; Bianchi 2014, hereafter B2014). As such, the GALEX near ultraviolet or NUV band and far ultraviolet or FUV band, have become standards for the description of the spectral energy distribution (SED) of sources in broad band photometry. The NUV band ranges from 1771 Å to 2831 Å, with an effective wavelength of 2315.7 Å, and the FUV band ranges from 1344 Å to 1786 Å with an effective wavelength of 1538.6 Å (Morrissey et al. 2007, hereafter M2007).

The UV detectors used by the GALEX mission were sensitive Microchannel Plate (MCP) type detectors with a global count rate limit of 100 000 counts s^{-1} (M2007). As a result, the GALEX survey avoided the Galactic plane (B2014). Moreover, the photometric database does not extend to bright UV sources that are ideally suited for calibration purposes.

The International Ultraviolet Explorer (IUE) (Boggess et al. 1978, herefater B1978) contains the largest data set of UV spectra. Most of them were obtained in photometric conditions: good guiding, large aperture (10×20 arcsec), and low dispersion ($\lambda/\delta\lambda \sim 300$). We have used this spectral data base to compute the FUV and NUV synthetic magnitudes of stellar sources observed with IUE under this configuration (31 982 spectra).

In this research note, we describe the methods followed to derive the FUV and NUV magnitudes from the IUE spectra, and quantify the photometric accuracy of these results by comparing GALEX and IUE-based photometry for the white dwarfs (WDs) contained in both samples. We also describe the contents and characteristics of the database submitted to the Centre de Données Stellaires at Strasbourg (CDS).

A.2 The IUE database of stellar spectra

The IUE database contains 63 755 spectra obtained through the large aperture (10×20 arcsec) in low dispersion mode; from those, we have selected only the stellar sources[2]. This amounts to a grand total of 31 982 stellar spectra.[3]

The IUE low dispersion spectra were recorded with three cameras: long wavelength prime (LWP), long wavelength redundant (LWR), and short wavelength

---

[1] `http://galexgi.gsfc.nasa.gov`

[2] `http://sdc.cab.inta-csic.es/ines/InForm.html#class`.

[3] Not included in this census are: IUE sky images misclassified among the stellar sources or individual objects belonging to the SMC, LMC, clusters, and associations with identification not recognised by the Centre de Données Stellaires (CDS, Strasbourg).

prime (SWP) (B1978). From the 31 982 stellar spectra, 16 467 are SWP observations, 10 349 are LWP observations, and 5166 are LWR observations. Good quality spectra (according to the criteria defined in Sect. A.4) are available for 1889 stars in the SWP camera and 1157 stars in the LWP or LWR cameras.

A.3 The GALEX photometric bands in the IUE spectra

GALEX was a 50-cm primary space telescope with a Ritchey-Chrétien mounting, simultaneously feeding two detectors sensitive to near and far UV making use of a multilayer dichroic beamsplitter (Morrissey et al. 2005, Ma2005). The GALEX photometric bands are defined in the mission documentation (M2007) and can be downloaded from the GALEX official webpage[4]. The FUV and NUV bands cover the spectral ranges 1344 – 1786 Å and 1771 – 2831 Å respectively (M2007); the transmittance curves are shown in Figure A.1. FUV and NUV AB magnitudes are determined by means of the conversion:

$$\mathrm{FUV} = -2.5 \times \log\left(\frac{\mathrm{Flux\quad FUV}}{1.40 \times 10^{-15}\,\mathrm{erg\,s^{-1}cm^{-2}}\mathring{A}^{-1}}\right) + 18.82 \qquad (A.1)$$

$$\mathrm{NUV} = -2.5 \times \log\left(\frac{\mathrm{Flux\quad NUV}}{2.06 \times 10^{-16}\,\mathrm{erg\,s^{-1}cm^{-2}}\mathring{A}^{-1}}\right) + 20.08 \qquad (A.2)$$

(M2007).

The IUE long (1850 – 3300 Å) and short (1150 – 1980 Å) wavelength ranges (B1978) do not match exactly the GALEX bands. While GALEX FUV is completely contained in the IUE SW range, GALEX NUV is split between the LW and SW cameras. For this reason, we need to join SWP and LW spectra in order to compute NUV magnitudes. Therefore NUV photometry can only be provided for non-variable sources.

A.4 Methods

A.4.1 Data Selection

Spectra have been retrieved from the IUE Newly Extracted Spectra (INES) Archive; data in this archive were processed using an optimised extraction algorithm that prevents the introduction of artefacts during the extraction while preserving the photometric accuracy (see Rodríguez-Pascual et al. 1999 for more details). The INES Archive is a final release from the European IUE Observatory.

---

[4] `http://galexgi.gsfc.nasa.gov/docs/galex/Documents/PostLaunchResponseCurveData.html`.

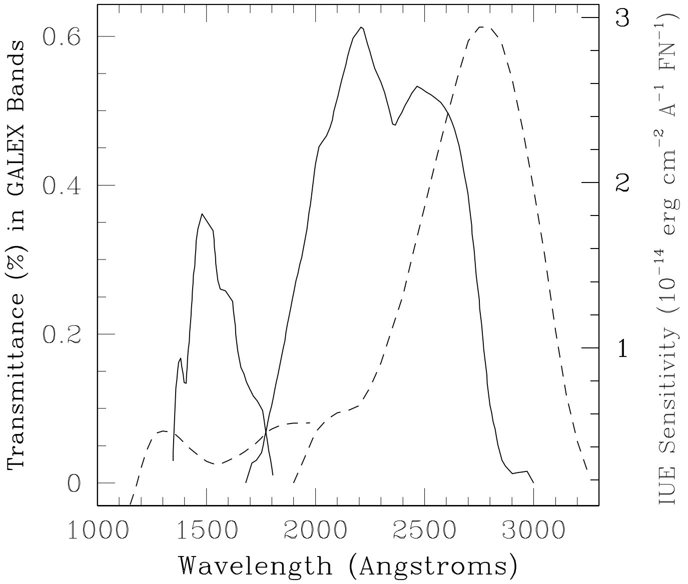

Figure A.1: GALEX transmission curves (solid) compared with IUE sensitivity curves (dashed) for the SWP and LWR cameras from Bohlin et al. (1980).

The spectra are provided as `FITS` files binary tables that include four columns with: *Wavelength* (Å), *Flux* (erg cm^{-2} s^{-1} Å^{-1}), *Flux error* (erg cm^{-2} s^{-1} Å^{-1}) after pipeline processing,[5] and *Quality Flag* (QF), a quality measure for each pixel. $QF = 0$ indicates that the pixel flux is reliable, otherwise $QF < 0$. Negative QFs are given in powers of 2 ($QF = -2^n$ with $n = 1 \ldots 14$) and n is an identifier of the various possible sources of inaccuracies in the pixel photometry: microphonic noise, saturated pixel, reseaux mark, and others[6].

The database contains all data including overexposed or underexposed spectra as well as observations that suffered problems during the downlink, calibration, processing and other processes. To avoid including bad spectra in the photometric database, we removed from our list:

- spectra with more than 10% of the pixels in the IUE spectrum flagged with $QF < 0$. The vast majority of the spectra contain reseau marks for the

---

[5] See González-Riestra et al. 2001 for the absolute calibration of the INES IUE fluxes.

[6] See `https://archive.stci.eduiue/manual/newsips/node20.html` for details

geometric calibration of the raw data and pixels flagged with $QF < 0$ close to the edge of the spectrum. For this reason we have worked with a tolerance of 10%.

- spectra with average *Flux* smaller than three times the average *Flux error* in the corresponding GALEX wavelength range. Calibrated data include flux and flux error at each wavelength; this is the standard 3σ criterium applied to remove underexposed spectra from the working list.

LW spectra require a more detailed examination since the peak transmittance of the GALEX NUV filter is at 2300 Å, in an area often underexposed in the spectrum of the cool stars observed with the IUE. To evaluate the Signal-to-Noise Ratio (SNR) in this region, we define four windows in the 1975 Å - 2375 Å range: `REG I` ($1975 - 2075$Å), `REG II` ($2075 - 2175$Å), `REG III` ($2175 - 2275$Å), and `REG IV` ($2275 - 2375$Å). Within these windows we compute the mean flux and the dispersion. We reject the spectra if the mean flux is negative or if the standard deviation is ten times higher than the mean in any of the regions `II-III-IV`. We allow for a factor of ten to prevent removing sources with steep energy distributions or strong features.

A.4.2 Calculation of the FUV and NUV synthetic magnitudes

The integrated flux in the FUV band is computed from the SWP IUE spectra after multiplication by the normalised transmittance of the FUV filter. The flux of the flagged bad pixels ($QF < 0$) has been interpolated from good nearby pixels. The AB magnitude is calculated using Eq. A.1 (see Sect. A.3).

To evaluate the NUV synthetic magnitude, it is first necessary to determine whether the sources are variable (see Sect. A.4.4 for a description of the procedure). In case there is no evidence of variability, the SW and LW are joined into a single spectrum; the matching wavelength is set at 1975 Å. After this, the spectrum is multiplied by the normalised transmittance of the NUV filter. The flux of the flagged bad pixels ($QF < 0$) has been interpolated from good nearby pixels. The AB magnitude is calculated using Eq. A.2 (see Sect. A.3). In case there are multiple observations and the source is found not to vary, synthetic magnitudes are computed from the average flux.

A.4.3 Error determination

For each spectrum and band, the *Flux error* provided by the mission (Col. #3 in the data) is multiplied by the GALEX normalised transmittance to evaluate the total error in each band denoted as $S_{\rm FUV}$ and $S_{\rm NUV}$ for the FUV and NUV bands respectively. From that, magnitude errors are provided for the FUV band,

$+e_F$ and $-e_F$, and NUV band, $+e_N$, and $-e_N$; the errors are asymmetric around the magnitude value because of the logarithmic scale. In case there are multiple observations and the source is found not to vary, errors are from the *Flux errors*.

A.4.4 Multiple observations. Variable stars

There are 598 stars in the IUE archive with multiple observations in the SW range and 409 stars with multiple observations in the LW range. For those, variability has been tested.

Stars with multiple observations in the IUE SW range

We compute for each SWP observation, i, the weighted flux in the GALEX FUV band, $F_{\rm FUV}(i)$, calculated as:

$$F_{\rm FUV}(i) = \int F_i(\lambda) G_{\rm FUV}(\lambda) d\lambda, \tag{A.3}$$

with $G_{\rm FUV}$ being the normalised GALEX FUV transmission curve (see Figure A.1). The weighted *Flux error*, $S_{\rm FUV}$(i), is determined in the same manner:

$$S_{\rm FUV}(i) = \int S_i(\lambda) G_{\rm FUV}(\lambda) d\lambda, \tag{A.4}$$

with $S_{\rm FUV}(i)$ being the *Flux error* (see Figure A.1).

After this, the average $\langle F_{\rm FUV} \rangle$, the dispersion $\sigma(F_{\rm FUV})$, and the average *Flux error* $\langle S_{\rm FUV} \rangle$ are computed. We flag a star as variable if $\sigma(F_{\rm FUV}) \geq 3 \times \langle S_{\rm FUV} \rangle$. Very noisy data have already been rejected in the data selection process (see Sect. A.4.1).

Stars with multiple observations in the IUE LW range

The procedure is similar to that described for the SW range but, in this case, the variability test is carried out only over the range of the NUV band contained in the LW images.

We compute for each LW observation, i, the weighted flux in the $1975 - 3000$ Å range, $F_{\rm GaLW}(i)$, calculated as:

$$F_{\rm GaLW}(i) = \int_{1975}^{3000} F_i(\lambda) G_{\rm NUV}(\lambda) d\lambda, \tag{A.5}$$

with $G_{\rm NUV}$ being the normalised GALEX NUV transmission curve (see Figure A.1), as well as the weighted *Flux error*, $S_{\rm GaLW}$(i),

$$S_{\rm GaLW}(i) = \int_{1975}^{3000} S_i(\lambda) G_{\rm NUV}(\lambda) d\lambda. \tag{A.6}$$

The average $\langle F_{\mathrm{GaLW}} \rangle$, the dispersion $\sigma(F_{\mathrm{GaLW}})$, and the average *Flux error* $\langle S_{\mathrm{GaLW}} \rangle$ are then computed. We flag a star as variable if $\sigma(F_{\mathrm{GaLW}}) \geq 3 \times \langle S_{\mathrm{GaLW}} \rangle$.

In summary

According to these criteria, 52 stars are found to be variable in the LW range and 88 in the SW range; only 36 stars are found to be variable in both ranges. Therefore, $\sim$ 13% of the stars with multiple observations in the LW range are found to be variable and $\sim$ 15% of the stars with multiple observations in the SW range are found to be variable.

An additional search for variable sources was carried out by comparing the fluxes in the window where SW and LW spectra overlap for every source. Three additional stars have been identified as variables from this test, namely HD 37209, HD 56014, and HD 14399, and have been excluded from the catalogue.

A.5 Photometric accuracy

The IUE sample (of non-variable stars) provides good synthetic photometry for 103 WDs. 43 of these 103 WDs have a counterpart in the GALEX GR5 AIS survey (Bianchi et al., 2011a) within a search radius of 3”. We have used this subset to check the photometric accuracy of the synthetic magnitudes computed in this work (see Table A.1 for their synthetic and GALEX magnitudes). The limiting magnitude of GALEX AIS[7] (NUV $\sim$ 20.5 mag) is high above the sensitivity threshold of IUE in low dispersion mode; therefore counterparts are identified for all sources within the area mapped by GALEX. We note that in May 2009, the FUV detector in GALEX stopped working and as a result, releases later to GR5 (such as GR6/7) only add new sources in the NUV band[8] (B2014).

---

[7] `https://archive.stsci.edu/prepds/gcat/gcat_gasc_gmsc.html`.

[8] In fact, late GALEX releases also add very weak FUV sources, identified by being the counterpart of a NUV source. These sources are too weak to have been observed with IUE.

Table A.1: Synthetic photometry in the GALEX bands of WD observed with IUE: WDs with GALEX counterpart. NA means 'not available' data.

ID IUE	RA	DEC	IUE-based synthetic phot.						GALEX phot.			
	(ICRS)	(ICRS)	FUV	$+e_F$	$-e_F$	NUV	$+e_N$	$-e_N$	FUV	e_F	NUV	e_N
WD 0005+511	00:08:18.17	+51:23:16.6	11.09	0.06	-0.06	NA	NA	NA	12.190	0.004	13.178	0.004
EQ 0027+259	00:29:37.96	+26:10:28.47	13.60	0.07	-0.06	13.22	0.30	-0.24	13.567	0.008	13.785	0.006
WD 0039+04	00:42:6.12	+05:09:23.36	12.01	0.08	-0.07	NA	NA	NA	NA	NA	13.189	0.004
WD 0050-332	00:53:17.44	-32:59:56.6	11.47	0.07	-0.07	12.13	0.11	-0.10	NA	NA	12.365	0.003
WD 0112+104	01:14:37.8	+10:41:6	14.40	0.15	-0.13	14.66	0.28	-0.22	14.425	0.010	14.623	0.007
WD 0134+833	01:41:28.74	+83:34:58.9	12.34	0.07	-0.06	12.70	0.10	-0.09	12.923	0.002	12.938	0.002
WD 0232+035	02:35:7.59	+03:43:56.8	10.39	0.07	-0.06	11.01	0.11	-0.10	NA	NA	12.371	0.003
WD 0302+027	03:04:37.34	+02:56:57.9	13.31	0.11	-0.10	13.69	0.13	-0.11	13.008	0.007	13.968	0.007
WD 0320-539	03:22:14.83	-53:45:16.5	13.13	0.09	-0.08	NA	NA	NA	13.325	0.004	13.747	0.003
WD 0342+026	03:45:34.58	+02:47:52.81	10.44	0.07	-0.07	10.76	0.12	-0.11	NA	NA	12.751	0.003
WD 0453-296	04:55:35.94	-29:28:59.96	15.01	0.21	-0.17	15.03	0.23	-0.19	15.029	0.015	14.995	0.010
HS 0713+3958	07:17:2.7	+39:53:25	14.57	0.11	-0.10	15.05	0.23	-0.19	14.643	0.012	14.977	0.009
WD 0846+249	08:49:5.88	+24:45:7.93	14.45	0.08	-0.08	NA	NA	NA	14.436	0.013	15.147	0.011
WD 0853+163	08:56:18.96	+16:11:3.8	15.28	0.14	-0.13	15.31	0.50	-0.34	15.273	0.022	15.201	0.013
WD 0945+246	09:48:46.65	+24:21:26	14.38	0.08	-0.08	13.89	0.21	-0.18	14.479	0.011	13.955	0.005
PG 0958-073	10:00:47.25	-07:33:31.01	12.44	0.07	-0.06	12.90	0.13	-0.11	12.517	0.006	13.190	0.005
WD 1034+001	10:37:3.81	-00:08:19.31	10.85	0.06	-0.06	11.62	0.09	-0.09	NA	NA	12.865	0.002
WD 1114+072	11:16:49.35	+06:59:33	11.85	0.07	-0.06	12.24	0.13	-0.11	12.360	0.003	13.119	0.004
WD 1144+005	11:46:35.17	+00:12:33.6	13.69	0.09	-0.09	NA	NA	NA	12.921	0.008	13.691	0.006
WD 1211+332	12:13:56.25	+32:56:31.4	12.64	0.07	-0.06	13.22	0.11	-0.10	12.718	0.008	13.396	0.004
WD 1230+052	12:33:12.57	+04:57:37.7	12.04	0.07	-0.06	12.34	0.10	-0.09	12.544	0.004	13.732	0.004
WD 1233+427	12:35:51.14	+42:22:39.72	10.82	0.06	-0.06	11.13	0.12	-0.11	12.710	0.007	12.831	0.004
WD 1302+283	13:04:48.63	+28:07:29.3	13.69	0.11	-0.10	14.10	0.24	-0.19	13.802	0.009	14.238	0.005
WD 1326-037	13:29:16.39	-03:58:51.75	15.22	0.12	-0.11	15.20	0.33	-0.26	15.295	0.015	15.204	0.009
WD 1406+590	14:08:32.23	+59:40:25.1	11.93	0.11	-0.10	12.28	0.21	-0.18	12.690	0.003	12.548	0.002
WD 1445+152	14:48:14.38	+15:04:49.93	15.62	0.29	-0.23	15.57	0.38	-0.28	15.462	0.027	15.421	0.016

TableA.1 – continue

ID IUE	RA	DEC	IUE-based synthetic phot.						GALEX phot.			
	(ICRS)	(ICRS)	FUV	$+e_F$	$-e_F$	NUV	$+e_N$	$-e_N$	FUV	e_F	NUV	e_N
WD 1636+351	16:38:26.32	+35:00:11.9	13.09	0.09	-0.09	13.75	0.37	-0.28	13.236	0.005	13.854	0.003
PG 1637+346	16:39:36.02	+34:32:30.36	15.01	0.18	-0.16	NA	NA	NA	14.403	0.008	14.656	0.005
HS 1650+7229	16:49:16.1	+72:24:12	15.44	0.12	-0.11	NA	NA	NA	15.581	0.032	16.050	0.013
WD 1708+602	17:09:15.9	+60:10:11	11.82	0.04	-0.04	NA	NA	NA	12.707	0.005	12.565	0.003
WD 2034-532	20:38:16.84	-53:04:25.4	14.56	0.12	-0.11	NA	NA	NA	14.533	0.014	14.190	0.007
WD 2059+013	21:02:19.3	+01:32:15.9	13.93	0.09	-0.08	14.21	0.23	-0.19	13.982	0.007	14.364	0.005
WD 2110+127	21:13:21.06	+12:57:9.4	12.41	0.12	-0.11	NA	NA	NA	12.787	0.006	13.182	0.005
BPS CS 22951-0067	21:49:38.91	-43:06:14.28	14.70	0.08	-0.08	16.35	0.53	-0.36	13.511	0.010	14.312	0.004
WD 2149+021	21:52:25.38	+02:23:19.54	12.24	0.06	-0.06	12.51	0.12	-0.11	12.604	0.007	12.688	0.005
WD 2207-303	22:10:29.22	-30:05:43.7	12.63	0.06	-0.06	NA	NA	NA	12.596	0.004	13.539	0.003
HS 2237+8154	22:37:15.57	+82:10:27.32	17.45	1.40	-0.59	NA	NA	NA	17.396	0.040	16.923	0.021
WD 2246+223	22:49:5.76	+22:36:32.31	17.57	1.27	-0.57	NA	NA	NA	17.736	0.038	15.109	0.006
WD 2316+123	23:18:45.1	+12:36:2.9	16.70	0.56	-0.37	15.74	0.26	-0.21	16.889	0.045	15.783	0.011
WD 2331-475	23:34:2.2	-47:14:26.5	12.17	0.08	-0.07	NA	NA	NA	12.419	0.004	13.405	0.003
WD 2333-002	23:35:41.47	+00:02:19	14.22	0.12	-0.11	NA	NA	NA	14.149	0.014	14.719	0.010
WD 2342+806	23:45:2.26	+80:56:59.7	12.49	0.07	-0.07	13.27	0.11	-0.10	12.954	0.005	13.520	0.004
WD 2353+026	23:56:27.72	+02:57:5.61	13.85	0.11	-0.10	14.58	0.24	-0.20	13.829	0.007	14.357	0.006

As shown in Figure A.2, GALEX- and IUE-based UV photometries compare well except for the brightest sources; GALEX photometry is affected by photon count loses at high count rates. Following Camarota & Holberg (2014) (hereafter CH), we have fitted the samples to a quadratic function using the least-squares method:

$$M_{\mathrm{GAL}} = c_0 + c_1 M_{\mathrm{IUE}} + c_2 M_{\mathrm{IUE}}^2 \tag{A.7}$$

with M_{GAL} the WD magnitude as per the GALEX AIS catalogue and M_{IUE} the IUE-based synthetic magnitude derived in this work. The coefficients of the fit, c_0, c_1 , and c_2, are given in Table A.2. We found a very good agreement with CH's fits in the FUV photometry and a significant discrepancy in the NUV band that we ascribe to a possible typographic error in the parameters in CH's Table 2. The FUV and NUV synthetic photometry for the rest of the WDs in the IUE sample is provided in Table A.3.

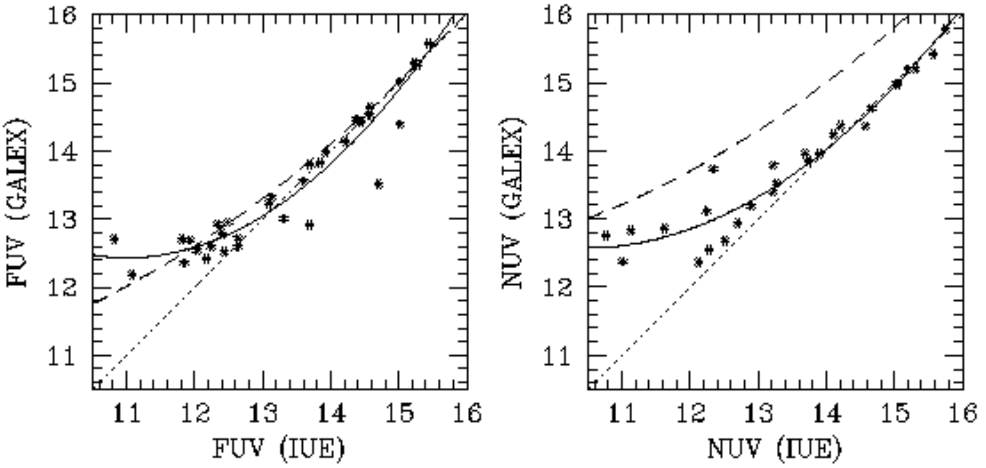

Figure A.2: IUE versus GALEX photometry for the WDs sample. The dotted line represents the 1:1 correspondence, the solid line represents the fit in Table A.2 and the dashed line represents CH's fit.

Table A.3: Synthetic photometry in the GALEX bands of WDs observed with IUE: that is, WDs without GALEX counterpart. NA means no available data.

ID IUE	RA	DEC	IUE-based synthetic phot.					
	(ICRS)	(ICRS)	FUV	$+e_F$	$-e_F$	NUV	$+e_N$	$-e_N$
WD 2357+296	00:00:7.25	+29:57:0.31	13.06	0.11	-0.10	NA	NA	NA
WD 0017+136	00:20:1.79	+13:52:48.1	15.27	0.12	-0.10	15.09	0.17	-0.14
WD 0101+039	01:04:21.68	+04:13:37.06	10.89	0.11	-0.10	11.23	0.12	-0.10
WD 0104+50	01:07:11.02	+51:10:22.74	11.85	0.06	-0.06	NA	NA	NA
WD 0128-387	01:30:28.03	-38:30:38.7	15.84	0.26	-0.21	15.37	0.16	-0.14

TableA.3 − continue

ID IUE	RA	DEC	IUE-based synthetic phot.					
	(ICRS)	(ICRS)	FUV	$+e_F$	$-e_F$	NUV	$+e_N$	$-e_N$
WD 0131-164	01:34:24.07	-16:07:8.38	11.98	0.06	-0.06	12.83	0.11	-0.10
WD 0135-052	01:37:59.34	-04:59:44.3	NA	NA	NA	15.15	0.26	-0.21
WD 0141-675	01:43:1.04	-67:18:29.37	NA	NA	NA	17.13	3.06	-0.72
WD 0148+467	01:52:2.96	+47:00:6.65	12.60	0.06	-0.05	12.67	0.14	-0.12
WD 0214+568	02:17:33.52	+57:06:47.5	12.49	0.07	-0.06	NA	NA	NA
PG 0216+032	02:19:19	+03:26:54	12.45	0.06	-0.05	13.18	0.13	-0.11
WD 0227+050	02:30:16.62	+05:15:50.68	12.10	0.06	-0.05	12.43	0.10	-0.09
WD 0229-481	02:30:53.3	-47:55:26.2	12.41	0.06	-0.06	NA	NA	NA
WD 0232+525	02:36:19.54	+52:44:12.5	13.33	0.07	-0.06	NA	NA	NA
KUV 02503-0238	02:52:51	-02:25:17.99	14.63	0.12	-0.11	14.76	0.52	-0.35
WD 0255-705	02:56:17.21	-70:22:10.86	NA	NA	NA	14.84	1.08	-0.53
WD 0346-011	03:48:50.19	-00:58:32.02	12.02	0.11	-0.10	12.73	0.09	-0.08
KUV 685-13	04:50:13.52	+17:42:6.21	12.07	0.09	-0.08	12.59	0.16	-0.14
WD 0455-282	04:57:13.9	-28:07:54	11.76	0.07	-0.06	12.41	0.17	-0.15
WD 0509-007	05:12:6.39	-00:42:6	12.01	0.06	-0.06	NA	NA	NA
WD 0531-022	05:34:18	-02:15:0	14.28	0.43	-0.31	NA	NA	NA
WD 0612+177	06:15:18.69	+17:43:41	11.93	0.07	-0.07	12.48	0.17	-0.15
WD 0640+015	06:43:16.02	+01:30:12.6	13.81	0.08	-0.08	NA	NA	NA
WD 0651-020	06:54:13	-02:09:12	12.94	0.07	-0.06	13.59	0.21	-0.17
WD 0715-703	07:15:16.59	-70:25:5.6	12.08	0.07	-0.06	NA	NA	NA
WD 0836+237	08:39:33.3	+23:34:9	14.43	0.45	-0.32	NA	NA	NA
BD+48 1777	09:30:46.78	+48:16:23.77	8.87	0.05	-0.05	9.29	0.12	-0.11
PG 0934+553	09:38:20.35	+55:05:50.08	10.47	0.07	-0.07	NA	NA	NA
WD 1013-050	10:16:28.68	-05:20:32.06	12.07	0.06	-0.06	12.71	0.11	-0.10
WD 1042-690	10:44:10.23	-69:18:18.03	11.88	0.05	-0.05	12.29	0.10	-0.09
WD 1105-048	11:07:59.95	-05:09:25.89	12.90	0.06	-0.05	13.08	0.10	-0.10
WD 1123+189	11:26:19.06	+18:39:17.85	12.08	0.06	-0.05	12.73	0.10	-0.09
WD 1234+482	12:36:45.18	+47:55:22.34	12.30	0.09	-0.08	12.94	0.11	-0.10
WD 1302+597	13:04:32.19	+59:27:32.78	13.33	0.07	-0.07	13.66	0.16	-0.14
WD 1321+36	13:23:35.26	+36:07:59.51	10.11	0.05	-0.05	10.40	0.10	-0.09
BD-07 3632	13:30:13.64	-08:34:29.5	12.33	0.10	-0.09	12.40	0.18	-0.15
WD 1337+705	13:38:50.48	+70:17:7.66	11.84	0.06	-0.05	12.23	0.12	-0.11
WD 1403-077	14:06:4.83	-07:58:31.21	13.66	0.08	-0.08	NA	NA	NA
WD 1424+534	14:25:55.46	+53:15:25.14	13.50	0.07	-0.07	14.23	0.21	-0.18
CD-37 10500B	15:47:30.07	-37:55:8.11	16.76	1.73	-0.64	13.97	0.20	-0.17
WD 1615-154	16:17:55.26	-15:35:51.93	11.65	0.08	-0.08	12.28	0.11	-0.10
CD-38 10980	16:23:33.84	-39:13:46.16	9.62	0.06	-0.06	10.15	0.10	-0.09
WD 1639+537	16:40:57.16	+53:41:9.6	NA	NA	NA	17.09	0.86	-0.48
WD 1657+343	16:58:51.12	+34:18:53.29	14.37	0.10	-0.09	NA	NA	NA
WD 1713+695	17:13:6.12	+69:31:25.7	13.07	0.15	-0.13	13.13	0.51	-0.34
WD 1725+586	17:26:43.36	+58:37:32.06	13.41	0.25	-0.20	NA	NA	NA
WD 1900+706	19:00:10.25	+70:39:51.2	13.88	0.15	-0.13	NA	NA	NA
** LDS 678A	19:20:34.92	-07:40:0.07	14.83	0.23	-0.19	NA	NA	NA
WD 1936+327	19:38:28.21	+32:53:19.9	12.54	0.08	-0.08	NA	NA	NA

TableA.3 – continue

ID IUE	RA (ICRS)	DEC (ICRS)	IUE-based synthetic phot. FUV	$+e_F$	$-e_F$	NUV	$+e_N$	$-e_N$
LS II +18 9	19:43:31.21	+18:24:34.58	10.20	0.07	-0.06	10.77	0.10	-0.09
WD 2007-303	20:10:56.85	-30:13:6.64	12.13	0.06	-0.06	12.28	0.11	-0.10
RX J2013.1+4002	20:13:9.37	+40:02:24.25	12.10	0.06	-0.06	NA	NA	NA
WD 2028+390	20:29:56.16	+39:13:32	12.02	0.06	-0.06	12.56	0.17	-0.14
WD 2123-82	21:31:5.18	-82:40:53.25	12.46	0.07	-0.06	12.35	0.20	-0.17
WD 2211-495	22:14:11.91	-49:19:27.26	9.40	0.05	-0.05	10.23	0.10	-0.09
WD 2313-021	23:16:12.42	-01:50:35.06	11.79	0.07	-0.06	12.09	0.10	-0.09
GD 1110	23:19:24.43	-08:52:37.91	11.87	0.06	-0.05	NA	NA	NA
WD 2317-054	23:19:58.4	-05:09:56.16	10.07	0.05	-0.05	10.47	0.10	-0.09
GD 1309	23:29:12	-10:05:0	11.68	0.07	-0.06	12.09	0.11	-0.10
WD 2349+286	23:51:56	+28:55:12	14.39	0.22	-0.18	NA	NA	NA

A.6 The catalogue

The catalogue contains FUV magnitudes for all stars (with and without multiple observations) and NUV magnitudes only for non-variable stars, or stars with just one good observation, as pointed out in Sect. A.4.2. The number of observations used for the variability evaluation are indicated for all catalogue entries; $\sim 65\%$ of the sources have only one good observation.

Appendix A.A contains an excerpt of the on-line catalogue. For each source, the following entries are provided:

- Object identification in the IUE Archive.
- Right Ascension and Declination (ICRS).
- Number of SWP observations used to compute FUV.
- Synthetic FUV magnitude (Eq. A.3) computed from the mean flux, if several observations are used (see section A.4.2).
- Error in the synthetic FUV magnitude computed from the mean flux and error (see section A.4.3).
- Number of LW observations used to compute NUV.
- Synthetic NUV magnitude (obtained from SWP and LW mean fluxes).
- Error in the synthetic NUV magnitude (obtained from SWP and LW mean fluxes).

Table A.2: Quadratic fit parameters for the WDs sample

Property	FUV	FUV
c_0	31.2738	24.9204
c_1	-3.4197	-2.3688
c_2	0.1552	0.1136
χ^2/dof	0.0064	0.0058
No. of stars	34	24
Lower bound	10.8	10.8
Upper bound	15.5	15.7

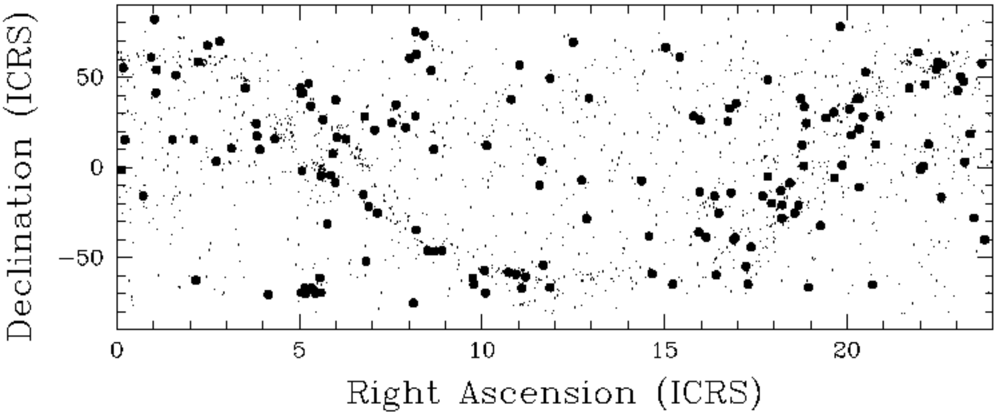

Figure A.3: Distribution in the sky of the sources in the catalogue. Variable sources (as per the criteria in Sect. A.4.4) are indicated with filled circles.

For the 88 stars found to be variable in the SW range, additional entries are provided in a supplementary catalogue (an excerpt is shown in Appendix A.B) with the FUV synthetic magnitude for each observation (see Sect. A.4.4). The following entries are provided:

- Object identification in the IUE Archive.
- Right Ascension and Declination (ICRS).
- Observation date and time.
- Synthetic FUV magnitude computed from the flux.
- Error in the synthetic FUV magnitude computed from the flux and error.

The catalogue contains synthetic FUV magnitudes for 1628 sources, ranging from FUV = 1.81 to FUV = 18.65. In the NUV band, the catalogue includes observations for 999 stars ranging from NUV = 3.34 to NUV= 17.74 mag. The distribution of sources in the sky is plotted in Figure A.3; we highlight the good coverage of the Galactic plane. A summary statistics of the catalogue contents is available in Table A.4. This work adds UV photometry for 1490 new sources, most of them hot (O-A spectral type) stars. The catalogue is available to the community through the services of the Centre de Données Stellaires.

A.7 Conclusions

From an initial sample of 31 982 stellar IUE spectra, we computed the synthetic photometry for:

- 1628 sources in the GALEX FUV band with magnitudes ranging from FUV = 1.81 to FUV = 18.65.
- 999 sources in the GALEX NUV band with NUV ranging from NUV = 3.34 to NUV = 17.74 mag.

The FUV and NUV synthetic photometry compares well with GALEX. A sample of WD's observed with IUE and GALEX were used for the test; a good agreement with CH was found for the FUV band but not for the NUV band.

The catalogue is available to the community through the services of the Centre de Données Stellaires. It adds UV photometry for 1490 new sources with respect to the GALEX AIS catalogue, most of them hot (O-A spectral type) stars. The sources in the catalogue are distributed over the full sky, including the Galactic plane.

A.A Catalogue excerpt

An excerpt (first ten entries) of the on-line catalogue is shown in Table A.5 (see Sect. A.6, for a detailed description of the fields).

A.B FUV magnitude - Variable stars

An excerpt (first ten entries) of the list of FUV magnitudes for variable stars is shown in Table A.6 (see Sect. A.6 for a description of the fields).

Table A.4: Catalogue contents

	IUE class	Number of stars		No. of IUE spectra used	
ID	description	All	in GALEX$^{(a)}$	SW	LW
10	WC	22	0	70	57
11	WN	38	0	165	49
12	Main Sequence O	106	1	150	**119**
13	Supergiant O	38	0	58	27
14	Oe	4	0	6	2
15	Of	10	0	19	5
16	SD O	68	29	176	457
17	WD O	15	5	20	62
20	B0-B2 V-IV	142	5	293	293
21	B3-B5 V-IV	68	1	87	110
22	B6-B9.5 V-IV	138	7	217	**136**
23	B0-B2 III-I	111	2	169	64
24	B3-B5 III-I	25	1	48	24
25	B6-B9.5 III-I	57	3	85	**42**
26	Be	28	1	67	92
27	Bp	36	2	63	57
28	sd B	36	15	39	27
29	WDB	13	7	46	32
30	A0-A3 V-IV	111	5	150	117
31	A4-A9 V-IV	28	2	32	21
32	A0-A3 III-I	25	2	31	17
33	A4-A9 III-I	17	2	20	8
34	Ae	4	1	55	4
35	Am	13	1	16	12
36	Ap	20	1	70	87
37	WDA	73	26	101	102
38	Horizontal Branch Stars	26	6	33	18
40	F0-F2	39	3	41	51
41	F3-F9	52	8	60	47
42	Fp	1	1	1	1
44	G IV-V	74	20	210	106
45	G III-I	40	7	66	37
46	K V-IV	50	14	323	112
47	K III-I	35	8	61	16
48	M V-IV	22	2	106	52
49	M III-I	15	5	35	16
50	R, N or S Types	7	4	9	6
51	Long Period Variable Stars	1	0	1	3
52	Irregular Variables	10	0	18	15
53	Regular Variables	30	10	24	104
54	Dwarf Novae	33	17	62	61
55	Classical Novae	21	3	39	51
58	T Tauri	20	5	30	96

(a) Identified by cross correlation with the GALEX AIS GR5 catalogue. A search radius of 3 arcsec is used.

Table A.5: Catalogue layout (ten first entries).

Object	RA(2000)	Dec(2000)	Nobs	FUV	$+e_{\mathrm{F}}$	$-e_{\mathrm{F}}$	Nobs	NUV	$+e_{\mathrm{N}}$	$-e_N$
	hh:mm:ss.ss	dd:mm:ss.ss	SWP		ABmag		LW		ABmag	
CD-40 15307	00:00:20.14	-39:23:55.24	1	10.143	0.003	-0.003	1	10.165	0.004	-0.004
WD 2357+296	00:00:7.25	+29:57:0.31	2	13.062	0.008	-0.008	0	NA	NA	NA
HD 225094	00:03:25.71	+63:38:25.88	3	8.811	0.002	-0.002	1	8.639	0.003	-0.003
HD 225132	00:03:44.39	-17:20:9.57	6	6.422	0.001	-0.001	1	6.082	0.002	-0.002
HD 108	00:06:3.39	+63:40:46.76	1	8.363	0.003	-0.003	0	NA	NA	NA
HD 186	00:06:47.96	+44:36:46.2	1	9.072	0.003	-0.003	1	9.213	0.004	-0.004
BD+59 2829	00:06:48.3	+60:36:0.83	1	11.846	0.003	-0.003	0	NA	NA	NA
PG 0004+133	00:07:33.78	+13:35:57.66	1	13.036	0.005	-0.005	1	13.276	0.007	-0.007
WD 0005+511	00:08:18.17	+51:23:16.6	1	11.092	0.003	-0.003	0	NA	NA	NA
HD 358	00:08:23.26	+29:05:25.55	1	3.193	0.003	-0.003	0	NA	NA	NA

Table A.6: FUV magnitude for variable stars layout (ten first entries).

Object	RA(ICRS)	Dec(ICRS)	Obsdate	Obstime	FUV	+eFUV	-eFUV
HD 352	00:08:12.1	-02:26:51.76	1985-08-02	10:10:00	15.020	0.010	-0.010
HD 352	00:08:12.1	-02:26:51.76	1981-05-20	02:02:03	14.345	0.004	-0.004
HD 352	00:08:12.1	-02:26:51.76	1984-06-14	02:06:56	15.186	0.008	-0.008
HD 5394	00:56:42.53	+60:43:0.27	1982-01-28	00:37:38	6.571	0.023	-0.023
HD 5394	00:56:42.53	+60:43:0.27	1988-07-10	13:18:22	1.899	0.002	-0.002
HD 5394	00:56:42.53	+60:43:0.27	1988-07-10	14:46:38	1.843	0.002	-0.002
HD 5679	01:02:18.45	+81:52:32.08	1978-05-15	17:07:54	9.457	0.003	-0.003
HD 5679	01:02:18.45	+81:52:32.08	1981-08-04	08:17:42	15.110	0.028	-0.027
V* RX And	01:04:35.54	+41:17:57.8	1980-02-09	04:05:26	14.019	0.007	-0.007
V* RX And	01:04:35.54	+41:17:57.8	1980-02-28	03:50:44	13.895	0.007	-0.007

B Python routine for dust charge distribution

In this Appendix, the implementation of the routine for the computation of a particle's charge described in Chapter 5, Sec. 5.1 is shown. It consists of a file with two classes, one for a dust grain and another for the gas, and another file with the main body of the problem. The input parameters are provided in a separated file, and an example is shown at the end of this chapter as a reference.

```
############################################################################
#                  File: dust_distribution_classes.py                      #
############################################################################
import numpy as np

# Global variables
e_1 = 4.8032e-10 # elementary charge
e_2 = 23.0708e-20 # squared elementary charge, in esu
h_planck = 6.6260755e-27 # Planck constant, erg s
erg_eV = 6.2415e+11 # conversion, 1erg = 6.2415e+11 eV
#

# # # # # # # # # # #
#    Dust Grain     #
# # # # # # # # # # #
class DustGrain:
        """
        Class that defines an interstellar dust grain. It will be determined by the radius,
        charge (Z) and composition (material). Given them, we can also set the Work Function,
        ionization potential, electron  affinity, minimum energy to produce a spontaneous
        detachment of an electron, and the photoelectric threshold frequency.
        Electron Affinity, Ionization Potential, and Emin are taken from Weingartner & Draine (2001)
        All units are given in CGS.
        Attributes:
                rad : radius (cm)
                Nc  : number of Carbon atoms (Eq. 1 of Weingartner et al. (2001)
                Z   : charge (dimensionless)
                material: either silicate or carbonnaceous
                W   : work function (erg)
                EA  : electron affinity (erg)
                IPv : ionization potential of the valence band (erg)
                Emin: minimum energy required for tunneling (erg)
                freq_phot: minimum frequency required to produce a photoelectron (Hz)
        """
        def __init__(self,rad,Z,material):
                """
                rad: float value, in microns. Has to be greater than 0.03 microns
                Z:   integer. Grain charge.
                material: string. Grain's composition. Must be silicate or carbonaceous.
                """
                global e_2, h_planck,erg_eV
                if rad >= 0.001:
                       self.rad = rad*1e-4 # We work in cgs
                       self.Nc = 468*np.power(self.rad/1e-7,3)
                else:
```

```
                        raise ValueError("Only grains with radius greater than 0.001 microns
are allowed")
                if isinstance(Z,int):
                        self.Z = Z
                else:
                        raise AttributeError("Dust Charge must be integer")
                self.material = material
                if self.material == "silicate":
                        self.W = 8*1.6021772e-12 # erg
                        self.EA = 3*1.6021772e-12+(self.Z-0.5)*e_2/self.rad # erg
                elif self.material == "carbonaceous":
                        self.W = 4.4*1.6021772e-12 # erg
                        self.EA = self.W + (self.Z-0.5)*e_2/self.rad -
                                e_2*4e-8/(self.rad*(self.rad+7e-8)) # erg
                else:
                        raise AttributeError("This material is not implemented")
                self.IPv = self.W + (self.Z + 0.5)*e_2/self.rad +
                        (self.Z+2)*e_2*0.3e-8/(self.rad**2)
                # Minimum energy required for tunneling Emin

                if self.Z >= -1:
                        self.Emin = 0
                else:
                        Emin = -(Z+1)*(e_2/rad)/(np.power(1+27e-8/rad,0.75))  # eV
                        self.Emin = Emin/erg_eV

                # Minimum frequency for photoelectric effect freq_phot
                self.freq_phot = (self.IPv + self.Emin)/h_planck # Hz




# # # # # # # # # # #
#       Gas         #
# # # # # # # # # # #
class Gas:
      """
      Class that defines the gas. It has to account for the composition of
      the gas (mainly hydrogen), as well as its density (cm-3), temperature,
      and ionization fraction.
      Attributes:
                comp: composition
                T   : temperature (K)
                dens: density (cm-3)
                ioniz_frac: ionization fraction
                max_freq: maximum frequency that can propagate through the gas (Hz)
                dneutral: density of neutral species (cm-3)
                dion    : ion density (cm-3)
                delec   : electron density (cm-3)
                ion_mass: mass of the ionic species (g)
                electron_mass: mass of an electron (g)
      """
      def __init__(self,comp,T,dens,ioniz_frac):
                if T < 0 or dens < 0 or ioniz_frac < 0:
                        raise ValueError("T/dens/ioniz_frac cannot be negative!")
                else:
                        if comp == "H":
                           self.comp = comp
                           self.T = T
                           self.dens = dens
```

```
                          self.ioniz_frac = ioniz_frac
                          self.dion = self.dens*self.ioniz_frac
                          self.dneutral = self.dens-self.dion
                          self.delec = self.dion # Atomic hydrogen only has one electron
                          self.ion_mass = 1.6726e-24 # mass of HII, g
                          self.elec_mass = 9.1094e-28 # mass of an electron, g
                          self.max_energy = 13.6 # Maximum energy of an electron that
                                          can propagate inside the gas, eV
                       elif comp == "H2+HCO+":
                          self.comp = comp
                          self.T = T
                          self.dens = dens
                          self.ioniz_frac = ioniz_frac
                          self.dion = self.dens*self.ioniz_frac # cm3
                          self.dneutral = self.dens-self.dion
                          self.delec = self.dion # as many electrons as HCO+ ions
                          self.ion_mass = 29*1.67e-24 # mass of HCO+, g
                          self.elec_mass = 9.1094e-28 # mass of an electron, g
                          self.max_energy = 13.6 # Maximum energy of an electron that
                                          can propagate inside the gas, eV
                       else:
                          raise Warning("Only pure hydrogen gas (H) or (H2+HCO+)
                          have been implemented up to now")
# -------------------------------------------------------

############################################################################
#                     File: dust_distribution_main.py                      #
############################################################################
from dust_distribution_classes import DustGrain, Gas
from scipy import integrate
from scipy.interpolate import interp1d
import numpy as np
import pandas as pd
import pickle
import matplotlib.pyplot as plt

k_bolt = 1.3807e-16 # Boltzmann's constant, erg/K
le = 10e-8 # Electron length, in cm.  Taken to be 10A.
e_2 = 23.0708e-20 # squared elementary charge, in esu
h_planck = 6.6260755e-27 # Planck constant, erg s
erg_eV = 6.2415e+11 # conversion, 1erg = 6.2415e+11 eV
speed_of_light = 2.99792458e+10 # Speed of light in vacuum, cm s-1

# # # # # # # # # # # # # # # # # # # #
#         Jion and Je           #
# # # # # # # # # # # # # # # # # # # #

def J_accretion(Grain,Gas,species):
      """
      Function that computes the ion/electron accretion rate of a given Grain in a given Gas.
               Input:
               Grain: DustGrain object
               Gas  : Gas object
               species: 1 for ions, -1 for electrons
      Output:
               Jspec: accretion rate for selected species
      """
      global k_bolt
      if species == 1:
               ni = Gas.dion
               vi = np.sqrt(8*k_bolt*Gas.T/(np.pi*Gas.ion_mass))
```

```
    elif species == -1:
            ni = Gas.delec
            vi = np.sqrt(8*k_bolt*Gas.T/(np.pi*Gas.elec_mass))
    else:
            raise ValueError("Species not available. Choose ions (1) or electrons (-1)")
    Jhat = get_Jhat(Grain,Gas,species)
    sticking_coeff = get_sticking_coeff(species,Grain)
    return ni*sticking_coeff*vi*np.pi*np.power(Grain.rad,2)*Jhat

def get_Jhat(Grain,Gas,species):
    """
    Function that computes the scaling coefficient Jhat, following Draine & Sutin (1987).
    We consider that ions are singly charged, because my initial problem only considers
    gas of purely H.
    Input:
            Grain: DustGrain object
            Gas: Gas object
    Output:
            Jhat: coefficient for computing the accretion rate
    """
    global e_2
    rel_ch = Grain.Z/species # Ze/qi = Z/+-1
    red_temp = Grain.rad*k_bolt*Gas.T/e_2 # Reduced temperature akT/(qi^2)
    if rel_ch == 0:
            Jhat = 1+np.sqrt(np.pi/(2*red_temp))
    elif rel_ch < 0:
            Jhat = (1-rel_ch/red_temp)*(1+np.sqrt(2/(red_temp-2*rel_ch)))
    else:
            xi = 1+np.power(3*rel_ch,-0.5)
            th = rel_ch/xi - 1/(2*np.power(xi,2)*(np.power(xi,2)-1))
            Jhat = np.square(1+np.power(4*red_temp+3*rel_ch,-0.5))*np.exp(-th/red_temp)
    return Jhat

def get_sticking_coeff(species,Grain):
    """
    Function that obtains the ion/electron sticking coefficient for a grain, following
    Weingartner & Draine (2001)
    We assume that ions, if they eventually collide, will always stick.
    Electron sticking will obey formulae (28-29-30)
    Input:
            species: index of species. -1 electron, 1 ion
            Grain: DustGrain object
    Output:
            sticking_prob: sticking probability. Floating between 0 and 1, near 0.5.
    """
    global le
    if species == 1:
            sticking_prob = 1
    else:
            if Grain.Z <= 0:
                    sticking_prob = 0.5*(1-np.exp(-Grain.rad/le))/(1+np.exp(20-Grain.Nc))
            else:
                    sticking_prob = 0.5*(1-np.exp(-Grain.rad/le))
    return sticking_prob


# # # # # # # # # # # # # # # # # # #
#  Interstellar Radiation Field   #
#  Mathis, Mezger & Panagia 1983  #
# # # # # # # # # # # # # # # # # # #
```

```
def MMP83(freq):
      """
      Interstellar radiation field by Mathis, Mezger & Panagia (1983) with
      weights corrected as in Draine (2011).
      Input:
               freq: frequency desired (Hz)
      Output:
               freq*rad_dens: radiation density (erg cm-3)
      """
      global h_planck
      global erg_eV
      global speed_of_light
      energy_eV = freq*h_planck*erg_eV
      if  energy_eV >= 13.6:
               return 0
      elif energy_eV < 13.6 and energy_eV >= 11.2:
               return 3.328e-9*np.power(energy_eV,-4.4172)
      elif energy_eV < 11.2 and energy_eV >= 9.26:
               return 8.463e-13*np.power(energy_eV,-1)
      elif energy_eV < 9.26 and energy_eV >= 5.04:
               return 2.005e-14*np.power(energy_eV,0.6678)
      else:
               return 1e-14*bb_edens(freq,7500)+1.65e -
                      13*bb_edens(freq,4000)+7e-13*bb_edens(freq,3000)

def bb_edens(freq,T):
      """
      Formula of the Planck's BlackBody spectrum's energy density in frequencies.
      Input:
               freq: frequency (Hz)
               T: temperature (K)
      Output:
               rad_dens: radiation density (ergs cm-3)
      """
      global h_planck
      global speed_of_light
      global k_bolt
      num = 8*np.pi*np.power(freq,4)*h_planck
      denom = np.power(speed_of_light,3)*(np.exp(h_planck*freq/(k_bolt*T))-1)
      return num/denom



# # # # # # # # # # # # # # # # # # #
#      Jpe conduction term       #
# # # # # # # # # # # # # # # # # # #

def Jpe_cond(Grain,Gas,ISRF):
      """
      Photoelectric rate corresponding to photodetachment of conduction electrons.
      It depends on the photodetachment cross section.
      Input:
               Grain: DustGrain object
               Gas:   Gas object
      Output:
               Jpe_cond: photodetachment rate of the conduction band
      """
      global h_planck, speed_of_light
      global erg_eV
      if Grain.Z >= 0:
               return 0
```

```
      else:
               freq_max = Gas.max_energy/erg_eV/h_planck
               freq_pdt = get_freq_pdt(Grain)
               f = lambda nu: speed_of_light*sigma_pdt(Grain,nu)*ISRF(nu)/
                                       (h_planck*np.square(nu))
               return integrate.quad(f,freq_pdt,freq_max)[0]

def sigma_pdt(Grain,freq):
      """
      Function that returns the photodetachment cross section of a negatively charged grain.
      We use Eq. 20 from Weingartner & Draine (2001)
      Input:
               freq: frequency of the photon (erg)
      Output:
               sigma_pdt: photodetachment cross section
      """
      global h_planck
      freq_pdt = get_freq_pdt(Grain)
      x = h_planck*(freq-freq_pdt)/(3/erg_eV)
      return 1.2e-17*np.absolute(Grain.Z)*x/np.square(1+np.square(x)/3)

def get_freq_pdt(Grain):
      """
      Function that obtains the minimum frequency required for photodetachment to occur.
      Eq. 18 from Weingartner & Draine (2001)
      Input:
               Grain: DustGrain object
      Output:
               freq_pdt: minimum frequency (Hz)
      """
      global h_planck
      Grain_aux = DustGrain(Grain.rad*1e4,Grain.Z + 1, Grain.material)
      return (Grain_aux.EA + Grain.Emin)/h_planck

# # # # # # # # # # # # # # # # # #
#         Jpe valence term        #
# # # # # # # # # # # # # # # # # #

def Jpe_val(Grain,Gas,f_lin,f_spline,Qabs_fun,ISRF):
      """
      Photoelectric rate corresponding to photoelectric effect of valence electrons.
      It depends on the absorption coefficiency, photoelectric yield and radiation field.
      Input:
               Grain: DustGrain object
               Gas: Gas object
      Output:
               Jpe_val: rate of valence photoelectrons released
      """
      global h_planck
      global erg_eV,speed_of_light
      freq_max = Gas.max_energy/erg_eV/h_planck
      freq_pet = get_freq_pet(Grain)
      f = lambda nu: speed_of_light*ISRF(nu)*Qabs_fun(speed_of_light*1e4/nu)*
              PhotYield(Grain,nu,freq_pet,f_lin,f_spline)/(h_planck*np.square(nu))
      x = np.linspace(freq_pet,freq_max,num=2000)
      y = np.zeros(len(x))
      i = 0
      while i < len(x):
               y[i] = f(x[i])
               i += 1
      return np.pi*np.square(Grain.rad)*integrate.trapz(y,x)
```

```
def Qabs(material,rad):
      """
      Absorption coefficient of a dust grain at a given frequency.
      Absorption properties vary with material and wavelength, and it is necessary to have
      precise measures.
      Here I use  the tables provided by Draine in his webpage to compute a function that
      will return the refractive index.
      Input:
               material: grain material
               radius: dust grain radius, in microns
      Output:
               Qabs_fun: absorption coefficient function, dependent on the wavelength in microns
      """
      if material == "silicate":
               data = pd.read_csv("Qabs_Sil_81")
      else: # material == "carbonaceous"
               data = pd.read_csv("Qabs_Gra_81")

      if rad >= 1e-3 and rad <=10: # Values taken from Qabs_Sil_81 and Qabs_Gra_81
               kw = list(data.columns.values)
               i = 0
               available_rads = []
               while i < len(kw):
                     if "=" in kw[i]:
                            line = kw[i].split("=")
                            available_rads.append(float(line[1]))
                     i+=1
               ldo = pd.to_numeric(data['wav_microns'])
               if rad in available_rads:
                     ind = available_rads.index(rad)
                     Qabs = data[kw[ind+1]]
               else:
                     first_elem = next(x[0] for x in enumerate(available_rads) if x[1]>rad)
                     rad_low = available_rads[first_elem-1]
                     Q_low = data[kw[first_elem]]
                     rad_up = available_rads[first_elem]
                     Q_up = data[kw[first_elem+1]]
                     # Build Qabs from a linear interpolation between
                     upper and lower values
                     slp = (Q_up-Q_low)/(rad_up-rad_low)
                     Qabs = (rad-rad_low)*slp + Q_low
      else:
               raise ValueError("Absorption coefficient Qabs cannot be computed at that radius")

      return interp1d(ldo,Qabs,kind='linear')

def get_freq_pet(Grain):
      """
      This function returns the photoelectric threshold frequency for a given grain.
      Input:
               Grain: DustGrain object
      Output:
               freq_pet: photoelectric threshold (erg)
      """
      global h_planck
      if Grain.Z >= -1:
               return Grain.IPv/h_planck
      else:
```

```
		return (Grain.IPv + Grain.Emin)/h_planck

def PhotYield(Grain,freq,freq_pet,f_lin,f_spline):
	"""
	This function computes the photoelectric yield. It is the probability that a
	photoelectron is emitted.
	Input:
		Grain: Dust Grain object
		freq_pet: photoelectric threshold
		freq:  frequency (erg)
	Output:
		phot_yield: photoelectric yield
	"""
	global h_planck, e_2
	# y0 depends on an additional parameter theta
	if Grain.Z >= 0:
		theta = h_planck*(freq-freq_pet) +  (Grain.Z+1)*e_2/Grain.rad
	else:
		theta = h_planck*(freq-freq_pet)
	return y2(Grain,freq,freq_pet)*min(y0(Grain,theta)*y1(Grain,freq,f_lin,f_spline),1)


def y0(Grain,theta):
	"""
	Parameter needed to compute the fraction of electrons that are converted
	into photoelectrons. It depends on the Grain charge and the material.
	Input:
		Grain: Dust Grain object
		theta: parameter (erg)
	Output:
		y0: charge factor of the photoelectric yield
	"""
	if Grain.material == "silicate":
		y0 = 0.5*(theta/Grain.W)/(1+5*theta/Grain.W)
	else: # Carbonaceous
		y0 = 9e-3*np.power(theta/Grain.W,5)/(1+3.7e-2*np.power(theta/Grain.W,5))
	return y0


def y2(Grain,freq,freq_pet):
	"""
	Parameter that accounts for the fraction of attempting electrons that finally escapes.
	Computed using Eq. 11 by Weingartner & Draine (2001).
	Input:
		Grain: DustGrain object
		freq: frequency (Hz)
		freq_pet: photoelectric threshold frequency (Hz)
	Output:
		y2: fraction of attempting electrons that escapes.
	"""
	global h_planck, e_2
	if Grain.Z >= 0:
		Ehigh = h_planck*(freq-freq_pet)
		Elow =  -(Grain.Z+1)*e_2/Grain.rad
		return np.square(Ehigh)*(Ehigh-3*Elow)/np.power(Ehigh-Elow,3)
	else:
		return 1
```

```
def y1(Grain,freq,f_lin,f_spline):
      """
      Parameter needed to compute the fraction of electrons that are converted
      into photoelectrons.
      It accounts for a geometric factor. Depends on the grain radius and material.
      It is assumed that the escape length of electrons is 10A.
      It is also assumed that the photon attenuation length depends on a refractive
      index computed by Draine.
      Computed using Eq. 13 by Weingartner & Draine (2001).
      Input:
              Grain: DustGrain object
              freq: frequency (Hz)
      Output:
              y1: geometric factor of the photoelectric yield
      """
      la = get_attenuation_length(Grain,freq,f_lin,f_spline) # Photon attenuation length, cm
      le = 10e-8 # Electron escape length, 10 A, in cm
      alpha = Grain.rad/la + Grain.rad/le
      beta = Grain.rad/la
      return np.square(beta/alpha)*(np.square(alpha)-2*alpha+2-2*np.exp(-alpha))/
             (np.square(beta)-2*beta+2-2*np.exp(-beta))

def get_attenuation_length(Grain,freq,f_lin,f_spline):
      """
      This function return the attenuation length at a given frequency. We will use the
      refractive indexes given by Draine
      in https://www.astro.princeton.edu/~draine/dust/dust.diel.html
      Dust grains can be astrosilicates or carbonaceous, and the latter type is further
      subdivided into graphitic grains and PAHs.
      For the time being, I limit myself to astrosilicates. Graphite has been included
      under the tag 'carbonaceous'
      (12/10/2020).
      Input:
              Grain: DustGrain object
              freq: frequency (Hz)
      Output:
              la: attenuation length (cm)
      """
      global speed_of_light

      # We are interested in columns 0 and 4, named 'wave(um)' and 'Im(n)', respectively.
      # We are working with UV radiation, so I will consider only refractive index data with
      # wavelengths between 0 and 1 microns.
      lam = (speed_of_light/freq)*1e4 # Desired frequency is converted to wavelength in microns
      if Grain.material == "carbonaceous":
              # 1/3 - 2/3 approximation
              Im_n = get_Im_n(lam,f_lin[0],f_spline[0])/3 + get_Im_n(lam,f_lin[1],f_spline[1])*2/3
      else:
              Im_n = get_Im_n(lam,f_lin,f_spline)
      return lam*1e-4/(4*np.pi*Im_n)

def get_Im_n(lam,f_lin,f_spline):
      """
      Function that computes the refractive index at a given wavelength.
      It will only work properly for wavelengths lower than 1 micron.
      This function has only been tested for astrosilicate's refractive index.
      Input:
              lam: wavelength (microns)
      Output:
              Im_n: imaginary part of the refractive index
      """
```

```
      if lam <= 0.2:
               return  f_spline(lam)
      elif lam > 0.2: #and lam < 1:
               return f_lin(lam)
      else:
               raise ValueError("The frequency given corresponds to a wavelength
                                 greater than 1 micron")


# # # # # # # # # # # # # # # # # #
#         Read Input file         #
# # # # # # # # # # # # # # # # # #
def read_input_file():
      """
      Function that reads the parameters needed to perform the simulation.
      We need dust properties, gas properties, and a radiation field.
      Output:
               param: dictionary containing the data.
      """
      param = {}
      floats_are = ['rad','dens','frac_ion','rf_intensity']
      ints_are = ['Z0','Zmin','Zmax','T','rf']
      with open('DD_input_file.txt') as input_file:
               for line in input_file:
                   if "#" not in line and len(line)>1:
                          new_line = line.rstrip().replace(" ","").split("=")
                          if new_line[0] in floats_are:
                                         param[new_line[0]] = float(new_line[1])
                          elif new_line[0] in ints_are:
                                         param[new_line[0]] = int(new_line[1])
                          else:
                                         param[new_line[0]] = new_line[1]
      return(param)



# # # # # # # # # # # # # # # # # #
#      Charge distribution        #
# # # # # # # # # # # # # # # # # #
def dust_charge_distribution(Gas,rad,Z0,material,Zmin,Zmax,f_lin,f_spline,Qabs_fun,ISRF):
      """
      Program that computes the charge distribution of a population of dust grains
      in the interval [Zmin,Zmax].
      It applies recursively equation 21 from Weingartner & Draine 2001.
      Input:
               ISRF: interstellar radiation field
      Output:
               probabilities: array containing the probabilities for each value Z,
                              ordered with increasing Z.
      """
      prob_neg = np.array([1])
      prob_pos = np.array([1])
      Z = Z0 + 1
      while Z <= Zmax:
               J_pe = Jpe_val(DustGrain(rad,Z-1,material),Gas,f_lin,f_spline,Qabs_fun,ISRF)
                    + Jpe_cond(DustGrain(rad,Z-1,material),Gas,ISRF)
               J_ion = J_accretion(DustGrain(rad,Z-1,material),Gas,1)
               J_electron = J_accretion(DustGrain(rad,Z,material),Gas,-1)
               prob_pos = np.append(prob_pos,(J_pe+J_ion)*prob_pos[Z-Z0-1]/J_electron)
               Z +=1
      Z = Z0 - 1
```

```
      while Z >= Zmin:
               J_pe = Jpe_val(DustGrain(rad,Z,material),Gas,f_lin,f_spline,Qabs_fun,ISRF)
                    + Jpe_cond(DustGrain(rad,Z,material),Gas,ISRF)
               J_ion = J_accretion(DustGrain(rad,Z,material),Gas,1)
               J_electron = J_accretion(DustGrain(rad,Z+1,material),Gas,-1)
               prob_neg = np.append(prob_neg,prob_neg[Z0-Z-1]*J_electron/(J_pe+J_ion))
               Z-=1
      dust_distrib = np.delete(prob_neg,0)
      dust_distrib = dust_distrib[::-1]
      dust_distrib = np.append(dust_distrib,prob_pos)
      dust_distrib = dust_distrib/sum(dust_distrib)
      return dust_distrib

def main():
      """
      Main function that computes the charge probability distribution of a given population
      of dust grains.
      It reads the input from an input file, DD_input_file.txt.
      Output:
               dust_distrib.txt: file containing the values of Z with the corresponding
               probability
      """
      # read input data
      model_data = read_input_file()
      # Refractive index functions. In this way, I only compute them once.
      # It is necessary that the wavelength cut is set to 1 micron if we want to use
      spline interpolation
      # at short wavelengths. If you change it, be careful and check that your interpolation
      is not noisy.
      # See get_Im_n for more information.
      if model_data['material'] == "silicate":
               data = pd.read_csv('silicate_refractive_indexes.csv',comment="#",sep="\t")
               uv_cols = data['wave(um)']< 1 # Wavelengths lower than 1 micron
               x = data['wave(um)'][uv_cols]
               y = data['Im(n)'][uv_cols]
               f_lin = interp1d(x,y,kind="linear")
               f_spline = interp1d(x,y,kind="cubic")
      else:
               # Parallel
               data_para = pd.read_csv('graphite_refractive_indexes_para.csv',comment="#",sep="\t")
               uv_cols = data_para['wave(um)']< 1 # Wavelengths lower than 1 micron
               x_para = data_para['wave(um)'][uv_cols]
               y_para = data_para['Im(n)'][uv_cols]
               # Perpendicular
               data_perp = pd.read_csv('graphite_refractive_indexes_perp.csv',comment="#",sep="\t")
               uv_cols = data_perp['wave(um)']< 1 # Wavelengths lower than 1 micron
               x_perp = data_perp['wave(um)'][uv_cols]
               y_perp = data_perp['Im(n)'][uv_cols]
               # 1/3 - 2/3 approximation -> list
               f_lin = [interp1d(x_para,y_para,kind="linear"),interp1d(x_perp,y_perp,kind="linear")]
               f_spline = [interp1d(x_para,y_para,kind="cubic"),interp1d(x_perp,y_perp,kind="cubic")]
      # Absorption coefficient function must be defined before the main loop because in that way,
            it will be computed
      # only once, being more efficient.
      Qabs_fun = Qabs(model_data['material'],model_data['rad'])
      #GAS
      gas = Gas(model_data["composition"],model_data["T"],model_data["dens"],model_data["frac_ion"])
      # ISRF
      if model_data["rf"] == 1:
               ISRF = lambda nu: model_data["rf_intensity"]*MMP83(nu)
      else:
```

```
            raise ValueError("Only MMP83 radiation field has been implemented up to now.")

    # Main Body
    probabilities = dust_charge_distribution(gas,model_data["rad"],model_data["Z0"],
         model_data["material"],model_data["Zmin"],model_data["Zmax"],f_lin,f_spline,
         Qabs_fun,ISRF)
    Z_values = np.arange(model_data["Zmin"],model_data["Zmax"]+1)
    df = pd.DataFrame.from_dict({"Z":Z_values,"prob":probabilities})
    df.to_csv('DustCharge_Distribution.txt',sep="\t",index=False)
    fig = plt.figure()
    plt.plot(Z_values,probabilities,lw=2,color='b')
    plt.xlabel('Z')
    plt.ylabel('f(Z)')
    plt.title("Dust grain "+str(model_data["rad"])+" microns")
    plt.tight_layout()
    fig.savefig("Probabilities.eps")
    plt.close(fig)
    print("Chimpún")
```

```
############################################################################
#                        File: DD_input_file.txt                           #
############################################################################
# Input file to compute the distribution of Dust Grain Charges.
# Read carefully the instructions given below.
#
#                  GRAIN PROPERTIES
#
# rad: dust grain radius in microns
# material: grain material, either "silicate" or "carbonnaceous"
# Z0: reference charge. By default use Z0 = 0.
# Zmin: minimum charge desired.
# Zmax: maximum charge desired.
rad = 0.005
material = silicate
Z0 = 0
Zmin = -10
Zmax = 5
#                  GAS PROPERTIES
# composition: Gas composition. By default is set to H
# T: temperature in K
# dens: density in cm-3
# frac_ion: ionization fraction
composition = H
T = 6000
dens = 10
frac_ion = 0.1
#                  RADIATION FIELD
# rf: radiation field selected. 1 = MMP83
# rf_intensity: intensity of the radiation field, between 0 and 1.
rf = 1
rf_intensity = 1
```

Bibliography

Akshaya, M. S, Murthy, J, Ravichandran, S, Henry, R. C, & Overduin, J. The Diffuse Radiation Field at High Galactic Latitudes. *ApJ*, 858(2):101, May 2018. doi: 10.3847/1538-4357/aabcb9.

Aller, L. H, Keyes, C. D, Ross, J. E, & Omara, B. J. An analysis of the planetary nebula NGC 2867. *MNRAS*, 197:647–658, November 1981. doi: 10.1093/mnras/197.3.647.

Andrae, R, Fouesneau, M, Creevey, O, Ordenovic, C, Mary, N, et al. Gaia Data Release 2. First stellar parameters from Apsis. *A&A*, 616:A8, August 2018. doi: 10.1051/0004-6361/201732516.

André, P, Di Francesco, J, Ward-Thompson, D, Inutsuka, S. I, Pudritz, R. E, et al. From Filamentary Networks to Dense Cores in Molecular Clouds: Toward a New Paradigm for Star Formation. In Beuther, H, Klessen, R. S, Dullemond, C. P, & Henning, T, editors, *Protostars and Planets VI*, page 27, January 2014. doi: 10.2458/azu_uapress_9780816531240-ch002.

André, P, Men'shchikov, A, Bontemps, S, Könyves, V, Motte, F, et al. From filamentary clouds to prestellar cores to the stellar IMF: Initial highlights from the Herschel Gould Belt Survey. *A&A*, 518:L102, July 2010. doi: 10.1051/0004-6361/201014666.

Armengot, M & Gómez de Castro, A. I. Signatures of diffuse interstellar gas in the Galaxy Evolution Explorer all-sky survey. *A&A*, 631:A59, November 2019. doi: 10.1051/0004-6361/201833808.

Armengot, M, Sánchez, N, López-Santiago, J, & Gómez de Castro, A. I. MOSAIX: a tool to built large mosaics from GALEX images. *Ap&SS*, 354(1):113–119, November 2014. doi: 10.1007/s10509-014-1997-5.

Arulanantham, N, France, K, Hoadley, K, Manara, C. F, Schneider, P. C, et al. A UV-to-NIR Study of Molecular Gas in the Dust Cavity around RY Lupi. *ApJ*, 855(2):98, March 2018. doi: 10.3847/1538-4357/aaaf65.

Arulanantham, N, France, K, Cazzoletti, P, Miotello, A, Manara, C. F, et al. Probing UV-sensitive Pathways for CN and HCN Formation in Protoplanetary Disks with the Hubble Space Telescope. *AJ*, 159(4):168, April 2020. doi: 10.3847/1538-3881/ab789a.

Arzoumanian, D, André, P, Didelon, P, Könyves, V, Schneider, N, et al. Characterizing interstellar filaments with Herschel in IC 5146. *A&A*, 529:L6, May 2011. doi: 10.1051/0004-6361/201116596.

Astrophysics Source Code Library. Astrophysics Source Code Library. `https://ascl.net/`, 1999.

Audit, E & Hennebelle, P. Thermal condensation in a turbulent atomic hydrogen flow. *A&A*, 433(1):1–13, April 2005. doi: 10.1051/0004-6361:20041474.

Bai, X.-N & Stone, J. M. Particle-gas Dynamics with Athena: Method and Convergence. *ApJS*, 190(2):297–310, Oct 2010. doi: 10.1088/0067-0049/190/2/297.

Bai, X.-N & Stone, J. M. Effect of Ambipolar Diffusion on the Nonlinear Evolution of Magnetorotational Instability in Weakly Ionized Disks. *ApJ*, 736(2):144, August 2011. doi: 10.1088/0004-637X/736/2/144.

Bakes, E. L. O & Tielens, A. G. G. M. The Photoelectric Heating Mechanism for Very Small Graphitic Grains and Polycyclic Aromatic Hydrocarbons. *ApJ*, 427:822, June 1994. doi: 10.1086/174188.

Ballesteros-Paredes, J, André, P, Hennebelle, P, Klessen, R. S, Kruijssen, J. M. D, et al. From Diffuse Gas to Dense Molecular Cloud Cores. *SSRv*, 216(5):76, June 2020. doi: 10.1007/s11214-020-00698-3.

Bally, J, Langer, W. D, Stark, A. A, & Wilson, R. W. Filamentary Structure in the Orion Molecular Cloud. *ApJL*, 312:L45, January 1987. doi: 10.1086/184817.

Barnard, E. E. The great photographic nebula of Orion, encircling the belt and theta nebula. *Popular Astronomy*, 2:151–154, January 1894.

Barstow, M. A, Boyce, D. D, Welsh, B. Y, Lallement, R, Barstow, J. K, et al. O VI in the Local Interstellar Medium. *ApJ*, 723(2):1762–1786, November 2010. doi: 10.1088/0004-637X/723/2/1762.

Barstow, M. A, Casewell, S. L, Holberg, J. B, & Kowalski, M. P. The status and future of EUV astronomy. *Advances in Space Research*, 53(6):1003–1013, March 2014. doi: 10.1016/j.asr.2013.08.007.

Basu, S & Mouschovias, T. C. Magnetic Braking, Ambipolar Diffusion, and the Formation of Cloud Cores and Protostars. III. Effect of the Initial Mass-to-Flux Ratio. *ApJ*, 453:271, November 1995. doi: 10.1086/176387.

Battisti, A. J, Calzetti, D, & Chary, R. R. Characterizing Dust Attenuation in Local Star-forming Galaxies: UV and Optical Reddening. *ApJ*, 818(1):13, February 2016. doi: 10.3847/0004-637X/818/1/13.

Battisti, A. J, Calzetti, D, & Chary, R. R. Characterizing Dust Attenuation in Local Star-forming Galaxies: Inclination Effects and the 2175 Å Feature. *ApJ*, 851(2):90, December 2017. doi: 10.3847/1538-4357/aa9a43.

Beckwith, K & Stone, J. M. A Second-order Godunov Method for Multi-dimensional Relativistic Magnetohydrodynamics. *ApJS*, 193(1):6, March 2011. doi: 10.1088/0067-0049/193/1/6.

Beitia-Antero, L & Gómez de Castro, A. I. Interstellar extinction in Orion: variation of the strength of the ultraviolet bump across the complex. *MNRAS*, 469(3):2531–2538, August 2017. doi: 10.1093/mnras/stx881.

Beitia-Antero, L, Gómez de Castro, A. I, & Vallejo, J. C. Formation of Dust Filaments in the Diffuse Envelopes of Molecular Clouds. *ApJ*, 908(1):112, February 2021. doi: 10.3847/1538-4357/abcda1.

Benvenuti, P, Dodorico, S, & Dopita, M. A. UV spectrum of supernova remnant reveals carbon depletion in the interstellar medium. *Natur*, 277:99–102, January 1979. doi: 10.1038/277099a0.

Berghöfer, T. W, Bowyer, S, Lieu, R, & Knude, J. The Thermal Pressure of the Hot Interstellar Medium Derived from Cloud Shadows in the Extreme Ultraviolet. *ApJ*, 500(2):838–846, June 1998. doi: 10.1086/305745.

Bianchi, L, Herald, J, Efremova, B, Girardi, L, Zabot, A, et al. GALEX catalogs of UV sources: statistical properties and sample science applications: hot white dwarfs in the Milky Way. *Ap&SS*, 335(1):161–169, September 2011a. doi: 10.1007/s10509-010-0581-x.

Bianchi, L. The Galaxy Evolution Explorer (GALEX). Its legacy of UV surveys, and science highlights. *Ap&SS*, 354(1):103–112, November 2014. doi: 10.1007/s10509-014-1935-6.

Bianchi, L, Efremova, B, Herald, J, Girardi, L, Zabot, A, et al. Catalogues of hot white dwarfs in the Milky Way from GALEX's ultraviolet sky surveys: constraining stellar evolution. *MNRAS*, 411(4):2770–2791, March 2011b. doi: 10.1111/j.1365-2966.2010.17890.x.

Bianchi, L, Conti, A, & Shiao, B. The ultraviolet sky: An overview from the GALEX surveys. *Advances in Space Research*, 53(6):900–912, March 2014. doi: 10.1016/j.asr.2013.07.045.

Bianchi, S & Schneider, R. Dust formation and survival in supernova ejecta. *MNRAS*, 378(3): 973–982, July 2007. doi: 10.1111/j.1365-2966.2007.11829.x.

Black, J. H. The physical state of primordial intergalactic clouds. *MNRAS*, 197:553–563, November 1981. doi: 10.1093/mnras/197.3.553.

Blandford, R & Eichler, D. Particle acceleration at astrophysical shocks: A theory of cosmic ray origin. *PhR*, 154(1):1–75, October 1987. doi: 10.1016/0370-1573(87)90134-7.

Bless, R. C & Savage, B. D. Ultraviolet Photometry from the Orbiting Astronomical Observatory. II. Interstellar Extinction. *ApJ*, 171:293, February 1972. doi: 10.1086/151282.

Blitz, L & Shu, F. H. The origin and lifetime of giant molecular cloud complexes. *ApJ*, 238: 148–157, May 1980. doi: 10.1086/157968.

Blitz, L & Thaddeus, P. Giant molecular complexes and OB associations. I. The Rosette molecular complex. *ApJ*, 241:676–696, October 1980. doi: 10.1086/158379.

Blitz, L, Fukui, Y, Kawamura, A, Leroy, A, Mizuno, N, et al. Giant Molecular Clouds in Local Group Galaxies. In Reipurth, B, Jewitt, D, & Keil, K, editors, *Protostars and Planets V*, page 81, January 2007.

Blustin, A. J, Landsman, W. B, Still, M, Rosen, S. R, Page, M. J, et al. High Spatial Resolution Mapping of Extinction in the SMC with the Swift-UVOT. In Wilson, A, editor, *The X-ray Universe 2005*, volume 604 of *ESA Special Publication*, page 69, January 2006.

Bocchio, M, Micelotta, E. R, Gautier, A. L, & Jones, A. P. Small hydrocarbon particle erosion in a hot gas. A comparative study. *A&A*, 545:A124, September 2012. doi: 10.1051/0004-6361/201219705.

Boggess, A, Carr, F. A, Evans, D. C, Fischel, D, Freeman, H. R, et al. The IUE spacecraft and instrumentation. *Natur*, 275(5679):372–377, October 1978. doi: 10.1038/275372a0.

Bohlin, R. C. Copernicus observations of interstellar absorption at Lyman Alpha. *ApJ*, 200: 402–414, September 1975. doi: 10.1086/153803.

Bohlin, R. C, Savage, B. D, & Drake, J. F. A survey of interstellar H I from Lalpha absorption measurements. II. *ApJ*, 224:132–142, August 1978. doi: 10.1086/156357.

Bohlin, R. C, Holm, A. V, Savage, B. D, Snijders, M. A. J, & Sparks, W. M. Photometric calibration of the international ultraviolet explorer (IUE) : low dispersion. *A&A*, 85:1–13, May 1980.

Bohlin, R. C & Bianchi, L. A Correction for GALEX Spectroscopic UV Flux Distributions from Comparisons with CALSPEC and IUE. *AJ*, 157(3):107, March 2019. doi: 10.3847/1538-3881/aafdb8.

Bohm, K. H & Bohm-Vitense, E. The ultraviolet spectrum of a strongly reddened, high-excitation Herbig-Haro object. *ApJ*, 277:216–219, February 1984. doi: 10.1086/161686.

Bok, B. J & Cordwell, C. S. A Study of Dark Nebulae. In Gordon, M. A & Snyder, L. E, editors, *Molecules in the Galactic Environment*, page 54, January 1973.

Boksenberg, A, Evans, R. G, Fowler, R. G, Gardner, I. S. K, Houziaux, L, et al. The ultraviolet sky-survey telescope in the TD-IA satellite. *MNRAS*, 163:291, January 1973. doi: 10.1093/mnras/163.3.291.

Bonnarel, F, Fernique, P, Bienaymé, O, Egret, D, Genova, F, et al. The ALADIN interactive sky atlas. A reference tool for identification of astronomical sources. *A&AS*, 143:33–40, April 2000. doi: 10.1051/aas:2000331.

Bonnell, I. A, Clarke, C. J, Bate, M. R, & Pringle, J. E. Accretion in stellar clusters and the initial mass function. *MNRAS*, 324(3):573–579, June 2001. doi: 10.1046/j.1365-8711.2001.04311.x.

Boris, J. Relativistic plasma simulation. In *Proc. Fourth Conf. on Numerical Simulation of Plasmas (Washington, DC: Naval Research Lab), 3*, 1970.

Boulanger, F, Abergel, A, Bernard, J. P, Burton, W. B, Desert, F. X, et al. The dust/gas correlation at high Galactic latitude. *A&A*, 312:256–262, August 1996.

Bowyer, S & Malina, R. F. The extreme ultraviolet explorer mission. *Advances in Space Research*, 11(11):205–215, January 1991. doi: 10.1016/0273-1177(91)90077-W.

Brandenburg, A & Dobler, W. Hydromagnetic turbulence in computer simulations. *Computer Physics Communications*, 147(1-2):471–475, Aug 2002. doi: 10.1016/S0010-4655(02)00334-X.

Bronaugh, D & Werner, A. *zyp: Zhang + Yue-Pilon trends package*, 2013. URL `https://CRAN.R-project.org/package=zyp`. R package version 0.10-1.

Brown, P. J, Smitka, M. T, Wang, L, Breeveld, A, de Pasquale, M, et al. Swift Ultraviolet Observations of Supernova 2014J in M82: Large Extinction from Interstellar Dust. *ApJ*, 805 (1):74, May 2015. doi: 10.1088/0004-637X/805/1/74.

Bruhweiler, F. C & Kondo, Y. The UV spectra of nearby white dwarfs and the nature of the local interstellar medium. *ApJ*, 259:232–243, August 1982. doi: 10.1086/160163.

Burton, M. G, Hollenbach, D. J, & Tielens, A. G. G. M. Line Emission from Clumpy Photodissociation Regions. *ApJ*, 365:620, December 1990. doi: 10.1086/169516.

Camarota, L & Holberg, J. B. White-dwarf-based evaluation of the GALEX absolute calibration. *MNRAS*, 438(4):3111–3118, March 2014. doi: 10.1093/mnras/stt2422.

Cambrésy, L, Marton, G, Feher, O, Tóth, L. V, & Schneider, N. Young stellar clusters in the Rosette molecular cloud. Arguments against triggered star formation. *A&A*, 557:A29, September 2013. doi: 10.1051/0004-6361/201321235.

Cardelli, J. A. The Abundance of Heavy Elements in Interstellar Gas. *Science*, 265(5169): 209–213, July 1994. doi: 10.1126/science.265.5169.209.

Cardelli, J. A, Clayton, G. C, & Mathis, J. S. The Relationship between Infrared, Optical, and Ultraviolet Extinction. *ApJ*, 345:245, October 1989. doi: 10.1086/167900.

Carroll, J. J, Frank, A, Blackman, E. G, Cunningham, A. J, & Quillen, A. C. Outflow-Driven Turbulence in Molecular Clouds. *ApJ*, 695(2):1376–1381, April 2009. doi: 10.1088/0004-637X/695/2/1376.

Carruthers, G. R. Rocket Observation of Interstellar Molecular Hydrogen. *ApJL*, 161:L81, August 1970. doi: 10.1086/180575.

Cassinelli, J. P, Cohen, D. H, Macfarlane, J. J, Drew, J. E, Lynas-Gray, A. E, et al. EUVE Spectroscopy of epsilon Canis Majoris (B2 II) from 70 to 730 Angstrom. *ApJ*, 438:932, January 1995. doi: 10.1086/175135.

Cazaux, S & Tielens, A. G. G. M. H_2 Formation on Grain Surfaces. *ApJ*, 604(1):222–237, 2004. doi: 10.1086/381775.

Cen, R. A Hydrodynamic Approach to Cosmology: Methodology. *ApJS*, 78:341, February 1992. doi: 10.1086/191630.

Chabrier, G. Galactic Stellar and Substellar Initial Mass Function. *PASP*, 115(809):763–795, July 2003. doi: 10.1086/376392.

Chen, B. Q, Liu, X. W, Yuan, H. B, Huang, Y, & Xiang, M. S. Dust-to-gas ratio, X_{CO} factor and CO-dark gas in the Galactic anticentre: an observational study. *MNRAS*, 448(3):2187–2196, April 2015. doi: 10.1093/mnras/stv103.

Chen, B. Q, Li, G. X, Yuan, H. B, Huang, Y, Tian, Z. J, et al. A large catalogue of molecular clouds with accurate distances within 4 kpc of the Galactic disc. *MNRAS*, 493(1):351–361, March 2020. doi: 10.1093/mnras/staa235.

Chen, C.-Y & Ostriker, E. C. Formation of Magnetized Prestellar Cores with Ambipolar Diffusion and Turbulence. *ApJ*, 785(1):69, April 2014. doi: 10.1088/0004-637X/785/1/69.

Choi, E & Stone, J. M. The Effect of Anisotropic Conduction on the Thermal Instability in the Interstellar Medium. *ApJ*, 747(2):86, March 2012. doi: 10.1088/0004-637X/747/2/86.

Clark, S. E, Peek, J. E. G, & Putman, M. E. Magnetically Aligned H I Fibers and the Rolling Hough Transform. *ApJ*, 789(1):82, July 2014. doi: 10.1088/0004-637X/789/1/82.

Clayton, G. C & Martin, P. G. Interstellar dust in the Large Magellanic Cloud. *ApJ*, 288: 558–568, January 1985. doi: 10.1086/162821.

Clayton, G. C & Fitzpatrick, E. L. Anomalous Dust in the Open Cluster Trumpler 37. *AJ*, 93: 157, January 1987. doi: 10.1086/114293.

Cochran, A. L, Levasseur-Regourd, A.-C, Cordiner, M, Hadamcik, E, Lasue, J, et al. The Composition of Comets. *SSRv*, 197(1-4):9–46, December 2015. doi: 10.1007/s11214-015-0183-6.

Colella, P. Multidimensional Upwind Methods for Hyperbolic Conservation Laws. *Journal of Computational Physics*, 87(1):171–200, March 1990. doi: 10.1016/0021-9991(90)90233-Q.

Collins, J. A, Shull, J. M, & Giroux, M. L. Highly Ionized High-Velocity Clouds: Hot Intergalactic Medium or Galactic Halo? *ApJ*, 623(1):196–212, April 2005. doi: 10.1086/428566.

Conti, P. S & Alschuler, W. R. Spectroscopic Studies of O-Type Stars. I. Classification and Absolute Magnitudes. *ApJ*, 170:325, December 1971. doi: 10.1086/151218.

Costa, A. H, Spangler, S. R, Sink, J. R, Brown, S, & Mao, S. A. Denser Sampling of the Rosette Nebula with Faraday Rotation Measurements: Improved Estimates of Magnetic Fields in H II Regions. *ApJ*, 821(2):92, April 2016. doi: 10.3847/0004-637X/821/2/92.

Cote, P, Abraham, B, Balogh, M, Capak, P, Carlberg, R, et al. Castor: A flagship canadian space telescope, October 2019. URL `https://doi.org/10.5281/zenodo.3758463`. White paper identifier W018.

Coudé, S, Bastien, P, Houde, M, Sadavoy, S, Friesen, R, et al. The JCMT BISTRO Survey: The Magnetic Field of the Barnard 1 Star-forming Region. *ApJ*, 877(2):88, June 2019. doi: 10.3847/1538-4357/ab1b23.

Cours, T, Cordier, D, Seignovert, B, Maltagliati, L, & Biennier, L. The 3 . 4 μm absorption in Titan's stratosphere: Contribution of ethane, propane, butane and complex hydrogenated organics. *Icar*, 339:113571, March 2020. doi: 10.1016/j.icarus.2019.113571.

Cramer, N. F & Vladimirov, S. V. Alfven waves in dusty interstellar plasmas. *PASA*, 14(2): 170–78, August 1997. doi: 10.1071/AS97170.

Crutcher, R. M. Magnetic Fields in Molecular Clouds: Observations Confront Theory. *ApJ*, 520 (2):706–713, August 1999. doi: 10.1086/307483.

Dalgarno, A, Yan, M, & Liu, W. Electron Energy Deposition in a Gas Mixture of Atomic and Molecular Hydrogen and Helium. *ApJS*, 125(1):237–256, November 1999. doi: 10.1086/313267.

dall'Oglio, G, Pizzo, L, Andreani, P, Merluzzi, P, & Rossi, L. 1 and 2 Millimeter Observations of Interstellar Dust from Antarctica. In Cutri, R. M & Latter, W. B, editors, *The First Symposium on the Infrared Cirrus and Diffuse Interstellar Clouds*, volume 58 of *Astronomical Society of the Pacific Conference Series*, page 156, January 1994.

Dame, T. M, Hartmann, D, & Thaddeus, P. The Milky Way in Molecular Clouds: A New Complete CO Survey. *ApJ*, 547(2):792–813, February 2001. doi: 10.1086/318388.

Davis, Leverett, J & Greenstein, J. L. The Polarization of Starlight by Aligned Dust Grains. *ApJ*, 114:206, September 1951. doi: 10.1086/145464.

de Zeeuw, P. T, Hoogerwerf, R, de Bruijne, J. H. J, Brown, A. G. A, & Blaauw, A. A HIPPARCOS Census of the Nearby OB Associations. *AJ*, 117(1):354–399, January 1999. doi: 10.1086/300682.

Dello Russo, N, Kawakita, H, Vervack, R. J, & Weaver, H. A. Emerging trends and a comet taxonomy based on the volatile chemistry measured in thirty comets with high-resolution infrared spectroscopy between 1997 and 2013. *Icar*, 278:301–332, November 2016. doi: 10.1016/j.icarus.2016.05.039.

Dickman, R. L. Star counts and visual extinctions in dark nebulae. *AJ*, 83:363–372, April 1978. doi: 10.1086/112212.

Dixon, W. V. D, Sankrit, R, & Otte, B. An Extended FUSE Survey of Diffuse O VI Emission in the Interstellar Medium. *ApJ*, 647(1):328–349, August 2006. doi: 10.1086/505168.

Do-Duy, T, Wright, C. M, Fujiyoshi, T, Glasse, A, Siebenmorgen, R, et al. Crystalline silicate absorption at 11.1 μm: ubiquitous and abundant in embedded YSOs and the interstellar medium. *MNRAS*, 493(3):4463–4517, April 2020. doi: 10.1093/mnras/staa396.

Dobbs, C. L, Pringle, J. E, & Burkert, A. Giant molecular clouds: what are they made from, and how do they get there? *MNRAS*, 425(3):2157–2168, September 2012. doi: 10.1111/j.1365-2966.2012.21558.x.

Dominik, C & Nübold, H. Magnetic Aggregation: Dynamics and Numerical Modeling. *Icarus*, 157(1):173–186, May 2002. doi: 10.1006/icar.2002.6813.

Dong, H, Li, Z, Wang, Q. D, Lauer, T. R, Olsen, K. A. G, et al. High-resolution mapping of dust via extinction in the M31 bulge. *MNRAS*, 459(2):2262–2273, June 2016. doi: 10.1093/mnras/stw778.

Dong, R & Stone, J. M. Buoyant Bubbles in Intracluster Gas: Effects of Magnetic Fields and Anisotropic Viscosity. *ApJ*, 704(2):1309–1320, October 2009. doi: 10.1088/0004-637X/704/2/1309.

Dorofeeva, V. A. Chemical and Isotope Composition of Comet 67P/Churyumov-Gerasimenko: The Rosetta-Philae Mission Results Reviewed in the Context of Cosmogony and Cosmochemistry. *Solar System Research*, 54(2):96–120, April 2020. doi: 10.1134/S0038094620020021.

Draine, B. T. Interstellar Dust Grains. *ARA&A*, 41:241–289, January 2003a. doi: 10.1146/annurev.astro.41.011802.094840.

Draine, B. T. Scattering by Interstellar Dust Grains. II. X-Rays. *ApJ*, 598(2):1026–1037, December 2003b. doi: 10.1086/379123.

Draine, B. T & Bertoldi, F. Structure of Stationary Photodissociation Fronts. *ApJ*, 468:269, September 1996. doi: 10.1086/177689.

Draine, B. T & Lee, H. M. Optical Properties of Interstellar Graphite and Silicate Grains. *ApJ*, 285:89, October 1984. doi: 10.1086/162480.

Draine, B. T & Li, A. Infrared Emission from Interstellar Dust. I. Stochastic Heating of Small Grains. *ApJ*, 551(2):807–824, April 2001. doi: 10.1086/320227.

Draine, B. T & Salpeter, E. E. Destruction mechanisms for interstellar dust. *ApJ*, 231:438–455, July 1979. doi: 10.1086/157206.

Draine, B. T & Sutin, B. Collisional Charging of Interstellar Grains. *ApJ*, 320:803, September 1987. doi: 10.1086/165596.

Draine, B. T. Astrophysics of Dust in Cold Clouds. In *The Cold Universe*, page 213, January 2004.

Draine, B. T. *Physics of the Interstellar and Intergalactic Medium*. Princeton Series in Astrophysics, 2011.

Duan, J.-Z, Wang, C.-L, Zhang, J.-R, Ma, S.-Q, Hong, X.-R, et al. Influence of charging process and size distribution of dust grain on the electric conductivity of dusty plasma. *Physics of Plasmas*, 19(8):083703, August 2012. doi: 10.1063/1.4744972.

Duffell, P. C & MacFadyen, A. I. TESS: A Relativistic Hydrodynamics Code on a Moving Voronoi Mesh. *ApJS*, 197(2):15, Dec 2011. doi: 10.1088/0067-0049/197/2/15.

Dullemond, C. Radmc-3d. `http://www.ita.uni-heidelberg.de/~dullemond/software/radmc-3d/`, 2017.

Dupuis, J, Vennes, S, Bowyer, S, Pradhan, A. K, & Thejll, P. Hot White Dwarfs in the Local Interstellar Medium: Hydrogen and Helium Interstellar Column Densities and Stellar Effective Temperatures from Extreme-Ultraviolet Explorer Spectroscopy. *ApJ*, 455:574, December 1995. doi: 10.1086/176605.

Edelstein, J, Bowyer, S, Korpela, E. J, Lampton, M, Trapero, J, et al. EURD observations of interstellar radiation. *Ap&SS*, 276(1):177–185, March 2001.

Elmegreen, B. G. The formation of giant cloud complexes by the Parker-Jeans instability. *ApJ*, 253:655–665, February 1982. doi: 10.1086/159666.

Elmegreen, B. G, Efremov, Y, Pudritz, R. E, & Zinnecker, H. Observations and Theory of Star Cluster Formation. In Mannings, V, Boss, A. P, & Russell, S. S, editors, *Protostars and Planets IV*, page 179, May 2000.

Elmegreen, B. G. On the Rapid Collapse and Evolution of Molecular Clouds. *ApJ*, 668(2): 1064–1082, October 2007. doi: 10.1086/521327.

Elmegreen, B. G. Gravitational Instabilities in Two-component Galaxy Disks with Gas Dissipation. *ApJ*, 737(1):10, August 2011. doi: 10.1088/0004-637X/737/1/10.

Elmegreen, B. G & Scalo, J. Interstellar Turbulence I: Observations and Processes. *ARA&A*, 42 (1):211–273, September 2004. doi: 10.1146/annurev.astro.41.011802.094859.

Federman, S. R, Glassgold, A. E, Jenkins, E. B, & Shaya, E. J. The abundance of CO in diffuse interstellar clouds - an ultraviolet survey. *ApJ*, 242:545–559, December 1980. doi: 10.1086/158489.

Ferlet, R. Abundance of interstellar nitrogen. *A&A*, 98:L1–L3, May 1981.

Ferrarotti, A. S & Gail, H. P. Composition and quantities of dust produced by AGB-stars and returned to the interstellar medium. *A&A*, 447(2):553–576, February 2006. doi: 10.1051/0004-6361:20041198.

Ferrière, K. M. The interstellar environment of our galaxy. *Reviews of Modern Physics*, 73(4): 1031–1066, October 2001. doi: 10.1103/RevModPhys.73.1031.

Field, G. B. The physics of the interstellar medium. *Highlights of Astronomy*, 3:37–49, January 1974.

Field, G. B, Goldsmith, D. W, & Habing, H. J. Cosmic-Ray Heating of the Interstellar Gas. *ApJL*, 155:L149, March 1969. doi: 10.1086/180324.

Field, G. B. Thermal Instability. *ApJ*, 142:531, August 1965. doi: 10.1086/148317.

Field, G. B & Saslaw, W. C. A Statistical Model of the Formation of Stars and Interstellar Clouds. *ApJ*, 142:568, August 1965. doi: 10.1086/148318.

Finkbeiner, D. P. A Full-Sky Hα Template for Microwave Foreground Prediction. *ApJS*, 146(2): 407–415, June 2003. doi: 10.1086/374411.

Fissel, L. M, Ade, P. A. R, Angilè, F. E, Ashton, P, Benton, S. J, et al. Relative Alignment between the Magnetic Field and Molecular Gas Structure in the Vela C Giant Molecular Cloud Using Low- and High-density Tracers. *ApJ*, 878(2):110, June 2019. doi: 10.3847/1538-4357/ab1eb0.

Fitzpatrick, E. L & Massa, D. An Analysis of the Shapes of Ultraviolet Extinction Curves. I. The 2175 Angstrom Bump. *ApJ*, 307:286, August 1986. doi: 10.1086/164415.

Fitzpatrick, E. L & Massa, D. An Analysis of the Shapes of Interstellar Extinction Curves. V. The IR-through-UV Curve Morphology. *ApJ*, 663(1):320–341, July 2007. doi: 10.1086/518158.

Fitzpatrick, E. L, Massa, D, Gordon, K. D, Bohlin, R, & Clayton, G. C. An Analysis of the Shapes of Interstellar Extinction Curves. VII. Milky Way Spectrophotometric Optical-through-ultraviolet Extinction and Its R-dependence. *ApJ*, 886(2):108, December 2019. doi: 10.3847/1538-4357/ab4c3a.

Flagey, N, Noriega-Crespo, A, Boulanger, F, Carey, S. J, Brooke, T. Y, et al. Evidence for Dust Evolution Within the Taurus Complex from Spitzer Images. *ApJ*, 701(2):1450–1463, August 2009. doi: 10.1088/0004-637X/701/2/1450.

Fortov, V. E, Khrapak, A. G, Khrapak, S. A, Molotkov, V. I, & Petrov, O. F. REVIEWS OF TOPICAL PROBLEMS: Dusty plasmas. *Physics Uspekhi*, 47(5):447–492, May 2004. doi: 10.1070/PU2004v047n05ABEH001689.

Foster, T, Kothes, R, & Brown, J. C. A Relation between the Warm Neutral and Ionized Media Observed in the Canadian Galactic Plane Survey. *ApJL*, 773(1):L11, August 2013. doi: 10.1088/2041-8205/773/1/L11.

France, K, Fleming, B, Egan, A, Suresh, A, de Cicco, N, et al. The Colorado Ultraviolet Transit Experiment (CUTE): Exploring Extreme Exoplanets. In *American Astronomical Society Meeting Abstracts #235*, volume 235 of *American Astronomical Society Meeting Abstracts*, page 271.09, January 2020.

Frisch, P. C. The nearby interstellar medium. *Natur*, 293(5831):377–379, October 1981. doi: 10.1038/293377a0.

Frisch, P. C & York, D. G. Synthesis maps of ultraviolet observations of neutral interstellar gas. *ApJL*, 271:L59–L63, August 1983. doi: 10.1086/184095.

Frisch, P. C. Characteristics of Nearby Interstellar Matter. *SSRv*, 72(3-4):499–592, May 1995. doi: 10.1007/BF00749006.

Froebrich, D, Murphy, G. C, Smith, M. D, Walsh, J, & Del Burgo, C. A large-scale extinction map of the Galactic Anticentre from 2MASS. *MNRAS*, 378(4):1447–1460, July 2007. doi: 10.1111/j.1365-2966.2007.11886.x.

Fromang, S & Stone, J. M. Turbulent resistivity driven by the magnetorotational instability. *A&A*, 507(1):19–28, November 2009. doi: 10.1051/0004-6361/200912752.

Fukui, Y, Kawamura, A, Wong, T, Murai, M, Iritani, H, et al. Molecular and Atomic Gas in the Large Magellanic Cloud. II. Three-dimensional Correlation Between CO and H I. *ApJ*, 705 (1):144–155, November 2009. doi: 10.1088/0004-637X/705/1/144.

Fukui, Y, Tsuge, K, Sano, H, Bekki, K, Yozin, C, et al. Formation of the young massive cluster R136 triggered by tidally-driven colliding H i flows. *PASJ*, 69(3):L5, June 2017. doi: 10.1093/pasj/psx032.

Gaensler, B. M, Madsen, G. J, Chatterjee, S, & Mao, S. A. The Vertical Structure of Warm Ionised Gas in the Milky Way. *PASA*, 25(4):184–200, November 2008. doi: 10.1071/AS08004.

Gaia Collaboration et al. Gaia Data Release 2. Summary of the contents and survey properties. *A&A*, 616:A1, August 2018. doi: 10.1051/0004-6361/201833051.

Gail, H. P & Sedlmayr, E. Mineral formation in stellar winds. I. Condensation sequence of silicate and iron grains in stationary oxygen rich outflows. *A&A*, 347:594–616, July 1999.

Gardiner, T. A & Stone, J. M. An unsplit Godunov method for ideal MHD via constrained transport. *Journal of Computational Physics*, 205(2):509–539, May 2005. doi: 10.1016/j.jcp.2004.11.016.

Gardiner, T. A & Stone, J. M. An unsplit Godunov method for ideal MHD via constrained transport in three dimensions. *Journal of Computational Physics*, 227(8):4123–4141, Apr 2008. doi: 10.1016/j.jcp.2007.12.017.

Gardner, F. F & Whiteoak, J. B. The Polarization of Cosmic Radio Waves. *ARA&A*, 4:245, January 1966. doi: 10.1146/annurev.aa.04.090166.001333.

Gaudi, B. S, Seager, S, Mennesson, B, Kiessling, A, Warfield, K, et al. The Habitable Exoplanet Observatory (HabEx) Mission Concept Study Final Report. *arXiv e-prints*, art. arXiv:2001.06683, January 2020.

Gehrels, N, Chincarini, G, Giommi, P, Mason, K. O, Nousek, J. A, et al. The Swift Gamma-Ray Burst Mission. *ApJ*, 611(2):1005–1020, August 2004. doi: 10.1086/422091.

Gendelev, L & Krumholz, M. R. Evolution of Blister-type H II Regions in a Magnetized Medium. *ApJ*, 745(2):158, February 2012. doi: 10.1088/0004-637X/745/2/158.

Gent, F. A, Mac Low, M. M, Käpylä, M. J, Sarson, G. R, & Hollins, J. F. Modelling supernova-driven turbulence. *Geophysical and Astrophysical Fluid Dynamics*, 114(1-2):77–105, March 2020. doi: 10.1080/03091929.2019.1634705.

Gingold, R. A & Monaghan, J. J. Smoothed particle hydrodynamics: theory and application to non-spherical stars. *MNRAS*, 181:375–389, Nov 1977. doi: 10.1093/mnras/181.3.375.

Ginzburg, V. L & Syrovatskii, S. I. Cosmic Magnetobremsstrahlung (synchrotron Radiation). *ARA&A*, 3:297, January 1965. doi: 10.1146/annurev.aa.03.090165.001501.

Girichidis, P, Federrath, C, Banerjee, R, & Klessen, R. S. Importance of the initial conditions for star formation - II. Fragmentation-induced starvation and accretion shielding. *MNRAS*, 420(1):613–626, February 2012. doi: 10.1111/j.1365-2966.2011.20073.x.

Girichidis, P, Walch, S, Naab, T, Gatto, A, Wünsch, R, et al. The SILCC (SImulating the LifeCycle of molecular Clouds) project - II. Dynamical evolution of the supernova-driven ISM and the launching of outflows. *MNRAS*, 456(4):3432–3455, March 2016. doi: 10.1093/mnras/stv2742.

Girichidis, P, Offner, S. S. R, Kritsuk, A. G, Klessen, R. S, Hennebelle, P, Kruijssen, J. M. D, Krause, M. G. H, Glover, S. C. O, & Padovani, M. Physical Processes in Star Formation. *SSRv*, 216(4):68, June 2020. doi: 10.1007/s11214-020-00693-8.

Glassgold, A. E, Galli, D, & Padovani, M. Cosmic-Ray and X-Ray Heating of Interstellar Clouds and Protoplanetary Disks. *ApJ*, 756(2):157, September 2012. doi: 10.1088/0004-637X/756/2/157.

Gnat, O & Ferland, G. J. Ion-by-ion Cooling Efficiencies. *ApJS*, 199(1):20, March 2012. doi: 10.1088/0067-0049/199/1/20.

Godunov, S. K. A Difference Scheme for Numerical Solution of Discontinuous Solution of Hydrodynamic Equations. *Mat. Sbornik*, 47(1):271–306, 1959.

Goldreich, P & Kwan, J. Molecular Clouds. *ApJ*, 189:441–454, May 1974. doi: 10.1086/152821.

Goldsmith, P. F. Molecular Depletion and Thermal Balance in Dark Cloud Cores. *ApJ*, 557(2): 736–746, August 2001. doi: 10.1086/322255.

Goldsmith, P. F, Heyer, M, Narayanan, G, Snell, R, Li, D, et al. Large-Scale Structure of the Molecular Gas in Taurus Revealed by High Linear Dynamic Range Spectral Line Mapping. *ApJ*, 680(1):428–445, June 2008. doi: 10.1086/587166.

Gómez de Castro, A. I & EUVO Collaboration. Euvo: The uv window into the universe, 2019. URL `https://www.cosmos.esa.int/documents/1866264/3219248/GomezdeCastroAI_WP_Emergence_of_life_GomezdeCastro.pdf/825574e0-5f4c-12c5-ae8a-76b6d75c0696?t=1565184636548`. White paper submitted to ESA's Voyage 2050.

Gómez de Castro, A. I, Lopez-Santiago, J, Sestito, P, Gudiel, V. R, López Martínez, F, et al. The ultraviolet survey of the Gould Belt: general properties of the Taurus star forming region. *Ap&SS*, 335(1):97–103, September 2011. doi: 10.1007/s10509-011-0687-9.

Gómez de Castro, A. I, López-Santiago, J, López-Martínez, F, Sánchez, N, de Castro, E, et al. Variation of the ultraviolet extinction law across the Taurus-Auriga star-forming complex. A GALEX based study. *MNRAS*, 449(4):3867–3878, June 2015. doi: 10.1093/mnras/stv413.

Gómez de Castro, A. I, Beitia-Antero, L, Miravet-Fuster, C. E, Tarabini, L, Tomás, A, et al. Earth as an exoplanet mission concept for a lunar orbiting cubesat. *Journal of Astronomical Telescopes, Instruments, and Systems*, 5:044004, October 2019. doi: 10.1117/1.JATIS.5.4.044004.

Gómez de Castro, A. I & Canet, A. *The investigation of the origin of life at ultraviolet wavelengths, chapter in UV Astronomy and the quest for the origin of life*, page 200. Elsevier, 2021.

Gong, H & Ostriker, E. C. Dense Core Formation in Supersonic Turbulent Converging Flows. *ApJ*, 729(2):120, March 2011. doi: 10.1088/0004-637X/729/2/120.

González-Riestra, R, Cassatella, A, & Wamsteker, W. The INES system. IV. The IUE absolute flux scale. *A&A*, 373:730–745, July 2001. doi: 10.1051/0004-6361:20010646.

Greenstein, J. L. The Ratio of Interstellar Absorption to Reddening. *ApJ*, 104:403, November 1946. doi: 10.1086/144872.

Haffner, L. M, Dettmar, R. J, Beckman, J. E, Wood, K, Slavin, J. D, et al. The warm ionized medium in spiral galaxies. *Reviews of Modern Physics*, 81(3):969–997, July 2009. doi: 10.1103/RevModPhys.81.969.

Hall, J. S. Observations of the Polarized Light from Stars. *Science*, 109(2825):166–167, February 1949. doi: 10.1126/science.109.2825.166.

Hartmann, L. Flows, Fragmentation, and Star Formation. I. Low-Mass Stars in Taurus. *ApJ*, 578(2):914–924, October 2002. doi: 10.1086/342657.

Hartmann, L, Ballesteros-Paredes, J, & Bergin, E. A. Rapid Formation of Molecular Clouds and Stars in the Solar Neighborhood. *ApJ*, 562(2):852–868, December 2001. doi: 10.1086/323863.

Hartquist, T. W, Havnes, O, & Morfill, G. E. The Effects of Dust on the Dynamics of Astronomical and Space Plasmas. *FCPh*, 15:107–142, January 1992.

Hasegawa, T. I, Herbst, E, & Leung, C. M. Models of Gas-Grain Chemistry in Dense Interstellar Clouds with Complex Organic Molecules. *ApJS*, 82:167, September 1992. doi: 10.1086/191713.

Havnes, O. A streaming instability interaction between the solar wind and cometary dust. *A&A*, 193(1-2):309–312, March 1988.

Hayakawa, S. Scattering of Cosmic X-Rays by Interstellar Dust Grains. *Progress of Theoretical Physics*, 43(5):1224–1230, May 1970. doi: 10.1143/PTP.43.1224.

Heger, M. L. The spectra of certain class B stars in the regions 5630A-6680A and 3280A-3380A. *Lick Observatory Bulletin*, 10(337):146–147, January 1922.

Hennebelle, P & Pérault, M. Dynamical condensation in a magnetized and thermally bistable flow. Application to interstellar cirrus. *A&A*, 359:1124–1138, July 2000.

Hennebelle, P. On the origin of non-self-gravitating filaments in the ISM. *A&A*, 556:A153, August 2013. doi: 10.1051/0004-6361/201321292.

Hennebelle, P & Falgarone, E. Turbulent molecular clouds. *A&ARv*, 20:55, November 2012. doi: 10.1007/s00159-012-0055-y.

Hennebelle, P & Iffrig, O. Simulations of magnetized multiphase galactic disc regulated by supernovae explosions. *A&A*, 570:A81, October 2014. doi: 10.1051/0004-6361/201423392.

Hennebelle, P & Inutsuka, S.-i. The role of magnetic field in molecular cloud formation and evolution. *Frontiers in Astronomy and Space Sciences*, 6:5, March 2019. doi: 10.3389/fspas.2019.00005.

Henning, T, Linz, H, Krause, O, Ragan, S, Beuther, H, et al. The seeds of star formation in the filamentary infrared-dark cloud G011.11-0.12. *A&A*, 518:L95, July 2010. doi: 10.1051/0004-6361/201014635.

Henry, R. C, Murthy, J, Overduin, J, & Tyler, J. The Mystery of the Cosmic Diffuse Ultraviolet Background Radiation. *ApJ*, 798(1):14, January 2015. doi: 10.1088/0004-637X/798/1/14.

Henshaw, J. D, Kruijssen, J. M. D, Longmore, S. N, Riener, M, Leroy, A. K, et al. Ubiquitous velocity fluctuations throughout the molecular interstellar medium. *Nature Astronomy*, 4:1064–1071, July 2020. doi: 10.1038/s41550-020-1126-z.

Hill, A. S, Joung, M. R, Mac Low, M.-M, Benjamin, R. A, Haffner, L. M, et al. Vertical Structure of a Supernova-driven Turbulent, Magnetized Interstellar Medium. *ApJ*, 750(2):104, May 2012. doi: 10.1088/0004-637X/750/2/104.

Hiltner, W. A. Polarization of Light from Distant Stars by Interstellar Medium. *Science*, 109(2825):165, February 1949. doi: 10.1126/science.109.2825.165.

Hirashita, H & Yan, H. Shattering and coagulation of dust grains in interstellar turbulence. *MNRAS*, 394(2):1061–1074, Apr 2009. doi: 10.1111/j.1365-2966.2009.14405.x.

Hoang, T & Lazarian, A. A Unified Model of Grain Alignment: Radiative Alignment of Interstellar Grains with Magnetic Inclusions. *ApJ*, 831(2):159, November 2016. doi: 10.3847/0004-637X/831/2/159.

Hobbs, L. M, York, D. G, Snow, T. P, Oka, T, Thorburn, J. A, et al. A Catalog of Diffuse Interstellar Bands in the Spectrum of HD 204827. *ApJ*, 680(2):1256–1270, June 2008. doi: 10.1086/587930.

Hocuk, S & Cazaux, S. Interplay of gas and ice during cloud evolution. *A&A*, 576:A49, April 2015. doi: 10.1051/0004-6361/201424503.

Hollenbach, D & McKee, C. F. Molecule Formation and Infrared Emission in Fast Interstellar Shocks. III. Results for J Shocks in Molecular Clouds. *ApJ*, 342:306, July 1989. doi: 10.1086/167595.

Hollenbach, D & Salpeter, E. E. Surface Recombination of Hydrogen Molecules. *ApJ*, 163:155, January 1971. doi: 10.1086/150754.

Hollenbach, D, Kaufman, M. J, Neufeld, D, Wolfire, M, & Goicoechea, J. R. The Chemistry of Interstellar OH^+, H_2O^+, and H_3O^+: Inferring the Cosmic-Ray Ionization Rates from Observations of Molecular Ions. *ApJ*, 754(2):105, August 2012. doi: 10.1088/0004-637X/754/2/105.

Hopkins, P. F. Some Stars are Totally Metal: A New Mechanism Driving Dust across Star-forming Clouds, and Consequences for Planets, Stars, and Galaxies. *ApJ*, 797(1):59, December 2014. doi: 10.1088/0004-637X/797/1/59.

Hopkins, P. F. A new class of accurate, mesh-free hydrodynamic simulation methods. *MNRAS*, 450(1):53–110, Jun 2015. doi: 10.1093/mnras/stv195.

Hopkins, P. F & Raives, M. J. Accurate, meshless methods for magnetohydrodynamics. *MNRAS*, 455(1):51–88, Jan 2016. doi: 10.1093/mnras/stv2180.

Hopkins, P. F & Squire, J. Ubiquitous instabilities of dust moving in magnetized gas. *MNRAS*, 479(4):4681–4719, October 2018. doi: 10.1093/mnras/sty1604.

Hopkins, P. F, Squire, J, & Seligman, D. Simulating diverse instabilities of dust in magnetized gas. *MNRAS*, 496(2):2123–2154, April 2020. doi: 10.1093/mnras/staa1046.

Hörz, F, Bastien, R, Borg, J, Bradley, J. P, Bridges, J. C, et al. Impact Features on Stardust: Implications for Comet 81P/Wild 2 Dust. *Science*, 314(5806):1716, December 2006. doi: 10.1126/science.1135705.

Hoyle, F & Ellis, G. R. A. On the Existence of an Ionized Layer about the Galactic Plane. *Australian Journal of Physics*, 16:1, March 1963. doi: 10.1071/PH630001.

Hu, R, Peterson, L, & Wolf, E. T. O_2- and CO-rich Atmospheres for Potentially Habitable Environments on TRAPPIST-1 Planets. *ApJ*, 888(2):122, January 2020. doi: 10.3847/1538-4357/ab5f07.

Hull, A, Heap, S, Woodruff, R, Mehle, G, Tomic, M, et al. The CETUS Probe Mission Concept 1.5m Optical Telescope Assembly: A high A-Omega approach for ultraviolet astrophysics. In *American Astronomical Society Meeting Abstracts #231*, volume 231 of *American Astronomical Society Meeting Abstracts*, page 140.13, January 2018.

Hynes, K. M & Gyngard, F. The Presolar Grain Database. In *Lunar and Planetary Science Conference*, Lunar and Planetary Science Conference, page 1198, March 2009.

Iglesias-Groth, S. Fullerenes and Buckyonions in the Interstellar Medium. *ApJL*, 608(1):L37–L40, June 2004. doi: 10.1086/422216.

Inoue, T & Inutsuka, S.-i. Two-Fluid Magnetohydrodynamic Simulations of Converging H I Flows in the Interstellar Medium. I. Methodology and Basic Results. *ApJ*, 687(1):303–310, November 2008. doi: 10.1086/590528.

Inoue, T & Inutsuka, S.-i. Formation of Turbulent and Magnetized Molecular Clouds via Accretion Flows of H I Clouds. *ApJ*, 759(1):35, November 2012. doi: 10.1088/0004-637X/759/1/35.

Inoue, T & Inutsuka, S.-i. Formation of H I Clouds in Shock-compressed Interstellar Medium: Physical Origin of Angular Correlation between Filamentary Structure and Magnetic Field. *ApJ*, 833(1):10, December 2016. doi: 10.3847/0004-637X/833/1/10.

Inoue, T, Inutsuka, S.-i, & Koyama, H. The Role of Ambipolar Diffusion in the Formation Process of Moderately Magnetized Diffuse Clouds. *ApJL*, 658(2):L99–L102, April 2007. doi: 10.1086/514816.

Ishihara, T, Kobayashi, N, Enohata, K, Umemura, M, & Shiraishi, K. Dust Coagulation Regulated by Turbulent Clustering in Protoplanetary Disks. *ApJ*, 854(2):81, February 2018. doi: 10.3847/1538-4357/aaa976.

Iwasaki, K, Tomida, K, Inoue, T, & Inutsuka, S.-i. The Early Stage of Molecular Cloud Formation by Compression of Two-phase Atomic Gases. *ApJ*, 873(1):6, March 2019. doi: 10.3847/1538-4357/ab02ff.

Jansen, F, Lumb, D, Altieri, B, Clavel, J, Ehle, M, et al. XMM-Newton observatory. I. The spacecraft and operations. *A&A*, 365:L1–L6, January 2001. doi: 10.1051/0004-6361:20000036.

Jelinsky, P, Vallerga, J. V, & Edelstein, J. First Spectral Observations of the Diffuse Background with the Extreme Ultraviolet Explorer. *ApJ*, 442:653, April 1995. doi: 10.1086/175469.

Jenkins, E. B & Meloy, D. A. A Survey with Copernicus of Interstellar O VI Absorption. *ApJL*, 193:L121, November 1974. doi: 10.1086/181647.

Jenkins, E. B, Drake, J. F, Morton, D. C, Rogerson, J. B, Spitzer, L, et al. Spectrophotometric Results from the Copernicus Satellite. V. Abundances of Molecules in Interstellar Clouds. *ApJL*, 181:L122, May 1973. doi: 10.1086/181198.

Jenkins, E. B, Jura, M, & Loewenstein, M. Copernicus observations of C I : pressures and Carbon abundances in diffuse interstellar clouds. *ApJ*, 270:88–104, July 1983. doi: 10.1086/161100.

Jenkins, E. B, Oegerle, W. R, Gry, C, Vallerga, J, Sembach, K. R, et al. The Ionization of the Local Interstellar Medium as Revealed by Far Ultraviolet Spectroscopic Explorer Observations of N, O, and AR toward White Dwarf Stars. *ApJL*, 538(1):L81–L85, July 2000. doi: 10.1086/312786.

Jenkins, E. B. Interstellar Atomic Abundances. In McWilliam, A & Rauch, M, editors, *Origin and Evolution of the Elements*, page 336, January 2004.

Jenkins, E. B. The Fractional Ionization of the Warm Neutral Interstellar Medium. *ApJ*, 764(1):25, February 2013. doi: 10.1088/0004-637X/764/1/25.

Jenkins, E. B & Tripp, T. M. The Distribution of Thermal Pressures in the Interstellar Medium from a Survey of C I Fine-Structure Excitation. *ApJS*, 137(2):297–340, December 2001. doi: 10.1086/323326.

Jones, A. P. Variations on a theme - the evolution of hydrocarbon solids. I. Compositional and spectral modelling - the eRCN and DG models. *A&A*, 540:A1, April 2012a. doi: 10.1051/0004-6361/201117623.

Jones, A. P. Variations on a theme - the evolution of hydrocarbon solids. II. Optical property modelling - the optEC$_{(s)}$ model. *A&A*, 540:A2, April 2012b. doi: 10.1051/0004-6361/201117624.

Jones, A. P. Variations on a theme - the evolution of hydrocarbon solids. III. Size-dependent properties - the optEC$_{(s)}$(a) model. *A&A*, 542:A98, June 2012c. doi: 10.1051/0004-6361/201118483.

Jones, A. P & Nuth, J. A. Dust destruction in the ISM: a re-evaluation of dust lifetimes. *A&A*, 530:A44, June 2011. doi: 10.1051/0004-6361/201014440.

Jones, A. P, Fanciullo, L, Köhler, M, Verstraete, L, Guillet, V, Bocchio, M, & Ysard, N. The evolution of amorphous hydrocarbons in the ISM: dust modelling from a new vantage point. *A&A*, 558:A62, October 2013. doi: 10.1051/0004-6361/201321686.

Jones, A. P, Köhler, M, Ysard, N, Bocchio, M, & Verstraete, L. The global dust modelling framework THEMIS. *A&A*, 602:A46, June 2017. doi: 10.1051/0004-6361/201630225.

Jones, A. P, Ysard, N, Köhler, M, Fanciullo, L, Bocchio, M, et al. The cycling of carbon into and out of dust. *Faraday Discussions*, 168:313, January 2014. doi: 10.1039/C3FD00128H.

Kalberla, P. M. W & Kerp, J. The Hi Distribution of the Milky Way. *ARA&A*, 47(1):27–61, September 2009. doi: 10.1146/annurev-astro-082708-101823.

Kameswara Rao, N, De Marco, O, Krishna, S, Murthy, J, Ray, A, et al. Planetary nebulae with UVIT. II. Revelations from far-UV vision of Butterfly nebula NGC 6302. *A&A*, 620:A138, December 2018. doi: 10.1051/0004-6361/201833507.

Keeney, B. A, Stocke, J. T, Danforth, C. W, Shull, J. M, Pratt, C. T, et al. Characterizing the Circumgalactic Medium of Nearby Galaxies with HST/COS and HST/STIS Absorption-line Spectroscopy. II. Methods and Models. *ApJS*, 230(1):6, May 2017. doi: 10.3847/1538-4365/aa6b59.

Kennicutt, R. C & Evans, N. J. Star Formation in the Milky Way and Nearby Galaxies. *ARA&A*, 50:531–608, September 2012. doi: 10.1146/annurev-astro-081811-125610.

Kitsionas, S, Federrath, C, Klessen, R. S, et al. Algorithmic comparisons of decaying, isothermal, supersonic turbulence. *A&A*, 508(1):541–560, Dec 2009. doi: 10.1051/0004-6361/200811170.

Klassen, M, Pudritz, R. E, & Kirk, H. Filamentary flow and magnetic geometry in evolving cluster-forming molecular cloud clumps. *MNRAS*, 465(2):2254–2276, February 2017. doi: 10.1093/mnras/stw2889.

Klessen, R. S. Star Formation in Molecular Clouds. In Charbonnel, C & Montmerle, T, editors, *EAS Publications Series*, volume 51 of *EAS Publications Series*, pages 133–167, November 2011. doi: 10.1051/eas/1151009.

Klessen, R. S & Glover, S. C. O. Physical Processes in the Interstellar Medium. *Saas-Fee Advanced Course*, 43:85, January 2016. doi: 10.1007/978-3-662-47890-5_2.

Knacke, R. F & Thomson, R. K. Infrared Extinction Cross Sections of Silicate Grains. *PASP*, 85(505):341, June 1973. doi: 10.1086/129467.

Koch, E. W & Rosolowsky, E. W. Filament identification through mathematical morphology. *MNRAS*, 452(4):3435–3450, October 2015. doi: 10.1093/mnras/stv1521.

Koechlin, L, Serre, D, Deba, P, Pelló, R, Peillon, C, et al. The fresnel interferometric imager. *Experimental Astronomy*, 23(1):379–402, March 2009. doi: 10.1007/s10686-008-9112-y.

Köhler, M, Ysard, N, & Jones, A. P. Dust evolution in the transition towards the denser ISM: impact on dust temperature, opacity, and spectral index. *A&A*, 579:A15, July 2015. doi: 10.1051/0004-6361/201525646.

Kroupa, P. The Initial Mass Function of Stars: Evidence for Uniformity in Variable Systems. *Science*, 295(5552):82–91, January 2002. doi: 10.1126/science.1067524.

Krumholz, M. R, McKee, C. F, & Tumlinson, J. The Atomic-to-Molecular Transition in Galaxies. I. An Analytic Approximation for Photodissociation Fronts in Finite Clouds. *ApJ*, 689(2): 865–882, December 2008. doi: 10.1086/592490.

Kuhn, M. A, Hillenbrand, L. A, Sills, A, Feigelson, E. D, & Getman, K. V. Kinematics in Young Star Clusters and Associations with Gaia DR2. *ApJ*, 870(1):32, January 2019. doi: 10.3847/1538-4357/aaef8c.

Kumar, M. S. N, Palmeirim, P, Arzoumanian, D, & Inutsuka, S. I. Unifying low and high mass star formation through density amplified hubs of filaments. *arXiv e-prints*, art. arXiv:2008.00295, August 2020.

Kumar, R, Pradhan, A. C, Mohapatra, A, Moharana, A, Ojha, D. K, et al. Ultraviolet Imaging Telescope (UVIT) observation of the Galactic globular cluster NGC 7492. *MNRAS*, 502(1): 313–327, March 2021. doi: 10.1093/mnras/staa4032.

Kunz, M. W, Bogdanović, T, Reynolds, C. S, & Stone, J. M. Buoyancy Instabilities in a Weakly Collisional Intracluster Medium. *ApJ*, 754(2):122, August 2012. doi: 10.1088/0004-637X/754/2/122.

Lada, C. J & Lada, E. A. Embedded Clusters in Molecular Clouds. *ARA&A*, 41:57–115, January 2003. doi: 10.1146/annurev.astro.41.011802.094844.

Lada, C. J, Lada, E. A, Clemens, D. P, & Bally, J. Dust Extinction and Molecular Gas in the Dark Cloud IC 5146. *ApJ*, 429:694, July 1994. doi: 10.1086/174354.

Laibe, G & Price, D. J. Dusty gas with smoothed particle hydrodynamics - I. Algorithm and test suite. *MNRAS*, 420(3):2345–2364, Mar 2012a. doi: 10.1111/j.1365-2966.2011.20202.x.

Laibe, G & Price, D. J. Dusty gas with smoothed particle hydrodynamics - II. Implicit timestepping and astrophysical drag regimes. *MNRAS*, 420(3):2365–2376, Mar 2012b. doi: 10.1111/j.1365-2966.2011.20201.x.

Laibe, G & Price, D. J. Dust and gas mixtures with multiple grain species - a one-fluid approach. *MNRAS*, 444(2):1940–1956, Oct 2014. doi: 10.1093/mnras/stu1367.

Lallement, R, Vergely, J. L, Valette, B, Puspitarini, L, Eyer, L, et al. 3D maps of the local ISM from inversion of individual color excess measurements. *A&A*, 561:A91, January 2014. doi: 10.1051/0004-6361/201322032.

Lallement, R, Babusiaux, C, Vergely, J. L, Katz, D, Arenou, F, et al. Gaia-2MASS 3D maps of Galactic interstellar dust within 3 kpc. *A&A*, 625:A135, May 2019. doi: 10.1051/0004-6361/201834695.

Lang, W. J, Masheder, M. R. W, Dame, T. M, & Thaddeus, P. The lambda -Orionis Ring in CO. *A&A*, 357:1001–1012, May 2000.

Lazarian, A & Hoang, T. Magnetic Properties of Dust Grains, Effect of Precession, and Radiative Torque Alignment. *ApJ*, 883(2):122, October 2019. doi: 10.3847/1538-4357/ab3d39.

Lazarian, A & Yan, H. Grain Dynamics in Magnetized Interstellar Gas. *ApJL*, 566(2):L105–L108, February 2002. doi: 10.1086/339675.

Lee, H, Hopkins, P. F, & Squire, J. The dynamics of charged dust in magnetized molecular clouds. *MNRAS*, 469(3):3532–3540, Aug 2017. doi: 10.1093/mnras/stx1097.

Lehe, R, Parrish, I. J, & Quataert, E. The Heating of Test Particles in Numerical Simulations of Alfvénic Turbulence. *ApJ*, 707(1):404–419, December 2009. doi: 10.1088/0004-637X/707/1/404.

Lehner, N, Jenkins, E. B, Gry, C, Moos, H. W, Chayer, P, et al. Far Ultraviolet Spectroscopic Explorer Survey of the Local Interstellar Medium within 200 Parsecs. *ApJ*, 595(2):858–879, October 2003. doi: 10.1086/377493.

Lehner, N, Howk, J. C, Thom, C, Fox, A. J, Tumlinson, J, et al. High-velocity clouds as streams of ionized and neutral gas in the halo of the Milky Way. *MNRAS*, 424(4):2896–2913, August 2012. doi: 10.1111/j.1365-2966.2012.21428.x.

Lenz, D, Hensley, B. S, & Doré, O. A New, Large-scale Map of Interstellar Reddening Derived from H I Emission. *ApJ*, 846(1):38, September 2017. doi: 10.3847/1538-4357/aa84af.

Leung, C. M. Radiation transport in dense interstellar dust clouds. *ApJ*, 199:340–360, July 1975. doi: 10.1086/153697.

Li, A & Greenberg, J. M. A unified model of interstellar dust. *A&A*, 323:566–584, July 1997.

Li, H.-b, Fang, M, Henning, T, & Kainulainen, J. The link between magnetic fields and filamentary clouds: bimodal cloud orientations in the Gould Belt. *MNRAS*, 436(4):3707–3719, December 2013. doi: 10.1093/mnras/stt1849.

Lieu, R, Bowyer, S, Lampton, M, Jelinsky, P, & Edelstein, J. EUVE First Light Observation of the Diffuse Sky Background. *ApJL*, 417:L41, November 1993. doi: 10.1086/187089.

Lombardi, M, Alves, J, & Lada, C. J. 2MASS wide field extinction maps. IV. The Orion, Monoceros R2, Rosette, and Canis Major star forming regions. *A&A*, 535:A16, November 2011. doi: 10.1051/0004-6361/201116915.

Lombardi, M, Bouy, H, Alves, J, & Lada, C. J. Herschel-Planck dust optical-depth and column-density maps. I. Method description and results for Orion. *A&A*, 566:A45, June 2014. doi: 10.1051/0004-6361/201323293.

Lorek, S, Lacerda, P, & Blum, J. Local growth of dust- and ice-mixed aggregates as cometary building blocks in the solar nebula. *A&A*, 611:A18, March 2018. doi: 10.1051/0004-6361/201630175.

Lucy, L. B. A numerical approach to the testing of the fission hypothesis. *AJ*, 82:1013–1024, Dec 1977. doi: 10.1086/112164.

Mac Low, M.-M & Klessen, R. S. Control of star formation by supersonic turbulence. *Reviews of Modern Physics*, 76(1):125–194, January 2004. doi: 10.1103/RevModPhys.76.125.

Mac Low, M.-M, Klessen, R. S, Burkert, A, & Smith, M. D. Kinetic Energy Decay Rates of Supersonic and Super-Alfvénic Turbulence in Star-Forming Clouds. *PhRvL*, 80(13):2754–2757, March 1998. doi: 10.1103/PhysRevLett.80.2754.

Martin, C. L & Kennicutt, Robert C., J. Soft X-Ray Emission from NGC 5253 and the Ionized Interstellar Medium. *ApJ*, 447:171, July 1995. doi: 10.1086/175863.

Martin, D. C, Fanson, J, Schiminovich, D, Morrissey, P, Friedman, P. G, et al. The Galaxy Evolution Explorer: A Space Ultraviolet Survey Mission. *ApJL*, 619(1):L1–L6, January 2005. doi: 10.1086/426387.

Martins, F, Mahy, L, Hillier, D. J, & Rauw, G. A quantitative study of O stars in NGC 2244 and the Monoceros OB2 association. *A&A*, 538:A39, February 2012. doi: 10.1051/0004-6361/201117458.

Massa, D & Fitzpatrick, E. L. Ultraviolet Extinction toward Five Open Clusters, and the Accuracy of IUE Extinction Measurements. *ApJS*, 60:305, June 1986. doi: 10.1086/191088.

Mathis, J. S, Rumpl, W, & Nordsieck, K. H. The size distribution of interstellar grains. *ApJ*, 217:425–433, October 1977. doi: 10.1086/155591.

Mathis, J. S, Mezger, P. G, & Panagia, N. Interstellar radiation field and dust temperatures in the diffuse interstellar matter and in giant molecular clouds. *A&A*, 500:259–276, November 1983.

Mautner, M. N, Abdelsayed, V, El-Shall, M. S, Thrower, J. D, Green, S. D, Collings, M. P, & McCoustra, M. R. S. Meteorite nanoparticles as models for interstellar grains: Synthesis and preliminary characterisation. *Faraday Discussions*, 133:103, January 2006. doi: 10.1039/b518207g.

McClure-Griffiths, N. M, Dickey, J. M, Gaensler, B. M, Green, A. J, & Haverkorn, M. Magnetically Dominated Strands of Cold Hydrogen in the Riegel-Crutcher Cloud. *ApJ*, 652(2):1339–1347, December 2006. doi: 10.1086/508706.

McKee, C. F & Ostriker, J. P. A theory of the interstellar medium: three components regulated by supernova explosions in an inhomogeneous substrate. *ApJ*, 218:148–169, November 1977. doi: 10.1086/155667.

McKinnon, R, Vogelsberger, M, Torrey, P, Marinacci, F, & Kannan, R. Simulating galactic dust grain evolution on a moving mesh. *MNRAS*, 478(3):2851–2886, August 2018. doi: 10.1093/mnras/sty1248.

Mennella, V. H Atom Irradiation of Carbon Grains under Simulated Dense Interstellar Medium Conditions: The Evolution of Organics from Diffuse Interstellar Clouds to the Solar System. *ApJ*, 718(2):867–875, August 2010. doi: 10.1088/0004-637X/718/2/867.

Meyer, D. M, Jura, M, & Cardelli, J. A. The Definitive Abundance of Interstellar Oxygen. *ApJ*, 493(1):222–229, January 1998. doi: 10.1086/305128.

Mierkiewicz, E. J, Reynolds, R. J, Roesler, F. L, Harlander, J. M, & Jaehnig, K. P. Detection of Diffuse Interstellar [O II] Emission from the Milky Way Using Spatial Heterodyne Spectroscopy. *ApJL*, 650(1):L63–L66, October 2006. doi: 10.1086/508745.

Miville-Deschênes, M. A, Joncas, G, Falgarone, E, & Boulanger, F. High resolution 21 cm mapping of the Ursa Major Galactic cirrus: Power spectra of the high-latitude H I gas. *A&A*, 411:109–121, November 2003. doi: 10.1051/0004-6361:20031297.

Miville-Deschênes, M.-A, Murray, N, & Lee, E. J. Physical Properties of Molecular Clouds for the Entire Milky Way Disk. *ApJ*, 834(1):57, January 2017. doi: 10.3847/1538-4357/834/1/57.

Mondal, C, Subramaniam, A, & George, K. Ultraviolet Imaging Telescope View of Dwarf Irregular Galaxy IC 2574: Is the Star Formation Triggered Due to Expanding H I Shells? *AJ*, 158 (6):229, December 2019. doi: 10.3847/1538-3881/ab4ea1.

Moos, H. W, Cash, W. C, Cowie, L. L, Davidsen, A. F, Dupree, A. K, et al. Overview of the Far Ultraviolet Spectroscopic Explorer Mission. *ApJL*, 538(1):L1–L6, July 2000. doi: 10.1086/312795.

Morrissey, P, Schiminovich, D, Barlow, T. A, Martin, D. C, Blakkolb, B, et al. The On-Orbit Performance of the Galaxy Evolution Explorer. *ApJL*, 619(1):L7–L10, January 2005. doi: 10.1086/424734.

Morrissey, P, Conrow, T, Barlow, T. A, Small, T, Seibert, M, et al. The Calibration and Data Products of GALEX. *ApJS*, 173(2):682–697, December 2007. doi: 10.1086/520512.

Morton, D. C. Interstellar Abundances Toward Zeta Ophiuchi. *ApJL*, 193:L35, October 1974. doi: 10.1086/181625.

Morton, D. C & Hu, E. M. Interstellar absorption lines toward Gamma Arae. *ApJ*, 202:638–649, December 1975. doi: 10.1086/154019.

Morton, D. C, Drake, J. F, Jenkins, E. B, Rogerson, J. B, Spitzer, L, et al. Spectrophotometric Results from the Copernicus Satellite. II. Composition of Interstellar Clouds. *ApJL*, 181:L103, May 1973. doi: 10.1086/181195.

Morton, D. C. The Far-Ultraviolet Spectra of Six Stars in Orion. *ApJ*, 147:1017, March 1967. doi: 10.1086/149091.

Morton, D. C & Spitzer, Lyman, J. Line Spectra of Delta and pi Scorpii in the Far-Ultraviolet. *ApJ*, 144:1, April 1966. doi: 10.1086/148586.

Mouschovias, T. C. Nonhomologous contraction and equilibria of self-gravitating, magnetic interstellar clouds embedded in an intercloud medium: star formation. II. Results. *ApJ*, 207: 141–158, July 1976. doi: 10.1086/154478.

Mouschovias, T. C. Static Equilibria of the Interstellar Gas in the Presence of Magnetic and Gravitational Fields: Large-Scale Condensations. *ApJ*, 192:37–50, August 1974. doi: 10.1086/153032.

Murga, M. S, Kirsanova, M. S, Vasyunin, A. I, & Pavlyuchenkov, Y. N. Impact of PAH photodissociation on the formation of small hydrocarbons in the Orion Bar and the horsehead PDRs. *MNRAS*, 497(2):2327–2339, July 2020. doi: 10.1093/mnras/staa2026.

Murphy, E. M, Sembach, K. R, Gibson, B. K, Shull, J. M, Savage, B. D, et al. Far Ultraviolet Spectroscopic Explorer Spectroscopy of High-Velocity Cloud Complex C. *ApJL*, 538(1):L35–L38, July 2000. doi: 10.1086/312801.

Murthy, J, Henry, R. C, Moos, H. W, Landsman, W. B, Linsky, J. L, et al. IUE Observations of Hydrogen and Deuterium in the Local Interstellar Medium. *ApJ*, 315:675, April 1987. doi: 10.1086/165169.

Murthy, J & Sahnow, D. J. Observations of the Diffuse Far-Ultraviolet Background with the Far Ultraviolet Spectroscopic Explorer. *ApJ*, 615(1):315–322, November 2004. doi: 10.1086/424441.

Myers, P. C, Goodman, A. A, Gusten, R, & Heiles, C. Observations of Magnetic Fields in Diffuse Clouds. *ApJ*, 442:177, March 1995. doi: 10.1086/175433.

Nagai, T, Inutsuka, S.-i, & Miyama, S. M. An Origin of Filamentary Structure in Molecular Clouds. *ApJ*, 506(1):306–322, October 1998. doi: 10.1086/306249.

Nakagawa, Y, Nakazawa, K, & Hayashi, C. Growth and sedimentation of dust grains in the primordial solar nebula. *Icar*, 45(3):517–528, March 1981. doi: 10.1016/0019-1035(81)90018-X.

Nakamura, F & Li, Z.-Y. Magnetically Regulated Star Formation in Three Dimensions: The Case of the Taurus Molecular Cloud Complex. *ApJ*, 687(1):354–375, November 2008. doi: 10.1086/591641.

Nakano, T. Star Formation in Magnetic Clouds. *ApJ*, 494(2):587–604, February 1998. doi: 10.1086/305230.

Nandy, K, Thompson, G. I, Jamar, C, Monfils, A, & Wilson, R. Studies of ultraviolet interstellar extinction with the sky-survey telescope of the TD-1 satellite. I. Results for three galactic regions. *A&A*, 44:195–203, November 1975.

Nandy, K, Thompson, G. I, Jamar, C, Monfils, A, & Wilson, R. Studies of ultraviolet interstellar extinction with the sky-survey telescope of the TD-1 satellite. II. Results for different regions throughout the galactic plane. *A&A*, 51(1):63–69, August 1976.

Nomura, H & Nakagawa, Y. Dust Size Growth and Settling in a Protoplanetary Disk. *ApJ*, 640 (2):1099–1109, April 2006. doi: 10.1086/500251.

Nozawa, T & Fukugita, M. Properties of Dust Grains Probed with Extinction Curves. *ApJ*, 770 (1):27, June 2013. doi: 10.1088/0004-637X/770/1/27.

Nozawa, T, Kozasa, T, Habe, A, Dwek, E, Umeda, H, et al. Evolution of Dust in Primordial Supernova Remnants: Can Dust Grains Formed in the Ejecta Survive and Be Injected into the Early Interstellar Medium? *ApJ*, 666(2):955–966, September 2007. doi: 10.1086/520621.

Ntormousi, E, Burkert, A, Fierlinger, K, & Heitsch, F. Formation of Cold Filamentary Structure from Wind-blown Superbubbles. *ApJ*, 731(1):13, April 2011. doi: 10.1088/0004-637X/731/1/13.

Nübold, H, Poppe, T, Rost, M, Dominik, C, & Glassmeier, K.-H. Magnetic aggregation. II. Laboratory and microgravity experiments. *Icar*, 165(1):195–214, Sep 2003. doi: 10.1016/S0019-1035(03)00153-2.

Nuth, J. A, Berg, O, Faris, J, & Wasilewski, P. Magnetically Enhanced Coagulation of Very Small Iron Grains. *Icar*, 107(1):155–163, Jan 1994. doi: 10.1006/icar.1994.1013.

Oegerle, W. R, Tripp, T. M, Sembach, K. R, Jenkins, E. B, Bowen, D. V, et al. Far Ultraviolet Spectroscopic Explorer Observations of the Galactic and Intergalactic Medium toward H1821+643. *ApJL*, 538(1):L23–L26, July 2000. doi: 10.1086/312798.

Oegerle, W. R, Jenkins, E. B, Shelton, R. L, Bowen, D. V, & Chayer, P. A Survey of O VI Absorption in the Local Interstellar Medium. *ApJ*, 622(1):377–389, March 2005. doi: 10.1086/427792.

Oort, J. H. Outline of a theory on the origin and acceleration of interstellar clouds and O associations. *Bulletin of the Astronomical Institutes of the Netherlands*, 12:177, September 1954.

Ormel, C. W, Spaans, M, & Tielens, A. G. G. M. Dust coagulation in protoplanetary disks: porosity matters. *A&A*, 461(1):215–232, January 2007. doi: 10.1051/0004-6361:20065949.

Ossenkopf, V. Dust coagulation in dense molecular clouds : the formation of fluffy aggregates. *A&A*, 280:617–646, December 1993.

Ostriker, E. C, Gammie, C. F, & Stone, J. M. Kinetic and Structural Evolution of Self-gravitating, Magnetized Clouds: 2.5-dimensional Simulations of Decaying Turbulence. *ApJ*, 513(1):259–274, March 1999. doi: 10.1086/306842.

Ostriker, E. C, Stone, J. M, & Gammie, C. F. Density, Velocity, and Magnetic Field Structure in Turbulent Molecular Cloud Models. *ApJ*, 546(2):980–1005, January 2001. doi: 10.1086/318290.

Overbeck, J. W. Small-Angle Scattering of Celestial X-Rays by Interstellar Grains. *ApJ*, 141:864, April 1965. doi: 10.1086/148180.

Padoan, P, Cambrésy, L, Juvela, M, Kritsuk, A, Langer, W. D, et al. Can We Trust the Dust? Evidence of Dust Segregation in Molecular Clouds. *ApJ*, 649(2):807–815, October 2006. doi: 10.1086/507068.

Padoan, P, Pan, L, Haugbølle, T, & Nordlund, Å. Supernova Driving. I. The Origin of Molecular Cloud Turbulence. *ApJ*, 822(1):11, May 2016. doi: 10.3847/0004-637X/822/1/11.

Page, M. J, Brindle, C, Talavera, A, Still, M, Rosen, S. R, et al. The XMM-Newton serendipitous ultraviolet source survey catalogue. *MNRAS*, 426(2):903–926, October 2012. doi: 10.1111/j.1365-2966.2012.21706.x.

Page, M. J, Yershov, V, Breeveld, A, Kuin, P, Mignani, R, et al. The Swift UVOT serendipitous source catalogue. In *Proceedings of Swift: 10 Years of Discovery (SWIFT 10*, page 37, December 2014.

Palmeirim, P, André, P, Kirk, J, Ward-Thompson, D, Arzoumanian, D, et al. Herschel view of the Taurus B211/3 filament and striations: evidence of filamentary growth? *A&A*, 550:A38, February 2013. doi: 10.1051/0004-6361/201220500.

Panopoulou, G. V, Psaradaki, I, Skalidis, R, Tassis, K, & Andrews, J. J. A closer look at the 'characteristic' width of molecular cloud filaments. *MNRAS*, 466(3):2529–2541, April 2017. doi: 10.1093/mnras/stw3060.

Parrish, I. J, Stone, J. M, & Lemaster, N. The Magnetothermal Instability in the Intracluster Medium. *ApJ*, 688(2):905–917, December 2008. doi: 10.1086/592380.

Paruta, P, Hendrix, T, & Keppens, R. Dust grain coagulation modelling : From discrete to continuous. *Astronomy and Computing*, 16:155–165, Jul 2016. doi: 10.1016/j.ascom.2016.05.002.

Pattle, K, Ward-Thompson, D, Berry, D, Hatchell, J, Chen, H.-R, et al. The JCMT BISTRO Survey: The Magnetic Field Strength in the Orion A Filament. *ApJ*, 846(2):122, September 2017. doi: 10.3847/1538-4357/aa80e5.

Peacock, S, Barman, T, Shkolnik, E. L, Loyd, R. O. P, Schneider, A. C, et al. HAZMAT VI: The Evolution of Extreme Ultraviolet Radiation Emitted from Early M Stars. *ApJ*, 895(1):5, May 2020. doi: 10.3847/1538-4357/ab893a.

Pedregosa, F, Varoquaux, G, Gramfort, A, Michel, V, Thirion, B, et al. Scikit-learn: Machine learning in Python. *Journal of Machine Learning Research*, 12:2825–2830, 2011.

Peek, J. E. G & Schiminovich, D. Ultraviolet Extinction at High Galactic Latitudes. *ApJ*, 771 (1):68, July 2013. doi: 10.1088/0004-637X/771/1/68.

Peek, J. E. G, Babler, B. L, Zheng, Y, Clark, S. E, Douglas, K. A, et al. The GALFA-H I Survey Data Release 2. *ApJS*, 234(1):2, January 2018. doi: 10.3847/1538-4365/aa91d3.

Peimbert, M. Physical conditions of the Orion Nebula derived from optical and ultraviolet data. *Annals of the New York Academy of Sciences*, 395:24–30, October 1982. doi: 10.1111/j.1749-6632.1982.tb43375.x.

Peters, T, Klessen, R. S, Mac Low, M.-M, & Banerjee, R. Limiting Accretion onto Massive Stars by Fragmentation-induced Starvation. *ApJ*, 725(1):134–145, December 2010. doi: 10.1088/0004-637X/725/1/134.

Phelps, R. L & Lada, E. A. Spatial Distribution of Embedded Clusters in the Rosette Molecular Cloud: Implications for Cluster Formation. *ApJ*, 477(1):176–182, March 1997. doi: 10.1086/303713.

Phillips, A. P, Gondhalekar, P. M, & Pettini, M. A study of element depletions in interstellar gas. *MNRAS*, 200:687–703, August 1982. doi: 10.1093/mnras/200.3.687.

Pilipp, W, Hartquist, T. W, Havnes, O, & Morfill, G. E. The Effects of Dust on the Propagation and Dissipation of Alfven Waves in Interstellar Clouds. *ApJ*, 314:341, March 1987. doi: 10.1086/165064.

Pilleri, P, Montillaud, J, Berné, O, & Joblin, C. Evaporating very small grains as tracers of the UV radiation field in photo-dissociation regions. *A&A*, 542:A69, June 2012. doi: 10.1051/0004-6361/201015915.

Piontek, R. A & Ostriker, E. C. Thermal and Magnetorotational Instability in the Interstellar Medium: Two-dimensional Numerical Simulations. *ApJ*, 601(2):905–920, February 2004. doi: 10.1086/380785.

Planck Collaboration. Planck 2018 results. XI. Polarized dust foregrounds. *arXiv e-prints*, art. arXiv:1801.04945, January 2018a.

Planck Collaboration. Planck 2018 results. XII. Galactic astrophysics using polarized dust emission. *arXiv e-prints*, art. arXiv:1807.06212, July 2018b.

Planck Collaboration et al. Planck intermediate results. XXXII. The relative orientation between the magnetic field and structures traced by interstellar dust. *A&A*, 586:A135, February 2016a. doi: 10.1051/0004-6361/201425044.

Planck Collaboration et al. Planck intermediate results. XXXIV. The magnetic field structure in the Rosette Nebula. *A&A*, 586:A137, February 2016b. doi: 10.1051/0004-6361/201525616.

Planck Collaboration et al. Planck intermediate results. XXXV. Probing the role of the magnetic field in the formation of structure in molecular clouds. *A&A*, 586:A138, February 2016c. doi: 10.1051/0004-6361/201525896.

Pointon, S. K, Kacprzak, G. G, Nielsen, N. M, Muzahid, S, Murphy, M. T, et al. Relationship between the Metallicity of the Circumgalactic Medium and Galaxy Orientation. *ApJ*, 883(1): 78, September 2019. doi: 10.3847/1538-4357/ab3b0e.

Polychroni, D, Schisano, E, Elia, D, Roy, A, Molinari, S, et al. Two Mass Distributions in the L 1641 Molecular Clouds: The Herschel Connection of Dense Cores and Filaments in Orion A. *ApJL*, 777(2):L33, November 2013. doi: 10.1088/2041-8205/777/2/L33.

Predehl, P & Schmitt, J. H. M. M. X-raying the interstellar medium: ROSAT observations of dust scattering halos. *A&A*, 500:459–475, January 1995.

Prevot, M. L, Lequeux, J, Maurice, E, Prevot, L, & Rocca-Volmerange, B. The typical interstellar extinction in the Small Magellanic Cloud. *A&A*, 132:389–392, March 1984.

Price, D. J & Federrath, C. A comparison between grid and particle methods on the statistics of driven, supersonic, isothermal turbulence. *MNRAS*, 406(3):1659–1674, Aug 2010. doi: 10.1111/j.1365-2966.2010.16810.x.

Price, D. J & Laibe, G. A fast and explicit algorithm for simulating the dynamics of small dust grains with smoothed particle hydrodynamics. *MNRAS*, 451(1):813–826, Jul 2015. doi: 10.1093/mnras/stv996.

Price, D. J, Federrath, C, & Brunt, C. M. The Density Variance-Mach Number Relation in Supersonic, Isothermal Turbulence. *ApJL*, 727(1):L21, Jan 2011. doi: 10.1088/2041-8205/727/1/L21.

Price, D. J, Wurster, J, Tricco, T. S, Nixon, C, Toupin, S, et al. Phantom: A Smoothed Particle Hydrodynamics and Magnetohydrodynamics Code for Astrophysics. *PASA*, 35:e031, Sep 2018. doi: 10.1017/pasa.2018.25.

Prochaska, J. X, Burchett, J. N, Tripp, T. M, Werk, J. K, Willmer, C. N. A, et al. The COS Absorption Survey of Baryon Harbors: The Galaxy Database and Cross-correlation Analysis of O VI Systems. *ApJS*, 243(2):24, August 2019. doi: 10.3847/1538-4365/ab2b9a.

Punsly, B. Evidence of the Dynamics of Relativistic Jet Launching in Quasars. *ApJ*, 806(1):47, June 2015. doi: 10.1088/0004-637X/806/1/47.

Qasim, D, Fedoseev, G, Chuang, K. J, He, J, Ioppolo, S, et al. An experimental study of the surface formation of methane in interstellar molecular clouds. *Nature Astronomy*, 4:781–785, April 2020. doi: 10.1038/s41550-020-1054-y.

R Core Team. *R: A Language and Environment for Statistical Computing*. R Foundation for Statistical Computing, Vienna, Austria, 2020. URL `https://www.R-project.org/`.

Rachford, B. L, Snow, T. P, Tumlinson, J, Shull, J. M, Blair, W. P, et al. A Far Ultraviolet Spectroscopic Explorer Survey of Interstellar Molecular Hydrogen in Translucent Clouds. *ApJ*, 577(1):221–244, September 2002. doi: 10.1086/342146.

Rai, R. K & Rastogi, S. Modelling anomalous extinction using nanodiamonds. *MNRAS*, 423(3): 2941–2948, July 2012. doi: 10.1111/j.1365-2966.2012.21109.x.

Rand, R. J & Lyne, A. G. New Rotation Measures of Distant Pulsars in the Inner Galaxy and Magnetic Field Reversals. *MNRAS*, 268:497, May 1994. doi: 10.1093/mnras/268.2.497.

Rand, R. J & Kulkarni, S. R. The Local Galactic Magnetic Field. *ApJ*, 343:760, August 1989. doi: 10.1086/167747.

Redfield, S, Wood, B. E, & Linsky, J. L. Physical structure of the local interstellar medium. *Advances in Space Research*, 34(1):41–45, January 2004. doi: 10.1016/j.asr.2003.02.053.

Redfield, S & Linsky, J. L. The Structure of the Local Interstellar Medium. I. High-Resolution Observations of Fe II, Mg II, and Ca II toward Stars within 100 Parsecs. *ApJS*, 139(2): 439–465, April 2002. doi: 10.1086/338650.

Reipurth, B. *Handbook of Star Forming Regions, Volume I: The Northern Sky*, volume 4. The Southern Sky ASP Monograph Publications, 2008a.

Reipurth, B. *Handbook of Star Forming Regions, Volume II: The Southern Sky*, volume 5. The Southern Sky ASP Monograph Publications, 2008b.

Reynolds, R. J. The Column Density and Scale Height of Free Electrons in the Galactic Disk. *ApJL*, 339:L29, April 1989. doi: 10.1086/185412.

Reynolds, R. J, Scherb, F, & Roesler, F. L. Observations of Diffuse Galactic HA and [n II] Emission. *ApJ*, 185:869–876, November 1973. doi: 10.1086/152461.

Rodríguez-Pascual, P. M, González-Riestra, R, Schartel, N, & Wamsteker, W. The IUE INES System: Improved data extraction procedures for IUE. *A&AS*, 139:183–197, October 1999. doi: 10.1051/aas:1999388.

Rogerson, J. B, Spitzer, L, Drake, J. F, Dressler, K, Jenkins, E. B, et al. Spectrophotometric Results from the Copernicus Satellite. I. Instrumentation and Performance. *ApJL*, 181:L97–L102, May 1973. doi: 10.1086/181194.

Roman-Duval, J, Israel, F. P, Bolatto, A, Hughes, A, Leroy, A, et al. Dust/gas correlations from Herschel observations. *A&A*, 518:L74, July 2010. doi: 10.1051/0004-6361/201014575.

Román-Zúñiga, C. G, Elston, R, Ferreira, B, & Lada, E. A. A FLAMINGOS Deep Near-Infrared Imaging Survey of the Rosette Complex. I. Identification and Distribution of the Embedded Population. *ApJ*, 672(2):861–887, January 2008. doi: 10.1086/523785.

Sagiv, I, Gal-Yam, A, Ofek, E. O, Waxman, E, Aharonson, O, et al. Science with a Wide-field UV Transient Explorer. *AJ*, 147(4):79, April 2014. doi: 10.1088/0004-6256/147/4/79.

Sanchez, N, Gómez de Castro, A. I, Lopez-Martinez, F, & López-Santiago, J. Young stellar object candidates toward the Orion region selected from GALEX. *A&A*, 572:A89, December 2014. doi: 10.1051/0004-6361/201424629.

Savage, A. H, Spangler, S. R, & Fischer, P. D. Probing the Rosette Nebula Stellar Bubble with Faraday Rotation. *ApJ*, 765(1):42, March 2013. doi: 10.1088/0004-637X/765/1/42.

Savage, B. D, Bohlin, R. C, Drake, J. F, & Budich, W. A survey of interstellar molecular hydrogen. I. *ApJ*, 216:291–307, August 1977. doi: 10.1086/155471.

Savage, B. D, Sembach, K. R, Jenkins, E. B, Shull, J. M, York, D. G, et al. Far Ultraviolet Spectroscopic Explorer Observations of O VI Absorption in the Galactic Halo. *ApJL*, 538(1): L27–L30, July 2000. doi: 10.1086/312792.

Savage, B. D & Lehner, N. Properties of O VI Absorption in the Local Interstellar Medium. *ApJS*, 162(1):134–160, January 2006. doi: 10.1086/497915.

Scalo, J. M. The Stellar Initial Mass Function. *FCPh*, 11:1–278, May 1986.

Schirmer, T, Abergel, A, Verstraete, L, Ysard, N, Juvela, M, et al. Dust evolution across the Horsehead nebula. *A&A*, 639:A144, July 2020. doi: 10.1051/0004-6361/202037937.

Schneider, N, Motte, F, Bontemps, S, Hennemann, M, di Francesco, J, et al. The Herschel view of star formation in the Rosette molecular cloud under the influence of NGC 2244. *A&A*, 518: L83, July 2010. doi: 10.1051/0004-6361/201014627.

Schneider, N, Csengeri, T, Hennemann, M, Motte, F, Didelon, P, et al. Cluster-formation in the Rosette molecular cloud at the junctions of filaments. *A&A*, 540:L11, April 2012. doi: 10.1051/0004-6361/201118566.

Schneider, S & Elmegreen, B. G. A catalog of dark globular filaments. *ApJS*, 41:87–95, September 1979. doi: 10.1086/190609.

Scowen, P. A, Ardila, D, Jensen, L, Gamaunt, J, Nikzad, S, et al. SPARCS payload assembly, integration, and test update. In *Society of Photo-Optical Instrumentation Engineers (SPIE) Conference Series*, volume 11444 of *Society of Photo-Optical Instrumentation Engineers (SPIE) Conference Series*, page 114440A, December 2020. doi: 10.1117/12.2562582.

Seab, C. G, Snow, T. P., J, & Joseph, C. L. Ultraviolet extinction curves derived from IUE data. *ApJ*, 246:788–793, June 1981. doi: 10.1086/158972.

Sembach, K. R, Savage, B. D, Shull, J. M, Jenkins, E. B, Murphy, E. M, et al. Far Ultraviolet Spectroscopic Explorer Observations of O VI in High-Velocity Clouds. *ApJL*, 538(1):L31–L34, July 2000. doi: 10.1086/312785.

Sharma, E, Gopinathan, M, Soam, A, Lee, C. W, Kim, S, et al. Distance, magnetic field, and kinematics of the filamentary cloud LDN 1157. *A&A*, 639:A133, July 2020. doi: 10.1051/0004-6361/202037438.

Shingledecker, C. N, Lamberts, T, Laas, J. C, Vasyunin, A, Herbst, E, et al. Efficient Production of S_8 in Interstellar Ices: The Effects of Cosmic-Ray-driven Radiation Chemistry and Nondiffusive Bulk Reactions. *ApJ*, 888(1):52, January 2020. doi: 10.3847/1538-4357/ab5360.

Shu, F. H, Adams, F. C, & Lizano, S. Star formation in molecular clouds: observation and theory. *ARA&A*, 25:23–81, January 1987. doi: 10.1146/annurev.aa.25.090187.000323.

Shull, J. M & van Steenberg, M. E. Galactic interstellar abundance surveys with IUE. I. Neutral hydrogen. *ApJ*, 294:599–614, July 1985. doi: 10.1086/163327.

Shustov, B, Gómez de Castro, A. I, Sachkov, M, Vallejo, J. C, Marcos-Arenal, P, et al. The World Space Observatory Ultraviolet (WSO-UV), as a bridge to future UV astronomy. *Ap&SS*, 363 (4):62, April 2018. doi: 10.1007/s10509-018-3280-7.

Simons, M. A. J, Lamberts, T, & Cuppen, H. M. Formation of COMs through CO hydrogenation on interstellar grains. *A&A*, 634:A52, February 2020. doi: 10.1051/0004-6361/201936522.

Simons, S & Williams, I. P. Growth of Interstellar Grains by Coagulation. *Ap&SS*, 32(2):493–498, Feb 1975. doi: 10.1007/BF00643159.

Singh, K. P, Tandon, S. N, Agrawal, P. C, Antia, H. M, Manchanda, R. K, et al. ASTROSAT mission. In Takahashi, T, den Herder, J.-W. A, & Bautz, M, editors, *Space Telescopes and Instrumentation 2014: Ultraviolet to Gamma Ray*, volume 9144 of *Society of Photo-Optical Instrumentation Engineers (SPIE) Conference Series*, page 91441S, July 2014. doi: 10.1117/12.2062667.

Sirk, M. M, Vallerga, J. V, Finley, D. S, Jelinsky, P, & Malina, R. F. Performance of the Extreme Ultraviolet Explorer Imaging Telescopes. *ApJS*, 110(2):347–356, June 1997. doi: 10.1086/313002.

Skrutskie, M. F, Cutri, R. M, Stiening, R, Weinberg, M. D, Schneider, S, et al. The Two Micron All Sky Survey (2MASS). *AJ*, 131(2):1163–1183, February 2006. doi: 10.1086/498708.

Smith, R. J, Glover, S. C. O, & Klessen, R. S. On the nature of star-forming filaments - I. Filament morphologies. *MNRAS*, 445(3):2900–2917, December 2014. doi: 10.1093/mnras/stu1915.

Snow, T. P., J. The depletion of interstellar elements and the interaction between gas and dust in space. *ApJL*, 202:L87–L90, December 1975. doi: 10.1086/181987.

Snow, T. P & McCall, B. J. Diffuse Atomic and Molecular Clouds. *ARA&A*, 44(1):367–414, September 2006. doi: 10.1146/annurev.astro.43.072103.150624.

Sofia, U. J, Wolff, M. J, Rachford, B, Gordon, K. D, Clayton, G. C, et al. FUSE Measurements of Far-Ultraviolet Extinction. I. Galactic Sight Lines. *ApJ*, 625(1):167–180, May 2005. doi: 10.1086/429690.

Somerville, W. B, Allen, R. G, Carnochan, D. J, He, L, McNally, D, et al. Ultraviolet Interstellar Polarization Observed with the Hubble Space Telescope. *ApJL*, 427:L47, May 1994. doi: 10.1086/187361.

Sorathia, K. A, Reynolds, C. S, Stone, J. M, & Beckwith, K. Global Simulations of Accretion Disks. I. Convergence and Comparisons with Local Models. *ApJ*, 749(2):189, April 2012. doi: 10.1088/0004-637X/749/2/189.

Spitzer, L., J & Jenkins, E. B. Ultraviolet studies of the interstellar gas. *ARA&A*, 13:133–164, January 1975. doi: 10.1146/annurev.aa.13.090175.001025.

Spitzer, Lyman, J. Behavior of Matter in Space. *ApJ*, 120:1, July 1954. doi: 10.1086/145876.

Spitzer, Lyman, J & Zabriskie, F. R. Interstellar Research with a Spectroscopic Satellite. *PASP*, 71(422):412, October 1959. doi: 10.1086/127416.

Spitzer, L, Drake, J. F, Jenkins, E. B, Morton, D. C, Rogerson, J. B, et al. Spectrophotometric Results from the Copernicus Satellite.IV. Molecular Hydrogen in Interstellar Space. *ApJL*, 181:L116, May 1973. doi: 10.1086/181197.

Springel, V. The cosmological simulation code GADGET-2. *MNRAS*, 364(4):1105–1134, Dec 2005. doi: 10.1111/j.1365-2966.2005.09655.x.

Springel, V. E pur si muove: Galilean-invariant cosmological hydrodynamical simulations on a moving mesh. *MNRAS*, 401(2):791–851, Jan 2010. doi: 10.1111/j.1365-2966.2009.15715.x.

Stecher, T. P & Donn, B. On Graphite and Interstellar Extinction. *ApJ*, 142:1681, November 1965. doi: 10.1086/148461.

Stecher, T. P. Interstellar Ectinction in the Ultraviolet. *ApJ*, 142:1683, November 1965. doi: 10.1086/148462.

Stecher, T. P & Milligan, J. E. Stellar Spectrophotometry from above the Atmosphere. *ApJ*, 136:1, July 1962. doi: 10.1086/147346.

Stephens, T. L & Dalgarno, A. Kinetic Energy in the Spontaneous Radiative Dissociation of Molecular Hydrogen. *ApJ*, 186:165–168, November 1973. doi: 10.1086/152484.

Stone, J. M & Gardiner, T. A. Implementation of the Shearing Box Approximation in Athena. *ApJS*, 189(1):142–155, July 2010. doi: 10.1088/0067-0049/189/1/142.

Stone, J. M & Norman, M. L. ZEUS-2D: A Radiation Magnetohydrodynamics Code for Astrophysical Flows in Two Space Dimensions. I. The Hydrodynamic Algorithms and Tests. *ApJS*, 80:753, Jun 1992a. doi: 10.1086/191680.

Stone, J. M & Norman, M. L. ZEUS-2D: A Radiation Magnetohydrodynamics Code for Astrophysical Flows in Two Space Dimensions. II. The Magnetohydrodynamic Algorithms and Tests. *ApJS*, 80:791, Jun 1992b. doi: 10.1086/191681.

Stone, J. M, Mihalas, D, & Norman, M. L. ZEUS-2D: A Radiation Magnetohydrodynamics Code for Astrophysical Flows in Two Space Dimensions. III. The Radiation Hydrodynamic Algorithms and Tests. *ApJS*, 80:819, Jun 1992. doi: 10.1086/191682.

Stone, J. M, Gardiner, T. A, Teuben, P, Hawley, J. F, & Simon, J. B. Athena: A New Code for Astrophysical MHD. *ApJS*, 178(1):137–177, Sep 2008. doi: 10.1086/588755.

Subramaniam, A, Sahu, S, Postma, J. E, Côté, P, Hutchings, J. B, et al. The Horizontal Branch Population of NGC 1851 as Revealed by the Ultraviolet Imaging Telescope (UVIT). *AJ*, 154 (6):233, December 2017. doi: 10.3847/1538-3881/aa94c3.

Sujatha, N. V, Murthy, J, Karnataki, A, Henry, R. C, & Bianchi, L. GALEX Observations of Diffuse UV Radiation at High Spatial Resolution from the Sandage Nebulosity. *ApJ*, 692(2): 1333–1338, February 2009. doi: 10.1088/0004-637X/692/2/1333.

Sun, M, Jiang, B. W, Zhao, H, Gao, J, Gao, S, et al. The Ultraviolet Extinction in the GALEX Bands. *ApJ*, 861(2):153, July 2018. doi: 10.3847/1538-4357/aac776.

Sun, W, Chen, Y, Feng, L, Chu, Y.-H, Chen, C. H. R, et al. Giant H II Regions in M101. I. X-Ray Analysis of Hot Gas. *ApJ*, 760(1):61, November 2012. doi: 10.1088/0004-637X/760/1/61.

Taff, L. G & Savedoff, M. P. The mass distribution of objects under-going collisions with applications to interstellar HI clouds. *MNRAS*, 164:357, January 1973. doi: 10.1093/mnras/164.4.357.

Tamfal, T, Drażkowska, J, Mayer, L, & Surville, C. A Subgrid Model for the Growth of Dust Particles in Hydrodynamical Simulations of Protoplanetary Disks. *ApJ*, 863(1):97, August 2018. doi: 10.3847/1538-4357/aad1f4.

Tandon, S. N, Hutchings, J. B, Ghosh, S. K, Subramaniam, A, Koshy, G, et al. In-orbit Performance of UVIT and First Results. *Journal of Astrophysics and Astronomy*, 38(2):28, June 2017. doi: 10.1007/s12036-017-9445-x.

Teyssier, R. Cosmological hydrodynamics with adaptive mesh refinement. A new high resolution code called RAMSES. *A&A*, 385:337–364, Apr 2002. doi: 10.1051/0004-6361:20011817.

The LUVOIR Team. The LUVOIR Mission Concept Study Final Report. *arXiv e-prints*, art. arXiv:1912.06219, December 2019.

Tricco, T. S & Price, D. J. Constrained hyperbolic divergence cleaning for smoothed particle magnetohydrodynamics. *Journal of Computational Physics*, 231(21):7214–7236, Aug 2012. doi: 10.1016/j.jcp.2012.06.039.

Tricco, T. S, Price, D. J, & Bate, M. R. Constrained hyperbolic divergence cleaning in smoothed particle magnetohydrodynamics with variable cleaning speeds. *Journal of Computational Physics*, 322:326–344, Oct 2016. doi: 10.1016/j.jcp.2016.06.053.

Troland, T. H & Heiles, C. Interstellar Magnetic Field Strengths and Gas Densities: Observational and Theoretical Perspectives. *ApJ*, 301:339, February 1986. doi: 10.1086/163904.

Trumpler, R. J. Preliminary results on the distances, dimensions and space distribution of open star clusters. *Lick Observatory Bulletin*, 420:154–188, January 1930. doi: 10.5479/ADS/bib/1930LicOB.14.154T.

Tumlinson, J, Shull, J. M, Rachford, B. L, Browning, M. K, Snow, T. P, et al. A Far Ultraviolet Spectroscopic Explorer Survey of Interstellar Molecular Hydrogen in the Small and Large Magellanic Clouds. *ApJ*, 566(2):857–879, February 2002. doi: 10.1086/338112.

Valls-Gabaud, D & MESSIER Collaboration. The MESSIER surveyor: unveiling the ultra-low surface brightness universe. In Gil de Paz, A, Knapen, J. H, & Lee, J. C, editors, *Formation and Evolution of Galaxy Outskirts*, volume 321, pages 199–201, March 2017. doi: 10.1017/S1743921316011388.

van der Walt, S, Schönberger, J. L, Nunez-Iglesias, J, Boulogne, F, Warner, J. D, et al. scikit-image: image processing in Python. *PeerJ*, 2:e453, 6 2014. ISSN 2167-8359. doi: 10.7717/peerj.453. URL `https://doi.org/10.7717/peerj.453`.

van Rhijn, P. J. Distribution of Stars According to Apparent Magnitude, Galactic Latitude and Galactic Longitude. *Publications of the Kapteyn Astronomical Laboratory Groningen*, 43:1–104, January 1929.

Vennes, S, Dupuis, J, Rumph, T, Drake, J, Bowyer, S, et al. The First Detection of Ionized Helium in the Local ISM: EUVE and IUE Spectroscopy of the Hot DA Dwarf GD 246. *ApJL*, 410:L119, June 1993. doi: 10.1086/186894.

Walch, S. K, Whitworth, A. P, Bisbas, T, Wünsch, R, & Hubber, D. Dispersal of molecular clouds by ionizing radiation. *MNRAS*, 427(1):625–636, November 2012. doi: 10.1111/j.1365-2966.2012.21767.x.

Weidenschilling, S. J. Aerodynamics of solid bodies in the solar nebula. *MNRAS*, 180:57–70, July 1977. doi: 10.1093/mnras/180.1.57.

Weingartner, J. C & Draine, B. T. Dust Grain-Size Distributions and Extinction in the Milky Way, Large Magellanic Cloud, and Small Magellanic Cloud. *ApJ*, 548(1):296–309, February 2001a. doi: 10.1086/318651.

Weingartner, J. C & Draine, B. T. Photoelectric Emission from Interstellar Dust: Grain Charging and Gas Heating. *ApJS*, 134(2):263–281, June 2001b. doi: 10.1086/320852.

Weingartner, J. C, Draine, B. T, & Barr, D. K. Photoelectric Emission from Dust Grains Exposed to Extreme Ultraviolet and X-Ray Radiation. *ApJ*, 645(2):1188–1197, July 2006. doi: 10.1086/504420.

Welsh, B. Y & Lallement, R. OVI in the local interstellar medium: FUSE observations towards B-stars within 200 pc. *A&A*, 490(2):707–714, November 2008. doi: 10.1051/0004-6361:200810221.

Welsh, B. Y, Sfeir, D. M, Sirk, M. M, & Lallement, R. EUV mapping of the local interstellar medium: the Local Chimney revealed? *A&A*, 352:308–316, December 1999.

Welsh, B. Y, Lallement, R, Vergely, J. L, & Raimond, S. New 3D gas density maps of NaI and CaII interstellar absorption within 300 pc. *A&A*, 510:A54, February 2010. doi: 10.1051/0004-6361/200913202.

Wilson, R. W, Jefferts, K. B, & Penzias, A. A. Carbon Monoxide in the Orion Nebula. *ApJL*, 161:L43, July 1970. doi: 10.1086/180567.

Windmark, F, Birnstiel, T, Güttler, C, Blum, J, Dullemond, C. P, et al. Planetesimal formation by sweep-up: how the bouncing barrier can be beneficial to growth. *A&A*, 540:A73, April 2012. doi: 10.1051/0004-6361/201118475.

Witt, A. N, Bohlin, R. C, & Stecher, T. P. The variation of galactic interstellar extinction in the ultraviolet. *ApJ*, 279:698–704, April 1984. doi: 10.1086/161934.

Wolfire, M. G, Hollenbach, D, McKee, C. F, Tielens, A. G. G. M, & Bakes, E. L. O. The Neutral Atomic Phases of the Interstellar Medium. *ApJ*, 443:152, April 1995. doi: 10.1086/175510.

Wolfire, M. G, Hollenbach, D, & McKee, C. F. The Dark Molecular Gas. *ApJ*, 716(2):1191–1207, June 2010. doi: 10.1088/0004-637X/716/2/1191.

Wood, B. E, Redfield, S, Linsky, J. L, Müller, H.-R, & Zank, G. P. Stellar Lyα Emission Lines in the Hubble Space Telescope Archive: Intrinsic Line Fluxes and Absorption from the Heliosphere and Astrospheres. *ApJS*, 159(1):118–140, July 2005. doi: 10.1086/430523.

Wurster, J, Price, D. J, & Bate, M. R. Can non-ideal magnetohydrodynamics solve the magnetic braking catastrophe? *MNRAS*, 457(1):1037–1061, Mar 2016. doi: 10.1093/mnras/stw013.

Wurster, J, Price, D. J, & Bate, M. R. The impact of non-ideal magnetohydrodynamics on binary star formation. *MNRAS*, 466(2):1788–1804, Apr 2017. doi: 10.1093/mnras/stw3181.

Yan, H, Lazarian, A, & Draine, B. T. Dust Dynamics in Compressible Magnetohydrodynamic Turbulence. *ApJ*, 616(2):895–911, Dec 2004. doi: 10.1086/425111.

Ybarra, J. E, Lada, E. A, Román-Zúñiga, C. G, Balog, Z, Wang, J, et al. The Progression of Star Formation in the Rosette Molecular Cloud. *ApJ*, 769(2):140, June 2013. doi: 10.1088/0004-637X/769/2/140.

York, D. G. Highly Ionized Atoms Observed with Copernicus. *ApJL*, 193:L127, November 1974. doi: 10.1086/181648.

York, D. G. The interstellar medium near the sun: the line of sight to Lambda Scorpii. *ApJL*, 196:L103–L106, March 1975. doi: 10.1086/181754.

York, D. G, Spitzer, L, Bohlin, R. C, Hill, J, Jenkins, E. B, et al. Interstellar abundances of oxygen and nitrogen. *ApJL*, 266:L55–L59, March 1983. doi: 10.1086/183977.

Youdin, A. N & Goodman, J. Streaming Instabilities in Protoplanetary Disks. *ApJ*, 620(1):459–469, February 2005. doi: 10.1086/426895.

Zhukhovitskii, D. I, Petrov, O. F, Hyde, T. W, Herdrich, G, Laufer, R, et al. Electrical conductivity of the thermal dusty plasma under the conditions of a hybrid plasma environment simulation facility. *New Journal of Physics*, 17(5):053041, May 2015. doi: 10.1088/1367-2630/17/5/053041.

Zinner, E. *Presolar Grains*, volume 1, pages 181–213. Davis, Andrew M., 2014.

Zsom, A & Dullemond, C. P. A representative particle approach to coagulation and fragmentation of dust aggregates and fluid droplets. *A&A*, 489(2):931–941, Oct 2008. doi: 10.1051/0004-6361:200809921.

Zsom, A, Ormel, C. W, Güttler, C, Blum, J, & Dullemond, C. P. The outcome of protoplanetary dust growth: pebbles, boulders, or planetesimals? II. Introducing the bouncing barrier. *A&A*, 513:A57, April 2010. doi: 10.1051/0004-6361/200912976.

Zuckerman, B & Evans, N. J., I. Models of Massive Molecular Clouds. *ApJL*, 192:L149, September 1974. doi: 10.1086/181613.

Zuckerman, B & Palmer, P. On the Orion infrared nebula/molecular cloud. *ApJL*, 199:L35–L38, July 1975. doi: 10.1086/181843.